



UNIVERSIDAD DE CHILE

FACULTAD DE CIENCIAS FÍSICAS Y MATEMÁTICAS

DEPARTAMENTO DE GEOLOGÍA

**SIGNATURA GEOQUÍMICA DE LOS SULFUROS DE MENA Y GANGA EN
EL YACIMIENTO DE CHUQUICAMATA SUBTERRÁNEO, CHILE**

**TESIS PARA OPTAR AL GRADO DE MAGÍSTER EN CIENCIAS, MENCIÓN GEOLOGÍA
MEMORIA PARA OPTAR AL TÍTULO DE GEÓLOGA**

CONSTANZA ALEJANDRA RIVAS ROMERO

PROFESOR GUÍA:
MARTIN REICH MORALES

MIEMBROS DE LA COMISIÓN:
FERNANDO BARRA PANTOJA
SERGIO PICHOTT HENRÍQUEZ

Este trabajo ha sido financiado por el Núcleo Milenio Trazadores de Metales

SANTIAGO DE CHILE
2020

**RESUMEN DE LA TESIS PARA OPTAR AL
GRADO DE:** Magíster en Ciencias, Mención
Geología.

POR: Constanza Rivas Romero

FECHA: Julio 2020

PROFESOR GUÍA: Martin Reich Morales

SIGNATURA GEOQUÍMICA DE LOS SULFUROS DE MENA Y GANGA EN EL YACIMIENTO CHUQUICAMATA SUBTERRÁNEO, CHILE

Los depósitos de pórfido Cu-Mo son una de las fuentes más importantes de Cu, Mo, Re y también de otros elementos traza como Au y Ag. A pesar de que la calcopirita, bornita y pirita son los sulfuros más comunes en este tipo de depósito, su signatura geoquímica se encuentra poco identificada. En particular, existe poca información acerca de la partición de elementos traza en los diferentes sulfuros de Cu-(Fe) durante los eventos de alteración hidrotermal y su vínculo como herramienta de exploración.

En este estudio, reportamos una base de datos geoquímica de calcopirita, bornita y pirita en el pórfido Cu-Mo Chuquicamata, ubicado en el norte de Chile. El objetivo de este estudio, el cual se encuentra enfocado en la nueva mina Chuquicamata Subterránea, fue el de evaluar cómo la presencia y asociación de elementos traza de cada uno de los sulfuros se relaciona con las diferentes alteraciones hidrotermales en el depósito. El estudio integra observaciones petrográficas de detalle, datos de análisis mediante microsonda electrónica (EMPA) y espectrometría de masas por plasma inductivamente acoplado con ablación láser (LA-ICP-MS) de los distintos sulfuros, en muestras obtenidas a partir de seis sondajes representativos del yacimiento, que interceptan las alteraciones cloríticas, potásica de fondo, potásica intensa y cuarzo-sericita.

Los resultados microanalíticos muestran que la calcopirita, bornita y pirita contienen un amplio rango de elementos traza, los cuales pueden variar de manera significativa entre las diferentes alteraciones hidrotermales. La calcopirita, por ejemplo, es un buen huésped de Se (≤ 11.000 ppm), Ag ($\leq 45,1$ ppm), Bi ($\leq 25,9$ ppm) e In ($\leq 22,8$ ppm). Las mayores concentraciones de Se e In en la calcopirita se encuentran asociadas a la alteración potásica de fondo, la cual corresponde a la de mayor temperatura, mientras que las menores concentraciones de estos dos elementos se encuentran asociadas con la alteración cuarzo-sericita que es de más baja temperatura. La bornita, por otra parte, corresponde al mayor huésped de Ag (≤ 752 ppm) y Bi (≤ 2.960 ppm) en el depósito, sin embargo, no se observaron correlaciones entre estos dos elementos en función de la alteración. En contraste, las altas concentraciones de Ag y Sn en bornita se encuentran asociadas con la alteración potásica intensa, mientras que concentraciones más bajas de estos dos elementos se encuentran asociadas con la alteración potásica de fondo. En los sulfuros analizados, la pirita corresponde al mayor huésped de elementos traza, con concentraciones significativas de Co (≤ 1.530 ppm), Ni (≤ 960 ppm), Cu (≤ 9.700 ppm) y Ag (≤ 450 ppm). Las concentraciones de Co, Ni, Ag y Cu en la pirita varían en las diferentes alteraciones: altas concentraciones de Ag y Cu se encuentran relacionadas con la alteración de alta temperatura (potásica de fondo), mientras que altos contenidos de Co se encuentran asociados con la alteración de menor temperatura (clorítica).

Los datos obtenidos indican que las concentraciones de elementos traza en calcopirita, bornita y pirita variaron en función de la alteración hidrotermal, y fueron probablemente resultado de cambios en las condiciones fisicoquímicas gobernantes durante la precipitación de los sulfuros (ej., temperatura, pH, f_{O_2} y/o la presencia de fases co-cristalizantes). En general, los resultados presentados en esta tesis proporcionan nueva información acerca de la partición de elementos traza en los distintos sulfuros de Cu-(Fe) en el depósito, y como éstos se relacionan con los principales eventos hidrotermales y de mineralización, controlando el *budget elemental* en Chuquicamata. En particular, nuestros datos muestran que las razones elementales en calcopirita (ej., Se/In) y pirita (ej., Ag/Co y Co/Cu) tienen un potencial de aplicación prometedor para vectorizar hacia la mineralización del pórfido y explorar zonas con recursos de mayores leyes.

A mis abuelitos, Amanda y René

*“Sé como el sándalo, que perfuma
el hacha del leñador que lo hiere”*
Rabindranath Tagore

AGRADECIMIENTOS

En primer lugar, quisiera agradecer a mi Profesor Guía, Martin Reich, por todo el apoyo brindado durante el desarrollo de este trabajo, por las enseñanzas entregadas, por siempre tener una gran disposición y entregar tranquilidad cuando se presentaron dificultades y, sobre todo, darme la confianza y motivación necesarias para desarrollar de buena manera la investigación. Del mismo modo, agradezco al profesor Fernando Barra por su ayuda y consejos, así como a Sergio Pichott, por darme la oportunidad de desarrollar este trabajo en Chuquicamata, el apoyo brindado y por la confianza depositada. También, a Daniel Gregory, por recibirme en Toronto, ayudarme con los análisis de microsonda, y por sus consejos y contribuciones al trabajo.

Quiero también agradecer al Núcleo Milenio Trazadores de Metales por el apoyo financiero entregado, y al Centro de Excelencia en Geotermia de Los Andes. Además, quisiera agradecer a la Gerencia de Exploraciones de Codelco, por la gestión y ayuda durante la etapa de muestreo, en especial a Bárbara Rey, quien se encargó de todos los aspectos técnicos. Igualmente, deseo destacar el apoyo de la SI de Geología de la División Chuquicamata de Codelco, por la información entregada y su gran disposición, en especial a Fernando Ramírez, quien me ayudó con el muestreo.

A los miembros de la Universidad de Chile, quienes de alguna u otra forma me ayudaron a lo largo de esta investigación. Gracias a Christian Nievias por su ayuda en el SEM, a Rurik Romero por su paciencia y gran ayuda para poder obtener los análisis de sulfuros mediante LA-ICP-MS, a pesar de todas las dificultades. También, a Blanca Baccolla y Maritza Acuña, quienes me ayudaron enormemente cada vez que tenía algún problema administrativo. A Yanan Liu de la Universidad de Toronto, quien me ayudó durante todo el análisis de microsonda electrónica. Este trabajo no habría sido lo mismo sin la ayuda de mis compañeros del Núcleo, así que les agradezco enormemente todas las ideas brindadas, sugerencias y apoyo cada vez que se presentó alguna dificultad. A mis amigas: Conita y Macarena, que siempre han estado a mi lado, dándome ánimo cuando lo he necesitado, gracias por mantener su amistad a lo largo de tantos años.

A mis padres, quienes me han dado su apoyo incondicional no tan solo a lo largo de la etapa universitaria, sino que a lo largo de toda mi vida. Gracias por todo lo que han hecho por mí, sus enseñanzas y su amor han sido el motor de todo este trabajo. Gracias por enseñarme a no rendirme nunca, a dar lo mejor en todo momento y por siempre estar cuando los he necesitado. No existen palabras para agradecer todo lo que han hecho por mí, los amo infinitamente. También, quisiera darle un gracias gigante a mi hermana mayor, quien siempre me ha cuidado y ha sido un apoyo fundamental a lo largo de toda mi vida, gracias hermanita por cuidarme y amarme, y a pesar de la distancia siempre estar pendiente, gracias por tener confianza en mí y darme el ejemplo, gran parte de la persona que soy hoy, te lo debo a ti. A mi cuñado, Sebastián, por su amistad y apoyo a lo largo de todos estos años. A mi abuelita que ya no se encuentra conmigo, pero sus enseñanzas no quedan indiferentes en estas líneas, gracias abuelita por enseñarme a luchar, no he conocido nunca a una mujer tan fuerte como tú y espero algún día llegar a ser la mitad de la mujer que eras, siempre te llevaré en mi corazón y tus enseñanzas y amor incondicional seguirán impregnados en mí para toda la vida. Finalmente, quisiera agradecer a Nicole, quien ha estado conmigo a lo largo de todo este camino y ha vivido tanto mis éxitos como frustraciones, gracias por la paciencia y el apoyo incondicional, por estar ahí cuando más lo he necesitado y calmarme en los momentos más difíciles, por entregarle felicidad a mi vida, sin tu apoyo no habría podido recorrer todo este camino, gracias por permitirme aprender de ti todos los días y hacerme crecer como persona. Eres una persona maravillosa y única que la vida me permitió conocer, y agradezco cada momento a tu lado.

TABLA DE CONTENIDO

CAPÍTULO 1: INTRODUCCIÓN	1
1.1 Estructura de la Tesis	1
1.2 Motivación	1
1.3 Objetivos	3
1.3.1 Objetivo general	3
1.3.2 Objetivos específicos	3
1.4 Hipótesis de trabajo	4
1.5 Publicaciones y resúmenes resultantes de este trabajo	4
1.5.1 Publicaciones	4
1.5.2 Resúmenes en congreso.....	4
CAPÍTULO 2: THE RELATION BETWEEN TRACE ELEMENT COMPOSITION OF CU-(FE) SULFIDES AND HYDROTHERMAL ALTERATION IN A PORPHYRY COPPER DEPOSIT: INSIGHTS FROM THE CHUQUICAMATA UNDERGROUND MINE, CHILE	5
2.1 ABSTRACT	5
2.2. INTRODUCTION	6
2.3 GEOLOGICAL BACKGROUND	7
2.4 SAMPLES AND METHODS	9
2.5 RESULTS	11
2.5.1 Hydrothermal alteration and mineralization.....	11
2.5.2 Sulfide textures and mineral inclusions.....	12
2.5.3 Major, minor and trace elements concentrations in sulfide minerals	12
2.5.3.1 Chalcopyrite	13
2.5.3.2 Bornite	13
2.5.3.3 Pyrite.....	14
2.6 DISCUSSION.....	14
2.6.1 Incorporation of trace elements in chalcopyrite, bornite and pyrite.....	14
2.6.2 Geochemical signature of Cu-(Fe) sulfides as a function of alteration	16
2.6.3 Implications for sulfides as vectors towards Cu mineralization.....	19
2.7 CONCLUDING REMARKS	20
2.8 ACKNOWLEDGMENTS	21
2.9 REFERENCES	22
2.10 FIGURES	31
CAPÍTULO 3: CONCLUSIONES	41

BIBLIOGRAFÍA	43
ANEXOS	46
ANEXO A: Anexo Metodológico	46
A.1 Condiciones de análisis SEM	46
A.2 Condiciones de análisis EMPA	46
A.3 Condiciones de análisis LA-ICP-MS	46
A.2 Análisis estadístico de datos composicionales	47
A.2.1 Estadística descriptiva	47
A.2.2 Análisis exploratorio de datos	47
A.3 Referencias Anexo Metodológico	47
ANEXO B: Gráficos complementarios datos con inclusiones vs. sin inclusiones	49
B.1 Calcopirita.....	49
B.2 Bornita	50
B.3 Pirlita.....	51
ANEXO C: Resultados de análisis EMPA en calcopirita del yacimiento Chuquicamata Subterráneo	52
ANEXO D: Resultados de análisis EMPA en bornita del yacimiento Chuquicamata Subterráneo	57
ANEXO E: Resultados de análisis EMPA en pirita del yacimiento Chuquicamata Subterráneo	60
ANEXO F: Resultados de análisis LA-ICP-MS en calcopirita del yacimiento Chuquicamata Subterráneo	67
ANEXO G: Resultados de análisis LA-ICP-MS en bornita del yacimiento Chuquicamata Subterráneo	74
ANEXO H: Resultados de análisis LA-ICP-MS en pirita del yacimiento Chuquicamata Subterráneo	78

ÍNDICE DE FIGURAS

- Figure 1.** A) Location of the Chuquicamata porphyry Cu-Mo deposit in relation to other deposits in the Antofagasta region, northern Chile. B) Geological map of the Chuquicamata District. Modified from Zentilli et al. (2018). 31
- Figure 2.** Geology of the Chuquicamata porphyry Cu-Mo deposit. Modified from Ossandón et al. (2001). 32
- Figure 3.** Representative cross-section showing the distribution of alteration zones in the Chuquicamata Underground mine. The upper limit of the alteration zones correspond to the bottom of the Chuquicamata open pit. Drill cores CHDD4587 and CHDD7808 are also shown. Relative position of selected samples within the drill cores are shown in gray and white..... 33
- Figure 4.** Photographs of main veinlet-types recognized at the Chuquicamata Underground mine. A) “A”-type veinlets with quartz and a halo of biotite; B) Chlorite veinlets with magnetite cross-cutting K-feldspar alteration; C) Hematite veinlets with magnetite; D) Pyrite veinlets with chlorite and magnetite associated to chloritic alteration; E) Chalcopyrite veinlets; F) “B”-type veinlet composed of quartz and molybdenite; G) “D”-type veinlet with pyrite-quartz-molybdenite-enargite; H) “D”-type veinlet with pyrite-chalcocite. Cc: Chalcocite, Chl: Chlorite, Cpy: Chalcopyrite, En: Enargite, Hm: Hematite, Kfs: K feldspar, Mt: Magnetite, Mb: Molybdenite, Pg: Plagioclase, Py: Pyrite, Qz: Quartz, Ser: Sericite..... 34
- Figure 5.** Paragenetic sequence described for the Chuquicamata Underground deposit. *Data sources: Sillitoe and McKee (1996), Reynolds et al. (1998), Mathur et al. (2001), Ballard et al. (2001), Rivera et al. (2012) and Barra et al. (2013) 35
- Figure 6.** Reflected light photomicrographs and SEM images of chalcopyrite, bornite and pyrite from representative samples. A) Pyrite-chalcopyrite veinlet from the chloritic alteration; B) Chalcopyrite replaced by covellite and digenite from the intense potassic alteration; C) Covellite and bornite replacing chalcopyrite from the intense potassic alteration; D) Pyrite-digenite-covellite veinlet in the quartz-sericite alteration; E) Scheelite micro-inclusion in chalcopyrite from the background potassic alteration zone; F) Au-Ag-tellurides micro-inclusions in bornite from the intense potassic alteration zone; G) Wittichenite inclusions in bornite-digenite in the quartz-sericite alteration zone; H) Wolframite micro-inclusion in pyrite from the quartz-sericite alteration zone. Bn: Bornite, Ccp: Chalcopyrite, Cv: Covellite, Dg: Digenite, Eng: Enargite, Py: Pyrite, Sch: Scheelite, Wf: Wolframite, Witt: Wittichenite..... 36
- Figure 7.** Concentration plot for minor and trace elements in sulfides from Chuquicamata Underground mine. Data are plotted in parts per million (ppm) on a vertical logarithmic scale. In each boxplot, minimum, median and maximum concentrations are marked, and the number of analyses above detection limit for each element is displayed inside each box. A) Boxplot of LA-ICP-MS data for selected minor and trace elements separated by sulfide (chalcopyrite, bornite and pyrite). B-D) Boxplot of LA-ICP-MS data for selected minor and trace element in chalcopyrite, bornite and pyrite (respectively) from different alteration zones in Chuquicamata Underground mine. 37
- Figure 8.** Representative LA-ICP-MS depth-concentration profiles (time vs. intensity) of selected isotopes in sulfides (chalcopyrite, bornite and pyrite). A) Depth-concentration profile of spot analysis from chalcopyrite, where flat signals are identified. B) Depth-concentration profile of spot analysis from bornite, where flat signals are identified. C) Depth-concentration profile of spot analysis from pyrite, where mostly “flat” signals are identified. D) Depth-concentration profile of spot analysis from pyrite, where the presence of galena, wittichenite (coupled ^{63}Cu and ^{209}Bi peaks), Cu, Co and Ag mineral particles are identified..... 38

- Figure 9.** Elemental concentration scatterplots in sulfides as a function of alteration from the Chuquicamata Underground deposit. A) In vs. Se scatterplot for chalcopyrite. B) Ag vs. Bi scatterplot for bornite. C) Ag vs. Sn scatterplot for bornite. D) Co vs. Ni scatterplot for pyrite. E) Ag vs. Co scatterplot for pyrite. F) Co vs. Cu scatterplot for pyrite. Data are plotted in parts per million (ppm) on a logarithmic scale. Only LA-ICP-MS data included. 39
- Figure 10.** A) Se/In ratios of chalcopyrite from Chuquicamata Underground deposit as a function of alteration. The average of each element ratio for each alteration is observed next to the horizontal line. B) Ag/Co vs Co/Cu scatterplot for pyrite from Chuquicamata Underground deposit. Data are plotted in parts per million (ppm) on a logarithmic scale. Only LA-ICP-MS data included. 40
- Figura 11.** Concentraciones de elementos menores y traza en calcopirita del yacimiento Chuquicamata Subterráneo. Todos los datos LA-ICP-MS se encuentran poteados en partes por millón (ppm) en una escala vertical logarítmica. En los boxplots, el color azul representa a todos los datos de LA-ICP-MS, mientras que en color blanco se observan los datos libres de inclusiones. En cada boxplot se muestran las concentraciones mínimas, máximas y la mediana, y el número de análisis sobre el límite de detección para cada elemento se encuentra dentro de cada caja. 49
- Figura 12.** Concentraciones de elementos menores y traza en bornita del yacimiento Chuquicamata Subterráneo. Todos los datos LA-ICP-MS se encuentran poteados en partes por millón (ppm) en una escala vertical logarítmica. En los boxplots, el color morado representa a todos los datos de LA-ICP-MS, mientras que en color blanco se observan los datos libres de inclusiones. En cada boxplot se muestran las concentraciones mínimas, máximas y la mediana, y el número de análisis sobre el límite de detección para cada elemento se encuentra dentro de cada caja. 50
- Figura 13.** Concentraciones de elementos menores y traza en pirita del yacimiento Chuquicamata Subterráneo. Todos los datos LA-ICP-MS se encuentran poteados en partes por millón (ppm) en una escala vertical logarítmica. En los boxplots, el color amarillo representa a todos los datos de LA-ICP-MS, mientras que en color blanco se observan los datos libres de inclusiones. En cada boxplot se muestran las concentraciones mínimas, máximas y la mediana, y el número de análisis sobre el límite de detección para cada elemento se encuentra dentro de cada caja. 51

CAPÍTULO 1: INTRODUCCIÓN

1.1 Estructura de la Tesis

El presente trabajo se centró en el estudio de la geoquímica de los sulfuros de mena (calcopirita y bornita) y ganga (pirita) en el yacimiento de pórfido Cu-Mo de Chuquicamata, ubicado en la Región de Antofagasta, Chile. En específico, la tesis se centró en el estudio de muestras obtenidas de sondajes de la nueva mina Chuquicamata Subterránea, la cual comenzó sus operaciones el año 2019. Para ello, se realizó la caracterización detallada de las principales asociaciones minerales presentes en las distintas zonas de alteración hidrotermal identificadas en el yacimiento.

La presente tesis se encuentra organizada en tres capítulos. En el presente capítulo introductorio (Capítulo 1), se presenta un marco general del problema a estudiar junto con los objetivos del estudio. El Capítulo 2 concentra toda la información obtenida en la tesis, la cual se presenta en un manuscrito en inglés titulado “The relation between trace element composition of Cu-(Fe) sulfides and hydrothermal alteration in a porphyry copper deposit: insights from the Chuquicamata Underground mine, Chile”, el cual se encuentra en revisión en la revista *Mineralium Deposita*. En éste, se presenta el marco geológico, los métodos, resultados y discusiones del estudio. Finalmente, en el Capítulo 3 se presentan las principales conclusiones de la tesis.

De manera adicional, se han incluido anexos que contienen información suplementaria y de apoyo a la tesis. El Anexo A consiste en un anexo que incluye detalles metodológicos de los análisis realizados mediante microscopía electrónica de barrido (SEM), microsonda electrónica (EMPA) y espectrometría de masas por plasma inductivamente acoplado con ablación láser (LA-ICP-MS), además de presentar la metodología para el tratamiento estadístico de los datos. En el Anexo B se reportan gráficos composicionales de los distintos sulfuros distinguiendo entre datos con inclusiones minerales vs. sin inclusiones. En los Anexos C al H se muestran, finalmente, todos los análisis composicionales llevados a cabo en los distintos sulfuros.

1.2 Motivación

Los depósitos tipo pórfido cuprífero corresponden a cuerpos mineralizados de baja ley (~ 0,3 – 1% Cu) y gran tonelaje (50 a 500 Mt), los cuales se encuentran asociados a arcos magnmáticos de márgenes continentales (Sillitoe, 1973, 2010; John et al., 2010). Actualmente, más del 60% de la producción de Cu mundial proviene de este tipo de depósito (Johnson, 2013), siendo Chile su mayor productor. La gran parte de la producción chilena de cobre proviene de 16 pórfidos cupríferos en explotación, destacando entre ellos los megadepósitos de Chuquicamata, La Escondida, El Teniente y Andina.

Dada la importancia económica nacional que posee este tipo de yacimiento y su explotación, es de gran relevancia poder entender el origen y la distribución de los elementos traza dentro del depósito, con el fin de aportar al entendimiento de la distribución de estos elementos en los distintos sulfuros en sistemas de pórfido, así como también poder elaborar herramientas que apoyen al desarrollo de la exploración distrital en el entorno de Chuquicamata, lo cual adquiere

con el paso del tiempo mayor relevancia, debido al aumento de dificultad para descubrir nuevos depósitos minerales con una ley económica de interés.

En las últimas décadas, una gran variedad de estudios han sido llevados a cabo para determinar la geoquímica de elementos traza de los sulfuros de Fe, Cu-Fe y Cu en distintos tipos de depósitos minerales (Cook et al., 2016; Fontboté et al., 2017; Reich et al., 2017). Sin embargo, la mayoría de éstos se han enfocado en pirita de depósitos de sulfuros masivos volcanogénicos (VMS), sedimentarios de Cu-U, magmáticos de Ni-Cu, epitermales y tipo Carlin de oro (ej., Large et al., 1999; Pals et al., 2003; Vaughan and Hyin, 2004; Palenik et al., 2004; Reich et al., 2005; Barker et al., 2009; Large et al., 2009; Cook et al., 2011; Godel et al., 2013; Deditius et al., 2014; Gregory et al., 2015a, b; Wohlgemuth-Ueberwasser et al., 2015; George et al., 2016, 2018; Kusebauch et al., 2019). Por otra parte, existen muy pocos estudios asociados a la geoquímica de sulfuros en pórfidos de cobre, y la mayoría se encuentra enfocada en metales preciosos (Au y Ag) o elementos del grupo del platino (PGE) (ej., Kesler et al., 2002; Arif and Baker, 2004; Pasava et al., 2010; McFall et al., 2018; Crespo et al., 2018, 2020, accepted). Un conocimiento adecuado acerca de la ocurrencia y los rangos de concentración de los distintos elementos traza en yacimientos tipo pórfido es de suma relevancia, puesto que los sulfuros de mena y ganga corresponden a uno de los principales huéspedes de elementos traza. Actualmente, existe muy poca información acerca de la concentración de elementos traza en los sulfuros en función de las distintas alteraciones hidrotermales, lo cual es sumamente relevante para: 1) Comprender de mejor manera la partición elemental bajo diferentes condiciones fisicoquímicas y evaluar su concentración en las diferentes alteraciones hidrotermales (ej., potásica, fílica o propilítica) y 2) Identificar potenciales asociaciones mineralógicas y geoquímicas en los sulfuros que podrían ser utilizadas para vectorizar hacia la mineralización del pórfido, y usadas como herramientas de exploración complementarias para encontrar recursos de mayores leyes.

Dado lo planteado anteriormente, es que en la presente tesis se reportan los resultados de un estudio detallado de la geoquímica de sulfuros de mena y ganga en el yacimiento Chuquicamata Subterráneo. Con ello, se espera contribuir al conocimiento acerca de la ocurrencia de elementos traza en el pórfido de Cu-Mo de Chuquicamata, en particular en dos aspectos fundamentales: en primer lugar, se busca entender qué elementos fueron incorporados en cada uno de los sulfuros durante la génesis del depósito, lo cual es crítico para entender la partición de elementos traza en el ambiente de pórfido bajo distintas condiciones fisicoquímicas. Segundo, identificar los posibles cambios en las condiciones fisicoquímicas (ej., temperatura, pH, fO_2 , aH_2S y salinidad, entre otros factores) que dieron lugar a la concentración (o dispersión) de elementos traza en las diferentes alteraciones hidrotermales en el yacimiento. Lo anterior tendría un impacto tanto en el conocimiento general del depósito en términos genéticos, como también en los procesos que dieron origen a la distribución de elementos traza en el depósito.

Para llevar a cabo los aspectos antes mencionados, se procedió a realizar un muestreo representativo de cada una de las alteraciones hidrotermales presentes en el yacimiento, tomando en cuenta su distribución espacial. Muestras representativas de cada alteración fueron obtenidas desde sondajes y caracterizadas petrográficamente, para posteriormente llevar a cabo análisis in-situ de los sulfuros constituyentes, con énfasis en la calcopirita, bornita y pirita. El enfoque microanalítico involucró una combinación de técnicas, entre microscopía óptica de polarización, microscopía electrónica de barrido (SEM), análisis in-situ de elementos menores y traza mediante microsonda electrónica (EMPA) y análisis de elementos traza mediante espectrometría de masas

por plasma inductivamente acoplado con ablación láser (LA-ICP-MS). Los detalles de las técnicas analíticas pueden encontrarse en el Anexo A.

1.3 Objetivos

1.3.1 Objetivo general

El objetivo principal de la presente tesis es determinar la ocurrencia y distribución de elementos menores y traza en los sulfuros de mena y ganga del yacimiento Chuquicamata Subterráneo. En particular, se pretende establecer cómo la signatura geoquímica de los sulfuros de Cu-(Fe) se relaciona con las diferentes alteraciones hidrotermales identificadas en el depósito.

1.3.2 Objetivos específicos

1. Identificar características distintivas de las diferentes asociaciones de alteración y de los sulfuros más abundantes en el yacimiento (calcopirita, bornita y pirita), mediante un estudio petrográfico de detalle, utilizando microscopía óptica de polarización y microscopía electrónica de barrido (SEM).
2. Determinar la secuencia paragenética del yacimiento Chuquicamata Subterráneo, con énfasis en las paragénesis de sulfuros y su evolución genética y temporal.
3. Constreñir la química mineral in-situ (elementos mayores, menores y traza) de los sulfuros de mena (calcopirita y bornita) y ganga (pirita) mediante una combinación de análisis de microsonda electrónica (EMPA) y espectrometría de masas por plasma inductivamente acoplado con ablación láser (LA-ICP-MS), determinando así rangos de concentración de elementos de niveles sub-ppm a wt.%.
4. Determinar la ocurrencia mineralógica de los elementos menores y traza en los sulfuros de mena (calcopirita y bornita) y ganga (pirita) en el yacimiento.
5. Identificar las posibles condiciones fisicoquímicas que contribuyeron a la concentración de elementos menores y traza en los sulfuros de mena (calcopirita y bornita) y ganga (pirita) en el depósito.
6. Evaluar el potencial de la geoquímica de sulfuros como posible herramienta de vectorización hacia zonas de interés en sistemas tipo pórfito y que sea aplicable en la exploración del distrito norte de CODELCO.

1.4 Hipótesis de trabajo

En los depósitos de tipo pórfito, la concentración de elementos traza en los sulfuros se encuentra fuertemente relacionada con la concentración de éstos en los fluidos mineralizadores (Zhu et al., 2016; Liu et al., 2020). Cambios en las condiciones fisicoquímicas del fluido resultarían en la variación de la signatura de elementos traza en los sulfuros que se observa hoy en día en el yacimiento. Por lo tanto, la distribución heterogénea de elementos traza en los sulfuros en función de la alteración sería un reflejo de cambios en las condiciones del fluido durante su evolución, y por ende su distribución tendría potencial como herramientas de vectorización hacia el evento de mineralización principal, tal como ha sido propuesto anteriormente para la pirita en yacimientos epitermales (Maydagán et al., 2013; Franchini et al., 2015; Kouhestani et al., 2017; Román et al., 2019).

1.5 Publicaciones y resúmenes resultantes de este trabajo

1.5.1 Publicaciones

Rivas-Romero, C., Reich, M., Barra, F., Gregory, D., and Pichott, S., 2020. The relation between trace element composition of Cu-(Fe) sulfides and hydrothermal alteration in a porphyry copper deposit: Insights from the Chuquicamata Underground mine, Chile. Manuscrito en revisión en *Mineralium Deposita* (Capítulo 2).

1.5.2 Resúmenes en congreso

Rivas-Romero, C., Reich, M., Barra, F. and Pichott, S., 2019. Major and trace element geochemistry of Cu-(Fe) sulfides and Cu sulfosalts from the Chuquicamata Underground mine, northern Chile. SEG Meeting 2019 “From Sierra to Craton”, Santiago, Chile, 7-10 Octubre, 2019.

CAPÍTULO 2: THE RELATION BETWEEN TRACE ELEMENT COMPOSITION OF CU-(FE) SULFIDES AND HYDROTHERMAL ALTERATION IN A PORPHYRY COPPER DEPOSIT: INSIGHTS FROM THE CHUQUICAMATA UNDERGROUND MINE, CHILE

Constanza Rivas-Romero^{1,2,*}, Martin Reich^{1,2}, Fernando Barra^{1,2}, Daniel Gregory³ and Sergio Pichott⁴

(1) Department of Geology and Andean Geothermal Center of Excellence (CEGA), Facultad de Ciencias Físicas y Matemáticas, Universidad de Chile, Plaza Ercilla 803, Santiago, Chile.

(2) Millennium Nucleus for Metal Tracing Along Subduction, Facultad de Ciencias Físicas y Matemáticas, Universidad de Chile, Santiago, Chile

(3) Department of Earth Sciences, Earth Sciences Centre, 22 Russell Street, Toronto, Ontario M5S 3B1, Canada

(4) CODELCO, Gerencia de Exploraciones, Casa Matriz, Huérfanos 1270, Santiago, Chile.

(*) Corresponding author: Constanza Rivas (constanzarivasromero@gmail.com)

Keywords: porphyry copper deposits, geochemical signature, EMPA, LA-ICP-MS, Chuquicamata Underground mine, Chile.

2.1 ABSTRACT

Porphyry Cu-Mo deposits are among the world's largest source of Cu, Mo and Re, and also are an important source of other trace elements such as Au and Ag. Despite the fact that chalcopyrite, bornite and pyrite are the most common sulfides in this deposit type, their trace element content remains poorly constrained. In particular, little is known about minor and trace elements partitioning into Cu-(Fe) sulfides as a function of temperature and pH of the hydrothermal fluid. In this study, we report a comprehensive geochemical database of chalcopyrite, bornite and pyrite in the super-giant Chuquicamata porphyry Cu-Mo deposit in northern Chile. The aim of our study, which focused on the new Chuquicamata Underground mine, was to evaluate the trace element composition of each sulfide from the different hydrothermal alteration assemblages in the deposit. Our approach combined electron microprobe analysis (EMPA) and laser ablation inductively coupled plasma mass spectrometry (LA-ICP-MS) data of sulfides obtained from six representative drill cores that crosscut the chloritic, background potassic, intense potassic and quartz-sericite alteration zones. Microanalytical results show that chalcopyrite, bornite and pyrite contain several trace elements, whose concentration can vary significantly between hydrothermal alteration assemblages. Chalcopyrite, for example, is a host of Se ($\leq 11,000$ ppm), Pb (≤ 83.00 ppm), Sn (≤ 68.20 ppm), Ag (≤ 45.1 ppm), Bi (≤ 25.9 ppm) and In (≤ 22.8 ppm). Higher concentrations of Se, In, Pb and Sn in chalcopyrite are related to the high temperature background potassic alteration, whereas lower concentrations of these elements are associated with the lower temperature alteration types, i.e., quartz-sericite and chloritic. Bornite, on the other hand, is only observed in the intense and background potassic alteration and is a major host of Ag (≤ 752 ppm) and Bi ($\leq 2,960$ ppm). Higher concentrations of Ag and Sn in bornite are associated with the intense potassic alteration, whereas lower concentrations of those two elements are observed in the background potassic alteration. Among all sulfide minerals analyzed, pyrite is the major host of trace elements with significant concentrations of Co ($\leq 1,530$ ppm), Ni (≤ 960 ppm), Cu ($\leq 9,700$ ppm).

ppm) and Ag (\leq 450 ppm). Cobalt, Ni, Ag and Cu contents in pyrite vary with alteration: higher Ag and Cu concentrations are related to the high temperature background potassic alteration, while the highest Co contents are associated with lower temperature alteration types (e.g., chloritic). These data indicate that the trace element concentration of chalcopyrite, bornite and pyrite changed as a function of hydrothermal alteration, and is controlled by several factors, including temperature, pH, fO_2 , fS_2 and presence of co-crystallizing phases. Overall, our results provide new information on how trace element partitioning into sulfides relates to the main hydrothermal and mineralization events, controlling the elemental budget at Chuquicamata. In particular, our data show that elemental ratios in chalcopyrite (e.g., Se/In) and pyrite (e.g., Ag/Co and Co/Cu) have a potential application for vectoring to porphyry mineralization and higher Cu resources.

2.2. INTRODUCTION

Porphyry copper deposits are currently the world's largest source of copper, molybdenum and rhenium. In these deposits, chalcopyrite and bornite are the main primary copper sulfides, and pyrite is a ubiquitous and abundant gangue sulfide. In the last decades, a large number of microanalytical studies have focused on determining the trace element geochemistry of Fe, Cu-Fe and Cu sulfides in several types of ore deposits (Cook et al., 2016; Fontboté et al., 2017; Reich et al., 2017, and references therein). However, most studies have targeted sulfides (predominantly pyrite) from volcanogenic massive sulfide deposits, sedimentary-hosted copper/uranium deposits, magmatic nickel-copper deposits, and Archean to Mesozoic lode, epithermal and Carlin-type gold deposits (e.g., Large et al., 1999; Pals et al., 2003; Vaughan and Kyin, 2004; Palenik et al., 2004; Reich et al., 2005; Barker et al., 2009; Large et al., 2009; Cook et al., 2011; Godel et al., 2013; Deditius et al., 2014; Gregory et al., 2015a, b, 2016; Wohlgemuth-Ueberwasser et al., 2015; George et al., 2016, 2018; Kusebauch et al., 2019). In contrast, and despite their economic importance, micro-analytical data for ore and gangue sulfides in porphyry copper deposits are sparse and focused mostly on precious metals (Au and Ag) and platinum group elements (PGE) (e.g., Kesler et al., 2002; Arif and Baker, 2004; Pašava et al., 2010; McFall et al., 2018; Crespo et al., 2018; 2020, accepted).

In porphyry copper and epithermal gold deposits, studies have reported that pyrite can host important concentrations of Au, Ni, Co, Cu, As and Te, in some cases reaching weight-percent levels (Arif and Baker, 2004; Hanley and MacKenzie, 2009; Pašava et al., 2010; Reich et al., 2013a; Cioacă et al., 2014; Deditius et al., 2014; Peterson and Mavrogenes, 2014; Zwahlen et al., 2014; Franchini et al., 2015; Tanner et al., 2016; Crespo et al., 2018; 2020, accepted). Data show that chalcopyrite can also host significant amounts of Ag, Au, Bi, In, Cd, Zn, Co, Ni, Te, As, Sb, Cr, Se and even PGEs (Kesler et al., 2002; Arif and Baker, 2004; Maydagán et al., 2013; Reich et al., 2013b; Cioacă et al., 2014; George et al., 2016, 2018; Crespo et al., 2018; 2020, accepted; Liu et al., 2020; Reich et al., 2020). However, chalcopyrite is a relatively poor host for trace elements when compared to bornite (Cook et al., 2011), although microanalytical data for the latter are limited in porphyry systems. Bornite is a well-known host of Ag and Bi in several ore deposit types, and in porphyries scarce studies report significant amounts of As, Au, Te, Pd, Pt and Se (Arif and Baker, 2004; Cook et al., 2011; Reich et al., 2013b; Cioacă et al., 2014; Crespo et al., 2018; 2020, accepted; Liu et al., 2020).

Despite these advances, geochemical studies of sulfides in porphyry copper deposits are still exploratory. For example, little is known about the trace element signature of the different

sulfide minerals as a function of hydrothermal alteration type. In porphyry systems, the trace element content of each sulfide will depend on the elemental concentrations of the mineralizing fluids, the mineral/fluid partitioning behavior of the elements and the presence of co-crystallizing sulfide phases. Therefore, changes in the physicochemical conditions of hydrothermal fluids and the thermodynamic stability of mineral assemblages will likely induce variations in the trace element content of ore and gangue sulfides. Hence, one fundamental question relates to which elements are incorporated (and potentially concentrated) into specific sulfides in the porphyry environment. A question of equal importance is the type and intensity of hydrothermal events that contributed with key elements, which were incorporated into the sulfides during the formation of the deposit. These two questions are closely linked because trace elements associated with different hydrothermal pulses or events will probably concentrate and partition into different sulfide minerals, for instance, chalcopyrite, bornite or pyrite. This may result in different concentration ranges (e.g., ppb to wt.% levels) and variable mineralogical forms of incorporation, e.g., solid solution versus micro- to nano-sized inclusions. Consequently, a precise knowledge about the trace element abundance in Cu-(Fe) sulfides as a function of alteration type in porphyry systems is of paramount importance to: 1) Better understand elemental partitioning under variable physicochemical conditions, and evaluate their concentration (or dispersal) in the different hydrothermal alteration events (e.g., potassic, phyllitic or propylitic), and 2) Potentially identifying mineralogical and geochemical features of the sulfides that may be diagnostic for vectoring to porphyry mineralization, and use as complementary exploration tools to find higher grade resources.

In this study, we carried out a microanalytical investigation of chalcopyrite, bornite and pyrite in the super-giant Chuquicamata porphyry Cu-Mo deposit in northern Chile. The purpose of our research was to evaluate how the trace element signature of each sulfide relates to the different hydrothermal alteration types. In particular, we focused on the new Chuquicamata Underground mine, which officially started operations in 2019. This new mine development, which will extend the life of the Chuquicamata deposit for the next 40 years, offers a unique opportunity to investigate the geochemical signature of the major ore and gangue sulfides at depth. To ensure samples were representative, we carried out a comprehensive drill core sampling of all major hydrothermal alteration types, taking into consideration their spatial distribution within the deposit. Samples of each alteration type were characterized petrographically using optical and electron microscopy methods, followed by in-situ mineral analyses using a combination of electron microprobe (EMPA) and laser ablation inductively coupled plasma mass spectrometry (LA-ICP-MS). Our main goal is to determine how minor and trace elements are distributed into chalcopyrite, bornite and pyrite during the evolution of a porphyry system. These data are further explored to provide insights on how sulfide precipitation – and hence trace element incorporation – relates to changing physicochemical conditions (i.e., temperature, pH, $f\text{O}_2$, $f\text{S}_2$) of the hydrothermal fluid.

2.3 GEOLOGICAL BACKGROUND

The Chuquicamata porphyry Cu-Mo deposit is located in the Atacama Desert of northern Chile, ~15 km north of Calama and at an altitude of 2,800 m above sea level (Fig. 1A). Chuquicamata is the largest deposit in the Chuquicamata district, which includes Radomiro Tomic, the exotic copper deposit of Mina Sur, the Ministro Hales mine, and the deposits of the Toki cluster (Fig. 1B). Total identified resources for the Chuquicamata district are estimated at 113.4 Mt of fine copper considering a cut-off Cu grade of 0.2 wt.%, from which the Chuquicamata porphyry Cu-

Mo deposit contributes 63.7 Mt (CODELCO Memoria Anual, 2018).

The porphyry deposits of the Chuquicamata district are part of a major belt of porphyry Cu deposits aligned along the Domeyko Fault System (Boric et al., 1990; Lindsay et al., 1995; Dilles et al., 1997), where the main structural feature observed is the West Fault (Fig. 1B). The Late Eocene-Early Oligocene (43-31 Ma) porphyry copper belt extends for about 1,400 km, from 18 to 31°S (Sillitoe, 1988; Sillitoe and Perelló, 2005). On its western margin, the Chuquicamata deposit is truncated by the West Fault, which locally separates weakly mineralized rocks from the barren Fortuna Granodiorite Complex towards the west (Figs. 1B and 2). The Fortuna Granodiorite Complex, a stock of hornblende-biotite granodiorite with phaneritic texture, has reported zircon U-Pb ages of 39.1 ± 0.4 and 38.5 ± 0.4 Ma (Ballard et al., 2001). The Triassic Elena Granodiorite, on the other hand, is located on the southeastern margin of the deposit (ca. 233 Ma; Rivera et al., 2012).

The Chuquicamata deposit includes both the open pit and the new underground mine and is hosted entirely within the Chuquicamata Intrusive Complex (Dilles et al., 1997; Ossandón et al., 2001; Faunes et al., 2005; Rivera et al., 2012) (Fig. 1B). This complex is divided into three main intrusive facies, the East, Banco and West Porphyries (Lindsay, 1997; Ossandón et al., 2001) (Fig. 2). The East Porphyry (zircon U-Pb age of 36.2 ± 0.4 Ma; Rivera et al., 2012) is volumetrically the most important and hosts most of the mineralization. It is locally intruded by smaller bodies of the Banco and West porphyries, both of which are most commonly located in the northern part of the deposit, and have a similar composition to that of the East Porphyry (Fig. 2). SHRIMP U-Pb zircon ages of the West and Banco porphyries are 34.03 ± 0.3 Ma and 34.10 ± 0.3 Ma, respectively (Ballard et al., 2001; Campbell et al., 2006).

Hydrothermal alteration at Chuquicamata was developed synchronous with the intrusion of West and Banco porphyries in a ductile to brittle regime, related to dextral strike-slip system (Lindsay, 1997). This early event produced an intense stockwork of “A-type” bornite-chalcopyrite quartz veinlets with a background potassic alteration halo defined by selective replacement of mafic minerals by secondary biotite and K-feldspar partially replacing plagioclase. This alteration halo affects most of the deposit, carrying scarce and mostly disseminated chalcopyrite, pyrite and bornite (Ossandón et al., 2001). This alteration event has been constrained by K-feldspar and biotite $^{40}\text{Ar}/^{39}\text{Ar}$ ages between 33.7 ± 0.2 Ma and 31.9 ± 0.2 Ma (Reynolds et al., 1998). In the outer fringes of this halo, chloritic alteration predominates with selective chloritization of mafic minerals and micro-veinlets of calcite, ankerite and hematite. Mineralization associated with the chloritic alteration corresponds mainly to pyrite, with minor chalcopyrite (Ossandón et al., 2001; Faunes et al., 2005).

Following this early event, an intense potassic alteration event took place and was responsible for the main hypogene mineralization at Chuquicamata. This event occurred with a preferred NNE orientation, probably related to repeated reactivation of the Messabi Fault – East Deformation Zone (Faunes et al., 2005). The intense potassic alteration is characterized by destruction of porphyry textures and by abundant veining and disseminated assemblages of bornite, digenite, chalcopyrite and covellite. This event was defined by two pulses, the first of which is characterized by an intense replacement of plagioclase and biotite by secondary K-feldspar, in some cases with secondary albite. The second pulse is characterized by the presence of grey-green sericite, which occurs disseminated in the halos of quartz veinlets. This event has been dated at 31.8 ± 0.4 Ma ($^{40}\text{Ar}/^{39}\text{Ar}$ biotite; Barra et al., 2013). During the transition between these two

consecutive pulses of intense potassic alteration, a series of massive quartz-molybdenite, “B-type” veinlets were formed. This veining produced a tabular, subvertical, NS to NNE oriented core zone in the central-south portion of the deposit, with average Mo grades ranging from 0.1 to 0.2% (Ossandón et al., 2001; Faunes et al., 2005). Rhenium-osmium molybdenite ages for the “B-type” veinlets are between 32.9 ± 0.2 Ma and 31.7 ± 0.2 Ma (Mathur et al., 2001; Barra et al., 2013). During the waning stage of the intense potassic alteration, chalcopyrite was deposited on the fringes of the alteration halo, generating an average grade of 0.8% Cu (Ossandón et al., 2001). This event mainly caused the formation of abundant chalcopyrite veinlets, which crosscut the “B-type” veinlets (Faunes et al., 2005).

The intense potassic event was followed by a pervasive stage of quartz-sericite alteration (phyllitic) distributed along a north-south elongated zone in the western part of the deposit, affecting mainly the area east of the West Fault. This alteration is characterized by the presence of aggregates of sericite, quartz and clays (kaolinite and illite), which generated a pervasive replacement of feldspar and biotite obliterating the original texture of the porphyry (Ossandón et al., 2001; Faunes et al., 2005; Rivera et al., 2012). Sulfide mineralization consists mainly of pyrite with variable amounts of digenite, covellite, enargite, chalcopyrite, tennantite, and bornite, and occurs in “D-type” veinlets (Lindsay, 1997; Ossandón et al., 2001; Faunes et al., 2005). This event has been dated between 31.9 ± 0.5 Ma and 30.6 ± 0.4 Ma determined by $^{40}\text{Ar}/^{39}\text{Ar}$ in sericite, biotite and K-feldspar (Reynolds et al., 1998; Barra et al., 2013). As a result of the superimposed quartz-sericite alteration on the intense potassic alteration, an intense potassic relict alteration was defined. Finally, hydrothermal alteration at Chuquicamata was followed by a stage of supergene oxidation, dated between 19 ± 0.7 and 15.2 ± 0.5 Ma (K/Ar in supergene alunite; Sillitoe and McKee, 1996). The main copper oxides developed in the supergene zone are chrysocolla, atacamite, brochantite and copper wad (Ossandón et al., 2001; Faunes et al., 2005; Reich et al., 2013c).

2.4 SAMPLES AND METHODS

Core samples were collected from six representative drill cores (CHDD 3618, CHDD 4587, CHDD 7795, CHDD 7808, CHDD 7815 and CHDD 8710) from the central and southern part of the Chuquicamata Underground mine. The selected drill cores crosscut the main alteration and mineralization units from top to bottom, ensuring that main alteration types are adequately represented. Figure 3 shows two of the six projected drill holes in a central section of the deposit (cross-section A-A' in Fig. 2). Drill core CHDD 4587 cuts the intense and background potassic alteration, whereas the longer CHDD 7808 drill core cuts most alteration zones (described in section 4.1). From all six drill cores, a total of 120 samples representative of the chloritic, background potassic, intense potassic and quartz-sericite alterations were chosen. Among these, 40 samples were inspected using polarized-light and scanning electron microscopy. Based on petrographic observation, a subset of 19 representative samples were selected for sulfide microanalysis. The sulfide minerals studied here include chalcopyrite, bornite and pyrite, which are the most abundant sulfides in the deposit.

Scanning electron microscopy (SEM) observations were carried out at the Andean Geothermal Centre of Excellence (CEGA), Universidad de Chile, using a FEI Quanta 250 SEM equipped with secondary electron (SE), energy dispersive X-ray spectrometry (EDS) and backscattered electron (BSE) detectors. The analytical parameters were: accelerating voltage of 15-20 kV and an emission current of $\sim 80\text{ }\mu\text{A}$, takeoff angle $\sim 35^\circ$, spot beam was 4-5 μm in diameter

and a working distance of ~10 mm. SEM observations were aimed at characterizing in detail the sulfide and silicate paragenesis, and also recognizing diagnostic micro-textures, as well as detecting the presence of micro-inclusions within sulfides.

Electron microprobe analysis (EMPA) of sulfide minerals was performed using a JEOL JXA-8230 microprobe equipped with five wavelength-dispersive spectrometers at the Electron Probe X-Ray Microanalyzer Laboratory of the University of Toronto in Canada. Operations conditions were: fully focused beam, beam energy of 20 keV and a beam size of ~1 μm in diameter. The beam current was 50 nA for spot analysis. Elements (represented by spectral lines) were acquired using the following analyzing crystals: LIF for Co K α , Cu K α , Fe K α , Zn K α and Ni K α ; TAP for As L α and Se L α ; and PETH for Te L α , Ag L α , Pb M α , Pd L α , Pt M α , S K α , Hg M α , Bi M α , Sb L α and Au M α . Standard specimens used for calibration were CoS (for Co), CuFeS₂ (for Cu, Fe and S), ZnS (for Zn), (Ni,Fe)₉S₈ (for Ni), FeAsS (for As), CuSe (for Se), PdTe (for Pd and Te), AgBiS₂ (for Ag and Bi), PbS (for Pb), PtTe₂ (for Pt), HgS (for Hg), PdSb (for Sb) and (Au, Cu)⁰ (80/20) (for Au). Counting time (peak) was 20 s for Co K α , Cu K α , Fe K α , Zn K α , Ni K α , Te L α , Ag L α , Pd L α and S K α ; 30 s for Sb L α ; 40 s for Pb M α , Pt M α , Hg M α and Bi M α ; 60 s for As L α and Se L α ; and 120 s for Au M α . The same (peak) counting time was used for total background readings. Mean detection limits ranged from 0.01 to 0.04 wt% for most analyzed elements.

Laser ablation inductively coupled plasma mass spectrometry (LA-ICP-MS) analyses were acquired on selected sulfide grains following the procedure described in Román et al. (2019). LA-ICP-MS analyses were carried out using a 193 nm ArF excimer laser (Teledyne-Photon Machines Analyte G2) coupled to a quadrupole ICP-MS (Thermo Fisher Scientific iCAP-Q) at the Mass Spectrometry Laboratory of the Andean Geothermal Center of Excellence (CEGA), Department of Geology, Universidad de Chile. Before each analytical session, the ICP-MS was tuned by ablating a NIST SRM 610 glass to ensure acceptable levels of plasma robustness (i.e., $^{238}\text{U}^+/\text{Th}^+$ between 0.95 – 1.05), oxide production ($\text{ThO}^+/\text{Th}^+ < 0.5\%$) and double-charged production ($^{22}\text{M}^+/^{44}\text{Ca}^{++}<0.01\%$) (Román et al., 2019). Ablation was carried out using a laser pulse frequency of 4 Hz, an energy density of 2 J/cm², and a spot size of 40 μm in most cases when the grain size allowed it. The laser spot size was reduced to 30–25 μm when analyzing small grains, or to prevent ablating visible mineral inclusions. Pure He was used as carrier gas and Ar was added to the gas stream to improve aerosol transport. For each analysis, gas background collection was measured for 30 s following by 52 s of laser ablation period. The isotopes monitored were: ^{34}S , ^{51}V , ^{52}Cr , ^{53}Cr , ^{55}Mn , ^{57}Fe , ^{59}Co , ^{60}Ni , ^{63}Cu , ^{65}Cu , ^{66}Zn , ^{69}Ga , ^{72}Ge , ^{73}Ge , ^{75}As , ^{77}Se , ^{82}Se , ^{95}Mo , ^{97}Mo , ^{105}Pd , ^{107}Ag , ^{109}Ag , ^{111}Cd , ^{115}In , ^{118}Sn , ^{120}Sn , ^{121}Sb , ^{123}Sb , ^{125}Te , ^{182}W , ^{185}Re , ^{189}Os , ^{195}Pt , ^{197}Au , ^{202}Hg , ^{205}Tl , ^{206}Pb , ^{207}Pb , ^{208}Pb and ^{209}Bi . A dwell time of 10 ms was used for all elements, except for Ag, Cd, In, Sn, Te, Au and Bi for which 30 ms were used. The calibration procedure considered both external and internal standard calibration (Longerich et al., 1996). Total Fe concentrations obtained previously by EMPA were used as the internal standard for chalcopyrite, bornite and pyrite. The MASS-1 pressed synthetic sulfide reference material (Wilson et al., 2002) was used as the primary standard. In addition, the GSE-1G glass reference material (Jochum et al., 2005) was employed as secondary standard for quality control. External standard measurements were performed at the beginning and at the end of each analysis round of 20 spot analyses. Data integration and reduction was performed using the IoliteTM (v. 3.63) data reduction software (Paton et al., 2011).

2.5 RESULTS

2.5.1 Hydrothermal alteration and mineralization

Historically, four main types of hydrothermal alteration have been described in the Chuquicamata deposit, i.e., background potassic, chloritic, intense potassic and quartz-sericite alteration (e.g., Lindsay, 1997; Ossandón et al., 2001; Arnott, 2003; Faunes et al., 2005; Rivera et al., 2012; Demané et al., 2018) (Fig. 3). These four types are also recognized in the underground mine, in addition to the relict intense potassic alteration (Faunes et al., 2005). Figure 4 shows photographs of the main alteration types, which are described in detail in the next paragraphs.

The background potassic alteration is an early stage alteration style characterized by abundant secondary biotite, K-feldspar, albite and minor calcite. The sulfide mineralogy comprises mainly chalcopyrite with bornite and pyrite occurring only locally. Mineralization occurs as disseminations and to a lesser extent as micro-veinlets. This alteration is represented by irregular “A-type” quartz-bearing veinlets, which are usually characterized by K-feldspar halos (Fig. 4A).

The chloritic alteration occurs in the most external portions of the system and is dominated by the presence of chlorite with albite, hematite and minor calcite-ankerite. Epidote is recognized locally in distal zones. Sulfide mineralization associated with this alteration type is mainly pyrite with local chalcopyrite. The chloritic alteration is represented by three types of veinlets: (i) Continuous mm-to-cm thick chlorite veinlets without an alteration halo (Fig. 4B); (ii) Discontinuous hematite veinlets without an alteration halo, commonly a few mm thick (Fig. 4C); (iii) Continuous pyrite veinlets, commonly associated with chlorite or magnetite disseminated in the veinlets, without an alteration halo (Fig. 4D).

The intense potassic alteration is characterized by the presence of secondary K-feldspar accompanied by secondary albite and quartz, grey-green sericite is also present, but it is very scarce and found only locally. The fabric of this alteration is cataclastic, frequently forming a micro-breccia with a fine matrix of micro- to crypto-crystalline quartz and K-feldspar, which are also present as micro-veinlets. Mineralization occurs as abundant fine disseminations and in micro-veinlets, and comprises assemblages of bornite \pm digenite \pm covellite, or chalcopyrite \pm bornite \pm covellite \pm digenite. Pyrite is usually not present in this alteration type. It is important to note that mineralization is not associated with the grey-green sericite. This alteration is characterized by two types of veinlets: (i) Continuous, cm-thick chalcopyrite veinlets (Fig. 4E); (ii) “B-type” veinlets, which are cm-thick, continuous and banded, usually without alteration halos, and composed of quartz \pm molybdenite (Fig. 4F).

East of the West fault (Fig. 3), a late quartz-sericite (phyllitic) alteration is superimposed on the previous potassic alteration. The quartz-sericite alteration comprises sericite aggregates with quartz that obliterate the original texture of the porphyry through the intensive replacement of feldspars and biotite. Higher sulfidation assemblages include pyrite \pm chalcopyrite, pyrite \pm digenite (\pm bornite), pyrite \pm covellite (\pm enargite), pyrite \pm enargite (\pm sphalerite) and pyrite \pm Cu sulfosalts. This alteration is characterized by the presence of cm-thick “D-type” veinlets which are continuous and composed by Cu-sulfides (chalcocite, covellite or digenite) and Cu-sulfosalts (enargite or tennantite) with pyrite as the dominant sulfide, usually associated with quartz (Fig. 4G-H). The relict intense potassic alteration is a superimposition of the quartz-sericite alteration over the intense potassic alteration and is characterized by the presence of minor grey-green sericite

and micro- to crypto-crystalline quartz and K-feldspar, which is typical of the intense potassic alteration zone, with abundant aggregates of quartz and sericite from the quartz-sericite alteration. Sulfides observed in this alteration include pyrite \pm digenite, \pm covellite, \pm bornite. Finally, supergene alteration is also observed at Chuquicamata Underground, and is represented by secondary chalcocite and covellite. Locally, sulfates and carbonates can be observed.

It is important to note that the relict intense potassic alteration and any other relation of superimposition (i.e., transition zones) is not considered in this study, due to its possible complexity. Thus, sulfides from clearly identified units (i.e., chloritic, background potassic, intense potassic and quartz-sericite alteration) were studied.

2.5.2 Sulfide textures and mineral inclusions

Figure 5 presents a paragenetic sequence for the studied deposit. Chalcopyrite is the dominant Cu sulfide, and is recognized in all four alteration zones, although it occurs predominantly within the background and intense potassic zones. Bornite is the second most important Cu sulfide within the Chuquicamata Underground mine. It occurs as anhedral grains and it is primarily present in the intense potassic alteration zone and to a lesser degree in the background potassic and quartz-sericite zones. Pyrite is the main gangue sulfide and is present mostly in the chloritic and quartz-sericite alteration zones.

Texturally, chalcopyrite, bornite and pyrite show different occurrences (Fig. 6A-D). Chalcopyrite occurs as anhedral to subhedral grains with variable presence of pores and mineral micro-inclusions; it can present intergrowth and replacement textures with pyrite, bornite and covellite, and in cases with chalcocite and sphalerite (Figs. 6A, B). Bornite occurs as anhedral grains, in cases showing porous textures and abundant mineral inclusions. Replacement textures are recognized between bornite and chalcopyrite, covellite and digenite (Fig. 6C). Pyrite occurs both as euhedral and pristine grains without mineral inclusions, and as anhedral to subhedral grains with porous textures and abundant micro-inclusions. In addition, it can form intergrowth and replacement textures with chalcopyrite, bornite, chalcocite, covellite, Cu-sulfosalts and molybdenite (Fig. 6D).

SEM observations revealed the presence of several types of mineral inclusions within the studied sulfides (Fig. 6E-H). In chalcopyrite, inclusions of sphalerite, galena, scheelite (CaWO_4) and electrum were recognized, although their occurrence is generally scarce. Bornite, on the other hand, usually contains more inclusions than chalcopyrite, most frequently Au-Ag tellurides, electrum and wittichenite (Cu_3BiS_3) (Figs. 6F-G). In general, bornite from the intense potassic alteration contains more inclusions than bornite from the background potassic alteration. Finally, inclusions in pyrite are commonly observed and in cases are very abundant. Among these, galena, wittichenite, scheelite and wolframite ($(\text{Fe-Mn})\text{WO}_4$) were recognized (Fig. 6H). In addition, Cu-sulfosalts and Au-Ag bearing inclusions were also observed in pyrite.

2.5.3 Major, minor and trace elements concentrations in sulfide minerals

EMPA and LA-ICP-MS data for chalcopyrite, bornite and pyrite are reported in Annexes 1 and 2. It is important to note that analyses were performed on clean mineral surfaces with no visible mineral inclusions. However, it is well documented that LA-ICP-MS spot analyses can be affected by the presence of (subsurface) micro- to nano-inclusions containing several elements (e.g.,

Gregory et al., 2015a; Román et al., 2019). Therefore, all LA-ICP-MS time vs. intensity depth-concentration profiles were carefully inspected for the presence of spikes indicating mineral inclusions. Results show that no significant contribution from inclusions is present, with the exception of a few spot analyses in pyrite (see section 5.1).

Figure 7 displays all sulfide LA-ICP-MS analyses, with summary statistics of trace element concentrations presented as boxplots. Most elements show a similar range of concentration in all sulfides (Fig. 7A), usually below 1,000 ppm. However, it is relevant to note that chalcopyrite has the highest concentrations of Se, In and Au of all analyzed sulfides. Indium is systematically detected in all spots, while Se and Au are detected only in a few grains, which could be due to the presence of nano-inclusions. Bornite, on the other hand, shows the highest contents of Ag, Bi, Cd and Sn, where all these elements are detected in almost all spots, except for Cd. In comparison with chalcopyrite and bornite, pyrite has the highest concentrations of Co, As, Sb and Pb, and also hosts significant concentrations of Cu, within these elements, only As and Sb are detected rather sporadically.

Individual elemental ranges for chalcopyrite, bornite and pyrite are plotted as a function of hydrothermal alteration type in boxplots (Fig. 7C-D). Distinct variations are observed, and the more significant features are described in the following sections, where EMPA data for major and minor element data are reported for chalcopyrite, bornite and pyrite, followed by LA-ICP-MS trace element data. LA-ICP-MS data are first described as a whole for each sulfide, and then as a function of alteration type, i.e., chloritic, background potassic, intense potassic and quartz-sericite zones.

2.5.3.1 Chalcopyrite

EMPA data show that major element concentrations in chalcopyrite range from 33.52 to 35.34 wt.% for Cu, 29.46 to 31.07 wt.% for Fe, and 33.69 to 35.42 wt.% for S (Annex 1A). Additionally, minor elements such as Co, Zn and Ag were detected, with concentrations of up to 0.05 wt.%, 0.36 wt.% and 0.08 wt.%, respectively (Annex 1A).

LA-ICP-MS analyses of chalcopyrite are shown in Figure 7B and presented in Annex 2A. All elements are below 100 ppm, with the exception of Se that shows high concentrations (up to 11,000 ppm) in a few spots. Silver and In are systematically detected with concentrations ranging from 0.82 to 45.1 ppm, and 1.08 to 22.8 ppm, respectively. Other elements detected systematically although in minor concentrations were Sn (\leq 68.2 ppm), Pb (\leq 83 ppm) and Bi (\leq 25.9 ppm). All other elements in Figure 7B were detected only in a few spots with concentrations below 5 ppm (\leq 3.8 ppm for W, \leq 1.26 ppm for Au, \leq 2.3 ppm for Hg, and \leq 0.25 ppm for Tl).

When the trace element dataset of chalcopyrite is inspected as a function of alteration (Fig. 7B), it is observed that several elements show the highest concentrations in the background potassic alteration, e.g., Se, In, Sn, W, and Pb. Bismuth and Ag, in contrast, show similar concentrations in all four alteration zones.

2.5.3.2 Bornite

Major element EMPA data in bornite show concentrations ranging from 60.20 to 68.55 wt.% for Cu, 7.24 to 11.71 wt.% for Fe, and 24.63 to 26.75 wt.% for S (Annex 1B). Also, minor elements, including Ag, Bi and Zn were measured, with concentrations reaching 0.53 wt.%, 0.5

wt.% and 0.06 wt.%, respectively (Annex 1B).

LA-ICP-MS analyses of bornite are reported in Annex 2B. Figure 7C shows that Bi was detected in all analyzed spots and has the highest concentrations from all elements (182-2,960 ppm), followed by Ag (81-752 ppm). Other measured elements include Se (119-770 ppm), Sn (1.29-352 ppm), W (0.02-18.90 ppm), Au (0.02-0.23 ppm), and Pb (0.67-43 ppm).

When plotted by alteration, LA-ICP-MS data show that bornite from the intense potassic alteration presents the highest Sn, W and Pb concentrations, while bornite from the background potassic alteration shows the highest Bi concentration (Fig. 7C).

2.5.3.3 Pyrite

EMPA data for pyrite show major element concentrations from 45.70 to 47.78 wt.% for Fe, and 50.21 to 53.91 wt.% for S (Annex 1C). In addition, minor elements such as Co, Ni and Cu were measured as well, with concentrations of up to 1.43 wt.%, 0.12 wt.% and 2.35 wt.%, respectively (Annex 1C).

Trace element LA-ICP-MS data for pyrite are summarized in Figure 7D and reported in Annex 2C. The data show that pyrite has a high trace element content, including Co (0.71-1,530 ppm), Ni (1.18 and 960 ppm), Cu (0.96 and 9,700 ppm), Mn (4.8-1,080 ppm), Zn (14-1,200 ppm), As (4.9 -1,760 ppm), Se (5-2,700 ppm), Ag (0.2-450 ppm), Sb (1.5-930 ppm), Pb (0.15-2,250 ppm), and Bi (0.05-460 ppm). Other trace elements are mostly below 30 ppm, i.e., Ge (\leq 10.1 ppm), Cd (\leq 4.3 ppm), In (\leq 0.9 ppm), Sn (\leq 47 ppm), Te (\leq 23 ppm), W (\leq 2.3 ppm) and Au (\leq 8.6 ppm).

Pyrite from the chloritic alteration zone shows the highest Co concentrations (Fig. 7D), and also contains elevated Ge, Se, Te, W and Au contents, whereas pyrite from the background potassic alteration shows elevated Mn, Ni, Cu, Zn, As, Ag, In, Sn, Sb and Pb concentrations. In the quartz-sericite alteration zone, pyrite displays intermediate concentrations of all elements.

2.6 DISCUSSION

2.6.1 Incorporation of trace elements in chalcopyrite, bornite and pyrite

Despite the importance of chalcopyrite as the most common copper sulfide, its trace element content has been poorly investigated in porphyry-related environments. Cook et al. (2011) reported that chalcopyrite is relatively a poor host for trace elements compared to bornite and chalcocite, and also the least preferred host when co-crystallizing with sphalerite and galena (George et al., 2016). However, it has been documented that chalcopyrite can host a wide range of elements, including Ag, Au, Bi, In, Cd, Zn, Co, Ni, Te, As, Sb, Cr, Se and PGEs (Kesler et al., 2002; Arif and Baker, 2004; Maydagán et al., 2013; Reich et al., 2013b; Cioacă et al., 2014; George et al., 2018; Crespo et al., 2018; 2020, accepted; Liu et al., 2020). Additionally, several studies have demonstrated that chalcopyrite can host important concentrations of Se (Carvalho et al., 2018; George et al., 2018; Reich et al., 2020), In (Kieft and Damman, 1990; Huston et al., 1995; Sinclair et al., 2006; Cook et al., 2011; Carvalho et al., 2018; George et al., 2016, 2018), and Sn (Maydagán et al., 2013; George et al., 2016, 2018). Our chalcopyrite data from the Chuquicamata Underground

mine are in agreement with results from Crespo et al. 2020 (accepted), which presented a trace element dataset for chalcopyrite from the Río Blanco porphyry Cu-Mo deposit in Central Chile. They reported significant Se (\leq 14,100 ppm) and Ag, In and Sn concentrations of up to 12.8 ppm, 26.30 ppm and 110 ppm, respectively, which are consistent with our values for Chuquicamata. Zinc is, in general, a relevant trace element detected in chalcopyrite from most deposit types, including porphyries (Maydagán et al., 2013; George et al., 2018; Liu et al., 2020; Crespo et al., 2020, accepted). However, at Chuquicamata Underground, Zn was not often detected, probably because Zn is preferentially partitioned into sphalerite and galena over chalcopyrite (George et al., 2018).

Figure 8A shows time-resolved down-hole profiles collected by LA-ICP-MS for chalcopyrite. Based on the relatively flat shape of the transient signal and the lack of major spikes pointing to inclusions, we infer that most trace elements are incorporated in solid solution within the chalcopyrite structure. However, the high concentration of Se found in some spots suggests that this element might also be present as clusters of micro- or nano-inclusions. In addition, mineral inclusions of scheelite and electrum were observed in certain grains of chalcopyrite from the background potassic alteration zone (Fig. 6E).

The incorporation of trace elements in the chalcopyrite structure is complex and several substitutions mechanisms have been evaluated, including coupled substitutions as proposed by Belissont et al. (2019), based on synchrotron XRF and XANES data. This coupled substitution involves monovalent (Cu^+ , Ag^+), bivalent (Zn^{+2} , Cd^{+2} , Pb^{+2}), trivalent (Fe^{+3} , In^{+3} , Sb^{+3}) and/or tetravalent (Se^{+4} , Sn^{+4} , Bi^{+4} , Ge^{+4}) ions. Coupled substitution was also proposed as a possible mechanism to explain trace element incorporation in Ag-rich chalcopyrite from the Cerro Pabellón geothermal system in Chile (Reich et al., 2020).

After chalcopyrite, bornite is a major carrier of Cu in porphyry copper deposits. Although data for porphyry systems are still limited, it has been reported that bornite in these deposits is a relevant host of Ag and Bi, reaching concentrations of up to thousands of ppm (Cook et al., 2011; Reich et al., 2013b; Cioacă et al., 2014; Crespo et al., 2018; 2020, accepted; Liu et al., 2020). Bornite is the second most important ore mineral at Chuquicamata Underground, and despite the fact that it incorporates only a limited range of trace elements, Ag and Bi are significantly concentrated. These two elements range from 100's to 1,000's ppm, respectively (Fig. 7C and Annex 2B), making bornite the major host of Ag and Bi in the deposit (Fig. 7A).

Silver and Bi incorporation into bornite is most likely in solid solution, based on the relatively flat signal in time-resolved down-hole profiles collected by LA-ICP-MS (Fig. 8B). Experimental studies in bornite have demonstrated that it can host significant concentrations of Bi, as much as 17 wt.% at 420°C (Sugaki et al., 1981, 1984), supporting a mechanism of solid solution incorporation. On the other hand, there is limited information about the solubility of Ag in sulfides (Cook et al., 2011). Therefore, and even though some mineral inclusions of electrum, wittichenite and Au-Ag-tellurides were detected in bornite during SEM observation (Fig. 6F-G), it is expected that Ag and Bi are dominantly incorporated as structurally bound elements in bornite via coupled substitution (Cook et al., 2011).

Pyrite has been traditionally selected for geochemical studies in several ore-forming environments due to its ability to incorporate several trace elements, including Au, As, Cu, Co, Ni, Pd, Pt, Se and Te (Arif and Baker, 2004; Deditius et al., 2009; Hanley and MacKenzie, 2009;

Pašava et al., 2010; Reich et al., 2013a; Cioacă et al., 2014; Deditius et al., 2014; Zwahlen et al., 2014; Franchini et al., 2015; Crespo et al., 2020, accepted). At Chuquicamata Underground, measured concentrations of Co, Ni, Cu, Zn, As, Se, Pb, Bi and Ag in pyrite were above 100 ppm (Fig. 7A and 7D). Among these, Co and Ni are the most relevant spanning three orders of magnitude, ranging from ~1 to ~1,000 ppm. Copper contents are significantly high, reaching up to ~10,000 ppm.

The ^{59}Co signal in time-resolved down-hole profiles collected by LA-ICP-MS, (Fig. 8C), strongly suggests that Co is dominantly present as a structurally bound element within pyrite. However, the presence of Co-bearing inclusions was inferred based on a few spiky spectra (Fig. 8D). It is likely that Co dominantly substitutes for Fe within the pyrite structure, due to the similar ionic radii and structural affinity between FeS_2 and CoS_2 end-members (Vaughan and Craig, 1978; Tossell et al., 1981; Abraitis et al., 2004; Gregory et al., 2015a, b). Similarly, the ^{60}Ni signals (Fig. 8C-D) also point to a solid solution incorporation mechanism for this element. In contrast, high Cu and Pb contents are most likely related to the presence of Cu- and Pb-bearing inclusions, respectively, as evidenced by spiky LA-ICP-MS profiles (Fig. 8D).

2.6.2 Geochemical signature of Cu-(Fe) sulfides as a function of alteration

Geochemical data from the different sulfide species allows investigation of the trace element signature of the studied sulfides with respect to hydrothermal alteration. At the Chuquicamata Underground mine, four main hydrothermal alteration and Cu-(Fe) sulfide mineralization events were identified, i.e., background potassic, intense potassic, chloritic and quartz-sericite (see section 4.1). The earliest event was associated with a magmatic-hydrothermal fluid of high temperature that generated the background potassic alteration with chalcopyrite and minor bornite and pyrite. Based on mineralogical associations, this event occurred at temperatures of ~600-450°C and under neutral to alkaline conditions (i.e., Gustafson and Hunt, 1975; Lindsay, 1997; Einaudi et al., 2003; Richards, 2005; Bodnar et al., 2014). This same (early) fluid generated a distal chloritic halo as it cooled down probably due to mixing with meteoric water. The resulting chloritic alteration is characterized by the presence of pyrite and lesser chalcopyrite (bornite in this alteration is absent). Mineral assemblages indicate formation under low temperature (~250-200°C) and neutral to alkaline conditions (similar to background potassic alteration), which is typically reported for this alteration type in porphyry copper deposits (i.e., Gustafson and Hunt, 1975; Dilles and Einaudi, 1992; Lindsay, 1997; Corbett and Leach, 1998; Einaudi et al., 2003; Richards, 2005; John, 2010). The main Cu mineralization event was related to an intense potassic alteration that is dominated by abundant bornite and chalcopyrite, and minor Cu-sulfides, i.e., digenite, covellite. This event was generated at an intermediate temperature, i.e. ~400°C, and under neutral to alkaline conditions (i.e., Gustafson and Hunt, 1975; Dilles and Einaudi, 1992; Lindsay, 1997; Ulrich and Heinrich, 2001; Rusk et al., 2008). On the other hand, the quartz-sericite alteration was associated with a low temperature (250-300°C), more acidic fluid ($\text{pH} \sim 5-6$) (e.g., Gustafson and Hunt, 1975; Lindsay, 1997; Corbett and Leach, 1998; John, 2010; Bodnar et al., 2014). This alteration event comprises pyrite, minor chalcopyrite, Cu sulfides and sulfosalts, and scant bornite.

The trace element signature of chalcopyrite, bornite and pyrite as a function of alteration type, is discussed below based on key variations observed in the elemental biplots (Fig. 9).

Figure 9A shows that higher concentrations of Se and In in chalcopyrite are related to the background potassic alteration, while lower concentrations of these two elements are associated

with the quartz-sericite alteration. Chalcopyrite from the chloritic alteration show intermediate Se and In concentrations. As seen in Figure 9A, In/Se ratios in chalcopyrite vary from ~1.0-0.01 for the chloritic and quartz-sericite zones (including one data point for the intense potassic alteration at 0.01), while lower In/Se ratios (~0.001) are characteristic of chalcopyrite from the background potassic alteration. Although no experimental data are available for Se and In partitioning into chalcopyrite, data in Figure 9A are in agreement with several studies documenting that the incorporation of Se and In into sulfide minerals is favored by high formation temperatures (Auclair et al., 1987; Qian et al., 1998; Schwarz-Schampera and Herzig, 2002; Frenzel et al., 2016). However, the low-temperature chloritic alteration has also a relatively high Se concentration when compared with the intense potassic (one data point) and quartz-sericite alteration. This feature indicates that temperature is not the only factor controlling Se incorporation into chalcopyrite, and thus variability must be examined with caution. Studies in other sulfide minerals (e.g., pyrite) have proposed that incorporation of Se in pyrite vary as a function of redox and pH conditions (Yamamoto et al., 1984; Layton-Matthews et al., 2008), although Keith et al. (2018) compared all these variables for various deposits and concluded that the main factor that controls Se incorporation is fluid temperature. For the case of In, complexation studies indicate that in Cl-rich systems, cooling can be an effective mechanism for complex destabilization (Loges et al., 2017). Also, it is reported that a decrease in temperature would have a strong impact on the solubility of In, and thus mixing with meteoric waters would be an effective mechanism for In enrichment (Schwarz-Schampera and Herzig, 2002). At the Chuquicamata Underground mine, In concentrations are also important in the low-temperature chloritic zone, suggesting that cooling and mixing may have impacted the stability of In-Cl complexes, enhancing In incorporation into chalcopyrite. Therefore, it is likely that temperature is the dominant control on Se and In concentrations in chalcopyrite, although other potential factors, including pH and redox changes and the presence of co-crystallizing phases, may also play a role (Qian et al., 1998; Sinclair et al., 2006; Cook et al., 2011; Carvalho et al., 2018; George et al., 2016, 2018). Despite the fact that Se is not systematically detected in chalcopyrite at Chuquicamata, this element is commonly reported in the literature within this sulfide. Thus, the variability of Se concentrations in chalcopyrite between alteration types, as recognized here, may point to changes in the physicochemical conditions of the fluid, although this interpretation must be taken with caution.

Silver vs. Bi data are plotted for bornite from the background potassic and intense potassic alteration zones (Fig. 9B). An almost vertical cluster of Ag-Bi values is observed, spanning Ag/Bi ratios of ~1. Crespo et al. (2020, accepted) reported a positive correspondence between Ag and Bi at the Río Blanco porphyry Cu deposit in Chile and noted that Ag concentrations in bornite increased with cooling. Those authors interpreted that the increase in Ag/Bi ratios was likely due to variations in temperature relate to the alteration type. However, and as noted above, we did not observe a correlation between alteration type and Ag/Bi ratios (Fig 9B). We explain this feature as the result of co-crystallization partitioning controls on Ag and Bi attributable to coexisting minerals that are associated with bornite at Chuquicamata Underground, i.e., chalcocite, covellite and wittichenite (Fig. 6C). Cook et al. (2011) reported that when bornite and chalcocite/digenite coexist, Ag is preferentially partitioned into chalcocite/digenite, whereas Bi is concentrated in bornite. The behavior of these two elements can be further analyzed in Figure 9B were most data points are associated with bornite coexisting with chalcocite/digenite/covellite assemblages. In contrast, the outlier bornite sample 3618M22_bn10 is not associated with chalcocite/digenite/covellite. Therefore, we suggest that the high concentration of Ag and Bi in the aforementioned sample is directly related to the absence of co-crystallizing Cu-sulfides. These results are in good agreement with those reported by Cook et al. (2011), which also noted that in

the absence of Cu-sulfides, bornite showed a higher concentration of Ag and Bi. Therefore, we conclude that the Ag-Bi relation in bornite at Chuquicamata Underground is more likely controlled by the presence of co-existing Cu-S phases rather than temperature.

Figure 9C shows a positive trend between Ag and Sn in bornite. In this plot, it is possible to observe that higher concentrations of Ag and Sn are related to the intense potassic alteration, while lower concentrations of these two elements are associated with the background potassic alteration. Specifically, bornite from the background potassic alteration is characterized by Ag/Sn ratios between ~100 and 10, while the Ag/Sn ratio in bornite from the intense potassic alteration vary significantly from ~100 down to ~1. It is well documented that the solubility of Ag is a function of temperature, pH, $a\text{H}_2\text{S}$ and salinity (Pokrovski et al., 2013). On the other hand, previous studies have reported that the solubility of cassiterite in HCl-bearing water vapor and also in granitic melts decreases with decreasing temperature, salinity and $f\text{O}_2$ (i.e., Bhalla et al., 2005; Migdisov and Williams-Jones., 2005). Even though no experimental data are available to precisely assess the physicochemical controls on Ag and Sn partitioning into bornite, it is possible that lower temperatures (and lower $f\text{O}_2$ conditions?) may have favored the incorporation of Ag and Sn in bornite during the intense potassic alteration stage. Furthermore, and considering that both the Ag and Sn content are closely related with Cu grades in hydrothermal ore deposits (Huston et al., 2011; Pokrovski et al., 2013; Carvalho et al., 2018), we argue that higher concentrations of Ag and Sn in bornite in the intense potassic alteration may be also related to the higher Cu precipitation during this stage, when compared to the background potassic alteration event.

Cobalt vs. Ni data of pyrite from the background potassic, chloritic and quartz-sericite alteration are displayed in Figure 9D. In general, Co/Ni ratios range between ~0.1 and ~100. It is important to note that all pyrite data from the background potassic alteration zone plot below Co/Ni = 1, while Co and Ni data of pyrite from the chloritic alteration are concentrated in the upper part of the diagram, at higher Co contents (Co/Ni ~1-10). Co-Ni data for pyrite from the quartz-sericite alteration are more scattered, although most data points plot above the 1:1 line, with maximum Co/Ni ratios at ~100. Previous studies have reported that Co in hydrothermal solutions is transported as chloride complexes, which are more susceptible to physicochemical changes (Migdisov et al., 2011; Liu et al., 2011). In particular, these works have identified that cooling may have an important effect on the destabilization of Co-Cl complexes , i.e., a decrease in temperature from 300°C to 25°C may generate a drop in Co solubility from 142 ppm to 5 ppm (Liu et al., 2011). This is consistent with the higher concentration of Co in pyrite from the low temperature chloritic alteration (Fig. 9D). In addition, it has been reported that an increase in pH and a decrease in $f\text{O}_2$ could also trigger destabilization of Co-Cl complexes (Liu et al., 2011; Brugger et al., 2016). Although these effects need to be further evaluated in future studies, it is likely that pH changes were less important on the behavior of Co at Chuquicamata, due to the fact that background potassic and chloritic alteration formed under similar pH conditions (neutral to slightly alkaline), but have the lowest and highest Co concentrations in pyrite, respectively (Fig. 9D). On the other hand, a decrease in Cl^- concentration could have impacted considerably the concentration of Co in the chloritic alteration zone, as a result of fluid dilution caused by mixing with meteoric waters.

Finally, Ni is expected to have followed a similar behavior than Co, considering that a decrease in temperature, Cl^- and $f\text{O}_2$, and an increase in pH, can lead to a lower Ni solubility (Liu et al., 2012; Jiang et al., 2017). However, Co is more mobile than Ni in hydrothermal fluids (Brugger et al., 2016). Therefore, and considering that Ni concentrations in pyrite at Chuquicamata are widely distributed in all alteration types (Fig. 9D), a more complex combination of

physicochemical factors may have generated the observed distribution of Co and Ni in pyrite.

Cobalt concentration in pyrite from each alteration type is plotted with respect to Ag (Fig. 9E) and Cu (Fig. 9F). In these diagrams, distinct clusters can be observed for pyrite from the different alteration types. For example, higher Ag and Cu concentrations in pyrite are related to high temperature alterations (e.g., background potassic), while higher Co contents are associated with the chloritic alteration. Pyrite Ag/Co ratios in the background potassic alteration vary between ~0.01 and 10, while pyrite from the chloritic alteration shows a Ag/Co ratio <0.1. On the other hand, Co/Cu ratios are higher in pyrite from the chloritic alteration (>1) and lower (<1) in the background potassic event. These observations are consistent with microanalytical data of pyrite reported for Río Blanco, showing that Ag and Cu are generally higher in the high temperature alteration assemblages (Crespo et al., 2020, accepted). In hydrothermal systems, Ag and Cu are transported as chloride complexes (Zotov et al., 1995; Liu and McPhail., 2005; Brugger et al., 2007; Pokrovski et al., 2013; Yin and Zajacz, 2018). The solubility of Ag and Cu in aqueous solutions is a function of temperature, pH, $a\text{H}_2\text{S}$ and salinity. Hence, complex destabilization is caused by chloride removal (or dilution), fluid neutralization, an increase in $f\text{O}_2$ or a decrease in temperature of the fluid. At Chuquicamata Underground, the highest concentrations of Ag and Cu in pyrite are detected in the background potassic alteration (Fig. 9E-F), which was generated at temperatures between 450 and 600°C. This temperature range is consistent with changes in the solubility of Ag and Cu in fluids, which may have affected the stability of the metal complex, and consequently, a more efficient incorporation into pyrite. Estimated temperatures for the chloritic and quartz-sericite alterations, are around 200-250°C and 250-300°C, respectively, which may explain the similar Ag and Cu concentrations in pyrite in both alteration types (Fig. 7D). However, more data are needed to better constrain the key parameters that control Ag and Cu incorporation in pyrite.

2.6.3 Implications for sulfides as vectors towards Cu mineralization

Several studies have proposed that sulfide geochemistry can be used as a tool to vector towards ore mineralization. Most recent examples are limited to pyrite in sedimentary exhalative or SEDEX (Mukherjee and Large, 2017), volcanogenic hosted massive sulfide or VHMS (Soltani et al., 2018), epithermal Au (Baker et al., 2006; Kouhestani et al., 2017; Román et al., 2019) or transitional epithermal-porphyry deposits (Maydagán et al., 2013; Franchini et al., 2015). Furthermore, Gregory et al. (2019) presented a statistical methodology to distinguish barren sedimentary pyrite from ore deposit pyrites, including SEDEX, VHMS, iron oxide-copper-gold (IOCG), orogenic Au and porphyry Cu systems. Besides pyrite, Cook et al. (2011) suggested that Se concentrations in Cu-Fe sulfides, such as bornite, could be used as a vector in exploration, indicating the possibility to track fluid sources in magmatic-hydrothermal deposits. Despite the fact that pyrite and chalcopyrite are ubiquitous in porphyry Cu deposits and that both sulfides are present in distal propylitic alteration halos, their potential as exploratory tools has not been fully investigated mainly because few studies have systematically reported geochemical data that can be correlated, in both time and space, with hydrothermal alteration types. Our data from the Chuquicamata Underground mine provide a unique opportunity to further evaluate the potential of Cu-(Fe) sulfides to explore for concealed porphyry Cu deposits or vector towards ore zones, as a complementary tool to porphyry indicator minerals (PIMs) such as zircon, apatite, magnetite and epidote/chlorite (Wilkinson et al., 2015, 2017; Cooke et al., 2017, 2020; Pacey et al., 2019).

Based on our results, we propose the use of Se and In concentrations to discriminate

chalcopyrite formed at high vs. low temperature conditions. Our data show that distinct variations in the chalcopyrite Se/In ratio are a function of temperature and by inference alteration type. Figure 10A shows that lower Se/In ratios are related to the chloritic and quartz-sericite alterations, while higher Se/In ratios are characteristic of the background potassic alteration (intense potassic alteration is only represented by one data point). On average, and as a first approximation, the chalcopyrite Se/In ratio varies from 33.9 to 845.2 in the low temperature alterations (quartz-sericite and chloritic) to the high temperature background potassic alteration, indicating an increase in almost two orders of magnitude. This trend should be corroborated in future studies and completed with more data from other porphyry Cu deposits.

Due to its ubiquity and widespread occurrence, pyrite is perhaps the most promising sulfide for geochemical vectoring. At Chuquicamata Underground, Ag/Co and Co/Cu ratios are proposed here based on the fact that they show opposite trends. As discussed in the previous section, higher Ag/Co ratios characterize pyrite from the background potassic alteration, whereas lower ratios are observed in the chloritic alteration (Fig. 9E). Co/Cu ratios, in contrast, are higher in the chloritic alteration and lower in the background potassic alteration (Fig. 9F). The Ag/Co vs Co/Cu plot shows a well-defined array, where Ag/Co ratios span four orders of magnitude increasing from ~0.001 to 10 from the chloritic to background potassic alteration, while Co/Cu ratios decrease from ~100 to 0.001 from the chloritic to background potassic alteration spanning five orders of magnitude (Fig. 10B). Intermediate ratios are identified in pyrite from the quartz-sericite alteration (Ag/Co~0.01-0.2; Co/Cu~0.01-1). Hence, we propose that the Ag/Co and Co/Cu ratios in pyrite could be used as a potential tool to discriminate between the low temperature distal zones of porphyry Cu deposits and the high temperature central core.

2.7 CONCLUDING REMARKS

The data presented in this study allow constraining the trace element signature of Cu-(Fe) sulfides at the Chuquicamata Underground mine and evaluate their geochemical variability as a function of hydrothermal alteration. Microanalyses of chalcopyrite, bornite and pyrite show that these sulfides contain several trace elements that are dominantly present in solid solution, although micro-particulate occurrences were also observed. Most of the elements detected show a similar range of concentration in the studied sulfides (usually <1,000 ppm), albeit wt.% levels of certain elements were found in some cases. Chalcopyrite, the main Cu ore phase, hosts relevant concentrations of Se and In, while bornite is an important carrier of Ag, Bi and Sn. In comparison, pyrite contains the largest diversity of trace elements with significant concentrations of Co, As, Sb and Pb, hosting also high concentrations of Cu, among other elements.

Cu-(Fe) sulfides at Chuquicamata show distinct geochemical signatures that are characteristic of each hydrothermal alteration type within this porphyry deposit. For example, high concentrations of Se and In in chalcopyrite are related to the high temperature background potassic alteration, while lower concentrations of these two elements are associated with the low temperature quartz-sericite and chloritic alteration. Selected variations in trace element concentration were also reported for bornite, with higher contents of Ag and Sn related to the intense potassic alteration and lower concentrations in the background potassic alteration. Pyrite shows the most notable variation in trace element concentration at Chuquicamata, with Co, Ag and Cu presenting distinct relations with alteration type. Higher Co concentrations occur in pyrite from the low temperature alteration (chloritic), while higher Ag and Cu contents are associated with high

temperature background potassic alteration. Based on these characteristics, the Se/In ratio in chalcopyrite and the Ag/Co vs. Co/Cu plot for pyrite are proposed to discriminate between the high temperature central core of porphyry Cu-Mo systems and the low temperature distal zones.

It is important to highlight that physicochemical conditions and co-crystallizing phases (in particular Cu-sulfides, such as chalcocite, digenite and covellite), play a pivotal role in controlling trace element distribution in the studied Cu-(Fe) sulfides. Factors such as temperature, pH, fO_2 , aH_2S and salinity of the hydrothermal fluid are the most critical parameters in controlling the partition of trace elements in the different sulfides phases. However, other effects related to the intrinsic nature and structure of each sulfide may have modulated trace element partitioning during each alteration event. Further studies are needed to constrain experimentally the speciation and mineralogical site of the various trace elements in chalcopyrite, bornite and pyrite, and assess their solid solubility limits under temperature, pressure, and oxygen/sulfur fugacity relevant to porphyry systems. Such studies should also assess the potential crystallographic controls on elemental partitioning in sulfides and the role of co-crystallizing phases, which remain largely unconstrained for most elements.

We stress that the reported trace element variations provide an opportunity to further explore the potential use of sulfide geochemistry in vectoring studies. However, we note that the use of elemental ratios in sulfides as vectors towards ore zones must follow a careful characterization of the ore and gangue minerals. Among many other factors, multiple mineralization pulses and superposition of hydrothermal events can dramatically change the distribution of trace elements within the sulfides. Furthermore, the concentration and distribution of trace elements in sulfides will depend on different factors, including the metal concentration in the hydrothermal fluid, the salinity, pH and the presence of complexing agents (Kouzmanov and Pokrovski, 2012; Audétat, 2019). Therefore, more data from other porphyry Cu deposits are required to compare results and test the use of the proposed ratios. Despite these inherent limitations, we conclude that geochemical vectoring methods using sulfides (pyrite, chalcopyrite, bornite) hold a promising potential as complementary exploration tools in porphyry Cu-Mo systems.

2.8 ACKNOWLEDGMENTS

This study was funded by the Iniciativa Científica Milenio through grant “Millenium Nucleus for Metal Tracing along Subduction”. Additional support was provided by FONDAP project 15090013 “Centro de Excelencia en Geotermia de Los Andes, CEGA”. The LA-ICP-MS analytical work was funded by CONICYT-FONDEQUIP instrumentation grant EQM120098. Yanan Liu at the University of Toronto and Rurik Romero Universidad de Chile are acknowledged for their help with electron microprobe and LA-ICP-MS analyses, respectively. Fernando Ramírez at CODELCO-Chuquicamata is acknowledged for his help during core sampling. We thank CODELCO-Gerencia de Exploraciones and CODELCO-Chuquicamata for providing data and access to the deposit and drill core mapping data. Constanza Rivas Romero thanks financial support by a M.Sc. scholarship from Iniciativa Científica Milenio.

2.9 REFERENCES

- Abrailis PK, Patrick RAD, Vaughan DJ (2004) Variations in the compositional, textural and electrical properties of natural pyrite: a review. *Int J Miner Process* 74: 41-59.
- Arif J, Baker T (2004) Gold paragenesis and chemistry at Batu Hijau, Indonesia: Implications for gold-rich porphyry copper deposits. *Miner Deposita* 39: 523-535.
- Arnott A (2003) Evolution of the hydrothermal alteration at the Chuquicamata Porphyry Copper System, northern Chile. Unpublished PhD Thesis, Dalhousie University, Halifax, Nova Scotia, Canada, pp 455.
- Auclair G, Fouquet Y, Bohn M (1987) Distribution of selenium in high-temperature hydrothermal sulfide deposits at 13° North, East Pacific Rise. *Can Min* 25: 577-587.
- Audébat A (2019) The Metal Content of Magmatic-Hydrothermal Fluids and Its Relationship to Mineralization Potential. *Econ Geol* 114: 1033-1056.
- Baker T, Mustard R, Brown V, Pearson N, Stanley CR, Radford NW, Butler I (2006) Textural and chemical zonation of pyrite at Pajingo: a potential vector to epithermal gold veins. *Geochem: Explor, Environ, Anal* 6: 283-293.
- Ballard JR, Palin JM, Williams IS, Campbell IH, Faunes A (2001) Two ages of porphyry intrusion resolved for the super-giant Chuquicamata copper deposit of northern Chile by ELA-ICP-MS and SHRIMP. *Geology* 29: 383-386.
- Barker SLL, Hickey KA, Cline JS, Dipple GM, Kilburn MR, Vaughan JR, Anthony Longo AA (2009) Uncloaking invisible gold: use of NanoSIMS to evaluate gold, trace elements, and sulfur isotopes in pyrite from Carlin-type gold deposits. *Econ Geol* 104: 897-904.
- Barra F, Alcota H, Rivera S, Valencia V, Munizaga F, Maksae V (2013) Timing and formation of porphyry Cu-Mo mineralization in the Chuquicamata district, northern Chile: new constraints from the Toki cluster. *Miner Deposita* 48: 629-651.
- Belissont R, Munoz M, Boiron MC, Luais B, Mathon O (2019) Germanium Crystal Chemistry in Cu-Bearing Sulfides from Micro-XRF Mapping and Micro-XANES Spectroscopy. *Minerals* 9: 227.
- Bhalla P, Holtz F, Linnen RL, Behrens H (2005) Solubility of cassiterite in evolved granitic melts: effect of T, fO_2 , and additional volatiles. *Lithos* 80: 387-400.
- Bodnar R, Lecumberri-Sanchez P, Moncada D, Steele-Macinnis M (2014) Fluid inclusions in Hydrothermal Ore Deposits. In: Holland HD, Turekian KK (Eds.), 2nd. *Treatise Cheochem* 13: 119-142.
- Boric R, Díaz F, Maksae V (1990) Geología y Yacimientos Metalíferos de la Región de Antofagasta. *Serv Nac Geol Miner Bol* 40: 246.

Brugger J, Etschmann B, Liu W, Testemale D, Hazemann JL, Emerich H, van Beek W, Proux O (2007) An XAS study of the structure and thermodynamics of Cu (I) chloride complexes in brines up to high temperature (400°C, 600 bar). *Geochim Cosmochim Acta* 71: 4920-4941.

Brugger J, Liu W, Etschmann B, Mei Y, Sherman D, Testemale D (2016) A review of the coordination chemistry of hydrothermal systems, or do coordination changes make ore deposits?. *Chem Geol* 447: 219-253.

Carvalho J, Relvas J, Pinto A, Frenzel M, Krause J, Gutzmer J, Pacheco N, Fonseca R, Santos S, Caetano P, Reis T, Gonçalves M (2018) Indium and selenium distribution in the Neves-Corvo deposit, Iberian Pyrite Belt, Portugal. *Mineral Mag* 82: S5-S41.

Cioacă ME, Munteanu M, Qi L, Costin G (2014) Trace element concentrations in porphyry copper deposits from Metaliferi Mountains, Romania: A reconnaissance study: *Ore Geol Rev* 63: 22-39.

CODELCO Memoria Anual (2018).
https://www.codelco.com/memoria2018/site/docs/20190405/20190405152423/memoria_anual_codelco_2018.pdf

Cook NJ, Ciobanu CL, Danyushevsky LV, Gilbert S (2011) Minor and trace elements in bornite and associated Cu-(Fe) sulfides: A LA-ICP-MS study. *Geochim Cosmochim Acta* 75: 6473-6496.

Cook NJ, Ciobanu CL, George LL, Zhu ZY, Wade B, Ehrig K (2016) Trace element analysis of minerals in magmatic-hydrothermal ores by laser ablation inductively-coupled plasma mass spectrometry: Approaches and opportunities. *Minerals* 6: 111.

Cooke DR, Agnew P, Hollings P, Baker M, Chang Z, Wilkinson JJ, White N, Zhang L, Thompson J, Gemmell JB, Fox N, Chen H, Wilkinson CC (2017) Porphyry indicator minerals (PIMS) and porphyry vectoring and fertility tools (PVFTS) – indicators of mineralization styles and recorders of Hypogene geochemical dispersion halos. In: Proceedings; Exploration 17, Toronto, October 22-25, 2017.

Cooke D, Agnew P, Hollings P, Baker M, Chang Z, Wilkinson J, Ahmed A, White N, Zhang L, Thompson J, Gemmell J, Danyushevsky L, Chen H (2020) Recent advances in the application of mineral chemistry to exploration for porphyry copper-gold-molybdenum deposits: detecting the geochemical fingerprints and footprints of hypogene mineralization and alteration. *Geochem: Explor, Environ, Anal* 20: 176.

Corbet GJ, Leach TM (1998) Southwest Pacific Rim gold-copper systems: Structure, alteration and mineralization. *Soc Econ Geology, Special Publication* 6: 240.

Crespo J, Reich M, Barra F, Verdugo JJ, Martínez C (2018) Critical metal particles in ore sulfides from the Río Blanco porphyry Cu-Mo deposit, Chile. *Minerals* 8: 519.

Crespo J, Reich M, Barra F, Verdugo JJ, Martínez C, Leisen M, Romero R, Morata D, Marquardt C (2020) Ocurrence and distribution of silver in the world-class Río Blanco porphyry Cu-Mo deposit, Central Chile. *Econ Geol*, accepted.

Deditius AP, Utsunomiya S, Ewing R, Kesler SE (2009) Nanoscale “liquid” inclusions of As-Fe-S in arsenian pyrite. *Am Mineral* 94: 391-394.

Deditius A, Reich M, Kesler SE, Utsunomiya S, Chryssoulis S, Walshe JL, Hough R, Ewing RC (2014) The coupled geochemistry of Au and As in pyrite from hydrothermal ore deposits. *Geochim Cosmochim Acta* 140: 644-670.

Demané E, Borquez K, Realini G (2018) Informe geológico actualización modelos de cobre, molibdeno y aresénico PND 2020, División Chuquicamata Superintendencia de Geología Gerencia de Recursos Mineros y Desarrollo: Internal report CODELCO.

Dilles JH, Tomlinson AJ, Martin MW, Blanco N (1997) El Abra and Fortuna Complexes: A porphyry copper batholith sinistrally displaced by the Falla Oeste. *Actas VIII Congreso Geológico Chileno, Antofagasta* 3: 1883-1887.

Dilles J, Einaudi M (1992) Wall-rock alteration and hydrothermal flow paths about the Ann-Mason porphyry copper deposits, Nevada; a 6 km vertical reconstruction. *Econ Geol* 87: 1963-2001.

Einaudi M, Hedenquist J, Inan E (2003) Sulfidation state of hydrothermal fluids: The porphyry-epithermal transition and beyond. In Simmons SF, Graham IJ (Eds.), *Volcanic, geothermal and ore-forming fluids: rulers and witnesses of processes within the Earth*. Soc Econ Geologists Geochem Soc, Special Publication 10: 285-313.

Faunes A, Hintze F, Siña A, Véliz H, Vivanco M (2005) Chuquicamata, Core of a Planetary Scale Cu-Mo Anomaly. In: Porter TM (Ed.), *Super porphyry copper and gold deposits: A global perspective* 1: 151-174.

Fontboté L, Kouzmanov K, Chiaradia M, Pokrovski GS (2017) Sulfide minerals in hydrothermal deposits. *Elements* 13: 97-103.

Franchini M, McFarlane C, Maydagán L, Reich M, Lentz DR, Meinret L, Bouhier V (2015) Trace metals in pyrite and marcasite from the Agua Rica porphyry-high sulfidation epithermal deposit, Catamarca, Argentina: textural features and metal zoning at the porphyry to epithermal transition. *Ore Geol Rev* 66: 366-387.

Frenzel M, Hirsch T, Gutzmer J (2016) Gallium, germanium, indium, and other trace and minor elements in sphalerite as a function of deposit type – A meta-analysis. *Ore Geol Rev* 76: 52-78.

George LL, Cook NJ, Ciobanu CL (2016) Partitioning of trace elements in co-crystallized sphalerite-galena-chalcopyrite hydrothermal ores. *Ore Geol Rev* 77: 97-116.

George LL, Cook NJ, Crowe BBP, Ciobanu CL (2018) Trace elements in hydrothermal chalcopyrite. *Mineral Mag* 82: 59-88.

Godel BM, Barnes SJ, Barnes SJ (2013) Deposition mechanisms of magmatic sulphide liquids: Evidence from high-resolution X-ray computed tomography and trace element chemistry of komatiite-hosted disseminated sulphides. *J Petrol* 54: 1455-1486.

Gregory DD, Large RR, Halpin JA, Baturina EL, Lyons TW, Wu S, Dantushevsky L, Sack PL, Chappaz A, Maslennikov VV, Bull SW (2015a) Trace element content of sedimentary pyrite in black shales. Econ Geol 110: 1389-1410.

Gregory DD, Large RR, Halpin JA, Steadman JA, Hickman AH, Ireland TR, Holden P (2015b) The chemical conditions of the late Archean Hamersley basin inferred from whole rock and pyrite geochemistry with $\Delta^{33}\text{S}$ and $\delta^{34}\text{S}$ isotope analyses. Geochim Cosmochim Acta 149: 223-250.

Gregory DD, Large RR, Bath AB, Steadman JA, Wu S, Danyushevsky L, Bull SW, Holden P, Ireland TR (2016) Trace Element Content of Pyrite from the Kapai Slate, St. Ives Gold District, Western Australia. Econ Geol 111: 1297-1320.

Gregory DD, Cracknell MJ, Large RR, McGoldrick P, Kuhn S, Maslennikov VV, Baker MJ, Fox N, Belousov I, Figueroa MC, Steadman JA, Fabris AJ, Lyons TW (2019) Distinguishing Ore Deposit Type and Barren Sedimentary Pyrite Using Laser Ablation-Inductively Coupled Plasma-Mass Spectrometry Trace Element Data and Statistical Analysis of Large Data Sets. Econ Geol 114: 771-786.

Gustafson LB, Hunt JP (1975) The porphyry copper deposit at El Salvador, Chile. Econ Geol 70: 875-912.

Hanley JJ, MacKenzie MK (2009) Incorporation of platinum-group elements and cobalt into subsidiary pyrite in alkali Cu-Au porphyry deposits: significant implications for precious metal distribution in felsic magmatic-hydrothermal systems. Am Geophys Union, Spring Meeting 2009: V14A-03.

Huston D, Sie S, Suter G, Cooke D, Both R (1995) Trace elements in sulfide minerals from eastern Australian volcanic-hosted massive sulfide deposits; Part I, Proton microprobe analyses of pyrite, chalcopyrite, and sphalerite, and Part II, Selenium levels in pyrite; comparison with delta ^{34}S values and implications for the source of sulfur in volcanogenic hydrothermal systems. Econ Geol 90: 1167-1196.

Huston D, Relvas J, Gemmell J, Drieberg S (2011) The role of granites in volcanic-hosted massive sulphide ore-forming systems: an assessment of magmatic-hydrothermal contributions. Miner Deposita 46: 473-507.

Jiang J, Zhu Y (2017) Geology and geochemistry of the Jianchaling hydrothermal nickel deposit: T-pH-fO₂-fS₂ conditions and nickel precipitation mechanism. Ore Geol Rev 91: 216-235.

Jochum KP, Willbold M, Raczek I, Stoll B, Herwing K (2005) Chemical Characterisation of the USGS Reference Glasses and BIR-1G Using EMPA, ID-TIMS, ID-ICP-MS and LA-ICP-MS. Geostand Newslett 29: 285-302.

John DA, Ayuso RA, Barton MD, Blakely RJ, Bodnar RJ, Dilles JH, Gray F, Graybeal FT., Mars JC, McPhee DK, Seal RR, Taylor RD, Vikre PG (2010) Porphyry copper deposit model, chap. B of Mineral deposit models for resource assessment: U.S. Geological Survey Scientific Investigations Report 2010-5070-B, pp 169.

Keith M, Smith D, Jenkin G, Holwell D, Dye M (2018) A review of Te and Se systematics in hydrothermal pyrite from precious metal deposits: Insights into ore-forming processes. *Ore Geol Rev* 96: 269-282.

Kesler SE, Chrysoulis SL, Simon G (2002) Gold in porphyry copper deposits: Its abundance and fate. *Ore Geol Rev* 21: 103-124.

Kieft K, Damman H (1990) Indium-bearing chalcopyrite and sphalerite from the Gasborn area, West Bergslagen, central Sweden. *Mineral Mag* 54: 109-112.

Kouhestani H, Ghaderi M, Large R, Zaw K (2017) Texture and chemistry of pyrite at Chah Zard epithermal gold-silver deposit, Iran. *Ore Geol Rev* 84: 80-101.

Kouzmanov K, Pokrovski GS (2012) Hydrothermal controls on metal distribution in porphyry Cu (-Mo-Au) systems. *Soc Econ Geology, Special Publication* 16: 573-618.

Kusebauch C, Gleeson SA, Oelze M (2019) Coupled partitioning of Au and As into pyrite controls formation of giant Au deposits. *Sci Adv* 5: eaav5891.

Large DJ, Sawlowocz Z, Spratt J (1999) A cobaltite-framboidal pyrite association from the Kupferschiefer; possible implications for trace element behaviour during the earliest stages of diagenesis. *Mineral Mag* 63: 353-361.

Large RR, Danyushevsky LV, Hollit C, Maslennikov V, Meffre S, Gilbert SE, Bull S, Scott RJ, Emsbo P, Thomas H, Singh B, Foster J (2009) Gold and trace element zonation in pyrite using a laser imaging technique: implications for the timing of gold in orogenic and Carlin-style sediment-hosted deposits. *Econ Geol* 104: 635-668.

Layton-Matthews D, Peter JM, Scott SD, Leybourne M (2008) Distribution, mineralogy, and geochemistry of selenium in felsic volcanic-hosted massive sulfide deposits of the Finlayson Lake district, Yukon Territory, Canada. *Econ Geol* 103: 61-88.

Lindsay DD, Zentilli M, Rojas J (1995) Evolution of an active ductile to brittle shear system controlling mineralization at the Chuquicamata porphyry copper deposit, northern Chile. *Int Geol Rev* 37: 945-958.

Lindsay DD (1997) Structural control and anisotropy of mineralization within the Chuquicamata porphyry copper deposit, northern Chile. Unpublished PhD Thesis, Dalhousie University, Halifax, Nova Scotia, Canada, pp 404.

Liu W, McPhail (2005) Thermodynamic properties of copper chloride complexes and copper transport in magmatic-hydrothermal solutions. *Chem Geol* 221: 21-39.

Liu W, Borg S, Testemale D, Etschmann B, Hazemann JL, Brugger J (2011) Speciation and thermodynamic properties for cobalt chloride complexes in hydrothermal fluids at 35-440°C and 600 bar: An in-situ XAS study. *Geochim Cosmochim Acta* 75: 1227-1248.

Liu W, Migdisov A, Williams-Jones A (2012) The stability of aqueous nickel (II) chloride

complexes in hydrothermal solutions: results of UV-visible spectroscopic experiments. *Geochim Cosmochim Acta* 94: 276-290.

Liu R, Chen G, Yang J (2020) Compositions of Cu-(Fe)-Sulfides in the 109 Reduced Granite-Related Cu Deposit, Xinjiang, Northwest China: Implications to the Characteristics of Ore-Forming Fluids. *Geofluids* 2020: 1-11.

Loges A, Testemale D, Huotari S, Honkanen AP, Potapkin V, Wagner T (2017) Hydrothermal fluoride and chloride complexation of indium: an EXAFS study. *Geophys Res Abstr* 19: 5392.

Longerich HP, Jackson SE, Günther D (1996) Laser ablation inductively coupled plasma mass spectrometric transient signal data acquisition and analyte concentration calculation. *J Anal At Spectrom* 11: 899-904.

Mathur R, Ruiz J, Munizaga F (2001) Insights into Andean metallogenesis from the perspective of Re-Os analyses of sulfides. Extended Abstract in II SSAGI International Conference 3: 34-36.

Maydagán L, Franchini M, Lentz D, Pons J, McFarlane C (2013) Sulfide composition and isotopic signature of the Altar Cu-Au deposit, Argentina: Constraints on the evolution of the porphyry-epithermal system. *Can Miner* 51: 813-840.

McFall KA, Naden J, Roberts S, Baker T, Spratt J, McDonald I (2018) Platinum-group minerals in the Skouries Cu-Au (Pd, Pt, Te) porphyry deposit. *Ore Geol Rev* 99: 344-364.

Migdisov AA, Williams-Jones AE (2005) An experimental study of cassiterite solubility in HCl-bearing water vapour at temperatures up to 350°C. Implications for tin ore formation. *Chem Geol* 217: 29-40.

Migdisov AA, Zezin D, Williams-Jones AE (2011) An experimental study of cobalt (II) complexation in Cl⁻ and H₂S-bearing hydrothermal solutions. *Geochim Cosmochim Acta* 75: 4065-4079.

Mukherjee I, Large R (2017) Application of pyrite trace element chemistry to exploration for SEDEX style Zn-Pb deposits: McArthur Basin, Northern Territory, Australia. *Ore Geol Rev* 81: 1249-1270.

Ossandón G, Fréraut R, Gustafson L, Lindsay D, Zentilli M (2001) Geology of the Chuquicamata Mine: A Progress Report. *Econ Geol* 96: 249-270.

Pacey A, Wilkinson J, Owens J, Priest D, Cooke D, Millar I (2019) The Anatomy of an Alkalic Porphyry Cu-Au System: Geology and Alteration at Northparkes Mines, New South Wales, Australia. *Econ Geol* 114: 441-472.

Palenik CS, Utsunomiya S, Reich M, Kesler SE, Ewing RC (2004) “Invisible” gold revealed: direct imaging of gold nanoparticles in a Carlin-type deposit. *Am Miner* 89: 1359-1366.

Pals D, Spry P, Chrysoulis S (2003) Invisible Gold and Tellurium in Arsenic-Rich Pyrite from the Emperor Gold Deposit, Fiji: Implications for Gold Distribution and Deposition. *Econ Geol* 98:

479-493.

Pašava J, Vymazalova A, Kosler J, Koneev R, Jukov AV, Khalmatov RA (2010) Platinum-group elements in ores from the Kalmakyr porphyry Cu-Au-Mo deposit, Uzbekistan: Bulk geochemical and laser ablation ICP-MS data. Miner Deposita 45: 411-418.

Paton C, Hellstrom J, Woodhead J, Hergt J (2011) Iolite: Freeware for the visualisation and processing of mass spectrometric data. J Anal At Spectrom 26: 2508-2518.

Peterson EC, Mavrogenes JA (2014) Linking high-grade gold mineralization to earthquake-induced fault-valve processes in the Porgera gold deposit, Papua New Guinea. Geology 42: 383-386.

Pokrovski G, Roux J, Ferlat G, Jonchiere R, Seitsonen A, Vuilleumier R, Hazemann JL (2013) Silver in geological fluids from in situ X-ray absorption spectroscopy and first-principles molecular dynamics. Geochim Cosmochim Acta 106: 501-523.

Qian Z, Xinzhi Z, Jiayong P, Shuxun S (1998) Geochemical Enrichment and Mineralization of Indium. Chin J Geochem 17: 221-225.

Reich M, Kesler SE, Utsunomiya S, Palenik CS, Chryssoulis S, Erwing RC (2005) Solubility of gold in arsenian pyrite. Geochim Cosmochim Acta 69: 2781-2796.

Reich M, Deditius A, Chryssoulis S, Li JW, Ma CQ, Parada MA, Barra F, Mittermayr F (2013a) Pyrite as a record of hydrothermal fluid evolution in a porphyry copper system: A SIMS/EMPA trace element study. Geochim Cosmochim Acta 104: 42-62.

Reich M, Palacios C, Barra F, Chryssoulis S (2013b) “Invisible” silver in chalcopyrite and bornite from the Mantos Blancos copper deposit. Eur J Mineral 25: 453-460.

Reich M, Snyder GT, Álvarez F, Pérez A, Palacios C, Vargas G, Cameron EM, Muramatsu Y, Fehn, U (2013c) Using iodine isotopes to constrain supergene fluid sources in arid regions: Insights from the Chuquicamata oxide blanket. Econ Geol 108: 163-171.

Reich M, Large R, Deditius A (2017) New advances in trace element geochemistry of ore minerals and accessory phases. Ore Geol Rev 87: 1215-1217.

Reich M, Román N, Barra F, Morata D (2020) Silver-Rich Chalcopyrite from the Active Cerro Pabellón Geothermal System, Northern Chile. Minerals 10: 113.

Reynolds P, Ravenhurst C, Zentilli M, Lindsay DD (1998) High precision $^{40}\text{Ar}/^{39}\text{Ar}$ dating of two consecutive hydrothermal events in the Chuquicamata porphyry copper system, Chile. Chem Geol 148: 45-60.

Richards J (2005) Cumulative factors in the generation of giant calc-alkaline porphyry Cu deposits. In: Porter TM (Ed.), Super porphyry copper and gold deposits: A global perspective 1: 7-25.

Rivera S, Alcota H, Proffett J, Díaz J, Leiva G., Vergara M (2012) Update of the Geologic Setting

and Cu-Mo Deposits of the Chuquicamata District, Northern Chile. In: Harris M, Camus F (Eds.), Geology and Genesis of major copper deposits and districts of the world: a tribute to Richard H. Sillitoe and J.W. Hedenquist. Soc Econ Geologists, Special Publication 16: 19-54.

Román N, Reich M, Leisen M, Morata D, Barra F (2019) Geochemical and micro-textural fingerprints of boiling in pyrite. *Geochim Cosmochim Acta* 246: 60-85.

Rusk BG, Reed MH, Dilles JH (2008) Fluid inclusion evidence for magmatic-hydrothermal fluid evolution in the porphyry copper-molybdenum deposit at Butte, Montana. *Econ Geol* 103: 307-334.

Schwartz-Scampera U, Herzig PM (2002) Indium: Geology, Mineralogy, and Economics. Springer-Verlag, Berlin.

Sillitoe RH, McKee EH (1996) Age of Supergene Oxidation and Enrichment in the Chilean Porphyry Copper Province. *Econ Geol* 91: 164-179.

Sillitoe RH (1998) Epochs of intrusion-related copper mineralization in the Andes. *J S Am Earth Sci* 1: 89-108.

Sillitoe RH, Perelló J (2005) Andean copper province: Tectonomagmatic settings, deposit types, metallogeny, exploration, and discovery. In: Hedenquist JW, Thompson JFH, Goldfarb RJ, Richards JP (Eds.), Economic Geology - 100th Anniversary Volume. Soc Econ Geologist, pp 845-890.

Sinclair WD, Kooiman G, Martin D, Kjarsgaard IM (2006) Geology, geochemistry and mineralogy of indium resources at Mount Pleasant, New Brunswick, Canada. *Ore Geol Rev* 28: 123-145.

Soltani A, McFarlane C, Lentz D, Walker J (2018) Assessment of pyrite composition by LA-ICP-MS techniques from massive sulfide deposits of the Bathurst Mining Camp, Canada: From textural and chemical evolution to its application as a vectoring tool for the exploration of VMS deposit. *Ore Geol Rev* 92: 656-671.

Sugaki A, Kitakaze A, Harada H (1981) Synthesis of minerals in the Cu-Fe-Bi-S system under hydrothermal condition and their phase relations. *Bull Mineral* 104: 484-495.

Sugaki A, Kitakaze A, Harada, H (1984) Hydrothermal synthesis and phase relations of the polymetallic sulfide system, especially on the Cu-Fe-Bi-S system. In: Sungawa I (Ed.), Materials Science of the Earth's Interior, Terra Publ, Tokyo, pp 545-583.

Tanner D, Henley RW, Mavrogenes JA, Holden P (2016) Sulfur isotope and trace element systematics of zoned pyrite crystals from the El Indio Au-Cu-Ag deposit, Chile. *Contrib Mineral Petrol* 171: 1-17.

Tossell JA, Vaughan DJ, Burdett JK (1981) Pyrite, marcasite, and arsenopyrite type minerals: crystal chemical and structural principles. *Phys Chem Minerals* 7: 177-184.

Ulrich T, Heinrich C (2001) Geology and genesis of the Bajo de la Alumbra porphyry Cu-Au

deposit, Argentina. *Econ Geol* 96: 1743-1774.

Vaughan JP, Craig JR (1978) Mineral Chemistry of Metal Sulfides. Cambridge University Press, Cambridge, United Kingdom.

Vaughan JP, Kyin A (2004) Refractory gold ores in Archean greenstones, Western Australia: mineralogy, gold paragenesis, metallurgical characterization and classification. *Mineral Mag* 68: 255-277.

Wilkinson J, Chang Z, Cooke D, Baker M, Wilkinson C, Inglis S, Chen H, Gemmell J (2015) The chlorite proximitors: A new tool for detecting porphyry ore deposits. *J Geochem Explor* 152: 10-26.

Wilkinson JJ, Cooke DR, Baker MJ, Chang Z, Wilkinson CC, Chen H, Fox N, Hollings P, White NC, Gemmell JB, Loader MA, Pace A, Sievwright RH, Hart LA, Brugge ER (2017) Porphyry indicator minerals and their mineral chemistry as vectoring and fertility tools. In: McClenaghan MB, Layton-Matthews D (Eds.), Application of Indicator Mineral Methods to Bedrock and Sediments, Geological Survey of Canada, pp 90.

Wilson SA, Ridley WL, Koenig AE (2002) Development of sulfide calibration standards for the laser ablation inductively-coupled plasma mass spectrometry technique. *J Anal At Spectrom* 17: 406-409.

Wohlgemuth-Ueberwasser CC, Viljoen F, Petersen S, Vorster C (2015) Distribution and solubility limits of trace elements in hydrothermal black smoker sulfides: An in-situ LA-ICP-MS study. *Geochim Cosmochim Acta* 159: 16-41.

Yamamoto M, Kase K, Tsutsumi M (1984) Fractionation of Sulfur Isotopes and Selenium between Coexisting Sulfide Minerals from the Besshi Deposit, Central Shikoku, Japan. *Mineral Deposita* 19: 237-242.

Yin Y, Zajacz Z (2018) The solubility of silver in magmatic fluids: Implications for silver transfer to the magmatic-hydrothermal ore-forming environment. *Geochim Cosmochim Acta* 238: 235-251.

Zentilli M, Maksae V, Boric R, Wilson J (2018) Spatial coincidence and similar geochemistry of Late Triassic and Eocene-Oligocene magmatism in the Andes of northern Chile: evidence from the MMH porphyry type Cu-Mo deposit, Chuquicamata District. *Int J Earth Sci* 107: 1097-1126.

Zotov AV, Kudrin AV, Levin KA, Shikina ND, Var'yash LN (1995) Experimental studies of the solubility and complexing of selected ore elements (Au, Ag, Cu, Mo, As, Sb, Hg) in aqueous solutions. In: Shmulovich KI, Yardley BWD, Gonchar GG (Eds.), Fluids in the Crust Equilibrium and Transport, Chapman & Hall, London, pp 95-138.

Zwahlen C, Cioldi S, Wagner T, Rey R, Heinrich C (2014) The porphyry Cu-(Mo-Au) deposit at Altar (Argentina): tracing gold distribution by vein mapping and LA-ICP-MS mineral analysis. *Econ Geol* 109: 1341-1358.

2.10 FIGURES

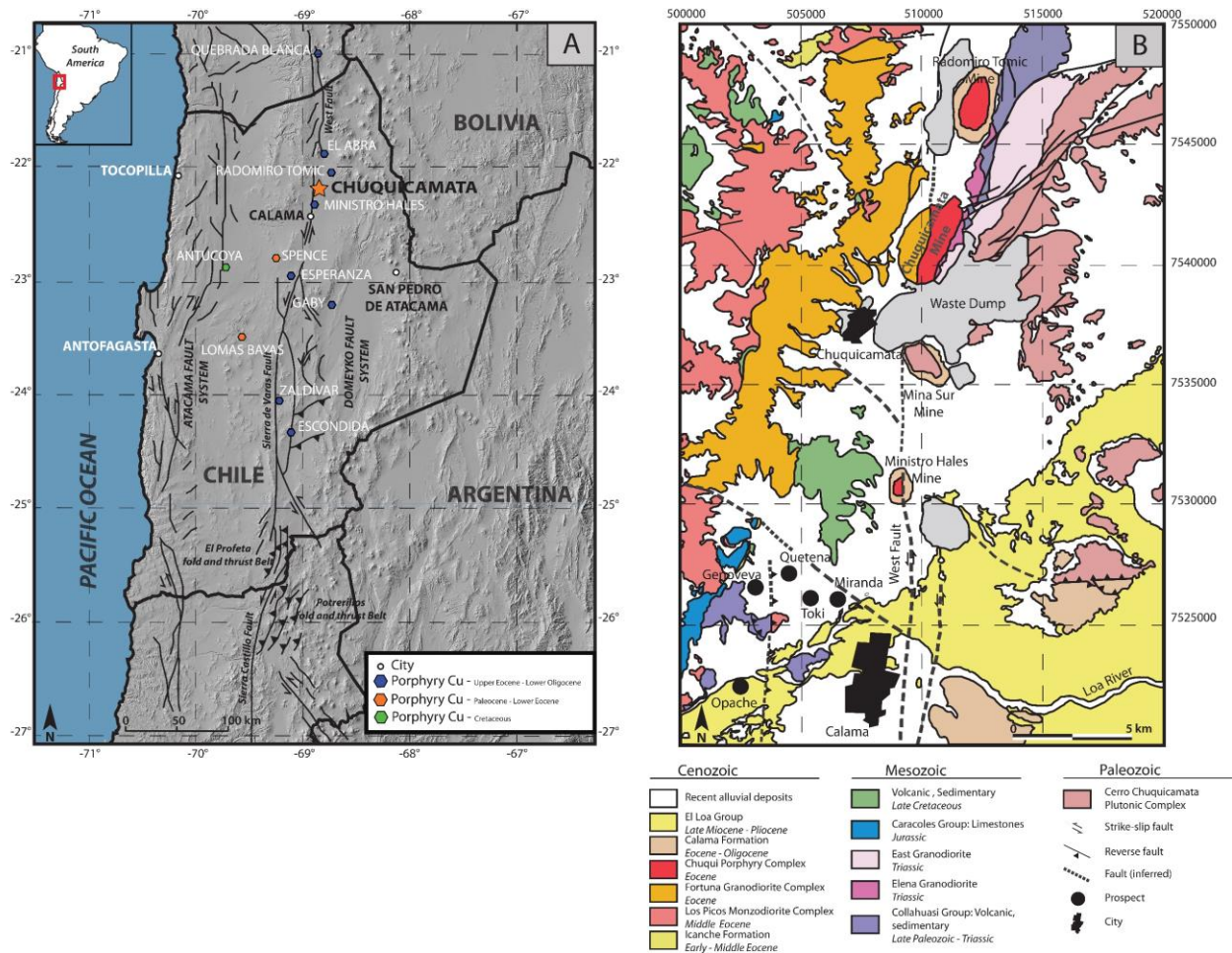


Figure 1. A) Location of the Chuquicamata porphyry Cu-Mo deposit in relation to other deposits in the Antofagasta region, northern Chile. B) Geological map of the Chuquicamata District. Modified from Zentilli et al. (2018).

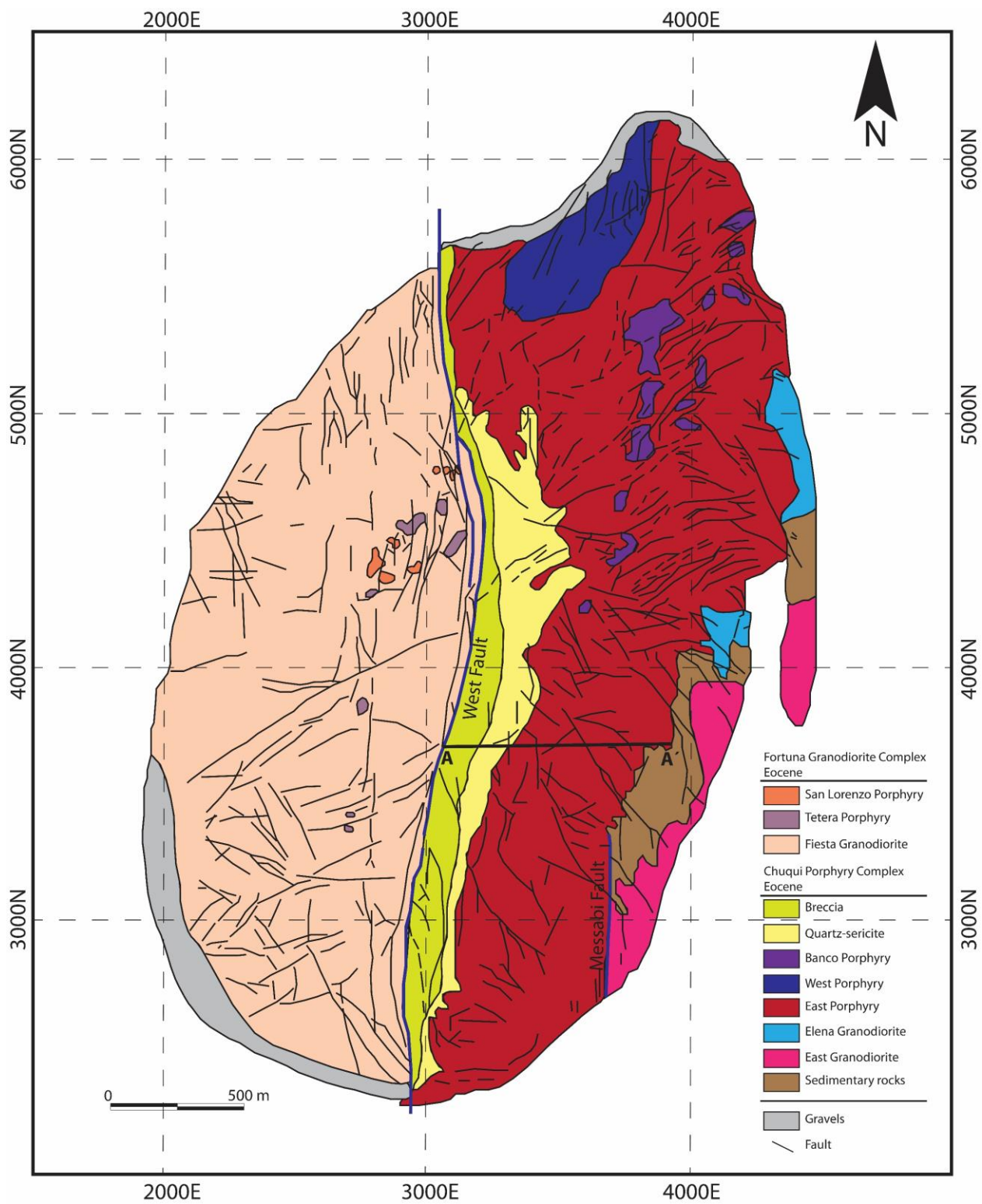


Figure 2. Geology of the Chuquicamata porphyry Cu-Mo deposit. Modified from Ossandón et al. (2001).

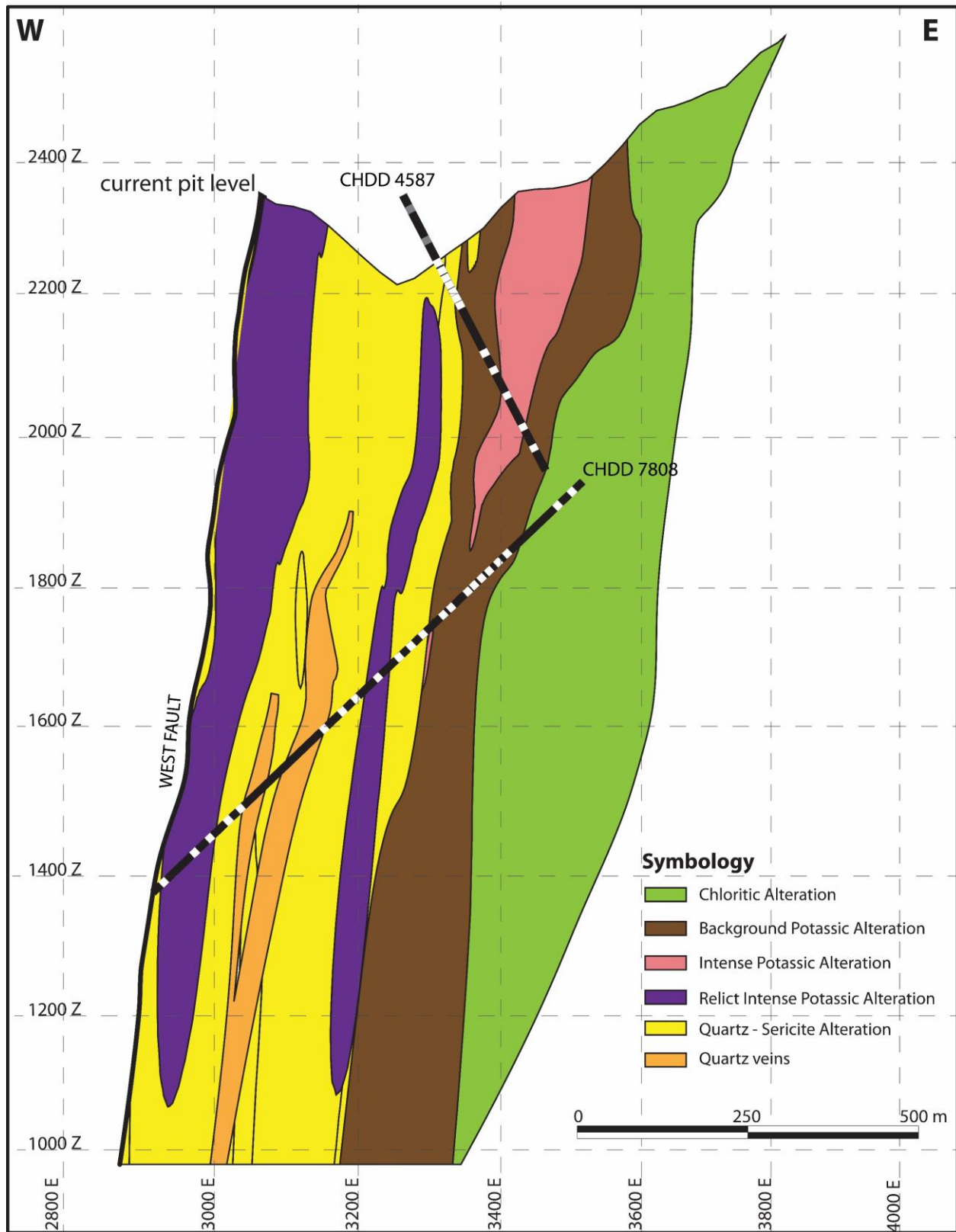


Figure 3. Representative cross-section showing the distribution of alteration zones in the Chuquicamata Underground mine. The upper limit of the alteration zones correspond to the bottom of the Chuquicamata open pit. Drill cores CHDD4587 and CHDD7808 are also shown. Relative position of selected samples within the drill cores are shown in gray and white.

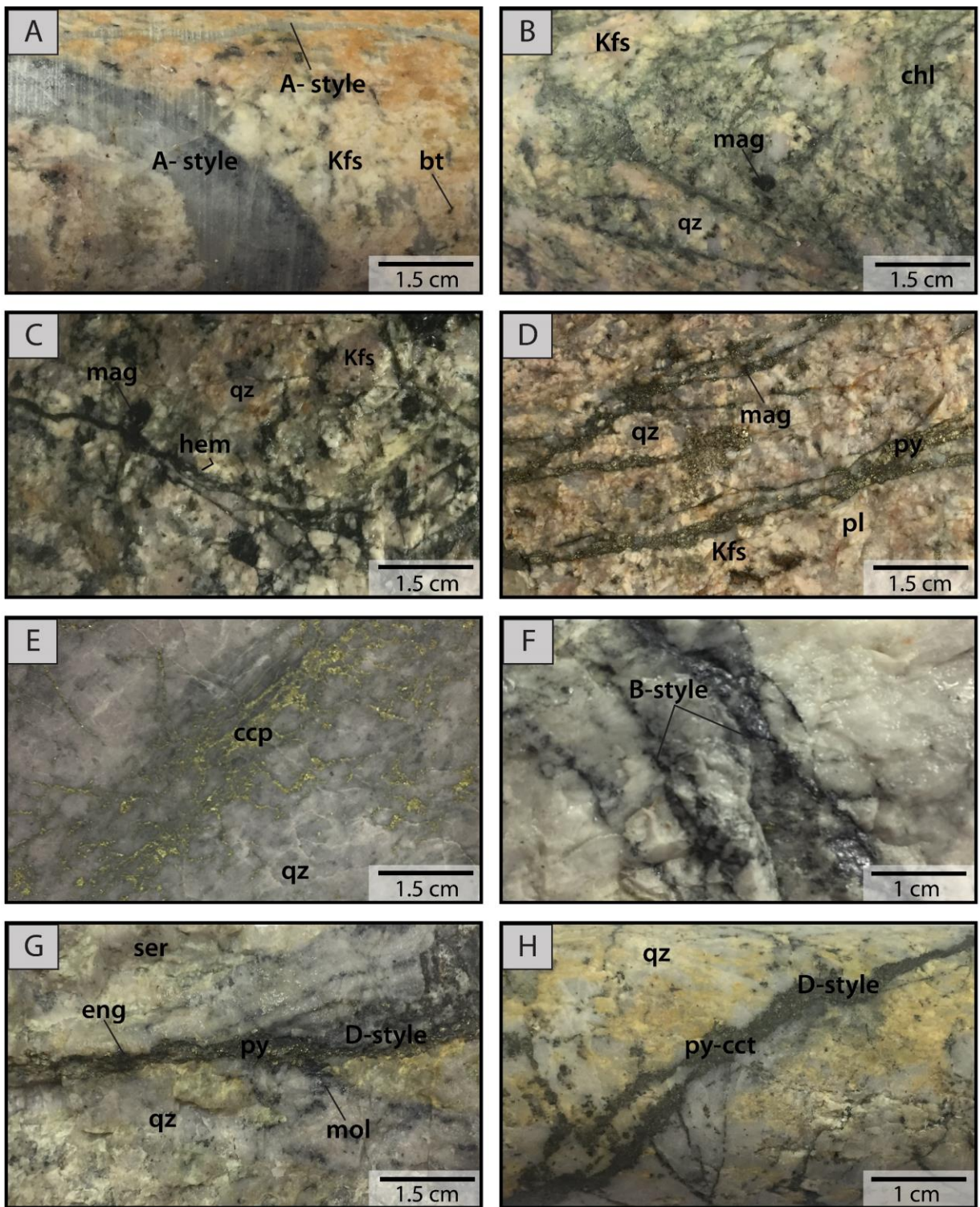


Figure 4. Photographs of main veinlet-types recognized at the Chuquicamata Underground mine. A) “A”-type veinlets with quartz and a halo of biotite; B) Chlorite veinlets with magnetite cross-cutting K-feldspar alteration; C) Hematite veinlets with magnetite; D) Pyrite veinlets with chlorite and magnetite associated to chloritic alteration; E) Chalcopyrite veinlets; F) “B”-type veinlet composed of quartz and molybdenite; G) “D”-type veinlet with pyrite-quartz-molybdenite-enargite; H) “D”-type veinlet with pyrite-chalcocite. Cct: Chalcocite, Chl: Chlorite, Ccp: Chalcopyrite, Eng: Enargite, Hem: Hematite, Kfs: K feldspar, Mag: Magnetite, Mol: Molybdenite, Pl: Plagioclase, Py: Pyrite, Qz: Quartz, Ser: Sericite.

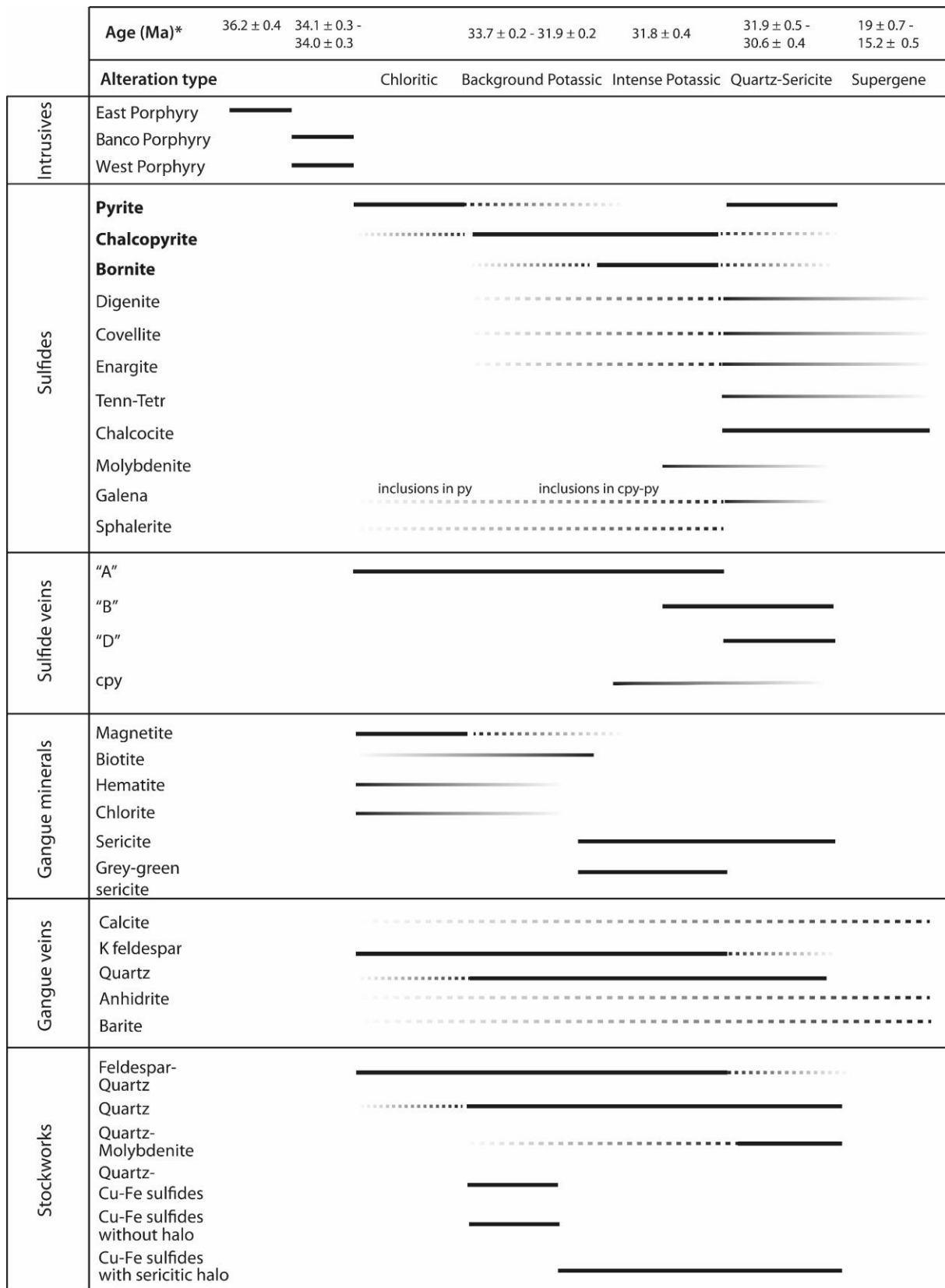


Figure 5. Paragenetic sequence described for the Chuquicamata Underground deposit. *Data sources: Sillitoe and McKee (1996), Reynolds et al. (1998), Mathur et al. (2001), Ballard et al. (2001), Rivera et al. (2012) and Barra et al. (2013)

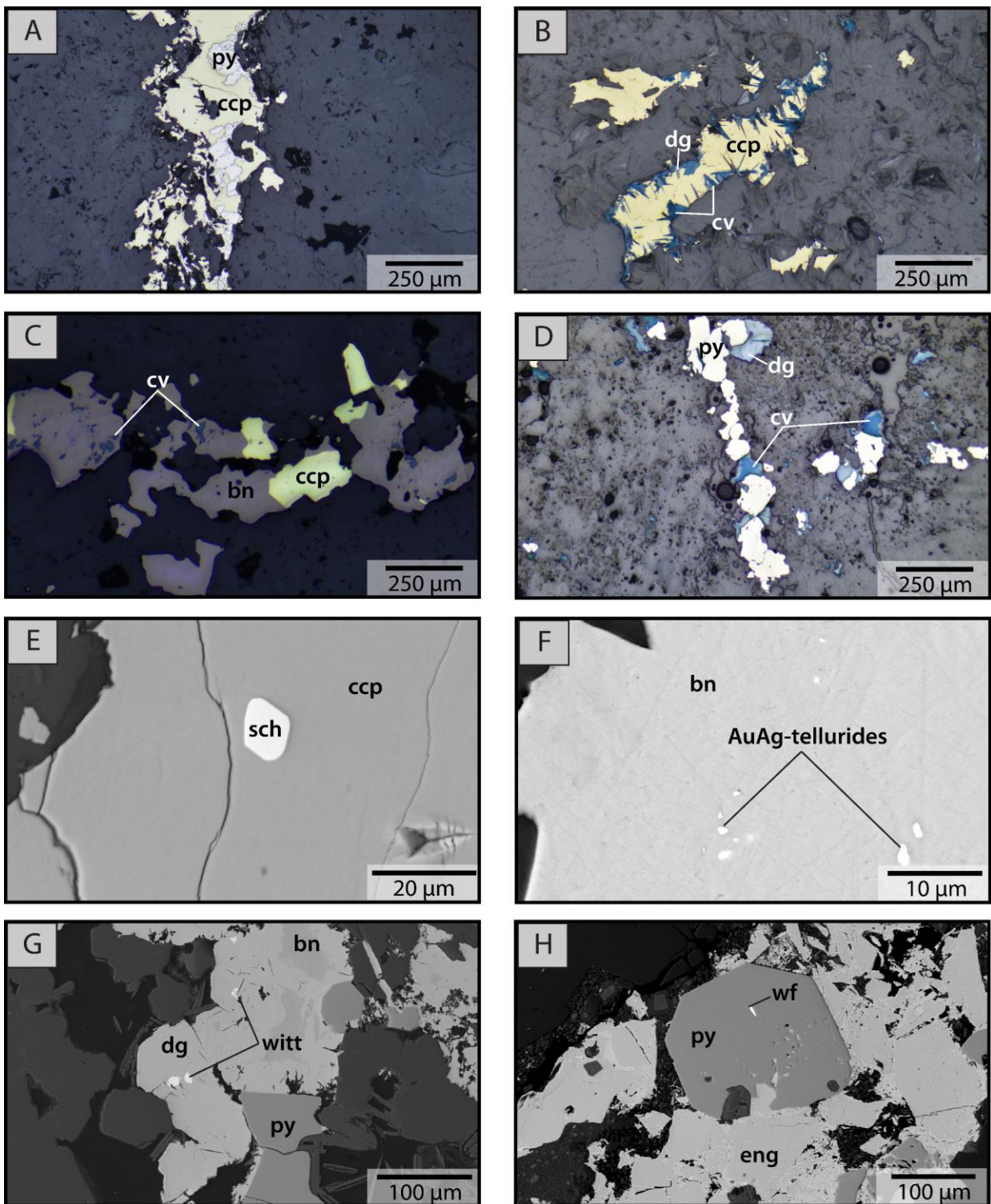


Figure 6. Reflected light photomicrographs and SEM images of chalcopyrite, bornite and pyrite from representative samples. A) Pyrite-chalcopyrite veinlet from the chloritic alteration; B) Chalcopyrite replaced by covellite and digenite from the intense potassic alteration; C) Covellite and bornite replacing chalcopyrite from the intense potassic alteration; D) Pyrite-digenite-covellite veinlet in the quartz-sericite alteration; E) Scheelite micro-inclusion in chalcopyrite from the background potassic alteration zone; F) Au-Ag-tellurides micro-inclusions in bornite from the intense potassic alteration zone; G) Wittichenite inclusions in bornite-digenite in the quartz-sericite alteration zone; H) Wolframite micro-inclusion in pyrite from the quartz-sericite alteration zone. Bn: Bornite, Ccp: Chalcopyrite, Cv: Covellite, Dg: Digenite, Eng: Enargite, Py: Pyrite, Sch: Scheelite, Wf: Wolframite.

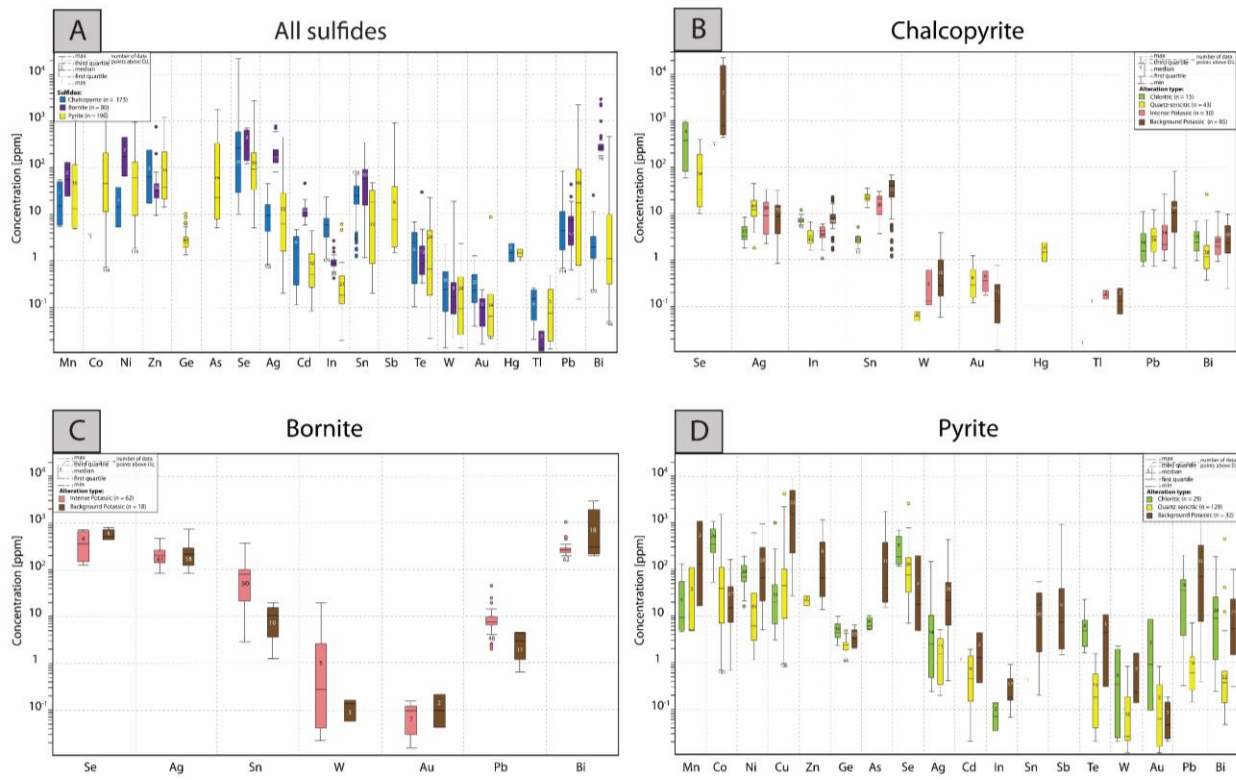


Figure 7. Concentration plot for minor and trace elements in sulfides from Chuquicamata Underground mine. Data are plotted in parts per million (ppm) on a vertical logarithmic scale. In each boxplot, minimum, median and maximum concentrations are marked, and the number of analyses above detection limit for each element is displayed inside each box. A) Boxplot of LA-ICP-MS data for selected minor and trace elements separated by sulfide (chalcopyrite, bornite and pyrite). B-D) Boxplot of LA-ICP-MS data for selected minor and trace element in chalcopyrite, bornite and pyrite (respectively) from different alteration zones in Chuquicamata Underground mine.

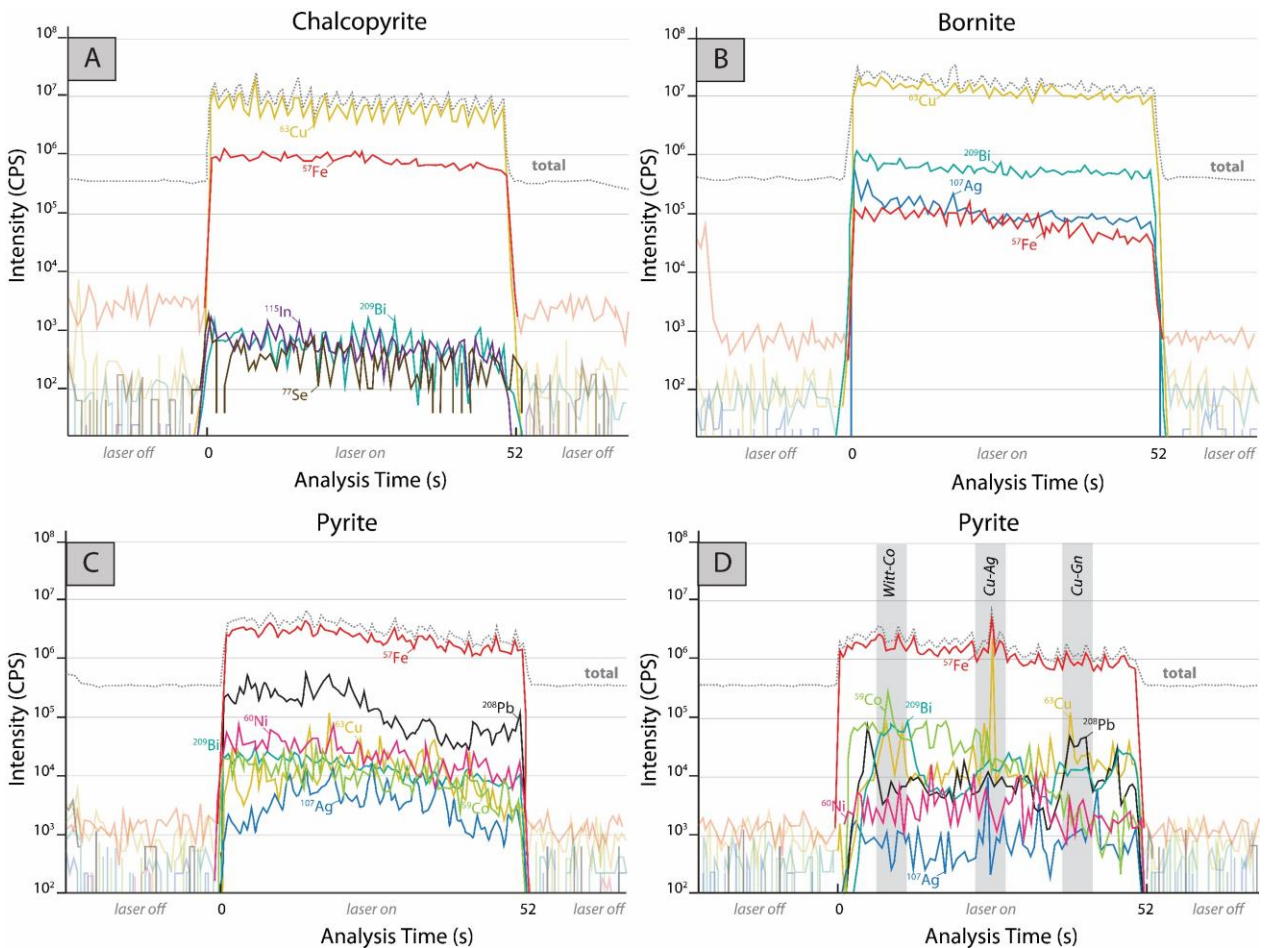


Figure 8. Representative LA-ICP-MS depth-concentration profiles (time vs. intensity) of selected isotopes in sulfides (chalcopyrite, bornite and pyrite). A) Depth-concentration profile of spot analysis from chalcopyrite, where flat signals are identified. B) Depth-concentration profile of spot analysis from bornite, where flat signals are identified. C) Depth-concentration profile of spot analysis from pyrite, where mostly “flat” signals are identified. D) Depth-concentration profile of spot analysis from pyrite, where the presence of galena, wittichenite (coupled ^{63}Cu and ^{209}Bi peaks), Cu, Co and Ag mineral particles are identified.

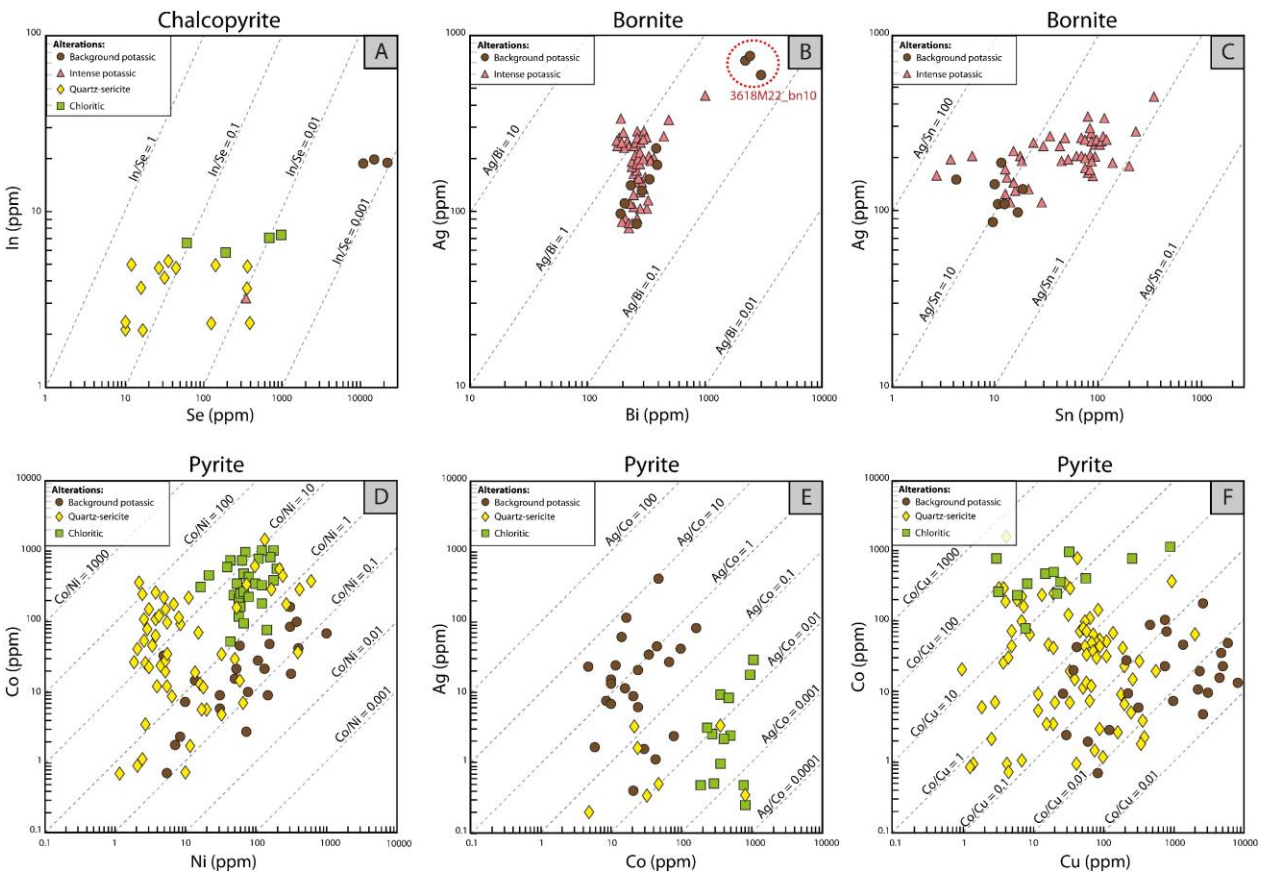


Figure 9. Elemental concentration scatterplots in sulfides as a function of alteration from the Chuquicamata Underground deposit. A) In vs. Se scatterplot for chalcopyrite. B) Ag vs. Bi scatterplot for bornite. C) Ag vs. Sn scatterplot for bornite. D) Co vs. Ni scatterplot for pyrite. E) Ag vs. Co scatterplot for pyrite. F) Co vs. Cu scatterplot for pyrite. Data are plotted in parts per million (ppm) on a logarithmic scale. Only LA-ICP-MS data included.

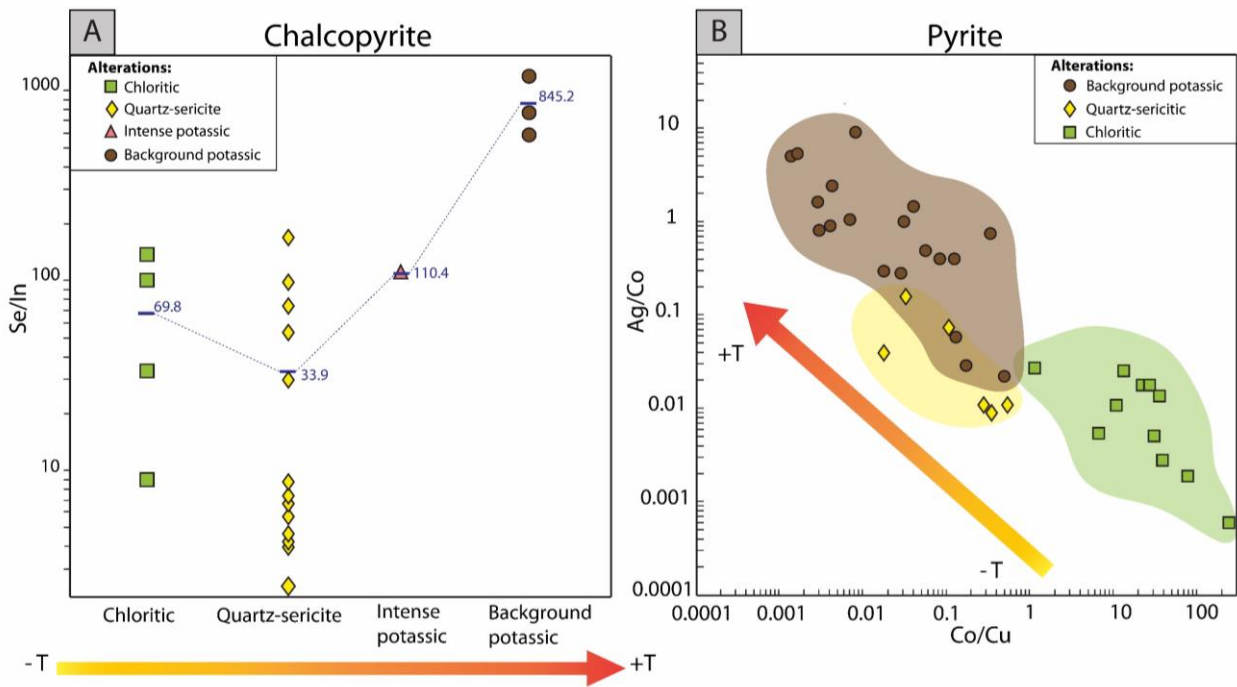


Figure 10. A) Se/In ratios of chalcopyrite from Chuquicamata Underground deposit as a function of alteration. The average of each element ratio for each alteration is observed next to the horizontal line. B) Ag/Co vs Co/Cu scatterplot for pyrite from Chuquicamata Underground deposit. Data are plotted in parts per million (ppm) on a logarithmic scale. Only LA-ICP-MS data included.

CAPÍTULO 3: CONCLUSIONES

Los datos presentados en este estudio permiten identificar la signatura de elementos traza de los sulfuros de Cu-(Fe) en el yacimiento de pórfito de Cu-Mo Chuquicamata, y evaluar la variabilidad geoquímica en función de la alteración hidrotermal en muestras de la mina Subterránea. Los microanálisis de la calcopirita, bornita y pirita muestran que estos sulfuros contienen un amplio rango de elementos traza, los cuales son incorporados preferentemente en la estructura cristalina de los sulfuros, sin embargo, también se observaron como micropartículas o inclusiones minerales. La mayoría de los elementos detectados presentan un rango de concentración similar en los sulfuros estudiados (usualmente < 1000 ppm), aunque ciertos elementos reportan concentraciones a nivel del porcentaje en peso. La calcopirita, la principal mena de Cu, contiene concentraciones relevantes de Se (≤ 11.000 ppm) e In ($\leq 22,8$ ppm), mientras que la bornita es el principal huésped de Ag, Bi y Sn en el depósito. Finalmente, en comparación con la calcopirita y bornita, la pirita contiene la mayor diversidad de elementos traza con concentraciones significativas de Co, As, Sb y Pb, y a la vez alberga altas concentraciones de Cu (≤ 9.700 ppm), entre otros elementos.

Los sulfuros de Cu-(Fe) en Chuquicamata muestran signaturas geoquímicas distintivas que son características de cada alteración hidrotermal dentro del pórfito. Por ejemplo, las mayores concentraciones de Se e In en la calcopirita se encuentran relacionadas con la alteración potásica de fondo, la cual corresponde a la alteración de mayor temperatura, mientras que las menores concentraciones de estos dos elementos se encuentran asociadas con las alteraciones cuarzo-sericítica y clorítica, las cuales se asocian a menores temperaturas. Variaciones de concentración en elementos traza también son reportadas para la bornita, con altos contenidos de Ag y Sn relacionados con la alteración potásica intensa y menores concentraciones en la alteración potásica de fondo. La pirita, por otro lado, muestra las variaciones más notables en Chuquicamata, con Co, Ag y Cu presentando relaciones distintas en función de la alteración. Altas concentraciones de Co se encuentran en la pirita de la alteración de menor temperatura (clorítica), mientras que mayores contenidos de Ag y Cu se encuentran asociados con la alteración de mayor temperatura (potásica de fondo). Basado en estas características, las razones de Se/In en la calcopirita y las razones Ag/Co vs. Co/Cu en la pirita son propuestas para discriminar entre la parte central de mayor temperatura del depósito y las zonas distales de menor temperatura.

Es importante notar que las condiciones fisicoquímicas jugaron un rol fundamental en la distribución de elementos traza en los sulfuros de Cu-(Fe) estudiados. Variables como la temperatura, pH, fO_2 , aH_2S y salinidad de los fluidos durante la alteración hidrotermal fueron los factores dominantes más probables. Sin embargo, otros efectos relacionados con la naturaleza intrínseca y la estructura de cada uno de los sulfuros podrían haber regulado la partición de elementos traza durante cada etapa de alteración. Estudios adicionales serán necesarios para constreñir experimentalmente la especiación y el sitio mineralógico de los elementos traza de interés en la calcopirita, bornita y pirita, y evaluar sus límites de solubilidad bajo temperatura, presión, y fugacidad de oxígeno/azufre relevante en sistemas de pórfito. Dichos estudios futuros también deberían evaluar los posibles controles cristalográficos en la distribución elemental en los sulfuros, y el rol de las fases co-cristalizantes, las cuales permanecen pobremente estudiadas para la mayoría de los elementos.

Finalmente, se enfatiza que las variaciones reportadas proveen una oportunidad única para explorar el potencial uso de la geoquímica de los sulfuros en estudios de vectorización. Sin

embargo, notamos que el uso de razones elementales en los sulfuros como vector hacia la mineralización debe seguir una caracterización y estudio detallado de la paragénesis de mena y ganga en el depósito, a medida que avance el reconocimiento en profundidad del yacimiento. Entre muchos otros factores, los múltiples pulsos de mineralización y la superposición de eventos hidrotermales pueden cambiar la distribución de metales dentro de los sulfuros. Además, y como se mencionó previamente, la concentración y distribución de metales en los sulfuros dependerá de diferentes factores, incluyendo la concentración del metal en el fluido, la salinidad, el pH y la presencia de agentes complejantes, entre otros (Kouzmanov and Pokrovski, 2012; Audétat, 2019). Por lo tanto, se requieren más datos de otros depósitos de pórfido de Cu para comparar los resultados y probar el uso de las razones propuestas. A pesar de estas limitaciones inherentes, concluimos que los métodos de vectorización geoquímica que usan sulfuros de Cu-(Fe) tienen un potencial prometedor como herramientas de exploración complementarias en los sistemas de pórfido Cu-Mo.

BIBLIOGRAFÍA

- Arif J, Baker T (2004) Gold paragenesis and chemistry at Batu Hijau, Indonesia: Implications for gold-rich porphyry copper deposits. *Miner Deposita* 39: 523-535.
- Audétat A (2019) The Metal Content of Magmatic-Hydrothermal Fluids and Its Relationship to Mineralization Potential. *Econ Geol* 114: 1033-1056.
- Barker SLL, Hickey KA, Cline JS, Dipple GM, Kilburn MR, Vaughan JR, Anthony Longo AA (2009) Uncloaking invisible gold: use of NanoSIMS to evaluate gold, trace elements, and sulfur isotopes in pyrite from Carlin-type gold deposits. *Econ Geol* 104: 897-904.
- Cook NJ, Ciobanu CL, Danyushevsky LV, Gilbert S (2011) Minor and trace elements in bornite and associated Cu-(Fe) sulfides: A LA-ICP-MS study. *Geochim Cosmochim Acta* 75: 6473-6496.
- Cook NJ, Ciobanu CL, George LL, Zhu ZY, Wade B, Ehrig K (2016) Trace element analysis of minerals in magmatic-hydrothermal ores by laser ablation inductively-coupled plasma mass spectrometry: Approaches and opportunities. *Minerals* 6: 111.
- Crespo J, Reich M, Barra F, Verdugo JJ, Martínez C (2018) Critical metal particles in ore sulfides from the Río Blanco porphyry Cu-Mo deposit, Chile. *Minerals* 8: 519.
- Crespo J, Reich M, Barra F, Verdugo JJ, Martínez C, Leisen M, Romero R, Morata D, Marquardt C (2020) Ocurrence and distribution of silver in the world-class Río Blanco porphyry Cu-Mo deposit, Central Chile. *Econ Geol*, accepted.
- Deditius A, Reich M, Kesler SE, Utsunomiya S, Chryssoulis S, Walshe JL, Hough R, Ewing RC (2014) The coupled geochemistry of Au and As in pyrite from hydrothermal ore deposits. *Geochim Cosmochim Acta* 140: 644-670.
- Fontboté L, Kouzmanov K, Chiaradia M, Pokrovski GS (2017) Sulfide minerals in hydrothermal deposits. *Elements* 13: 97-103.
- Franchini M, McFarlane C, Maydagán L, Reich M, Lentz DR, Meinret L, Bouhier V (2015) Trace metals in pyrite and marcasite from the Agua Rica porphyry-high sulfidation epithermal deposit, Catamarca, Argentina: textural features and metal zoning at the porphyry to epithermal transition. *Ore Geol Rev* 66: 366-387.
- George LL, Cook NJ, Ciobanu CL (2016) Partitioning of trace elements in co-crystallized sphalerite-galena-chalcopyrite hydrothermal ores. *Ore Geol Rev* 77: 97-116.
- George LL, Cook NJ, Crowe BBP, Ciobanu CL (2018) Trace elements in hydrothermal chalcopyrite. *Mineral Mag* 82: 59-88.
- Godel BM, Barnes SJ, Barnes SJ (2013) Deposition mechanisms of magmatic sulphide liquids: Evidence from high-resolution X-ray computed tomography and trace element chemistry of komatiite-hosted disseminated sulphides. *J Petrol* 54: 1455-1486.

Gregory DD, Large RR, Halpin JA, Baturina EL, Lyons TW, Wu S, Dantushevsky L, Sack PL, Chappaz A, Maslennikov VV, Bull SW (2015a) Trace element content of sedimentary pyrite in black shales. *Econ Geol* 110: 1389-1410.

Gregory DD, Large RR, Halpin JA, Steadman JA, Hickman AH, Ireland TR, Holden P (2015b) The chemical conditions of the late Archean Hamersley basin inferred from whole rock and pyrite geochemistry with $\Delta^{33}\text{S}$ and $\delta^{34}\text{S}$ isotope analyses. *Geochim Cosmochim Acta* 149: 223-250.

John DA, Ayuso RA, Barton MD, Blakely RJ, Bodnar RJ, Dilles JH, Gray F, Graybeal FT., Mars JC, McPhee DK, Seal RR, Taylor RD, Vikre PG (2010) Porphyry copper deposit model, chap. B of Mineral deposit models for resource assessment: U.S. Geological Survey Scientific Investigations Report 2010-5070-B, pp 169.

Johnson KM, Hammarstrom JM, Zientek ML, Dicken CL (2013). Estimate of Undiscovered Copper Resources of the World: USGS Fact Sheet 2014, 3004, pp 3.

Kesler SE, Chryssoulis SL, Simon G (2002) Gold in porphyry copper deposits: Its abundance and fate. *Ore Geol Rev* 21: 103-124.

Kouhestani H, Ghaderi M, Large R, Zaw K (2017) Texture and chemistry of pyrite at Chah Zard epithermal gold-silver deposit, Iran. *Ore Geol Rev* 84: 80-101.

Kouzmanov K, Pokrovski GS (2012) Hydrothermal controls on metal distribution in porphyry Cu (-Mo-Au) systems. *Soc Econ Geology, Special Publication* 16: 573-618.

Kusebauch C, Gleeson SA, Oelze M (2019) Coupled partitioning of Au and As into pyrite controls formation of giant Au deposits. *Sci Adv* 5: eaav5891.

Large DJ, Sawlowocz Z, Spratt J (1999) A cobaltite-framboidal pyrite association from the Kupferschiefer; possible implications for trace element behaviour during the earliest stages of diagenesis. *Mineral Mag* 63: 353-361.

Large RR, Danyushevsky LV, Hollit C, Maslennikov V, Meffre S, Gilbert SE, Bull S, Scott RJ, Emsbo P, Thomas H, Singh B, Foster J (2009) Gold and trace element zonation in pyrite using a laser imaging technique: implications for the timing of gold in orogenic and Carlin-style sediment-hosted deposits. *Econ Geol* 104: 635-668.

Liu R, Chen G, Yang J (2020) Compositions of Cu-(Fe)-Sulfides in the 109 Reduced Granite-Related Cu Deposit, Xinjiang, Northwest China: Implications to the Characteristics of Ore-Forming Fluids. *Geofluids* 2020: 1-11.

Maydagán L, Franchini M, Lentz D, Pons J, McFarlane C (2013) Sulfide composition and isotopic signature of the Altar Cu-Au deposit, Argentina: Constraints on the evolution of the porphyry-epithermal system. *Can Miner* 51: 813-840.

McFall KA, Naden J, Roberts S, Baker T, Spratt J, McDonald I (2018) Platinum-group minerals in the Skouries Cu-Au (Pd, Pt, Te) porphyry deposit. *Ore Geol Rev* 99: 344-364.

Palenik CS, Utsunomiya S, Reich M, Kesler SE, Ewing RC (2004) “Invisible” gold revealed: direct imaging of gold nanoparticles in a Carlin-type deposit. *Am Miner* 89: 1359-1366.

Pals D, Spry P, Chryssoulis S (2003) Invisible Gold and Tellurium in Arsenic-Rich Pyrite from the Emperor Gold Deposit, Fiji: Implications for Gold Distribution and Deposition. *Econ Geol* 98: 479-493.

Pasava J, Vymazalova A, Kosler J, Koneev R, Jukov AV, Khalmatov RA (2010) Platinum-group elements in ores from the Kalmakyr porphyry Cu-Au-Mo deposit, Uzbekistan: Bulk geochemical and laser ablation ICP-MS data. *Miner Deposita* 45: 411-418.

Reich M, Kesler SE, Utsunomiya S, Palenik CS, Chryssoulis S, Erwing RC (2005) Solubility of gold in arsenian pyrite. *Geochim Cosmochim* 69: 2781-2796.

Reich M, Large R, Deditius A (2017) New advances in trace element geochemistry of ore minerals and accessory phases. *Ore Geol Rev* 87: 1215-1217.

Román N, Reich M, Leisen M, Morata D, Barra F (2019) Geochemical and micro-textural fingerprints of boiling in pyrite. *Geochim Cosmochim Acta* 246: 60-85.

Sillitoe RH (1973) The tops and bottoms of porphyry copper deposits. *Econ Geol* 68: 799-815.

Sillitoe RH (2010) Porphyry copper systems. *Econ Geol* 105: 3-41.

Vaughan JP, Kyin A (2004) Refractory gold ores in Archean greenstones, Western Australia: mineralogy, gold paragenesis, metallurgical characterization and classification. *Mineral Mag* 68: 255-277.

Wohlgemuth-Ueberwasser CC, Viljoen F, Petersen S, Vorster C (2015) Distribution and solubility limits of trace elements in hydrothermal black smoker sulfides: An in-situ LA-ICP-MS study. *Geochim Cosmochim Acta* 159: 16-41.

Zhu ZY, Cook N, Yang T, Ciobanu C, Zhao KD, Jiang SY (2016) Mapping of sulfur isotopes and trace elements in sulfides by LA-(MC)-ICP-MS: potential analytical problems, improvements and implications. *Minerals* 6: 110.

ANEXOS

ANEXO A: Anexo Metodológico

A.1 Condiciones de análisis SEM

Observaciones mediante microscopio electrónico de barrido (SEM) fueron llevadas a cabo en el Centro de Excelencia en Geotermia de los Andes (CEGA), en la Universidad de Chile, utilizando un equipo FEI Quanta 250 equipado con electrones secundarios (SE), espectrómetros de energía dispersiva de rayos X (EDS) y electrones retrodispersados (BSE). En particular, los electrones secundarios se utiliza para observar diferencias en la topografía de la muestra, en este estudio principalmente se utilizó para verificar el pulido de la muestra. Los detectores EDS y BSE, por otro lado, son utilizados para determinar las diferencias químicas entre los distintos minerales, en donde el límite de detección es aproximadamente 0.1 wt.%.

Las condiciones analíticas utilizadas en el SEM son las siguientes: voltaje de aceleración de 15 – 20 kV y una corriente de emisión de ~80 μ A, un tamaño de haz entre 4 – 5 μ m y una distancia del haz a la muestra de ~10 mm. En general, cada análisis puntual realizado mediante el detector de electrones retrodispersados consistió en 60 s de lectura aproximadamente, con el fin de obtener un límite de detección apropiado.

A.2 Condiciones de análisis EMPA

Los análisis de microsonda electrónica fueron llevados a cabo en la microsonda JEOL JXA-8230 equipada con 5 espectrómetros de ondas dispersivas en la Universidad de Toronto. Las condiciones analíticas utilizadas fueron: haz totalmente enfocado, energía de haz de 20 keV con un tamaño de haz de ~ 1 μ m de diámetro. La energía del haz para los análisis puntuales y la obtención de mapas WDS fue de 50 nA.

Los elementos fueron adquiridos a partir del análisis de los siguientes cristales: LiF para Co K α , Cu K α , Fe K α , Zn K α y Ni K α ; TAP para As L α y Se L α ; y PETH para Te L α , Ag L α , Pb M α , Pd L α , Pt M α , S K α , Hg M α , Bi M α , Sb L α y Au M α . Los estándares utilizados para la calibración fueron CoS (para Co), CuFeS₂ (para Cu, Fe y S), ZnS (para Zn), (Ni,Fe)₉S₈ (para Ni), FeAsS (para As), CuSe (para Se), PdTe (para Pd y Te), AgBiS₂ (para Ag y Bi), PbS (para Pb), PtTe₂ (para Pt), HgS (para Hg), PdSb (para Sb), Au-Cu (80/20) (para Au). El tiempo de cuentas utilizado en el peak fue de 20 s para Co K α , Cu K α , Fe K α , Zn K α , Ni K α , Te L α , Ag L α , Pd L α y S K α ; 30 s para Sb L α ; 40 s para Pb M α , Pt M α , Hg M α y Bi M α ; 60 s para As L α y Se L α ; y 120 s for Au M α . El mismo tiempo de cuentas fue utilizado para el fondo (*background*). Obteniendo así límites de detección promedios desde los 0.01 a los 0.04 wt.% para la mayoría de los elementos analizados.

A.3 Condiciones de análisis LA-ICP-MS

Los análisis LA-ICP-MS fueron llevados a cabo utilizando un láser del tipo ArF excímero de duración de pulso < 4 ns, que produce un haz de alta intensidad en el rango UV de 193 nm (Teledyne-Photon Machines Analyte G2) acoplado con un espectrómetro de masas por inducción de plasma tipo cuadrupolo (ICP-MS) (Thermo Fisher Scientific iCAP-Q).

Cada análisis puntual consistió en 30 s de lectura de fondo (*background*) y 52 s de lectura durante la ablación de la muestra. Durante estas mediciones, se consideró un tiempo de barrido de cuadrupolo (sweep time) de 0,55 s. En general se usó un diámetro de haz de 40 μm , reduciendo a 30-20 μm en casos específicos, para evitar incorporar inclusiones minerales. La metodología usada fue similar a la de Román et al. (2019), que considera tasa de repetición de pulsos de 4 Hz y energía del haz de 1,5 J/cm², en este caso particular la energía utilizada fue de 2 J/cm²

Los análisis puntuales fueron realizados en tandas de 20 puntos, y al inicio y final de cada tanda fueron analizados, en duplicado, los materiales de referencia MASS-1 (Wilson et al., 2002) y GSE-1G (Jochum et al., 2005). El material MASS-1 fue usado para la cuantificación de las concentraciones (ej., como estándar primario), mientras que GSE-1G fue usado como estándar secundario, para validación de la calibración. La reducción de datos fue realizada en el software Iolite™ v. 3.6.3 (Paton et al., 2011).

A.2 Análisis estadístico de datos composicionales

A.2.1 Estadística descriptiva

Previo a la descripción de los datos composicionales, en el caso de la microsonda electrónica, se eliminaron aquellos datos que entregaban un error mayor al 2%, es decir, aquellos datos en donde el total obtenido se encontraba fuera del rango entre de 98-102%. Luego, para la descripción estadística tanto de los análisis mediante microsonda electrónica (EMPA) y ablación láser (LA-ICP-MS) se consideraron solamente aquellos datos sobre el límite de detección. Con estos datos, se calcularon el mínimo, máximo, mediana y promedio, los cuales fueron representados de manera gráfica en los diagramas de caja-bigote (boxplots). Estos gráficos se llevaron a cabo para todos los análisis realizados, así como también para subconjuntos de datos, por ejemplo, por sulfuro y alteración.

A.2.2 Análisis exploratorio de datos

Para el análisis exploratorio, se llevó a cabo una matriz de correlación de elementos para cada uno de los sulfuros analizados acompañados de gráficos de dispersión (scatterplots). La matriz de correlación fue calculada mediante el software ioGAS, a partir de las concentraciones en porcentaje en peso (wt. %) en el caso de la microsonda electrónica y en partes por millón (ppm) para ablación láser. Aquellos coeficientes de correlación mayores entregados en la matriz, es decir, cercanos a 1 o -1 fueron corroborados gráficamente, mediante gráficos de dispersión.

A la vez, a partir de los boxplots se distinguieron aquellos elementos que tenían comportamientos opuestos en las distintas alteraciones, utilizando de esta forma las razones de los elementos como una nueva variable. Con ello se identificaron tendencias mediante gráficos de dispersión.

A.3 Referencias Anexo Metodológico

Jochum KP, Willbold M, Raczek I, Stoll B, Herwing K (2005) Chemical Characterisation of the USGS Reference Glasses and BIR-1G Using EMPA, ID-TIMS, ID-ICP-MS and LA-ICP-MS. Geostand Newslett 29: 285-302.

Paton C, Hellstrom J, Woodhead J, Hergt J (2011) Iolite: Freeware for the visualisation and processing of mass spectrometric data. *J Anal At Spectrom* 26: 2508-2518.

Román N, Reich M, Leisen M, Morata D, Barra F (2019) Geochemical and micro-textural fingerprints of boiling in pyrite. *Geochim Cosmochim Acta* 246: 60-85.

Wilson SA, Ridley WL, Koenig AE (2002) Development of sulfide calibration standards for the laser ablation inductively-coupled plasma mass spectrometry technique. *J Anal At Spectrom* 17: 406-409.

ANEXO B: Gráficos complementarios datos con inclusiones vs. sin inclusiones

B.1 Calcopirita

Todos los datos obtenidos mediante análisis LA-ICP-MS en la calcopirita de la mina Chuquicamata Subterránea se encuentran en la Figura 11. En ella, se pueden observar los datos con inclusiones en comparación con los datos libres de inclusiones, los cuales fueron identificados mediante el estudio de las señales de ablación en profundidad. Es posible determinar a partir de esta figura que las diferencias entre ambos grupos de datos es mínima, indicando que la presencia de inclusiones en la calcopirita no es dominante, lo cual se condice con los datos presentados con anterioridad.

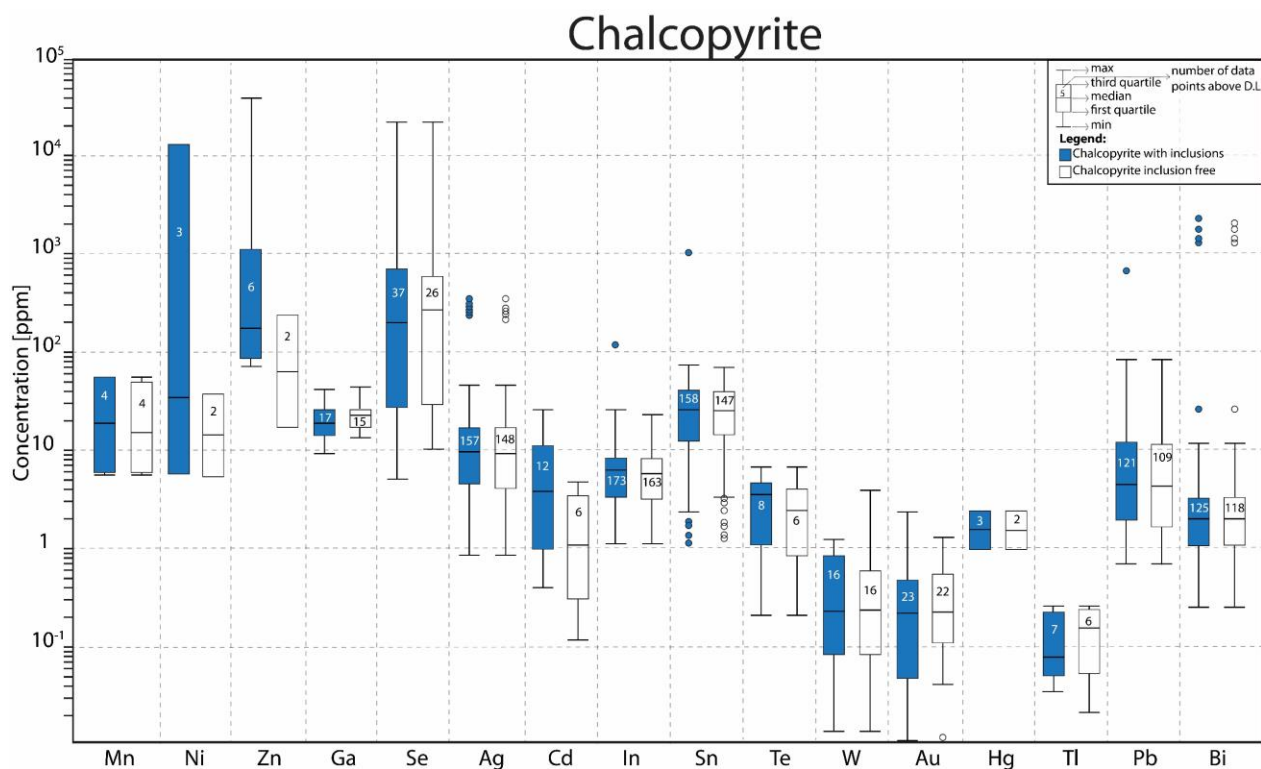


Figura 11. Concentraciones de elementos menores y traza en calcopirita del yacimiento Chuquicamata Subterráneo. Todos los datos LA-ICP-MS se encuentran pleteados en partes por millón (ppm) en una escala vertical logarítmica. En los boxplots, el color azul representa a todos los datos de LA-ICP-MS, mientras que en color blanco se observan los datos libres de inclusiones. En cada boxplot se muestran las concentraciones mínimas, máximas y la mediana, y el número de análisis sobre el límite de detección para cada elemento se encuentra dentro de cada caja.

B.2 Bornita

En la Figura 12 se muestran los datos composicionales mediante LA-ICP-MS de bornita de la mina Chuquicamata Subterránea. Al igual que en el caso de la calcopirita, es posible observar que no existen mayores diferencias composicionales entre los datos con inclusiones en comparación con los datos libres de inclusiones, lo cual es coherente con los datos mostrados con anterioridad.

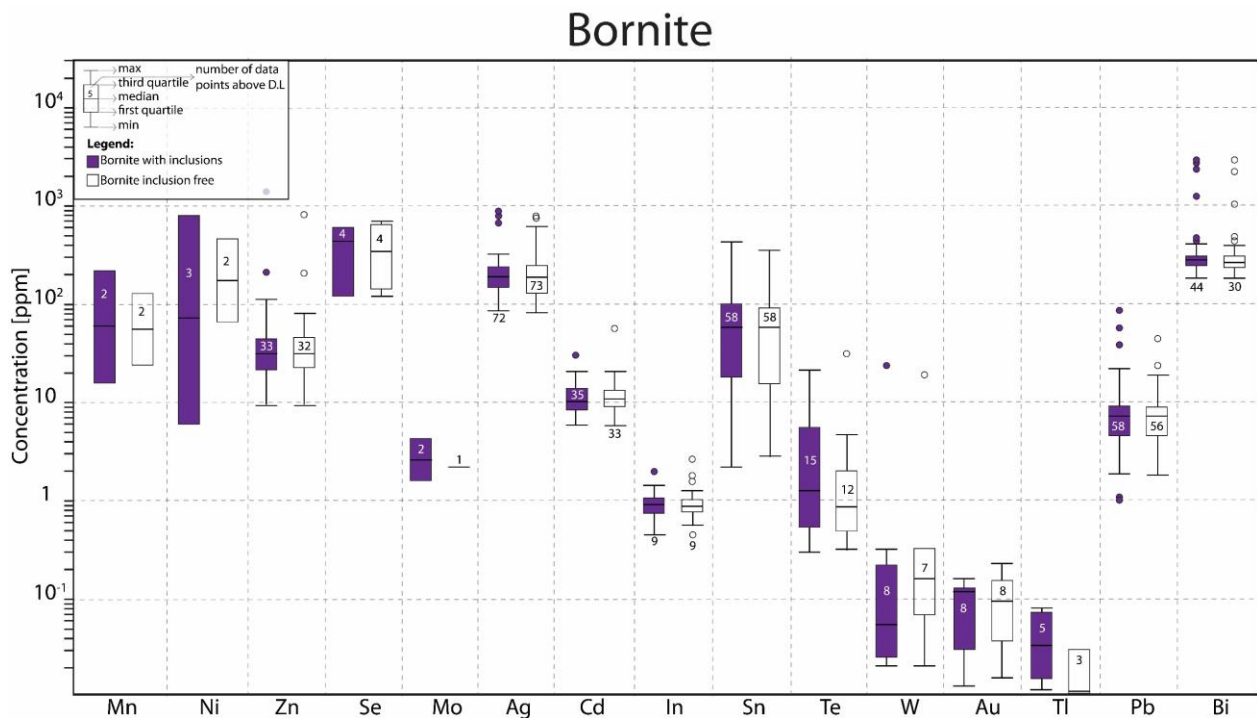
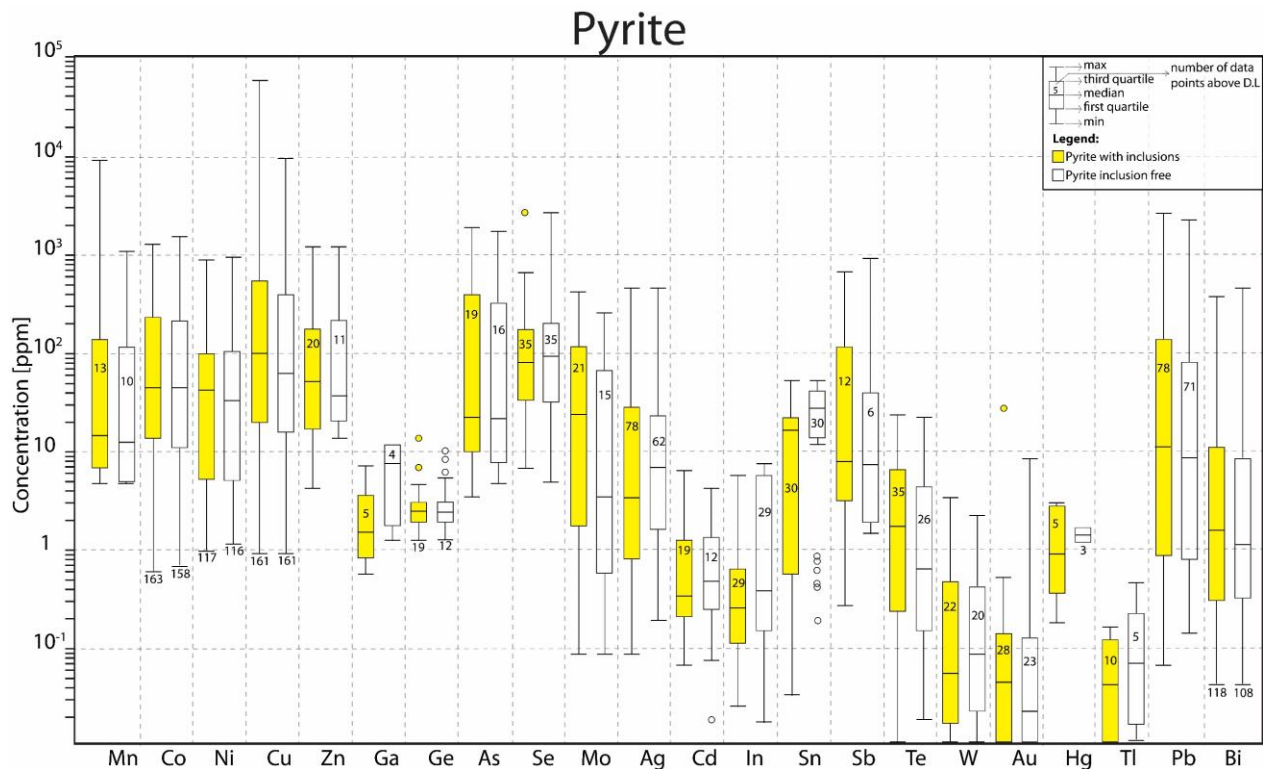


Figura 12. Concentraciones de elementos menores y traza en bornita del yacimiento Chuquicamata Subterráneo. Todos los datos LA-ICP-MS se encuentran ploteados en partes por millón (ppm) en una escala vertical logarítmica. En los boxplots, el color morado representa a todos los datos de LA-ICP-MS, mientras que en color blanco se observan los datos libres de inclusiones. En cada boxplot se muestran las concentraciones mínimas, máximas y la mediana, y el número de análisis sobre el límite de detección para cada elemento se encuentra dentro de cada caja.

B.3 Pirita

En la Figura 13 se muestran los datos composicionales mediante LA-ICP-MS de pirita de la mina Chuquicamata Subterránea. En este caso se puede observar que las concentraciones entre los datos con inclusiones en comparación con los sin inclusiones son bastante similares, sin embargo, se detectan algunas diferencias en Cu, Pb y Bi, ya sea en concentración o como en número de datos, lo que indicaría la presencia de inclusiones de estos elementos.



ANEXO C: Resultados de análisis EMPA en calcopirita del yacimiento Chuquicamata Subterráneo

Este anexo es equivalente a “Annex IA” indicado en el manuscrito.

Concentraciones se encuentran en porcentaje en peso (wt. %)

b.d.: bajo el límite de detección

Alteration	Sample	Cu	Fe	S	Au	Ag	Bi	Hg	Te	Se	Zn	As	Pb	Sb	Co	Ni	Pd	Pt	Total
Chloritic	8710M1_cpy1_2	33.52	30.31	34.57	b.d	b.d	b.d	b.d	b.d	b.d	b.d	b.d	b.d	b.d	0.03	b.d	b.d	b.d	98.45
Chloritic	8710M1_cpy1_8	34.58	30.56	34.60	b.d	b.d	b.d	b.d	b.d	b.d	b.d	b.d	b.d	b.d	0.03	b.d	b.d	b.d	99.78
Chloritic	8710M1_cpy1_9	35.13	30.77	35.32	b.d	b.d	b.d	b.d	b.d	b.d	b.d	b.d	b.d	b.d	0.03	b.d	b.d	b.d	101.30
Chloritic	8710M1_cpy2_1	34.26	30.44	34.92	b.d	b.d	b.d	b.d	b.d	b.d	b.d	b.d	b.d	b.d	0.02	b.d	b.d	b.d	99.69
Chloritic	8710M1_cpy2_2	34.32	30.53	35.03	b.d	b.d	b.d	b.d	b.d	b.d	b.d	b.d	b.d	b.d	0.03	b.d	b.d	b.d	99.94
Chloritic	8710M1_cpy2_4	34.43	30.25	35.21	b.d	b.d	b.d	b.d	b.d	b.d	b.d	b.d	b.d	b.d	0.02	b.d	b.d	b.d	99.94
Chloritic	8710M1_cpy3_1	34.91	30.76	35.14	b.d	b.d	b.d	b.d	b.d	b.d	b.d	b.d	b.d	b.d	b.d	b.d	b.d	b.d	100.87
Chloritic	8710M1_cpy3_2	34.90	30.98	35.09	b.d	b.d	b.d	b.d	b.d	b.d	b.d	b.d	b.d	b.d	0.03	b.d	b.d	b.d	101.02
Chloritic	8710M1_cpy3_3	34.61	30.52	34.86	b.d	b.d	b.d	b.d	b.d	b.d	b.d	b.d	b.d	b.d	0.03	b.d	b.d	b.d	100.08
Chloritic	8710M1_cpy3_4	34.32	30.43	35.02	b.d	b.d	b.d	b.d	b.d	b.d	b.d	b.d	b.d	b.d	0.03	b.d	b.d	b.d	99.85
Chloritic	8710M1_cpy3_5	34.76	30.81	35.13	b.d	b.d	b.d	b.d	b.d	b.d	b.d	b.d	b.d	b.d	b.d	b.d	b.d	b.d	100.76
Chloritic	8710M1_cpy3_6	34.23	29.95	34.89	b.d	b.d	b.d	b.d	b.d	b.d	0.04	b.d	b.d	b.d	0.03	b.d	b.d	b.d	99.16
Chloritic	8710M1_cpy3_7	34.57	30.48	35.02	b.d	b.d	b.d	b.d	b.d	b.d	b.d	b.d	b.d	b.d	0.04	b.d	b.d	b.d	100.12
Chloritic	8710M1_cpy4_1	34.79	30.72	35.27	b.d	b.d	b.d	b.d	b.d	b.d	b.d	b.d	b.d	b.d	b.d	b.d	b.d	b.d	100.81
Chloritic	8710M1_cpy4_2	34.57	30.52	34.97	b.d	b.d	b.d	b.d	b.d	b.d	b.d	b.d	b.d	b.d	b.d	b.d	b.d	b.d	100.14
Chloritic	8710M1_cpy4_3	34.87	30.75	35.23	b.d	b.d	b.d	b.d	b.d	b.d	b.d	b.d	b.d	b.d	0.03	b.d	b.d	b.d	100.91
Chloritic	8710M1_cpy4_4	34.90	30.66	35.22	b.d	b.d	b.d	b.d	b.d	b.d	b.d	b.d	b.d	b.d	0.03	b.d	b.d	b.d	100.86
Chloritic	8710M1_cpy4_5	34.76	30.92	35.09	b.d	b.d	b.d	b.d	b.d	b.d	b.d	b.d	b.d	b.d	0.03	b.d	b.d	b.d	100.84
Chloritic	8710M1_cpy4_6	34.85	30.62	35.25	b.d	b.d	b.d	b.d	b.d	b.d	b.d	b.d	b.d	b.d	b.d	b.d	b.d	b.d	100.76
Chloritic	8710M1_cpy4_7	34.79	30.70	34.93	b.d	b.d	b.d	b.d	b.d	b.d	b.d	b.d	b.d	b.d	0.03	b.d	b.d	b.d	100.49
Chloritic	8710M1_cpy4_8	34.94	30.57	34.83	b.d	b.d	b.d	b.d	b.d	b.d	b.d	b.d	b.d	b.d	0.04	b.d	b.d	b.d	100.41
Chloritic	8710M1_cpy5_1	34.94	30.86	35.39	b.d	b.d	b.d	b.d	b.d	b.d	b.d	b.d	b.d	b.d	0.03	b.d	b.d	b.d	101.24
Chloritic	8710M1_cpy5_2	34.92	30.77	35.15	b.d	b.d	b.d	b.d	b.d	b.d	b.d	b.d	b.d	b.d	0.03	b.d	b.d	b.d	100.91
Chloritic	8710M1_cpy5_3	34.88	30.89	35.41	b.d	b.d	b.d	b.d	b.d	b.d	b.d	b.d	b.d	b.d	0.02	b.d	b.d	b.d	101.25
Chloritic	8710M1_cpy5_4	34.71	30.81	35.17	b.d	b.d	b.d	b.d	b.d	b.d	b.d	b.d	b.d	b.d	0.02	b.d	b.d	b.d	100.74
Chloritic	8710M1_cpy5_5	34.87	30.77	35.14	b.d	b.d	b.d	b.d	b.d	b.d	b.d	b.d	b.d	b.d	0.03	b.d	b.d	b.d	100.84
Chloritic	7795M3_cpy6_1	34.49	30.32	35.01	b.d	0.02	b.d	b.d	b.d	b.d	b.d	b.d	b.d	b.d	0.03	b.d	b.d	b.d	99.90
Chloritic	7795M3_cpy6_2	34.70	30.22	34.75	b.d	b.d	b.d	b.d	b.d	b.d	b.d	b.d	b.d	b.d	0.03	b.d	b.d	b.d	99.71
Chloritic	7795M3_cpy6_3	34.85	30.25	34.95	b.d	b.d	b.d	b.d	b.d	b.d	b.d	b.d	b.d	b.d	b.d	b.d	b.d	b.d	100.10
Chloritic	7795M3_cpy7_1	35.04	30.73	34.94	b.d	0.02	b.d	b.d	b.d	b.d	b.d	b.d	b.d	b.d	0.02	b.d	b.d	b.d	100.77
Chloritic	7795M3_cpy7_2	34.94	30.64	34.87	b.d	b.d	b.d	b.d	b.d	b.d	0.04	b.d	b.d	b.d	0.02	b.d	b.d	b.d	100.53
Chloritic	7795M3_cpy7_3	34.35	30.18	34.53	b.d	b.d	b.d	b.d	b.d	b.d	b.d	b.d	b.d	b.d	b.d	b.d	b.d	b.d	99.10
Chloritic	7795M3_cpy7_4	34.45	30.09	34.47	b.d	0.02	b.d	b.d	b.d	b.d	b.d	b.d	b.d	b.d	0.03	b.d	b.d	b.d	99.07
Chloritic	7795M3_cpy8_1	34.35	30.24	34.76	b.d	b.d	b.d	b.d	b.d	b.d	b.d	b.d	b.d	b.d	0.04	b.d	b.d	b.d	99.42
Chloritic	7795M3_cpy8_2	34.36	30.35	34.48	b.d	b.d	b.d	b.d	b.d	b.d	b.d	b.d	b.d	b.d	0.03	b.d	b.d	b.d	99.24
Chloritic	7795M3_cpy8_3	34.53	30.04	34.45	b.d	b.d	b.d	b.d	b.d	b.d	b.d	b.d	b.d	b.d	b.d	b.d	b.d	b.d	99.07

Chloritic	7795M3_cpy9_1	34.32	29.70	34.47	b.d	b.d	b.d	b.d	b.d	b.d	b.d	b.d	b.d	b.d	0.03	b.d	b.d	b.d	98.53
Chloritic	7795M3_cpy9_2	34.45	30.22	34.63	b.d	b.d	b.d	b.d	b.d	b.d	b.d	b.d	b.d	b.d	0.03	b.d	b.d	b.d	99.35
Chloritic	7795M3_cpy9_3	34.70	30.33	34.66	b.d	b.d	b.d	b.d	b.d	b.d	b.d	b.d	b.d	b.d	0.03	b.d	b.d	b.d	99.75
Chloritic	7795M3_cpy9_4	34.64	30.07	34.71	b.d	b.d	b.d	b.d	b.d	b.d	b.d	b.d	b.d	b.d	b.d	b.d	b.d	b.d	99.47
Chloritic	7795M3_cpy10_1	34.52	30.32	34.72	b.d	b.d	b.d	b.d	b.d	b.d	b.d	b.d	b.d	b.d	0.03	b.d	b.d	b.d	99.62
Chloritic	7795M3_cpy10_2	34.98	30.45	34.85	b.d	0.02	b.d	0.03	b.d	b.d	b.d	100.34							
Chloritic	7795M3_cpy10_3	34.47	30.23	34.45	b.d	b.d	b.d	b.d	b.d	b.d	b.d	b.d	b.d	b.d	0.04	b.d	b.d	b.d	99.25
Chloritic	7795M3_cpy10_4	34.60	30.17	34.27	b.d	0.04	b.d	0.02	b.d	b.d	b.d	99.11							
Chloritic	7795M3_cpy10_5	34.63	30.32	34.45	b.d	b.d	b.d	b.d	b.d	b.d	b.d	b.d	b.d	b.d	0.03	b.d	b.d	b.d	99.44
Chloritic	7795M3_cpy10_6	34.61	30.24	34.48	b.d	b.d	b.d	b.d	b.d	b.d	b.d	b.d	b.d	b.d	0.03	b.d	b.d	b.d	99.37
Chloritic	7795M3_cpy10_7	35.03	30.45	34.81	b.d	b.d	b.d	b.d	b.d	b.d	b.d	b.d	b.d	b.d	0.03	b.d	b.d	b.d	100.38
Chloritic	7795M3_cpy10_8	35.06	30.36	34.63	b.d	b.d	b.d	b.d	b.d	b.d	b.d	b.d	b.d	b.d	0.03	b.d	b.d	b.d	100.10
Chloritic	7795M3_cpy10_9	34.58	30.03	34.49	b.d	b.d	b.d	b.d	b.d	b.d	b.d	b.d	b.d	b.d	0.02	b.d	b.d	b.d	99.20
Chloritic	7795M3_cpy10_10	34.57	29.97	34.30	b.d	b.d	b.d	b.d	b.d	b.d	b.d	b.d	b.d	b.d	b.d	b.d	b.d	b.d	98.90
Chloritic	7795M3_cpy10_11	34.65	29.93	34.14	b.d	b.d	b.d	b.d	b.d	b.d	b.d	b.d	b.d	b.d	0.04	b.d	b.d	b.d	98.76
Chloritic	7795M3_cpy11_1	34.80	30.02	34.34	b.d	b.d	b.d	b.d	b.d	b.d	b.d	b.d	b.d	b.d	0.04	b.d	b.d	b.d	99.24
Chloritic	7795M3_cpy11_2	34.56	30.13	34.48	b.d	b.d	b.d	b.d	b.d	b.d	b.d	b.d	b.d	b.d	0.04	b.d	b.d	b.d	99.22
Chloritic	7795M3_cpy11_3	34.75	30.19	34.18	b.d	b.d	b.d	b.d	b.d	b.d	b.d	b.d	b.d	b.d	0.03	b.d	b.d	b.d	99.21
Chloritic	7795M3_cpy11_4	34.65	29.96	34.18	b.d	b.d	b.d	b.d	b.d	b.d	b.d	b.d	b.d	b.d	b.d	b.d	b.d	b.d	98.86
Chloritic	7795M3_cpy11_5	34.42	30.03	34.67	b.d	b.d	b.d	b.d	b.d	b.d	b.d	b.d	b.d	b.d	0.02	b.d	b.d	b.d	99.15
Chloritic	7795M3_cpy12_1	34.58	30.00	34.13	b.d	b.d	b.d	b.d	b.d	b.d	b.d	b.d	b.d	b.d	0.03	b.d	b.d	b.d	98.75
Chloritic	7795M3_cpy12_2	34.68	29.88	34.21	b.d	b.d	b.d	b.d	b.d	b.d	b.d	b.d	b.d	b.d	b.d	b.d	b.d	b.d	98.82
Chloritic	7795M3_cpy12_3	34.41	29.76	33.86	b.d	b.d	b.d	b.d	b.d	b.d	b.d	b.d	b.d	b.d	b.d	b.d	b.d	b.d	98.09
Background Potassic	7795M9_cpy29_1	34.50	30.25	34.60	b.d	b.d	b.d	b.d	b.d	b.d	b.d	b.d	b.d	b.d	0.03	b.d	b.d	b.d	99.40
Background Potassic	7795M9_cpy29_1	34.74	30.78	34.80	b.d	0.02	b.d	0.03	b.d	b.d	b.d	100.39							
Background Potassic	7795M9_cpy29_2	34.52	30.72	35.08	b.d	b.d	b.d	b.d	b.d	b.d	b.d	b.d	b.d	b.d	0.04	b.d	b.d	b.d	100.39
Background Potassic	7795M9_cpy29_3	34.14	30.21	34.73	b.d	b.d	b.d	b.d	b.d	b.d	b.d	b.d	b.d	b.d	0.02	b.d	b.d	b.d	99.15
Background Potassic	7795M9_cpy29_5	34.30	30.28	34.76	b.d	b.d	b.d	b.d	b.d	b.d	b.d	b.d	b.d	b.d	0.02	b.d	b.d	b.d	99.38
Background Potassic	7795M9_cpy29_6	33.94	29.90	34.81	b.d	b.d	b.d	b.d	b.d	b.d	b.d	b.d	b.d	b.d	0.03	b.d	b.d	b.d	98.73
Background Potassic	7795M9_cpy29_7	33.93	29.92	34.62	b.d	b.d	b.d	b.d	b.d	b.d	b.d	b.d	b.d	b.d	0.03	b.d	b.d	b.d	98.52
Background Potassic	7795M9_cpy29_8	34.02	30.16	34.86	b.d	b.d	b.d	b.d	b.d	b.d	b.d	b.d	b.d	b.d	b.d	b.d	b.d	b.d	99.09
Background Potassic	7795M9_cpy29_9	33.90	29.89	34.73	b.d	b.d	b.d	b.d	b.d	b.d	b.d	b.d	b.d	b.d	b.d	b.d	b.d	b.d	98.60
Background Potassic	7795M9_cpy29_10	35.09	30.71	34.85	b.d	b.d	b.d	b.d	b.d	b.d	b.d	b.d	b.d	b.d	0.03	b.d	b.d	b.d	100.70
Background Potassic	7795M9_cpy29_11	34.95	30.81	34.79	b.d	b.d	b.d	b.d	b.d	b.d	b.d	b.d	b.d	b.d	0.02	b.d	b.d	b.d	100.60
Background Potassic	7795M9_cpy31_1	34.50	30.33	34.70	b.d	b.d	b.d	b.d	b.d	b.d	b.d	b.d	b.d	b.d	b.d	b.d	b.d	b.d	99.56
Background Potassic	7795M9_cpy31_2	34.59	30.57	34.51	b.d	b.d	b.d	b.d	b.d	b.d	b.d	b.d	b.d	b.d	0.03	b.d	b.d	b.d	99.73
Background Potassic	7795M9_cpy31_3	34.76	30.52	33.69	b.d	b.d	b.d	b.d	b.d	b.d	b.d	b.d	b.d	b.d	0.03	b.d	b.d	b.d	99.06
Background Potassic	7795M9_cpy31_4	34.88	30.89	35.08	b.d	b.d	b.d	b.d	b.d	b.d	b.d	b.d	b.d	b.d	0.03	b.d	b.d	b.d	100.92
Background Potassic	7795M9_cpy31_5	34.55	30.42	35.09	b.d	b.d	b.d	b.d	b.d	b.d	b.d	b.d	b.d	b.d	0.03	b.d	b.d	b.d	100.12
Background Potassic	7795M9_cpy31_6	34.62	30.36	34.84	b.d	b.d	b.d	b.d	b.d	b.d	b.d	b.d	b.d	b.d	b.d	b.d	b.d	b.d	99.87
Background Potassic	7795M9_cpy31_7	34.56	30.44	34.80	b.d	b.d	b.d	b.d	b.d	b.d	b.d	b.d	b.d	b.d	0.04	b.d	b.d	b.d	99.86
Background Potassic	7795M9_cpy31_8	34.68	30.42	35.22	b.d	b.d	b.d	b.d	b.d	b.d	b.d	b.d	b.d	b.d	b.d	b.d	b.d	b.d	100.39
Background Potassic	7795M9_cpy37_2	34.96	30.82	35.17	b.d	b.d	b.d	b.d	b.d	b.d	b.d	b.d	b.d	b.d	0.02	b.d	b.d	b.d	101.01
Background Potassic	7795M9_cpy37_3	34.80	30.65	35.04	b.d	b.d	b.d	b.d	b.d	b.d	b.d	b.d	b.d	b.d	0.02	b.d	b.d	b.d	100.56
Background Potassic	7795M9_cpy37_4	34.66	30.53	34.74	b.d	b.d	b.d	b.d	b.d	b.d	b.d	b.d	b.d	b.d	b.d	b.d	b.d	b.d	99.99

Background Potassic	7795M9_cpy37_5	34.89	30.86	35.05	b.d	b.d	b.d	b.d	b.d	b.d	b.d	b.d	b.d	b.d	0.02	b.d	b.d	b.d	100.84
Background Potassic	7795M9_cpy37_6	34.91	30.75	35.05	b.d	b.d	b.d	b.d	b.d	b.d	b.d	b.d	b.d	b.d	0.04	b.d	b.d	b.d	100.80
Background Potassic	7795M9_cpy37_7	35.04	30.78	35.28	b.d	b.d	b.d	b.d	b.d	b.d	b.d	b.d	b.d	b.d	0.05	b.d	b.d	b.d	101.16
Background Potassic	7795M9_cpy37_8	35.07	30.72	34.95	b.d	b.d	b.d	b.d	b.d	b.d	b.d	b.d	b.d	b.d	0.02	b.d	b.d	b.d	100.80
Background Potassic	7795M9_cpy37_9	34.82	30.66	34.64	b.d	b.d	b.d	b.d	b.d	b.d	b.d	b.d	b.d	b.d	b.d	b.d	b.d	b.d	100.17
Background Potassic	7795M9_cpy37_10	34.94	30.70	35.13	b.d	b.d	b.d	b.d	b.d	b.d	b.d	b.d	b.d	b.d	0.02	b.d	b.d	b.d	100.82
Background Potassic	7795M9_cpy38_1	35.09	30.77	34.92	b.d	b.d	b.d	b.d	b.d	b.d	b.d	b.d	b.d	b.d	b.d	b.d	b.d	b.d	100.82
Background Potassic	7795M9_cpy38_2	34.87	30.48	35.03	b.d	b.d	b.d	b.d	b.d	b.d	b.d	b.d	b.d	b.d	0.03	b.d	b.d	b.d	100.41
Background Potassic	7795M9_cpy38_3	35.00	30.68	35.31	b.d	b.d	b.d	b.d	b.d	b.d	b.d	b.d	b.d	b.d	0.03	b.d	b.d	b.d	101.05
Background Potassic	7795M9_cpy38_4	35.08	30.87	35.02	b.d	b.d	b.d	b.d	b.d	b.d	b.d	b.d	b.d	b.d	b.d	b.d	b.d	b.d	101.02
Background Potassic	7795M9_cpy38_5	34.80	30.62	34.96	b.d	b.d	b.d	b.d	b.d	b.d	b.d	b.d	b.d	b.d	0.02	b.d	b.d	b.d	100.42
Background Potassic	7795M9_cpy38_6	34.96	30.64	35.12	b.d	b.d	b.d	b.d	b.d	b.d	b.d	b.d	b.d	b.d	b.d	b.d	b.d	b.d	100.75
Background Potassic	7795M9_cpy38_7	34.92	30.79	35.20	b.d	b.d	b.d	b.d	b.d	b.d	b.d	b.d	b.d	b.d	0.03	b.d	b.d	b.d	100.97
Background Potassic	7795M9_cpy38_8	34.76	30.57	34.86	b.d	b.d	b.d	b.d	b.d	b.d	b.d	b.d	b.d	b.d	b.d	b.d	b.d	b.d	100.23
Background Potassic	7795M9_cpy38_9	34.84	30.85	35.37	b.d	b.d	b.d	b.d	b.d	b.d	b.d	b.d	b.d	b.d	0.03	b.d	b.d	b.d	101.11
Background Potassic	7795M9_cpy38_10	34.85	30.90	35.07	b.d	b.d	b.d	b.d	b.d	b.d	b.d	b.d	b.d	b.d	b.d	b.d	b.d	b.d	100.87
Background Potassic	7795M9_cpy38_11	34.91	30.97	35.36	b.d	b.d	b.d	b.d	b.d	b.d	b.d	b.d	b.d	b.d	0.03	b.d	b.d	b.d	101.30
Background Potassic	7795M9_cpy38_12	35.00	30.88	35.42	b.d	b.d	b.d	b.d	b.d	b.d	b.d	b.d	b.d	b.d	0.03	b.d	b.d	b.d	101.38
Background Potassic	7795M9_cpy38_13	34.96	30.72	35.14	b.d	b.d	b.d	b.d	b.d	b.d	b.d	b.d	b.d	b.d	b.d	b.d	b.d	b.d	100.88
Background Potassic	7795M9_cpy38_14	34.92	30.93	35.30	b.d	b.d	b.d	b.d	b.d	b.d	b.d	b.d	b.d	b.d	b.d	b.d	b.d	b.d	101.20
Background Potassic	7795M9_cpy38_15	34.95	31.07	35.34	b.d	b.d	b.d	b.d	b.d	b.d	b.d	b.d	b.d	b.d	0.04	b.d	b.d	b.d	101.41
Background Potassic	7795M9_cpy40_1	34.93	30.94	35.10	b.d	b.d	b.d	b.d	b.d	b.d	b.d	b.d	b.d	b.d	0.03	b.d	b.d	b.d	101.01
Background Potassic	7795M9_cpy40_2	34.86	30.77	35.18	b.d	b.d	b.d	b.d	b.d	b.d	b.d	b.d	b.d	b.d	0.03	b.d	b.d	b.d	100.89
Background Potassic	7795M9_cpy40_3	34.63	30.82	35.06	b.d	b.d	b.d	b.d	b.d	b.d	b.d	b.d	b.d	b.d	b.d	b.d	b.d	b.d	100.57
Background Potassic	4587M7_cpy13_2	34.95	30.63	34.91	b.d	b.d	b.d	b.d	b.d	b.d	b.d	b.d	b.d	b.d	0.03	b.d	b.d	b.d	100.55
Background Potassic	4587M7_cpy13_3	34.80	30.81	35.25	b.d	b.d	b.d	b.d	b.d	b.d	b.d	b.d	b.d	b.d	0.04	b.d	b.d	b.d	100.93
Background Potassic	4587M7_cpy13_4	34.50	30.55	34.75	b.d	b.d	b.d	b.d	b.d	b.d	b.d	b.d	b.d	b.d	0.03	b.d	b.d	b.d	99.84
Background Potassic	4587M7_cpy14_1	34.40	29.99	34.61	b.d	0.08	b.d	0.02	b.d	b.d	b.d	99.12							
Background Potassic	4587M7_cpy14_2	34.51	30.20	34.64	b.d	0.06	b.d	0.02	b.d	b.d	b.d	99.45							
Background Potassic	4587M7_cpy15_1	33.69	29.75	34.60	b.d	b.d	b.d	b.d	b.d	b.d	b.d	b.d	b.d	b.d	0.03	b.d	b.d	b.d	98.11
Background Potassic	4587M7_cpy15_2	33.82	29.75	34.55	b.d	0.03	b.d	0.03	b.d	b.d	b.d	98.18							
Background Potassic	4587M7_cpy15_3	34.56	30.36	35.24	b.d	0.02	b.d	0.03	b.d	b.d	b.d	100.23							
Background Potassic	4587M7_cpy15_4	33.70	29.94	34.40	b.d	b.d	b.d	b.d	b.d	b.d	b.d	b.d	b.d	b.d	0.03	b.d	b.d	b.d	98.09
Background Potassic	4587M7_cpy16_2	35.27	30.62	34.82	b.d	0.06	b.d	b.d	b.d	b.d	100.78								
Background Potassic	4587M7_cpy16_3	35.13	30.85	35.30	b.d	0.05	b.d	0.03	b.d	b.d	b.d	101.38							
Background Potassic	4587M7_cpy18_1	34.66	30.47	35.06	b.d	b.d	b.d	b.d	b.d	b.d	b.d	b.d	b.d	b.d	0.03	b.d	b.d	b.d	100.23
Background Potassic	4587M7_cpy18_2	34.89	30.65	35.17	b.d	b.d	b.d	b.d	b.d	b.d	b.d	b.d	b.d	b.d	b.d	b.d	b.d	b.d	100.76
Background Potassic	4587M7_cpy18_3	34.67	30.30	35.01	b.d	b.d	b.d	b.d	b.d	b.d	b.d	b.d	b.d	b.d	0.03	b.d	b.d	b.d	100.04
Background Potassic	3618M22_cpy19_1	34.81	29.71	34.21	b.d	b.d	b.d	b.d	b.d	b.d	b.d	b.d	b.d	b.d	0.03	b.d	b.d	b.d	98.79
Background Potassic	3618M22_cpy19_3	35.16	30.31	34.59	b.d	b.d	b.d	b.d	b.d	b.d	b.d	b.d	b.d	b.d	0.03	b.d	b.d	b.d	100.09
Background Potassic	3618M22_cpy19_4	35.10	30.32	34.42	b.d	b.d	b.d	b.d	b.d	b.d	b.d	b.d	b.d	b.d	0.02	b.d	b.d	b.d	99.92
Background Potassic	3618M22_cpy21_4	34.63	29.65	34.27	b.d	0.05	b.d	0.02	b.d	b.d	b.d	98.65							
Background Potassic	3618M22_cpy21_8	34.72	29.99	34.26	b.d	0.04	b.d	0.03	b.d	b.d	b.d	99.06							
Background Potassic	3618M22_cpy24_2	35.08	30.12	34.40	b.d	0.05	b.d	0.02	b.d	b.d	b.d	99.69							
Background Potassic	3618M22_cpy24_3	34.90	29.94	34.65	b.d	0.02	b.d	b.d	b.d	b.d	99.55								

Background Potassic	3618M22_cpy24_4	35.11	30.34	34.40	b.d	0.03	b.d	0.04	b.d	b.d	b.d	99.93							
Background Potassic	3618M22_cpy25_1	34.96	30.30	34.72	b.d	b.d	b.d	b.d	b.d	b.d	b.d	b.d	b.d	b.d	b.d	b.d	b.d	b.d	100.03
Background Potassic	3618M22_cpy25_2	35.04	30.31	34.43	b.d	b.d	b.d	b.d	b.d	b.d	b.d	b.d	b.d	b.d	0.02	b.d	b.d	b.d	99.86
Background Potassic	3618M22_cpy25_3	34.86	29.96	34.52	b.d	b.d	b.d	b.d	b.d	b.d	b.d	b.d	b.d	b.d	0.03	b.d	b.d	b.d	99.42
Background Potassic	3618M22_cpy26_1	35.05	30.38	34.67	b.d	b.d	b.d	b.d	b.d	b.d	b.d	b.d	b.d	b.d	0.02	b.d	b.d	b.d	100.17
Background Potassic	3618M22_cpy26_2	35.07	30.48	34.43	b.d	b.d	b.d	b.d	b.d	b.d	b.d	b.d	b.d	b.d	0.03	b.d	b.d	b.d	100.05
Background Potassic	3618M22_cpy26_3	35.00	30.09	34.23	b.d	b.d	b.d	b.d	b.d	b.d	b.d	b.d	b.d	b.d	0.03	b.d	b.d	b.d	99.40
Intense Potassic	7808M21_cpy43_1	34.70	29.88	34.54	b.d	b.d	b.d	b.d	b.d	b.d	b.d	b.d	b.d	b.d	0.03	b.d	b.d	b.d	99.17
Intense Potassic	7808M21_cpy43_2	34.82	29.92	34.73	b.d	b.d	b.d	b.d	b.d	b.d	b.d	b.d	b.d	b.d	0.03	b.d	b.d	b.d	99.56
Intense Potassic	7808M21_cpy43_3	35.20	29.80	34.69	b.d	b.d	b.d	b.d	b.d	b.d	b.d	b.d	b.d	b.d	0.02	b.d	b.d	b.d	99.77
Intense Potassic	7808M21_cpy43_4	34.54	29.46	34.61	b.d	b.d	b.d	b.d	b.d	b.d	b.d	b.d	b.d	b.d	0.03	b.d	b.d	b.d	98.69
Intense Potassic	7808M21_cpy43_5	34.79	29.62	34.35	b.d	0.03	b.d	b.d	b.d	b.d	98.88								
Intense Potassic	3618M25_cpy44_1	34.94	30.76	34.44	b.d	b.d	b.d	b.d	b.d	b.d	b.d	b.d	b.d	b.d	0.03	b.d	b.d	b.d	100.23
Intense Potassic	3618M25_cpy44_2	35.07	30.70	34.34	b.d	b.d	b.d	b.d	b.d	b.d	b.d	b.d	b.d	b.d	b.d	b.d	b.d	b.d	100.17
Intense Potassic	3618M25_cpy44_3	35.10	30.75	34.53	b.d	b.d	b.d	b.d	b.d	b.d	b.d	b.d	b.d	b.d	0.03	b.d	b.d	b.d	100.45
Intense Potassic	3618M25_cpy44_4	35.09	30.70	34.61	b.d	b.d	b.d	b.d	b.d	b.d	b.d	b.d	b.d	b.d	b.d	b.d	b.d	b.d	100.42
Intense Potassic	3618M25_cpy44_5	35.02	30.27	34.57	b.d	b.d	b.d	b.d	b.d	b.d	b.d	b.d	b.d	b.d	0.03	b.d	b.d	b.d	99.96
Intense Potassic	3618M25_cpy44_6	35.22	30.23	34.40	b.d	b.d	b.d	b.d	b.d	b.d	b.d	b.d	b.d	b.d	b.d	b.d	b.d	b.d	99.91
Intense Potassic	3618M25_cpy44_7	35.15	30.42	34.43	b.d	b.d	b.d	b.d	b.d	b.d	b.d	b.d	b.d	b.d	0.03	b.d	b.d	b.d	100.08
Intense Potassic	3618M25_cpy44_8	35.12	30.52	34.49	b.d	b.d	b.d	b.d	b.d	b.d	b.d	b.d	b.d	b.d	0.04	b.d	b.d	b.d	100.18
Intense Potassic	3618M25_cpy46_1	35.22	30.44	34.60	b.d	b.d	b.d	b.d	b.d	b.d	b.d	b.d	b.d	b.d	0.03	b.d	b.d	b.d	100.34
Intense Potassic	3618M25_cpy46_2	35.13	30.25	34.15	b.d	b.d	b.d	b.d	b.d	b.d	b.d	b.d	b.d	b.d	b.d	b.d	b.d	b.d	99.59
Intense Potassic	3618M25_cpy46_3	35.00	30.32	34.28	b.d	b.d	b.d	b.d	b.d	b.d	b.d	b.d	b.d	b.d	b.d	b.d	b.d	b.d	99.66
Intense Potassic	3618M25_cpy46_4	34.72	30.09	34.24	b.d	b.d	b.d	b.d	b.d	b.d	b.d	b.d	b.d	b.d	0.03	b.d	b.d	b.d	99.12
Intense Potassic	3618M25_cpy46_5	34.77	30.00	33.92	b.d	b.d	b.d	b.d	b.d	b.d	b.d	b.d	b.d	b.d	0.03	b.d	b.d	b.d	98.74
Intense Potassic	3618M25_cpy46_6	34.74	29.84	34.19	b.d	b.d	b.d	b.d	b.d	b.d	b.d	b.d	b.d	b.d	b.d	b.d	b.d	b.d	98.84
Intense Potassic	3618M25_cpy46_7	34.98	30.20	34.44	b.d	b.d	b.d	b.d	b.d	b.d	b.d	b.d	b.d	b.d	b.d	b.d	b.d	b.d	99.65
Intense Potassic	3618M25_cpy48_4	34.24	29.61	33.97	b.d	b.d	b.d	b.d	b.d	b.d	b.d	b.d	b.d	b.d	0.24	b.d	0.03	b.d	98.13
Intense Potassic	3618M25_cpy48_5	34.97	30.03	34.32	b.d	b.d	b.d	b.d	b.d	b.d	b.d	b.d	b.d	b.d	0.36	b.d	b.d	b.d	99.74
Intense Potassic	3618M25_cpy48_6	35.01	29.93	34.18	b.d	b.d	b.d	b.d	b.d	b.d	b.d	b.d	b.d	b.d	0.16	b.d	b.d	b.d	99.36
Intense Potassic	3618M25_cpy48_7	35.01	30.13	34.16	b.d	b.d	b.d	b.d	b.d	b.d	b.d	b.d	b.d	b.d	0.04	b.d	0.03	b.d	99.43
Intense Potassic	7795M10_cpy68_3	35.19	30.56	35.24	b.d	0.02	b.d	0.02	b.d	b.d	b.d	101.05							
Intense Potassic	7795M10_cpy68_4	34.71	30.23	34.88	b.d	b.d	b.d	b.d	b.d	b.d	b.d	b.d	b.d	b.d	0.02	b.d	b.d	b.d	99.88
Intense Potassic	7795M10_cpy68_5	35.21	30.42	35.04	b.d	b.d	b.d	b.d	b.d	b.d	b.d	b.d	b.d	b.d	b.d	b.d	b.d	b.d	100.72
Intense Potassic	7795M10_cpy68_6	35.21	30.64	34.73	b.d	b.d	b.d	b.d	b.d	b.d	b.d	b.d	b.d	b.d	0.04	b.d	b.d	b.d	100.69
Intense Potassic	7795M10_cpy69_4	34.93	30.44	35.00	b.d	0.05	b.d	0.03	b.d	b.d	b.d	100.46							
Intense Potassic	7795M10_cpy69_5	34.64	30.49	34.70	b.d	0.05	b.d	0.02	b.d	b.d	b.d	99.92							
Intense Potassic	7795M10_cpy70_1	34.73	30.43	35.05	b.d	b.d	b.d	b.d	b.d	b.d	b.d	b.d	b.d	b.d	0.03	b.d	b.d	b.d	100.27
Intense Potassic	7795M10_cpy70_2	35.34	30.61	35.36	b.d	b.d	b.d	b.d	b.d	b.d	b.d	b.d	b.d	b.d	0.03	b.d	b.d	b.d	101.40
Intense Potassic	7795M10_cpy70_3	34.93	30.44	35.13	b.d	b.d	b.d	b.d	b.d	b.d	b.d	b.d	b.d	b.d	b.d	b.d	b.d	b.d	100.54
Intense Potassic	7795M10_cpy70_4	34.71	30.36	35.32	b.d	b.d	b.d	b.d	b.d	b.d	b.d	b.d	b.d	b.d	0.03	b.d	b.d	b.d	100.45
Intense Potassic	7795M10_cpy70_5	34.69	30.19	35.02	b.d	b.d	b.d	b.d	b.d	b.d	b.d	b.d	b.d	b.d	b.d	b.d	b.d	b.d	99.95
Intense Potassic	7795M10_cpy72_5	34.63	30.37	34.91	b.d	0.04	b.d	0.04	b.d	b.d	b.d	100.03							
Intense Potassic	7795M10_cpy73_1	34.84	30.44	34.66	b.d	b.d	b.d	b.d	b.d	b.d	b.d	b.d	b.d	b.d	0.03	b.d	b.d	b.d	100.02
Intense Potassic	7795M10_cpy73_2	35.33	30.84	35.16	b.d	b.d	b.d	b.d	b.d	b.d	b.d	b.d	b.d	b.d	0.03	b.d	b.d	b.d	101.41

Intense Potassic	7795M10_cpy73_3	34.68	30.33	34.90	b.d	b.d	b.d	b.d	b.d	b.d	b.d	b.d	0.03	b.d	0.02	b.d	b.d	b.d	99.97
Intense Potassic	7795M10_cpy73_4	35.09	30.75	35.06	b.d	b.d	b.d	b.d	b.d	b.d	b.d	b.d	0.02	b.d	b.d	b.d	b.d	b.d	100.94
Intense Potassic	7795M10_cpy73_5	34.52	30.29	35.01	b.d	b.d	b.d	b.d	b.d	b.d	b.d	b.d	0.03	b.d	b.d	b.d	b.d	b.d	99.89
Intense Potassic	7795M10_cpy75_1	35.10	30.82	35.18	b.d	b.d	b.d	b.d	b.d	b.d	b.d	b.d	0.03	b.d	b.d	b.d	b.d	b.d	101.14
Intense Potassic	7795M10_cpy75_3	35.28	30.77	35.34	b.d	b.d	b.d	b.d	b.d	b.d	b.d	b.d	0.02	b.d	b.d	b.d	b.d	b.d	101.43
Intense Potassic	7795M10_cpy75_4	35.19	30.76	35.30	b.d	b.d	b.d	b.d	b.d	b.d	b.d	b.d	0.03	b.d	b.d	b.d	b.d	b.d	101.36
Intense Potassic	7795M10_cpy75_5	34.96	30.67	34.99	b.d	0.02	b.d	b.d	b.d	b.d	b.d	b.d	0.03	b.d	b.d	b.d	b.d	b.d	100.68
Quartz - sericite	3618M24_cpy77_1	34.23	29.78	34.66	b.d	b.d	b.d	b.d	b.d	b.d	b.d	b.d	0.03	b.d	b.d	b.d	b.d	b.d	98.77
Quartz - sericite	3618M24_cpy77_2	34.95	30.33	34.53	b.d	b.d	b.d	b.d	b.d	b.d	b.d	b.d	0.03	b.d	b.d	b.d	b.d	b.d	99.89
Quartz - sericite	3618M24_cpy77_3	35.00	30.36	34.57	b.d	b.d	b.d	b.d	b.d	b.d	b.d	b.d	0.03	b.d	b.d	b.d	b.d	b.d	100.00
Quartz - sericite	3618M24_cpy78_1	34.86	30.25	34.61	b.d	b.d	b.d	b.d	b.d	b.d	b.d	b.d	0.03	b.d	b.d	b.d	b.d	b.d	99.80
Quartz - sericite	3618M24_cpy78_2	34.22	29.69	34.12	b.d	b.d	b.d	b.d	b.d	b.d	b.d	b.d	0.03	b.d	b.d	b.d	b.d	b.d	98.10
Quartz - sericite	3618M24_cpy78_3	34.13	29.89	34.05	b.d	b.d	b.d	b.d	b.d	b.d	b.d	b.d	0.02	b.d	b.d	b.d	b.d	b.d	98.15
Quartz - sericite	3618M24_cpy78_4	34.51	29.73	34.46	b.d	b.d	b.d	b.d	b.d	b.d	b.d	b.d	0.03	b.d	b.d	b.d	b.d	b.d	98.74
Quartz - sericite	3618M24_cpy80_7	35.12	30.15	34.47	b.d	b.d	b.d	b.d	b.d	b.d	b.d	b.d	0.03	b.d	b.d	b.d	b.d	b.d	99.80
Quartz - sericite	3618M24_cpy82_1	35.17	30.29	34.89	b.d	b.d	b.d	b.d	b.d	b.d	b.d	b.d	0.05	b.d	b.d	b.d	b.d	b.d	100.43
Quartz - sericite	3618M24_cpy82_2	34.35	29.95	34.32	b.d	b.d	b.d	b.d	b.d	b.d	b.d	b.d	0.03	b.d	b.d	b.d	b.d	b.d	98.68
Quartz - sericite	3618M24_cpy82_3	34.94	30.37	34.65	b.d	b.d	b.d	b.d	b.d	b.d	b.d	b.d	0.03	b.d	b.d	b.d	b.d	b.d	100.01
Quartz - sericite	3618M24_cpy82_5	34.49	29.76	34.45	b.d	0.02	b.d	b.d	b.d	b.d	b.d	b.d	0.03	b.d	b.d	b.d	b.d	b.d	98.80
Quartz - sericite	3618M24_cpy82_6	34.23	29.78	34.32	b.d	b.d	b.d	b.d	b.d	b.d	b.d	b.d	0.02	b.d	b.d	b.d	b.d	b.d	98.40
Quartz - sericite	3618M24_cpy82_7	34.32	29.84	34.44	b.d	b.d	b.d	b.d	b.d	b.d	b.d	b.d	0.03	b.d	b.d	b.d	b.d	b.d	98.67
Quartz - sericite	3618M24_cpy82_8	34.22	29.86	34.30	b.d	b.d	b.d	b.d	b.d	b.d	b.d	b.d	0.03	b.d	b.d	b.d	b.d	b.d	98.46
Quartz - sericite	3618M24_cpy82_9	34.60	29.88	34.50	b.d	b.d	b.d	b.d	b.d	b.d	b.d	b.d	0.03	b.d	b.d	b.d	b.d	b.d	99.04
Quartz - sericite	3618M24_cpy82_10	35.01	30.16	35.05	b.d	b.d	b.d	b.d	b.d	b.d	b.d	b.d	0.02	b.d	b.d	b.d	b.d	b.d	100.28
Quartz - sericite	3618M24_cpy82_11	34.25	29.67	34.19	b.d	b.d	b.d	b.d	b.d	b.d	b.d	b.d	0.02	b.d	b.d	b.d	b.d	b.d	98.19
Quartz - sericite	3618M24_cpy83_1	35.19	30.21	34.90	b.d	b.d	b.d	b.d	b.d	b.d	b.d	b.d	0.03	b.d	0.04	b.d	b.d	b.d	100.41
Quartz - sericite	3618M24_cpy83_2	34.93	30.14	34.42	b.d	b.d	b.d	b.d	b.d	b.d	b.d	b.d	0.02	b.d	b.d	b.d	b.d	b.d	99.54
Quartz - sericite	3618M24_cpy83_3	35.14	30.16	34.78	b.d	b.d	b.d	b.d	b.d	b.d	b.d	b.d	0.03	b.d	0.03	b.d	b.d	b.d	100.19
Quartz - sericite	3618M24_cpy83_4	34.37	29.66	34.24	b.d	b.d	b.d	b.d	b.d	b.d	b.d	b.d	0.04	b.d	b.d	b.d	b.d	b.d	98.33
Quartz - sericite	3618M24_cpy83_5	34.56	29.79	34.51	b.d	b.d	b.d	b.d	b.d	b.d	b.d	b.d	0.02	b.d	b.d	b.d	b.d	b.d	98.90
Quartz - sericite	3618M24_cpy84_6	34.87	30.07	34.62	b.d	b.d	b.d	b.d	b.d	b.d	b.d	b.d	0.04	b.d	b.d	b.d	b.d	b.d	99.63
Quartz - sericite	3618M24_cpy84_7	34.90	30.17	34.61	b.d	0.02	b.d	b.d	b.d	b.d	b.d	b.d	0.04	b.d	b.d	b.d	b.d	b.d	99.78
Quartz - sericite	3618M24_cpy84_9	35.01	30.24	34.71	b.d	b.d	b.d	b.d	b.d	b.d	b.d	b.d	0.03	b.d	b.d	b.d	b.d	b.d	100.05

Statistic	Cu	Fe	S	Au	Ag	Bi	Hg	Te	Se	Zn	As	Pb	Sb	Co	Ni	Pd	Pt
Minimum	33.52	29.46	33.69	-	0.02	-	-	-	-	0.03	-	0.03	0.03	0.02	-	-	-
Maximum	35.34	31.07	35.42	-	0.08	-	-	-	-	0.36	-	0.03	0.03	0.05	-	-	-
Mean	34.75	30.35	34.75	-	0.04	-	-	-	-	0.08	-	0.03	0.03	0.03	-	-	-
Median	34.80	30.36	34.73	-	0.03	-	-	-	-	0.04	-	0.03	0.03	0.03	-	-	-

ANEXO D: Resultados de análisis EMPA en bornita del yacimiento Chuquicamata Subterráneo

Este anexo es equivalente a “Annex 1B” indicado en el manuscrito.

Concentraciones se encuentran en porcentaje en peso (wt. %)

b.d.: bajo el límite de detección

Alteration	Sample	Cu	Fe	S	Au	Ag	Bi	Hg	Te	Se	Zn	As	Pb	Sb	Co	Ni	Pd	Pt	Total
Background Potassic	4587M7_bn3_2	64.70	8.08	25.12	b.d	0.53	0.06	b.d	b.d	b.d	0.04	b.d	b.d	b.d	b.d	b.d	b.d	98.53	
Background Potassic	4587M7_bn3_4	64.06	8.26	25.23	b.d	0.47	0.05	b.d	b.d	b.d	b.d	b.d	b.d	b.d	b.d	b.d	b.d	98.10	
Background Potassic	4587M7_bn3_5	64.36	8.48	25.23	b.d	0.46	0.08	b.d	b.d	b.d	b.d	b.d	b.d	b.d	b.d	b.d	b.d	98.61	
Background Potassic	4587M7_bn3_6	64.65	8.39	24.77	b.d	0.50	0.04	b.d	b.d	b.d	b.d	b.d	b.d	b.d	b.d	b.d	b.d	98.39	
Background Potassic	4587M7_bn4_1	63.80	8.99	25.67	b.d	0.35	0.07	b.d	b.d	b.d	0.04	b.d	b.d	b.d	b.d	b.d	b.d	98.93	
Background Potassic	4587M7_bn4_2	63.82	8.77	25.68	b.d	0.34	0.09	b.d	b.d	b.d	0.04	b.d	b.d	b.d	b.d	b.d	b.d	98.76	
Background Potassic	4587M7_bn6_1	63.53	9.05	25.61	b.d	0.39	0.05	b.d	b.d	b.d	b.d	b.d	b.d	b.d	b.d	b.d	b.d	98.66	
Background Potassic	4587M7_bn6_2	65.14	8.79	25.40	b.d	0.35	0.05	b.d	b.d	b.d	b.d	b.d	b.d	b.d	b.d	b.d	b.d	99.75	
Background Potassic	4587M7_bn6_3	65.76	8.43	25.65	b.d	0.38	0.09	b.d	b.d	b.d	b.d	b.d	b.d	b.d	b.d	b.d	b.d	100.35	
Background Potassic	4587M7_bn7_1	65.38	8.64	25.88	b.d	0.15	b.d	b.d	b.d	b.d	b.d	b.d	b.d	b.d	b.d	b.d	b.d	100.08	
Background Potassic	4587M7_bn7_2	66.00	8.57	25.84	b.d	0.15	b.d	b.d	b.d	b.d	b.d	b.d	b.d	b.d	b.d	b.d	b.d	100.59	
Background Potassic	4587M7_bn7_3	66.09	8.40	25.48	b.d	0.18	b.d	b.d	b.d	b.d	b.d	b.d	b.d	b.d	b.d	b.d	b.d	100.21	
Background Potassic	4587M7_bn9_1	64.78	8.64	25.48	b.d	0.34	0.10	b.d	b.d	b.d	b.d	b.d	b.d	b.d	b.d	b.d	b.d	99.37	
Background Potassic	4587M7_bn9_2	67.22	8.23	25.75	b.d	0.25	0.07	b.d	b.d	b.d	b.d	b.d	b.d	b.d	b.d	b.d	b.d	101.56	
Background Potassic	4587M7_bn9_3	66.72	8.38	25.41	b.d	0.28	0.09	b.d	b.d	b.d	b.d	b.d	b.d	b.d	b.d	b.d	b.d	100.91	
Background Potassic	4587M7_bn9_4	67.27	8.26	25.42	b.d	0.19	0.06	b.d	b.d	b.d	b.d	b.d	b.d	b.d	b.d	b.d	b.d	101.24	
Background Potassic	4587M7_bn9_5	67.19	8.37	25.66	b.d	0.21	0.08	b.d	b.d	b.d	0.05	b.d	b.d	b.d	b.d	b.d	b.d	101.55	
Background Potassic	4587M7_bn9_6	67.06	8.29	25.50	b.d	0.21	0.08	b.d	b.d	b.d	b.d	b.d	b.d	b.d	b.d	b.d	b.d	101.16	
Background Potassic	3618M22_bn10_1	60.20	11.71	25.57	b.d	0.20	0.25	b.d	b.d	b.d	b.d	b.d	b.d	b.d	0.02	b.d	b.d	98.00	
Background Potassic	3618M22_bn10_2	63.16	10.54	26.24	b.d	0.20	0.21	b.d	b.d	b.d	b.d	b.d	b.d	b.d	0.02	b.d	b.d	100.40	
Background Potassic	3618M22_bn10_3	61.28	10.40	25.96	b.d	0.21	0.23	b.d	b.d	b.d	b.d	b.d	b.d	b.d	b.d	b.d	b.d	98.10	
Background Potassic	3618M22_bn10_4	61.86	10.35	25.93	b.d	0.19	0.23	b.d	b.d	b.d	b.d	b.d	b.d	b.d	b.d	b.d	b.d	98.60	
Intense Potassic	7808M21_bn15_1	62.87	10.68	25.30	b.d	0.08	b.d	b.d	b.d	0.02	b.d	b.d	b.d	b.d	b.d	b.d	b.d	99.00	
Intense Potassic	7808M21_bn15_2	66.83	7.94	25.28	b.d	0.08	b.d	b.d	b.d	b.d	b.d	b.d	b.d	b.d	b.d	b.d	b.d	100.18	
Intense Potassic	7808M21_bn15_3	65.81	8.32	25.68	b.d	0.09	b.d	b.d	b.d	b.d	0.05	b.d	b.d	b.d	b.d	b.d	b.d	99.98	
Intense Potassic	7808M21_bn16_1	66.14	8.23	24.74	b.d	0.11	b.d	b.d	b.d	0.03	0.05	b.d	b.d	0.04	b.d	b.d	b.d	99.33	
Intense Potassic	7808M21_bn16_2	66.01	7.93	24.97	b.d	0.12	b.d	b.d	b.d	0.06	b.d	b.d	b.d	b.d	b.d	b.d	b.d	99.12	
Intense Potassic	7808M21_bn16_3	66.50	7.41	24.92	b.d	0.11	b.d	b.d	b.d	b.d	b.d	b.d	b.d	b.d	b.d	b.d	b.d	98.95	
Intense Potassic	7808M21_bn16_4	67.20	7.96	25.27	b.d	0.10	b.d	b.d	b.d	b.d	0.04	b.d	b.d	b.d	b.d	b.d	b.d	100.61	
Intense Potassic	7808M21_bn17_5	66.61	7.67	25.21	b.d	0.07	b.d	b.d	b.d	b.d	b.d	b.d	b.d	b.d	b.d	b.d	b.d	99.62	
Intense Potassic	7808M21_bn17_6	65.65	7.66	25.42	b.d	0.07	b.d	b.d	b.d	0.04	b.d	b.d	b.d	b.d	b.d	b.d	b.d	98.87	
Intense Potassic	7808M21_bn17_7	65.10	7.97	25.03	b.d	0.08	b.d	b.d	b.d	b.d	b.d	b.d	b.d	b.d	b.d	b.d	b.d	98.23	
Intense Potassic	7808M21_bn17_9	64.84	9.71	25.11	b.d	0.07	b.d	b.d	b.d	0.04	0.04	b.d	b.d	b.d	b.d	b.d	b.d	99.80	
Intense Potassic	7808M21_bn17_10	67.12	8.09	25.39	b.d	0.08	b.d	b.d	b.d	b.d	0.04	b.d	b.d	b.d	b.d	b.d	b.d	100.79	
Intense Potassic	4587M13_bn19_1	66.57	8.09	24.68	b.d	0.08	b.d	b.d	b.d	b.d	b.d	b.d	b.d	b.d	b.d	b.d	b.d	99.45	
Intense Potassic	4587M13_bn19_2	67.36	7.66	24.81	b.d	0.10	b.d	b.d	b.d	b.d	b.d	b.d	b.d	b.d	b.d	b.d	b.d	99.97	
Intense Potassic	4587M13_bn19_3	68.29	7.77	24.86	b.d	0.09	b.d	b.d	b.d	b.d	b.d	b.d	b.d	b.d	b.d	b.d	b.d	101.05	

Intense Potassic	4587M13_bn19_4	66.63	7.40	24.65	b.d	0.10	b.d	b.d	b.d	b.d	b.d	b.d	b.d	b.d	b.d	b.d	b.d	98.81
Intense Potassic	4587M13_bn19_5	67.66	7.50	24.76	b.d	0.09	b.d	b.d	b.d	b.d	0.04	b.d	b.d	b.d	b.d	b.d	100.10	
Intense Potassic	4587M13_bn19_6	68.40	7.24	24.83	b.d	0.09	b.d	b.d	b.d	b.d	b.d	b.d	b.d	b.d	b.d	b.d	100.60	
Intense Potassic	4587M13_bn19_7	68.55	7.46	24.82	b.d	0.10	b.d	b.d	b.d	b.d	b.d	b.d	b.d	b.d	b.d	b.d	101.00	
Intense Potassic	4587M13_bn21_1	67.00	8.35	25.31	b.d	0.09	b.d	b.d	b.d	b.d	b.d	b.d	b.d	b.d	b.d	b.d	100.80	
Intense Potassic	4587M13_bn21_2	64.89	8.21	24.85	b.d	0.09	0.04	b.d	b.d	b.d	0.04	b.d	b.d	b.d	b.d	b.d	98.14	
Intense Potassic	4587M13_bn21_3	63.03	9.97	25.31	b.d	0.10	b.d	b.d	b.d	b.d	b.d	b.d	b.d	b.d	b.d	b.d	98.45	
Intense Potassic	4587M13_bn21_4	65.90	7.92	24.68	b.d	0.08	b.d	b.d	b.d	b.d	b.d	b.d	b.d	b.d	b.d	b.d	98.61	
Intense Potassic	4587M13_bn21_5	66.29	7.81	24.91	b.d	0.11	b.d	b.d	b.d	b.d	b.d	b.d	b.d	b.d	b.d	b.d	99.19	
Intense Potassic	4587M13_bn21_6	66.51	8.12	25.35	b.d	0.11	b.d	b.d	b.d	b.d	b.d	b.d	b.d	b.d	b.d	b.d	100.12	
Intense Potassic	7808M9_bn27_1	64.41	9.59	25.13	b.d	0.11	b.d	b.d	b.d	b.d	b.d	b.d	b.d	0.02	b.d	b.d	99.29	
Intense Potassic	7808M9_bn27_2	65.00	9.09	25.34	b.d	0.08	b.d	b.d	b.d	b.d	0.04	b.d	b.d	b.d	b.d	b.d	99.61	
Intense Potassic	7808M9_bn27_3	65.46	8.60	24.97	b.d	0.10	b.d	b.d	b.d	b.d	b.d	b.d	b.d	b.d	b.d	b.d	99.18	
Intense Potassic	7808M9_bn27_4	65.50	8.44	25.14	b.d	0.10	b.d	b.d	b.d	b.d	b.d	b.d	b.d	b.d	b.d	b.d	99.24	
Intense Potassic	7808M9_bn27_5	65.61	8.96	25.11	b.d	0.09	b.d	b.d	b.d	b.d	b.d	b.d	b.d	b.d	b.d	b.d	99.81	
Intense Potassic	7808M9_bn27_6	66.45	8.28	24.67	b.d	0.10	b.d	b.d	b.d	b.d	b.d	b.d	b.d	b.d	b.d	b.d	99.56	
Intense Potassic	7808M9_bn27_7	66.36	8.25	24.98	b.d	0.10	b.d	b.d	b.d	b.d	b.d	b.d	b.d	b.d	b.d	b.d	99.75	
Intense Potassic	7808M9_bn27_8	65.17	8.72	25.15	b.d	0.09	b.d	b.d	b.d	b.d	b.d	b.d	b.d	b.d	b.d	b.d	99.21	
Intense Potassic	7808M9_bn27_9	67.21	7.88	24.90	b.d	0.10	b.d	b.d	b.d	b.d	b.d	b.d	b.d	b.d	b.d	b.d	100.16	
Intense Potassic	7808M9_bn27_10	65.32	8.89	25.01	b.d	0.10	b.d	b.d	b.d	b.d	b.d	b.d	b.d	b.d	b.d	b.d	99.35	
Intense Potassic	7808M9_bn33_1	66.29	8.65	24.99	b.d	0.10	0.04	b.d	b.d	b.d	b.d	b.d	b.d	b.d	b.d	b.d	100.11	
Intense Potassic	7808M9_bn33_2	65.70	8.93	25.48	b.d	0.10	b.d	b.d	b.d	b.d	0.06	b.d	b.d	b.d	b.d	b.d	100.31	
Intense Potassic	7808M9_bn33_3	65.02	9.04	24.81	b.d	0.12	b.d	b.d	b.d	b.d	b.d	b.d	b.d	b.d	b.d	b.d	99.05	
Intense Potassic	7808M9_bn33_4	66.18	8.67	25.02	b.d	0.09	b.d	b.d	b.d	b.d	b.d	b.d	b.d	b.d	b.d	b.d	100.02	
Intense Potassic	7808M9_bn33_5	62.57	10.49	25.69	b.d	0.10	b.d	b.d	b.d	b.d	0.04	b.d	b.d	b.d	b.d	b.d	98.94	
Intense Potassic	7808M9_bn33_6	63.48	9.67	25.19	b.d	0.10	b.d	b.d	b.d	b.d	0.04	b.d	b.d	b.d	b.d	b.d	98.50	
Intense Potassic	7808M9_bn33_7	66.54	8.36	25.27	b.d	0.11	b.d	b.d	b.d	b.d	b.d	b.d	b.d	b.d	b.d	b.d	100.34	
Intense Potassic	7808M9_bn33_8	64.35	9.68	25.50	b.d	0.11	b.d	b.d	b.d	b.d	0.05	b.d	b.d	b.d	b.d	b.d	99.70	
Intense Potassic	7808M9_bn34_1	64.35	9.55	25.43	b.d	0.08	b.d	b.d	b.d	b.d	0.05	b.d	b.d	b.d	b.d	b.d	99.50	
Intense Potassic	7808M9_bn34_2	66.27	8.33	24.88	b.d	0.10	b.d	b.d	b.d	b.d	0.04	b.d	b.d	b.d	b.d	b.d	99.66	
Intense Potassic	7808M9_bn34_3	65.41	8.67	25.24	b.d	0.10	b.d	b.d	b.d	b.d	b.d	b.d	b.d	b.d	b.d	b.d	99.49	
Intense Potassic	7808M9_bn34_4	65.23	8.91	25.28	b.d	0.11	b.d	b.d	b.d	b.d	b.d	b.d	b.d	0.02	b.d	b.d	99.60	
Intense Potassic	7808M9_bn34_5	64.85	9.15	24.99	b.d	0.08	b.d	b.d	b.d	b.d	b.d	b.d	b.d	b.d	b.d	b.d	99.13	
Intense Potassic	7808M9_bn35_1	66.45	8.83	25.14	b.d	0.11	b.d	b.d	b.d	b.d	b.d	b.d	b.d	b.d	b.d	b.d	100.58	
Intense Potassic	7808M9_bn35_2	67.01	8.53	24.95	b.d	0.11	b.d	b.d	b.d	b.d	b.d	b.d	b.d	b.d	b.d	b.d	100.63	
Intense Potassic	7808M9_bn35_3	65.96	9.36	25.11	0.04	0.11	b.d	b.d	b.d	b.d	0.04	b.d	b.d	b.d	b.d	b.d	100.67	
Intense Potassic	7808M9_bn35_4	66.20	8.54	25.14	b.d	0.11	b.d	b.d	b.d	b.d	0.04	b.d	b.d	b.d	b.d	b.d	100.09	
Intense Potassic	7808M9_bn36_1	66.19	8.63	24.92	b.d	0.11	b.d	b.d	b.d	b.d	0.04	b.d	b.d	b.d	b.d	b.d	99.91	
Intense Potassic	7808M9_bn36_2	66.62	8.28	24.88	b.d	0.13	b.d	b.d	b.d	b.d	b.d	b.d	b.d	b.d	b.d	b.d	99.94	
Intense Potassic	7808M9_bn36_3	65.48	8.57	25.18	b.d	0.11	b.d	b.d	b.d	b.d	b.d	b.d	b.d	b.d	b.d	b.d	99.39	
Intense Potassic	7808M9_bn36_4	66.91	8.10	25.10	b.d	0.12	b.d	b.d	b.d	b.d	b.d	b.d	b.d	b.d	b.d	b.d	100.29	
Intense Potassic	7808M9_bn36_5	66.82	8.06	24.97	b.d	0.12	b.d	b.d	b.d	b.d	b.d	b.d	0.03	b.d	b.d	b.d	100.05	
Intense Potassic	7808M9_bn36_6	65.77	8.87	25.20	b.d	0.12	b.d	b.d	b.d	b.d	b.d	b.d	b.d	b.d	b.d	b.d	100.01	
Intense Potassic	7808M9_bn36_7	66.76	8.22	24.90	b.d	0.12	b.d	b.d	b.d	b.d	b.d	b.d	b.d	b.d	b.d	b.d	100.06	
Intense Potassic	7808M9_bn37_1	62.68	10.45	25.72	b.d	0.12	b.d	b.d	b.d	b.d	b.d	b.d	b.d	b.d	b.d	b.d	99.01	

Intense Potassic	7808M9_bn37_2	66.17	8.55	25.08	b.d	0.14	b.d	b.d	b.d	b.d	b.d	b.d	b.d	b.d	b.d	b.d	b.d	100.02
Intense Potassic	7808M9_bn37_3	67.29	8.09	24.63	b.d	0.12	b.d	b.d	b.d	b.d	0.04	b.d	b.d	b.d	b.d	b.d	b.d	100.19
Intense Potassic	7808M9_bn37_4	65.90	8.90	25.36	b.d	0.14	b.d	b.d	b.d	b.d	0.05	b.d	b.d	b.d	b.d	b.d	b.d	100.37
Intense Potassic	7808M9_bn37_5	64.01	9.87	25.33	b.d	0.11	b.d	b.d	b.d	b.d	b.d	b.d	b.d	b.d	b.d	b.d	b.d	99.38
Intense Potassic	7795M10_bn41_1	61.80	10.97	26.75	b.d	0.05	0.22	b.d	b.d	b.d	b.d	b.d	b.d	b.d	b.d	b.d	b.d	99.83
Intense Potassic	7795M10_bn42_1	63.92	9.92	26.00	b.d	0.12	0.19	b.d	b.d	b.d	b.d	b.d	b.d	b.d	b.d	b.d	b.d	100.18
Intense Potassic	7795M10_bn42_2	64.29	9.47	26.12	b.d	0.13	0.16	b.d	b.d	b.d	b.d	b.d	b.d	b.d	b.d	b.d	b.d	100.21
Intense Potassic	7795M10_bn42_3	64.39	9.72	26.07	b.d	0.14	0.16	b.d	b.d	b.d	b.d	b.d	b.d	b.d	b.d	b.d	b.d	100.50
Intense Potassic	7795M10_bn42_6	63.02	10.90	26.65	b.d	0.14	0.19	b.d	b.d	b.d	b.d	b.d	b.d	b.d	b.d	b.d	b.d	100.97
Intense Potassic	7795M10_bn42_7	65.86	8.69	26.36	b.d	0.16	0.15	b.d	b.d	b.d	b.d	b.d	b.d	b.d	b.d	b.d	b.d	101.21
Intense Potassic	7795M10_bn43_1	62.78	9.98	26.42	b.d	0.13	0.50	b.d	b.d	b.d	b.d	b.d	b.d	b.d	b.d	b.d	b.d	99.86
Intense Potassic	7795M10_bn43_2	63.81	9.58	26.21	b.d	0.13	0.42	b.d	b.d	b.d	b.d	b.d	b.d	b.d	b.d	b.d	b.d	100.19
Intense Potassic	7795M10_bn43_3	64.11	9.37	26.17	b.d	0.13	0.41	b.d	b.d	b.d	0.04	b.d	b.d	b.d	b.d	b.d	b.d	100.25
Intense Potassic	7795M10_bn43_4	62.82	10.11	26.38	b.d	0.13	0.45	b.d	b.d	b.d	0.04	b.d	b.d	b.d	b.d	b.d	b.d	99.93
Intense Potassic	7795M10_bn43_5	63.03	10.29	26.29	b.d	0.13	0.25	b.d	b.d	b.d	0.04	b.d	b.d	b.d	b.d	b.d	b.d	100.06
Intense Potassic	7795M10_bn43_6	65.19	8.82	26.04	b.d	0.15	0.19	b.d	b.d	b.d	0.06	b.d	b.d	b.d	b.d	b.d	b.d	100.45
Intense Potassic	7795M10_bn44_1	64.43	9.38	26.18	b.d	0.16	0.42	b.d	b.d	b.d	b.d	b.d	b.d	b.d	b.d	b.d	b.d	100.62
Intense Potassic	7795M10_bn44_2	64.30	9.32	25.88	b.d	0.16	0.45	b.d	b.d	b.d	b.d	b.d	b.d	b.d	b.d	b.d	b.d	100.13
Intense Potassic	7795M10_bn44_3	64.31	9.56	26.05	b.d	0.15	0.40	b.d	b.d	b.d	b.d	b.d	b.d	b.d	b.d	b.d	b.d	100.49
Intense Potassic	7795M10_bn44_4	64.16	9.47	26.23	b.d	0.17	0.49	b.d	b.d	b.d	b.d	b.d	b.d	b.d	b.d	b.d	b.d	100.58
Intense Potassic	7795M10_bn45_1	63.92	9.73	25.98	b.d	0.16	0.34	b.d	b.d	b.d	b.d	b.d	b.d	b.d	b.d	b.d	b.d	100.17
Intense Potassic	7795M10_bn45_2	64.66	9.14	25.73	b.d	0.18	0.36	b.d	b.d	b.d	b.d	b.d	b.d	b.d	b.d	b.d	b.d	100.11
Intense Potassic	7795M10_bn45_3	65.02	8.93	26.04	b.d	0.15	0.36	b.d	b.d	b.d	b.d	b.d	b.d	b.d	b.d	b.d	b.d	100.57
Intense Potassic	7795M10_bn45_4	63.74	9.84	26.30	b.d	0.15	0.41	b.d	b.d	b.d	b.d	b.d	b.d	b.d	b.d	b.d	b.d	100.48
Intense Potassic	7795M10_bn45_5	64.69	9.15	26.08	b.d	0.17	0.43	b.d	b.d	b.d	b.d	b.d	b.d	b.d	b.d	b.d	b.d	100.56

Statistic	Cu	Fe	S	Au	Ag	Bi	Hg	Te	Se	Zn	As	Pb	Sb	Co	Ni	Pd	Pt
Minimum	60.20	7.24	24.63	0.04	0.05	0.04	-	-	0.02	0.04	-	0.03	0.04	0.02	-	-	-
Maximum	68.55	11.71	26.75	0.04	0.53	0.50	-	-	0.06	0.06	-	0.03	0.04	0.02	-	-	-
Mean	65.28	8.84	25.40	0.04	0.15	0.21	-	-	0.04	0.04	-	0.03	0.04	0.02	-	-	-
Median	65.46	8.65	25.3	0.04	0.11	0.19	-	-	0.04	0.04	-	0.03	0.04	0.02	-	-	-

ANEXO E: Resultados de análisis EMPA en pirita del yacimiento Chuquicamata Subterráneo

Este anexo es equivalente a “Annex IC” indicado en el manuscrito.

Concentraciones se encuentran en porcentaje en peso (wt. %)

b.d.: bajo el límite de detección

Alteration	Sample	Cu	Fe	S	Au	Ag	Bi	Hg	Te	Se	Zn	As	Pb	Sb	Co	Ni	Pd	Pt	Total
Chloritic	8710M1_py11_1	b.d	47.33	52.99	b.d	0.07	b.d	b.d	b.d	100.41									
Chloritic	8710M1_py11_2	b.d	47.28	52.86	b.d	0.04	b.d	b.d	b.d	100.20									
Chloritic	8710M1_py11_3	b.d	47.05	52.92	b.d	0.03	b.d	b.d	b.d	100.03									
Chloritic	8710M1_py12_1	b.d	47.42	52.93	b.d	0.05	b.d	b.d	b.d	100.42									
Chloritic	8710M1_py12_2	b.d	47.31	52.80	b.d	0.10	b.d	b.d	b.d	100.24									
Chloritic	8710M1_py12_3	b.d	47.50	53.05	b.d	0.08	b.d	b.d	b.d	100.67									
Chloritic	8710M1_py13_1	b.d	47.10	52.88	b.d	0.21	0.03	b.d	b.d	100.23									
Chloritic	8710M1_py13_2	b.d	47.47	52.95	b.d	0.09	b.d	b.d	b.d	100.56									
Chloritic	8710M1_py13_3	b.d	47.43	52.85	b.d	0.11	b.d	b.d	b.d	100.40									
Chloritic	8710M1_py13_4	b.d	47.32	53.01	b.d	0.10	b.d	b.d	b.d	100.45									
Chloritic	8710M1_py14_1	b.d	47.20	52.84	b.d	0.11	b.d	b.d	b.d	100.20									
Chloritic	8710M1_py14_3	b.d	47.27	52.70	b.d	0.11	b.d	b.d	b.d	100.10									
Chloritic	8710M1_py14_4	b.d	47.27	52.86	b.d	0.20	b.d	b.d	b.d	100.34									
Chloritic	8710M1_py14_5	0.04	47.34	52.78	b.d	0.11	b.d	b.d	b.d	100.29									
Chloritic	8710M1_py14_6	0.06	47.72	52.72	b.d	0.07	b.d	b.d	b.d	100.57									
Chloritic	8710M1_py14_7	0.14	47.56	52.64	b.d	0.10	b.d	b.d	b.d	100.44									
Chloritic	8710M1_py15_1	b.d	47.26	52.46	b.d	0.10	b.d	b.d	b.d	99.83									
Chloritic	8710M1_py15_2	b.d	47.42	52.67	b.d	0.05	b.d	b.d	b.d	100.17									
Chloritic	8710M1_py15_3	b.d	47.13	52.50	b.d	0.10	b.d	b.d	b.d	99.77									
Chloritic	8710M1_py15_4	b.d	47.29	52.54	b.d	0.11	b.d	b.d	b.d	99.95									
Chloritic	8710M1_py15_5	b.d	47.07	52.61	b.d	0.11	b.d	b.d	b.d	99.82									
Chloritic	8710M1_py15_6	b.d	47.32	52.62	b.d	0.06	b.d	b.d	b.d	100.02									
Chloritic	8710M1_py15_7	b.d	47.36	52.46	b.d	0.06	b.d	b.d	b.d	99.89									
Chloritic	8710M1_py16_3	b.d	46.84	52.13	b.d	0.08	b.d	b.d	b.d	99.06									
Chloritic	8710M1_py17_4	b.d	47.34	52.70	b.d	0.07	b.d	b.d	b.d	100.14									
Chloritic	8710M1_py17_5	b.d	47.45	52.60	b.d	0.09	b.d	b.d	b.d	100.16									
Chloritic	8710M1_py17_6	b.d	47.16	52.33	b.d	0.11	b.d	b.d	b.d	99.61									
Chloritic	8710M1_py19_1	b.d	47.30	52.92	b.d	0.06	b.d	b.d	b.d	100.31									
Chloritic	8710M1_py19_2	b.d	47.06	52.82	b.d	0.09	b.d	b.d	b.d	100.02									
Chloritic	8710M1_py19_3	b.d	46.96	52.84	b.d	0.05	b.d	b.d	b.d	99.87									
Chloritic	8710M1_py19_5	b.d	46.92	52.97	b.d	0.28	b.d	b.d	b.d	100.19									
Chloritic	8710M1_py19_6	b.d	47.15	53.09	b.d	0.17	0.04	b.d	b.d	100.45									
Chloritic	8710M1_py2_1	b.d	46.38	52.43	b.d	0.32	0.03	b.d	b.d	99.17									
Chloritic	8710M1_py2_2	b.d	46.08	52.48	b.d	0.70	b.d	b.d	b.d	99.30									
Chloritic	8710M1_py2_3	b.d	46.41	52.48	b.d	0.15	b.d	b.d	b.d	99.07									
Chloritic	8710M1_py2_4	b.d	46.47	52.40	b.d	0.04	b.d	b.d	b.d	98.91									
Chloritic	8710M1_py2_5	b.d	46.51	52.52	b.d	0.04	b.d	b.d	b.d	99.09									

Chloritic	8710M1_py3_1	b.d	46.30	52.66	b.d	b.d	b.d	b.d	b.d	b.d	b.d	b.d	b.d	0.08	b.d	b.d	99.04	
Chloritic	8710M1_py3_2	b.d	46.11	52.55	b.d	b.d	b.d	b.d	b.d	b.d	b.d	b.d	b.d	0.18	b.d	b.d	98.87	
Chloritic	8710M1_py3_3	0.03	45.97	52.56	b.d	b.d	b.d	b.d	b.d	b.d	b.d	b.d	b.d	0.15	b.d	b.d	98.70	
Chloritic	8710M1_py4_1	b.d	45.70	52.32	b.d	b.d	b.d	b.d	b.d	b.d	b.d	b.d	b.d	0.04	b.d	b.d	98.08	
Chloritic	8710M1_py4_2	b.d	45.92	52.56	b.d	b.d	b.d	b.d	b.d	b.d	b.d	b.d	b.d	0.04	b.d	b.d	98.55	
Chloritic	8710M1_py4_3	b.d	45.98	52.46	b.d	b.d	b.d	b.d	b.d	b.d	b.d	b.d	b.d	0.04	b.d	b.d	98.49	
Chloritic	8710M1_py6_1	b.d	47.12	52.97	b.d	b.d	b.d	b.d	b.d	b.d	b.d	b.d	b.d	0.15	b.d	b.d	100.26	
Chloritic	8710M1_py6_2	b.d	47.04	52.91	b.d	b.d	b.d	b.d	b.d	b.d	b.d	b.d	b.d	0.05	b.d	b.d	100.01	
Chloritic	8710M1_py6_3	b.d	47.05	52.89	b.d	b.d	b.d	b.d	b.d	b.d	b.d	b.d	b.d	0.04	b.d	b.d	100.00	
Chloritic	8710M1_py6_4	b.d	47.25	52.98	b.d	b.d	b.d	b.d	b.d	b.d	b.d	b.d	b.d	0.07	b.d	b.d	100.32	
Chloritic	8710M1_py8_1	b.d	47.12	52.96	b.d	b.d	b.d	b.d	b.d	b.d	b.d	b.d	b.d	0.06	b.d	b.d	100.15	
Chloritic	8710M1_py8_2	b.d	46.83	53.15	b.d	b.d	b.d	b.d	b.d	b.d	b.d	b.d	b.d	0.04	b.d	b.d	100.04	
Chloritic	8710M1_py8_3	b.d	47.20	53.02	b.d	b.d	b.d	b.d	b.d	b.d	b.d	b.d	b.d	0.05	b.d	b.d	100.30	
Chloritic	8710M1_py8_4	b.d	47.14	53.38	b.d	b.d	b.d	b.d	b.d	b.d	b.d	b.d	b.d	0.05	b.d	b.d	100.60	
Chloritic	8710M1_py9_1	b.d	47.17	53.03	b.d	b.d	b.d	b.d	b.d	b.d	b.d	b.d	b.d	0.15	b.d	b.d	100.37	
Chloritic	8710M1_py9_2	b.d	47.30	53.14	b.d	b.d	b.d	b.d	b.d	b.d	b.d	b.d	b.d	0.05	b.d	b.d	100.51	
Chloritic	8710M1_py9_3	b.d	47.35	53.06	b.d	b.d	b.d	b.d	b.d	b.d	b.d	b.d	b.d	0.05	b.d	b.d	100.48	
Chloritic	8710M1_py9_4	b.d	47.33	53.30	b.d	b.d	b.d	b.d	b.d	b.d	b.d	b.d	b.d	0.09	b.d	b.d	100.73	
Chloritic	8710M1_py9_5	b.d	47.19	53.10	b.d	b.d	b.d	b.d	b.d	b.d	b.d	b.d	b.d	0.04	b.d	b.d	100.34	
Chloritic	8710M1_py10_2	b.d	47.03	53.21	b.d	b.d	b.d	b.d	b.d	b.d	b.d	b.d	b.d	0.07	b.d	b.d	100.34	
Chloritic	8710M1_py10_3	b.d	47.22	53.31	b.d	b.d	b.d	b.d	b.d	b.d	b.d	b.d	b.d	0.03	b.d	b.d	100.59	
Chloritic	8710M1_py10_4	b.d	47.01	53.38	b.d	b.d	b.d	b.d	b.d	b.d	b.d	b.d	b.d	0.03	b.d	b.d	100.46	
Chloritic	8710M1_py10_5	b.d	47.19	53.16	b.d	b.d	b.d	b.d	b.d	b.d	b.d	b.d	b.d	0.04	b.d	b.d	100.39	
Chloritic	8710M1_py10_6	b.d	47.21	53.30	b.d	b.d	b.d	b.d	b.d	b.d	b.d	b.d	b.d	0.04	b.d	b.d	100.57	
Background Potassic	7795M9_py20_1	0.68	46.68	53.80	b.d	b.d	b.d	b.d	b.d	b.d	b.d	b.d	b.d	0.04	b.d	b.d	101.23	
Background Potassic	7795M9_py20_2	2.35	45.88	52.08	b.d	b.d	b.d	b.d	b.d	b.d	b.d	b.d	b.d	0.06	b.d	b.d	100.44	
Background Potassic	7795M9_py21_1	0.52	47.13	53.37	b.d	b.d	b.d	b.d	b.d	b.d	b.d	b.d	b.d	0.03	b.d	b.d	101.05	
Background Potassic	7795M9_py21_2	0.47	47.03	53.19	b.d	b.d	b.d	b.d	b.d	b.d	b.d	b.d	b.d	0.03	b.d	b.d	100.72	
Background Potassic	7795M9_py21_4	0.78	47.15	53.91	b.d	b.d	b.d	b.d	b.d	b.d	b.d	b.d	b.d	0.04	b.d	b.d	101.91	
Background Potassic	7795M9_py22_1	0.23	47.12	53.50	b.d	b.d	b.d	b.d	b.d	b.d	b.d	b.d	b.d	0.05	b.d	b.d	100.91	
Background Potassic	7795M9_py22_2	0.53	46.73	53.38	b.d	b.d	b.d	b.d	b.d	b.d	b.d	b.d	b.d	0.03	b.d	b.d	100.69	
Background Potassic	7795M9_py22_3	1.71	46.84	52.77	b.d	b.d	b.d	b.d	b.d	b.d	b.d	b.d	b.d	0.04	0.029	b.d	b.d	101.43
Background Potassic	7795M9_py24_1	0.63	46.08	52.63	b.d	b.d	b.d	b.d	b.d	b.d	b.d	b.d	b.d	0.05	b.d	b.d	99.41	
Background Potassic	7795M9_py24_2	1.33	46.57	52.65	b.d	0.03	b.d	0.04	b.d	b.d	100.68							
Background Potassic	7795M9_py24_3	0.32	47.06	53.22	b.d	b.d	b.d	b.d	b.d	b.d	b.d	b.d	b.d	0.06	b.d	b.d	100.66	
Background Potassic	7795M9_py24_4	0.08	47.44	53.42	b.d	b.d	b.d	b.d	b.d	b.d	b.d	b.d	b.d	0.03	b.d	b.d	100.98	
Background Potassic	7795M9_py24_6	0.24	47.23	53.25	b.d	b.d	b.d	b.d	b.d	b.d	b.d	b.d	b.d	0.03	b.d	b.d	100.76	
Background Potassic	7795M9_py24_7	0.36	47.24	53.26	b.d	b.d	b.d	b.d	b.d	b.d	b.d	b.d	b.d	0.05	b.d	b.d	100.94	
Background Potassic	7795M9_py24_8	0.21	47.16	52.87	b.d	b.d	b.d	b.d	b.d	b.d	b.d	b.d	b.d	0.05	b.d	b.d	100.30	
Background Potassic	7795M9_py24_9	0.87	46.59	52.79	b.d	b.d	b.d	b.d	b.d	b.d	b.d	b.d	b.d	0.04	b.d	b.d	100.29	
Background Potassic	7795M9_py24_10	0.21	47.37	53.08	b.d	b.d	b.d	b.d	b.d	b.d	b.d	b.d	b.d	0.04	b.d	b.d	100.72	
Background Potassic	3618M19_py25_1	0.09	47.13	53.57	b.d	b.d	b.d	b.d	b.d	b.d	b.d	b.d	b.d	0.05	0.028	b.d	b.d	100.89
Background Potassic	3618M19_py25_2	0.04	47.24	53.50	b.d	b.d	b.d	b.d	b.d	b.d	b.d	b.d	b.d	0.05	b.d	b.d	100.83	
Background Potassic	3618M19_py25_3	b.d	47.29	53.87	b.d	b.d	b.d	b.d	b.d	b.d	b.d	b.d	b.d	0.05	b.d	b.d	101.26	
Background Potassic	3618M19_py25_4	b.d	47.37	53.57	b.d	b.d	b.d	b.d	b.d	b.d	b.d	b.d	b.d	0.03	b.d	b.d	101.00	

Background Potassic	3618M19_py26_1	b.d	47.09	53.61	b.d	b.d	b.d	0.06	0.025	b.d	b.d	100.80							
Background Potassic	3618M19_py26_2	0.05	47.15	53.42	b.d	b.d	b.d	0.05	b.d	b.d	b.d	100.69							
Background Potassic	3618M19_py26_3	b.d	47.12	53.57	b.d	b.d	b.d	b.d	b.d	b.d	0.06	b.d	b.d	b.d	0.03	0.026	b.d	b.d	100.83
Background Potassic	3618M19_py28_1	0.10	47.08	53.54	b.d	b.d	b.d	0.05	b.d	b.d	b.d	100.79							
Background Potassic	3618M19_py28_2	b.d	47.02	53.56	b.d	b.d	b.d	0.04	b.d	b.d	b.d	100.65							
Background Potassic	3618M19_py28_3	0.03	47.02	53.65	b.d	b.d	b.d	0.06	b.d	b.d	b.d	100.76							
Background Potassic	3618M19_py28_4	b.d	46.53	53.19	b.d	b.d	b.d	0.03	b.d	b.d	b.d	99.79							
Background Potassic	3618M19_py28_5	b.d	47.17	53.52	b.d	b.d	b.d	0.07	b.d	b.d	b.d	100.80							
Background Potassic	3618M19_py28_6	b.d	47.24	53.60	b.d	b.d	b.d	0.04	b.d	b.d	b.d	100.88							
Background Potassic	3618M19_py28_7	b.d	47.16	53.48	b.d	b.d	b.d	0.03	b.d	b.d	b.d	100.69							
Background Potassic	3618M19_py28_8	b.d	47.12	53.46	b.d	b.d	b.d	0.03	b.d	b.d	b.d	100.62							
Background Potassic	3618M19_py29_1	0.03	47.18	53.79	b.d	b.d	b.d	0.05	b.d	b.d	b.d	101.05							
Background Potassic	3618M19_py29_2	0.03	47.16	53.39	b.d	b.d	b.d	0.05	b.d	b.d	b.d	100.65							
Background Potassic	3618M19_py29_3	b.d	47.40	53.69	b.d	b.d	b.d	0.04	b.d	b.d	b.d	101.16							
Background Potassic	3618M19_py29_4	b.d	47.19	53.63	b.d	b.d	b.d	b.d	b.d	b.d	0.02	b.d	b.d	0.05	b.d	b.d	b.d	100.95	
Background Potassic	3618M19_py29_8	b.d	47.02	53.49	b.d	b.d	b.d	0.04	b.d	b.d	b.d	100.58							
Background Potassic	3618M19_py29_9	b.d	47.02	53.78	b.d	b.d	b.d	0.04	b.d	b.d	b.d	100.86							
Background Potassic	3618M19_py29_10	b.d	46.94	52.99	b.d	b.d	b.d	b.d	b.d	b.d	0.206	b.d	0.03	0.12	b.d	b.d	b.d	100.33	
Quartz - sericite	7808M15_py78_1	0.07	47.13	50.86	b.d	b.d	b.d	0.05	b.d	b.d	b.d	98.13							
Quartz - sericite	7808M15_py78_3	b.d	47.21	50.90	b.d	b.d	b.d	0.04	b.d	b.d	b.d	98.19							
Quartz - sericite	7808M15_py78_4	0.06	47.10	50.92	b.d	b.d	b.d	0.04	b.d	b.d	b.d	98.15							
Quartz - sericite	7808M15_py78_5	b.d	47.35	51.13	b.d	b.d	b.d	0.04	b.d	b.d	b.d	98.56							
Quartz - sericite	7808M15_py81_1	0.05	47.28	51.07	b.d	b.d	b.d	0.04	0.02	b.d	b.d	98.49							
Quartz - sericite	7808M15_py81_2	0.08	47.44	51.25	b.d	b.d	b.d	0.04	b.d	b.d	b.d	98.82							
Quartz - sericite	7808M15_py84_2	0.04	47.20	51.29	b.d	b.d	b.d	0.05	b.d	b.d	b.d	98.59							
Quartz - sericite	7808M15_py84_3	2.11	45.74	50.21	b.d	b.d	b.d	0.03	b.d	b.d	b.d	98.10							
Quartz - sericite	7808M15_py84_4	0.27	47.13	50.99	b.d	b.d	b.d	0.04	b.d	b.d	b.d	98.43							
Quartz - sericite	7808M15_py88_2	0.04	46.94	51.09	b.d	b.d	b.d	0.04	b.d	b.d	b.d	98.13							
Quartz - sericite	7808M15_py90_1	0.05	47.36	51.36	b.d	b.d	b.d	0.05	b.d	b.d	b.d	98.84							
Quartz - sericite	7808M15_py90_3	0.05	47.34	51.50	b.d	b.d	b.d	0.04	b.d	b.d	b.d	98.94							
Quartz - sericite	3618M9_py42_1	b.d	47.28	51.42	b.d	b.d	b.d	0.06	b.d	b.d	b.d	98.78							
Quartz - sericite	3618M9_py42_2	b.d	47.27	51.44	b.d	b.d	b.d	0.03	b.d	b.d	b.d	98.79							
Quartz - sericite	3618M9_py42_3	b.d	47.10	51.57	b.d	b.d	b.d	0.04	b.d	b.d	b.d	98.73							
Quartz - sericite	3618M9_py42_4	b.d	46.94	51.12	b.d	b.d	b.d	0.05	b.d	b.d	b.d	98.14							
Quartz - sericite	3618M9_py43_1	b.d	47.07	51.47	b.d	b.d	b.d	0.06	b.d	b.d	b.d	98.65							
Quartz - sericite	3618M9_py43_2	0.07	47.31	51.40	b.d	b.d	b.d	0.04	b.d	b.d	b.d	98.83							
Quartz - sericite	3618M9_py43_3	b.d	47.39	51.33	b.d	b.d	b.d	0.04	b.d	b.d	b.d	98.79							
Quartz - sericite	3618M9_py43_4	0.03	47.30	51.46	b.d	b.d	b.d	0.04	b.d	b.d	b.d	98.84							
Quartz - sericite	3618M9_py44_1	b.d	47.27	51.42	b.d	b.d	b.d	0.04	b.d	b.d	b.d	98.77							
Quartz - sericite	3618M9_py44_2	0.05	47.04	50.87	b.d	b.d	b.d	0.04	b.d	b.d	b.d	98.01							
Quartz - sericite	3618M9_py44_3	0.04	47.34	51.63	b.d	b.d	b.d	0.03	b.d	b.d	b.d	99.04							
Quartz - sericite	3618M9_py44_4	b.d	47.14	51.61	b.d	b.d	b.d	0.05	b.d	b.d	b.d	98.85							
Quartz - sericite	3618M9_py44_5	b.d	47.31	51.52	b.d	b.d	b.d	0.04	b.d	b.d	b.d	98.89							
Quartz - sericite	3618M9_py44_6	b.d	47.28	51.53	b.d	b.d	b.d	0.06	b.d	b.d	b.d	98.91							
Quartz - sericite	3618M9_py45_1	b.d	47.28	51.50	b.d	b.d	b.d	0.04	b.d	b.d	b.d	98.84							

Quartz - sericite	3618M9_py45_2	b.d	47.52	51.30	b.d	b.d	b.d	b.d	b.d	b.d	b.d	b.d	b.d	0.03	b.d	b.d	98.85
Quartz - sericite	3618M9_py45_3	b.d	45.96	51.20	b.d	b.d	b.d	b.d	b.d	b.d	b.d	b.d	b.d	1.43	b.d	b.d	98.60
Quartz - sericite	3618M9_py45_4	b.d	47.28	51.34	b.d	b.d	b.d	b.d	b.d	b.d	b.d	b.d	b.d	0.05	b.d	b.d	98.69
Quartz - sericite	3618M9_py45_5	b.d	47.17	51.43	b.d	b.d	b.d	b.d	b.d	b.d	b.d	b.d	b.d	0.04	b.d	b.d	98.66
Quartz - sericite	3618M9_py45_6	b.d	47.47	51.43	b.d	b.d	b.d	b.d	b.d	b.d	b.d	b.d	b.d	0.12	b.d	b.d	99.04
Quartz - sericite	3618M9_py45_7	b.d	47.45	51.54	b.d	b.d	b.d	b.d	b.d	b.d	b.d	b.d	b.d	0.04	b.d	b.d	99.04
Quartz - sericite	3618M9_py45_8	b.d	47.45	51.50	b.d	b.d	b.d	b.d	b.d	b.d	b.d	b.d	b.d	0.04	b.d	b.d	99.00
Quartz - sericite	3618M9_py45_9	b.d	47.19	51.47	b.d	b.d	b.d	b.d	b.d	0.04	b.d	b.d	b.d	0.03	b.d	b.d	98.76
Quartz - sericite	3618M9_py45_10	b.d	47.15	51.46	b.d	b.d	b.d	b.d	b.d	b.d	b.d	b.d	b.d	0.05	b.d	b.d	98.67
Quartz - sericite	3618M9_py45_11	b.d	47.04	51.34	b.d	b.d	b.d	b.d	b.d	b.d	b.d	b.d	b.d	0.04	b.d	b.d	98.44
Quartz - sericite	3618M9_py45_12	b.d	47.31	51.21	b.d	b.d	b.d	b.d	b.d	b.d	b.d	b.d	b.d	0.04	b.d	b.d	98.61
Quartz - sericite	3618M9_py47_1	0.10	47.27	51.20	b.d	b.d	b.d	b.d	b.d	b.d	b.d	b.d	b.d	0.04	b.d	b.d	98.63
Quartz - sericite	3618M9_py47_2	0.04	47.11	51.16	b.d	b.d	b.d	b.d	b.d	b.d	b.d	b.d	b.d	0.04	b.d	b.d	98.37
Quartz - sericite	3618M9_py47_3	b.d	47.40	51.37	b.d	b.d	b.d	b.d	b.d	b.d	b.d	b.d	b.d	0.06	b.d	b.d	98.87
Quartz - sericite	3618M9_py47_4	0.04	47.13	51.39	b.d	b.d	b.d	b.d	b.d	b.d	b.d	b.d	b.d	0.03	b.d	b.d	98.64
Quartz - sericite	3618M9_py47_5	b.d	47.08	51.45	b.d	b.d	b.d	b.d	b.d	b.d	b.d	b.d	b.d	0.05	b.d	b.d	98.62
Quartz - sericite	3618M9_py47_6	b.d	47.08	51.48	b.d	b.d	b.d	b.d	b.d	b.d	b.d	b.d	b.d	0.05	b.d	b.d	98.67
Quartz - sericite	3618M9_py47_7	b.d	46.99	51.22	b.d	b.d	b.d	b.d	b.d	b.d	b.d	b.d	b.d	0.04	b.d	b.d	98.28
Quartz - sericite	3618M9_py47_8	b.d	47.08	51.32	b.d	b.d	b.d	b.d	b.d	b.d	b.d	b.d	b.d	0.11	b.d	b.d	98.55
Quartz - sericite	3618M9_py47_10	b.d	46.82	51.41	b.d	b.d	b.d	b.d	b.d	b.d	b.d	b.d	b.d	0.05	b.d	b.d	98.30
Quartz - sericite	3618M1_py93_1	0.17	47.32	51.41	b.d	b.d	b.d	b.d	b.d	b.d	b.d	b.d	b.d	0.03	b.d	b.d	98.98
Quartz - sericite	3618M1_py93_2	0.11	47.43	51.04	b.d	b.d	b.d	b.d	b.d	b.d	b.d	b.d	b.d	0.05	b.d	b.d	98.64
Quartz - sericite	3618M1_py93_3	0.12	47.38	51.21	b.d	b.d	b.d	b.d	b.d	b.d	b.d	b.d	b.d	0.04	b.d	b.d	98.76
Quartz - sericite	3618M1_py93_5	0.06	47.29	51.47	b.d	b.d	b.d	b.d	b.d	b.d	b.d	b.d	b.d	0.05	b.d	b.d	98.87
Quartz - sericite	3618M1_py93_6	0.19	47.37	51.17	b.d	b.d	b.d	b.d	b.d	b.d	b.d	b.d	b.d	0.04	b.d	b.d	98.83
Quartz - sericite	3618M1_py93_7	0.06	47.55	50.92	b.d	b.d	b.d	b.d	b.d	b.d	b.d	b.d	b.d	0.05	b.d	b.d	98.61
Quartz - sericite	3618M1_py94_1	0.07	46.82	51.37	b.d	b.d	b.d	b.d	b.d	b.d	b.d	b.d	b.d	0.05	b.d	b.d	98.35
Quartz - sericite	3618M1_py94_2	0.06	47.18	51.22	b.d	b.d	b.d	b.d	b.d	b.d	b.d	b.d	b.d	0.05	b.d	b.d	98.53
Quartz - sericite	3618M1_py94_3	0.06	47.23	50.96	b.d	b.d	b.d	b.d	b.d	b.d	b.d	b.d	b.d	0.06	b.d	b.d	98.34
Quartz - sericite	3618M1_py94_4	0.25	47.60	50.93	b.d	b.d	b.d	b.d	b.d	b.d	b.d	b.d	b.d	0.04	b.d	b.d	98.86
Quartz - sericite	3618M1_py94_5	0.39	47.33	50.87	b.d	b.d	b.d	b.d	b.d	b.d	b.d	b.d	b.d	0.04	b.d	b.d	98.66
Quartz - sericite	3618M1_py94_8	0.04	47.47	50.79	b.d	b.d	b.d	b.d	b.d	b.d	b.d	b.d	b.d	0.05	b.d	b.d	98.38
Quartz - sericite	3618M1_py95_4	0.03	47.22	50.61	b.d	b.d	0.07	b.d	b.d	b.d	b.d	b.d	b.d	0.05	b.d	b.d	98.00
Quartz - sericite	3618M1_py95_5	0.04	47.39	50.70	b.d	b.d	b.d	b.d	b.d	b.d	b.d	b.d	b.d	0.04	b.d	b.d	98.18
Quartz - sericite	3618M24_py58_2	b.d	47.15	51.46	b.d	b.d	b.d	b.d	b.d	b.d	b.d	b.d	b.d	0.06	b.d	b.d	98.72
Quartz - sericite	3618M24_py58_3	b.d	47.14	51.48	b.d	b.d	b.d	b.d	b.d	b.d	b.d	b.d	b.d	0.05	b.d	b.d	98.71
Quartz - sericite	3618M24_py58_4	b.d	47.14	51.53	b.d	b.d	b.d	b.d	b.d	b.d	b.d	b.d	b.d	0.08	0.02	b.d	98.78
Quartz - sericite	3618M24_py58_5	b.d	47.11	51.36	b.d	b.d	b.d	b.d	b.d	b.d	b.d	b.d	b.d	0.07	b.d	b.d	98.58
Quartz - sericite	3618M24_py61_10	b.d	47.34	51.07	b.d	b.d	b.d	b.d	b.d	b.d	b.d	b.d	b.d	0.05	b.d	b.d	98.48
Quartz - sericite	3618M24_py61_11	b.d	47.30	51.36	b.d	b.d	b.d	b.d	b.d	b.d	b.d	b.d	b.d	0.03	b.d	b.d	98.71
Quartz - sericite	3618M24_py61_12	b.d	47.12	51.35	b.d	b.d	b.d	b.d	b.d	b.d	b.d	b.d	b.d	0.05	b.d	b.d	98.56
Quartz - sericite	3618M24_py62_1	b.d	47.32	51.35	b.d	b.d	b.d	b.d	b.d	b.d	b.d	b.d	b.d	0.06	b.d	b.d	98.74
Quartz - sericite	3618M24_py62_2	b.d	47.21	51.57	b.d	b.d	b.d	b.d	b.d	b.d	b.d	b.d	b.d	0.03	b.d	b.d	98.85
Quartz - sericite	3618M24_py62_3	b.d	47.03	51.45	b.d	b.d	b.d	b.d	b.d	b.d	b.d	b.d	b.d	0.05	b.d	b.d	98.56
Quartz - sericite	3618M24_py62_4	b.d	47.20	51.37	b.d	b.d	b.d	b.d	b.d	b.d	b.d	b.d	b.d	0.03	b.d	b.d	98.67

Quartz - sericite	3618M24_py62_5	b.d	46.81	51.34	b.d	b.d	b.d	0.06	b.d	b.d	98.24							
Quartz - sericite	3618M24_py62_6	b.d	47.14	51.41	b.d	b.d	b.d	0.04	b.d	b.d	98.61							
Quartz - sericite	3618M24_py62_7	b.d	47.12	51.26	b.d	b.d	b.d	0.06	b.d	b.d	98.47							
Quartz - sericite	3618M24_py62_8	b.d	47.11	51.54	b.d	b.d	b.d	0.05	b.d	b.d	98.73							
Quartz - sericite	3618M24_py62_9	b.d	47.19	51.60	b.d	b.d	b.d	0.04	b.d	b.d	98.85							
Quartz - sericite	3618M24_py62_10	b.d	47.20	51.53	b.d	b.d	b.d	0.04	b.d	b.d	98.79							
Quartz - sericite	3618M24_py64_1	b.d	47.34	51.62	b.d	b.d	b.d	0.04	b.d	b.d	99.02							
Quartz - sericite	3618M24_py64_2	b.d	47.39	51.93	b.d	b.d	b.d	0.04	b.d	b.d	99.38							
Quartz - sericite	3618M24_py64_3	b.d	47.44	51.75	b.d	b.d	b.d	0.04	b.d	b.d	99.28							
Quartz - sericite	3618M24_py64_4	b.d	47.25	51.73	b.d	b.d	b.d	0.09	b.d	b.d	99.11							
Quartz - sericite	3618M24_py64_5	b.d	47.28	51.60	b.d	b.d	b.d	0.09	b.d	b.d	98.97							
Quartz - sericite	3618M24_py64_8	0.03	46.96	51.57	b.d	b.d	b.d	0.10	0.05	b.d	b.d	98.74						
Quartz - sericite	3618M24_py65_1	b.d	47.37	51.45	b.d	b.d	b.d	0.04	b.d	b.d	98.87							
Quartz - sericite	3618M24_py65_2	b.d	47.27	51.68	b.d	b.d	b.d	0.04	0.02	b.d	b.d	99.06						
Quartz - sericite	3618M24_py65_3	b.d	47.37	51.63	b.d	b.d	b.d	0.05	0.02	b.d	b.d	99.07						
Quartz - sericite	7815M2_py31_1	0.04	47.07	51.75	b.d	b.d	b.d	0.03	b.d	b.d	98.93							
Quartz - sericite	7815M2_py31_2	b.d	47.47	51.72	b.d	b.d	b.d	0.04	b.d	b.d	99.26							
Quartz - sericite	7815M2_py31_3	b.d	47.06	51.61	b.d	b.d	b.d	0.04	b.d	b.d	98.76							
Quartz - sericite	7815M2_py31_4	0.05	47.27	51.75	b.d	b.d	b.d	b.d	b.d	b.d	0.04	b.d	b.d	0.04	b.d	b.d	99.19	
Quartz - sericite	7815M2_py34_1	0.12	47.13	51.80	b.d	b.d	b.d	0.03	b.d	b.d	99.12							
Quartz - sericite	7815M2_py34_2	b.d	47.57	51.72	b.d	b.d	b.d	0.04	b.d	b.d	99.38							
Quartz - sericite	7815M2_py34_3	0.10	47.50	51.45	b.d	b.d	b.d	0.05	b.d	b.d	99.13							
Quartz - sericite	7815M2_py36_1	b.d	47.07	51.63	b.d	b.d	b.d	0.04	b.d	b.d	98.76							
Quartz - sericite	7815M2_py36_2	b.d	47.15	51.75	b.d	b.d	b.d	0.03	b.d	b.d	98.95							
Quartz - sericite	7815M2_py36_3	b.d	47.10	52.04	b.d	b.d	b.d	0.04	b.d	b.d	99.20							
Quartz - sericite	7815M2_py38_1	0.10	47.23	52.16	b.d	b.d	b.d	0.04	b.d	b.d	99.56							
Quartz - sericite	7815M2_py38_2	0.10	47.15	51.91	b.d	b.d	b.d	0.04	b.d	b.d	99.22							
Quartz - sericite	7815M2_py38_3	0.15	47.07	52.40	b.d	b.d	b.d	b.d	b.d	b.d	0.04	b.d	b.d	0.04	b.d	b.d	99.71	
Quartz - sericite	7815M2_py38_4	0.23	47.01	52.33	b.d	b.d	b.d	b.d	b.d	b.d	0.03	b.d	b.d	0.05	b.d	b.d	99.68	
Quartz - sericite	7815M2_py38_5	0.27	46.98	52.31	b.d	b.d	b.d	0.05	b.d	b.d	99.65							
Quartz - sericite	7795M8_py99_1	b.d	47.39	52.54	b.d	b.d	b.d	0.04	b.d	b.d	100.01							
Quartz - sericite	7795M8_py99_2	b.d	47.50	52.53	b.d	b.d	b.d	0.04	b.d	b.d	100.11							
Quartz - sericite	7795M8_py99_3	0.03	47.58	52.19	b.d	b.d	b.d	0.05	b.d	b.d	99.87							
Quartz - sericite	7795M8_py99_4	b.d	47.55	52.20	b.d	b.d	b.d	0.04	b.d	b.d	99.84							
Quartz - sericite	7795M8_py99_5	b.d	47.54	52.20	b.d	b.d	b.d	0.04	b.d	b.d	99.80							
Quartz - sericite	7795M8_py100_1	b.d	47.62	52.17	b.d	b.d	b.d	0.03	b.d	b.d	99.85							
Quartz - sericite	7795M8_py100_2	b.d	47.44	52.27	b.d	b.d	b.d	0.05	b.d	b.d	99.80							
Quartz - sericite	7795M8_py100_3	0.04	47.61	52.45	b.d	b.d	b.d	0.04	b.d	b.d	100.19							
Quartz - sericite	7795M8_py100_4	b.d	47.78	52.31	b.d	b.d	b.d	0.04	b.d	b.d	100.13							
Quartz - sericite	7795M8_py100_5	b.d	47.57	52.02	b.d	b.d	b.d	0.05	b.d	b.d	99.65							
Quartz - sericite	7795M8_py100_6	b.d	47.70	52.04	b.d	b.d	b.d	0.04	b.d	b.d	99.81							
Quartz - sericite	7795M8_py106_1	b.d	47.62	52.01	b.d	b.d	b.d	0.06	b.d	b.d	99.77							
Quartz - sericite	7795M8_py106_2	b.d	47.59	51.85	b.d	b.d	b.d	0.04	b.d	b.d	99.52							
Quartz - sericite	7795M8_py106_3	b.d	47.30	52.03	b.d	b.d	b.d	0.05	b.d	b.d	99.40							
Quartz - sericite	7795M8_py106_4	b.d	47.20	52.14	b.d	b.d	b.d	0.05	b.d	b.d	99.42							

Quartz - sericite	7795M8_py106_5	b.d	47.38	51.93	b.d	0.02	b.d	b.d	99.35								
Quartz - sericite	7795M8_py109_1	b.d	47.39	52.26	b.d	b.d	b.d	99.69									
Quartz - sericite	7795M8_py109_2	b.d	47.17	52.06	b.d	0.06	b.d	b.d	99.31								
Quartz - sericite	7795M8_py109_3	b.d	47.15	52.03	b.d	0.05	b.d	b.d	99.26								
Quartz - sericite	7795M8_py109_4	b.d	47.25	52.45	b.d	0.03	b.d	b.d	99.76								
Quartz - sericite	7795M8_py109_5	b.d	47.39	52.26	b.d	0.04	b.d	b.d	99.75								
Quartz - sericite	7795M8_py110_1	b.d	47.44	52.24	b.d	0.03	b.d	b.d	99.74								
Quartz - sericite	7795M8_py110_2	b.d	47.51	52.33	b.d	0.04	b.d	b.d	99.93								
Quartz - sericite	7795M8_py110_3	b.d	47.25	51.90	b.d	0.04	b.d	b.d	99.20								
Quartz - sericite	7795M8_py110_4	0.05	47.47	52.01	b.d	0.05	b.d	b.d	99.62								
Quartz - sericite	7795M8_py110_5	0.04	47.43	52.21	b.d	0.03	b.d	b.d	99.74								
Quartz - sericite	7795M8_py112_1	0.04	47.46	52.22	b.d	0.05	b.d	b.d	99.80								
Quartz - sericite	7795M8_py112_2	b.d	47.56	52.14	b.d	0.03	b.d	b.d	99.78								
Quartz - sericite	7795M8_py112_3	b.d	47.57	51.88	b.d	0.04	b.d	b.d	99.51								
Quartz - sericite	7795M8_py112_4	b.d	47.56	52.39	b.d	0.04	b.d	b.d	100.01								
Quartz - sericite	7795M8_py112_5	b.d	47.29	52.36	b.d	0.07	b.d	b.d	99.73								
Quartz - sericite	7795M8_py112_6	b.d	47.49	52.68	b.d	0.05	b.d	b.d	100.22								
Quartz - sericite	7795M11_py50_1	b.d	47.27	52.72	b.d	0.04	b.d	b.d	100.03								
Quartz - sericite	7795M11_py50_2	b.d	47.56	52.20	b.d	0.05	b.d	b.d	99.84								
Quartz - sericite	7795M11_py50_3	0.07	47.33	52.59	b.d	0.04	b.d	b.d	100.04								
Quartz - sericite	7795M11_py50_4	0.04	47.22	52.63	b.d	0.04	b.d	b.d	99.93								
Quartz - sericite	7795M11_py50_5	0.14	47.43	52.55	b.d	0.03	b.d	b.d	100.16								
Quartz - sericite	7795M11_py50_6	b.d	47.49	52.44	b.d	0.04	b.d	b.d	100.00								
Quartz - sericite	7795M11_py50_7	0.06	47.36	52.46	b.d	0.04	b.d	b.d	99.92								
Quartz - sericite	7795M11_py50_8	b.d	47.31	52.57	b.d	0.04	b.d	b.d	99.94								
Quartz - sericite	7795M11_py50_9	0.09	47.22	52.66	b.d	0.04	b.d	b.d	100.03								
Quartz - sericite	7795M11_py52_2	0.11	47.45	52.44	b.d	0.03	b.d	b.d	100.03								
Quartz - sericite	7795M11_py52_3	b.d	46.74	52.01	b.d	0.04	b.d	b.d	98.84								
Quartz - sericite	7795M11_py52_4	0.04	47.45	52.79	b.d	0.03	b.d	b.d	100.31								
Quartz - sericite	7795M11_py52_5	b.d	47.59	52.57	b.d	0.04	b.d	b.d	100.22								
Quartz - sericite	7795M11_py52_6	b.d	47.49	52.40	b.d	0.03	b.d	b.d	99.94								
Quartz - sericite	7795M11_py54_1	0.13	47.50	52.73	b.d	0.05	b.d	b.d	100.41								
Quartz - sericite	7795M11_py54_2	0.06	47.50	52.69	b.d	0.02	b.d	b.d	100.30								
Quartz - sericite	7795M11_py54_3	0.03	47.31	52.54	b.d	0.09	b.d	b.d	99.98								
Quartz - sericite	7795M11_py54_4	0.03	47.52	52.79	b.d	0.05	b.d	b.d	100.41								
Quartz - sericite	7795M11_py54_5	b.d	47.31	52.80	b.d	0.05	b.d	b.d	100.22								
Quartz - sericite	7795M11_py54_6	0.04	47.40	52.81	b.d	0.05	b.d	b.d	100.31								
Quartz - sericite	7795M11_py54_7	0.03	47.54	52.87	b.d	0.03	b.d	b.d	100.48								
Quartz - sericite	7795M11_py54_8	0.06	47.29	52.69	b.d	0.03	b.d	b.d	100.08								
Quartz - sericite	7795M11_py54_9	b.d	47.40	52.72	b.d	0.03	b.d	b.d	100.19								
Quartz - sericite	7795M11_py54_10	b.d	47.48	52.77	b.d	0.03	b.d	b.d	100.30								
Quartz - sericite	7795M11_py54_11	b.d	47.52	52.93	b.d	0.04	b.d	b.d	100.50								
Quartz - sericite	7795M11_py54_12	b.d	47.55	52.87	b.d	0.05	b.d	b.d	100.51								
Quartz - sericite	7795M11_py55_1	b.d	47.27	52.80	b.d	0.04	b.d	b.d	100.12								
Quartz - sericite	7795M11_py55_2	b.d	47.40	52.93	b.d	0.03	b.d	b.d	100.39								

Quartz - sericite	7795M11_py55_3	b.d	47.42	52.77	b.d	100.26												
Quartz - sericite	7795M11_py55_4	b.d	47.45	53.20	b.d	100.73												
Quartz - sericite	7795M11_py57_1	0.18	47.33	53.18	b.d	100.76												
Quartz - sericite	7795M11_py57_2	b.d	47.08	53.08	b.d	100.23												
Quartz - sericite	7795M11_py57_3	0.38	47.33	53.48	b.d	101.26												
Quartz - sericite	7795M11_py57_4	0.03	47.55	52.92	b.d	100.56												
Quartz - sericite	7795M11_py57_5	b.d	47.32	53.17	b.d	100.54												

Statistic	Cu	Fe	S	Au	Ag	Bi	Hg	Te	Se	Zn	As	Pb	Sb	Co	Ni	Pd	Pt
Minimum	0.03	45.7	50.21	-	0.03	0.07	-	-	0.04	0.03	0.02	0.03	-	0.02	0.02	0.02	-
Maximum	2.35	47.78	53.91	-	0.03	0.07	-	-	0.04	0.06	0.02	0.206	-	1.43	0.12	0.02	-
Mean	0.22	47.19	52.27	-	0.03	0.07	-	-	0.04	0.04	0.02	0.07	-	0.06	0.03	0.02	-
Median	0.07	47.25	52.4	-	0.03	0.07	-	-	0.04	0.04	0.02	0.03	-	0.04	0.0285	0.02	-

ANEXO F: Resultados de análisis LA-ICP-MS en calcopirita del yacimiento Chuquicamata Subterráneo

Este anexo es equivalente a “Annex 2A” indicado en el manuscrito.

Concentraciones se encuentran en partes por millón (ppm)

b.d.: bajo el límite de detección

Alteration	Sample	V	Cr	Mn	Co	Ni	Zn	Ga	Ge	As	Se	Mo	Ag	Cd	In	Sn	Sb	Te	W	Au	Hg	Tl	Pb	Bi	
Chloritic	8710M1_cpy1_8	b.d	b.d	b.d	b.d	b.d	b.d	b.d	b.d	b.d	b.d	3,9	b.d	9,49	b.d	b.d	b.d	b.d	b.d	b.d	b.d	b.d	4,49		
Chloritic	8710M1_cpy1_9	b.d	b.d	b.d	b.d	b.d	b.d	b.d	b.d	b.d	b.d	3,6	b.d	11,95	5,2	b.d	b.d	b.d	b.d	b.d	b.d	b.d	b.d		
Chloritic	8710M1_cpy3_4	b.d	b.d	b.d	b.d	b.d	b.d	b.d	b.d	b.d	b.d	7,86	b.d	7,23	1,79	b.d	b.d	b.d	b.d	b.d	b.d	b.d	11	6,99	
Chloritic	8710M1_cpy3_5	b.d	b.d	b.d	b.d	b.d	b.d	b.d	b.d	b.d	b.d	8,34	b.d	7,67	2,34	b.d	b.d	b.d	b.d	b.d	b.d	0,02	1,6	3,73	
Chloritic	8710M1_cpy3_6	b.d	b.d	b.d	b.d	b.d	b.d	b.d	b.d	b.d	b.d	1,84	b.d	7,9	b.d	b.d	b.d	b.d	b.d	b.d	b.d	b.d	2,86		
Chloritic	8710M1_cpy4_1	b.d	b.d	b.d	b.d	b.d	b.d	b.d	b.d	b.d	b.d	3,02	b.d	7,45	2,8	b.d	b.d	b.d	b.d	b.d	b.d	b.d	1	2,25	
Chloritic	8710M1_cpy4_2	b.d	b.d	b.d	b.d	b.d	b.d	b.d	b.d	b.d	b.d	3,1	b.d	7,05	3,07	b.d	b.d	b.d	b.d	b.d	b.d	b.d	1,61	2,45	
Chloritic	8710M1_cpy4_3	b.d	b.d	b.d	b.d	b.d	b.d	b.d	b.d	b.d	b.d	5,45	b.d	6,12	2,68	b.d	b.d	b.d	b.d	b.d	b.d	b.d	b.d		
Chloritic	8710M1_cpy4_4	b.d	b.d	34,9	b.d	b.d	17	b.d	b.d	b.d	b.d	3,41	b.d	7,97	2,35	b.d	b.d	b.d	b.d	b.d	b.d	b.d	4,09	5,98	
Chloritic	8710M1_cpy4_6	b.d	b.d	b.d	b.d	b.d	b.d	b.d	b.d	b.d	700	b.d	2,25	b.d	7,05	3,18	b.d	b.d	b.d	b.d	b.d	b.d	3,63	2,52	
Chloritic	8710M1_cpy5_1	b.d	b.d	b.d	b.d	b.d	b.d	b.d	b.d	b.d	b.d	2,24	b.d	6,61	2,93	b.d	b.d	b.d	b.d	b.d	b.d	b.d	b.d		
Chloritic	8710M1_cpy5_2	b.d	b.d	b.d	b.d	b.d	b.d	b.d	b.d	b.d	1,00E+03	b.d	5,18	b.d	7,3	3,3	b.d	b.d	b.d	b.d	b.d	b.d	2,35	1,82	
Chloritic	8710M1_cpy5_3	b.d	b.d	b.d	b.d	b.d	b.d	b.d	b.d	b.d	200	b.d	2,83	b.d	5,9	1,71	b.d	b.d	b.d	b.d	b.d	b.d	1,38	1,78	
Chloritic	8710M1_cpy5_4	b.d	b.d	b.d	b.d	b.d	b.d	b.d	b.d	b.d	b.d	2,95	b.d	6,59	b.d	b.d	b.d	b.d	b.d	b.d	b.d	b.d	0,75	1,37	
Chloritic	8710M1_cpy5_5	b.d	b.d	b.d	b.d	b.d	b.d	b.d	b.d	b.d	b.d	60	b.d	3,31	b.d	6,58	2,66	b.d	b.d	b.d	b.d	b.d	b.d	0,8	1,05
Background Potassic	3618M22_cpy19_1	b.d	b.d	b.d	b.d	b.d	b.d	b.d	b.d	b.d	b.d	1,77	b.d	1,72	b.d	b.d	b.d	0,06	b.d	b.d	2,66	0,95			
Background Potassic	3618M22_cpy19_2	b.d	b.d	b.d	b.d	b.d	b.d	b.d	b.d	b.d	b.d	6,2	44	b.d	2,3	b.d	b.d	b.d	b.d	b.d	b.d	b.d	b.d		
Background Potassic	3618M22_cpy19_3	b.d	b.d	b.d	b.d	b.d	b.d	b.d	b.d	b.d	b.d	0,94	b.d	1,82	b.d	b.d	b.d	0,039	b.d	b.d	1,35	0,41			
Background Potassic	3618M22_cpy19_4	b.d	b.d	b.d	b.d	b.d	b.d	b.d	b.d	b.d	b.d	0,85	b.d	1,74	b.d	b.d	b.d	b.d	b.d	b.d	b.d	b.d	1,16	0,37	
Background Potassic	3618M22_cpy19_5	b.d	b.d	b.d	b.d	b.d	b.d	b.d	b.d	b.d	b.d	14,6	b.d	6,5	39,8	b.d	b.d	b.d	b.d	b.d	b.d	b.d	b.d		
Background Potassic	3618M22_cpy21_1	b.d	b.d	b.d	b.d	b.d	b.d	b.d	b.d	b.d	b.d	b.d	b.d	7,9	65	b.d	b.d	b.d	b.d	b.d	b.d	b.d	b.d		
Background Potassic	3618M22_cpy21_2	b.d	b.d	b.d	b.d	b.d	b.d	b.d	b.d	b.d	b.d	b.d	b.d	8,2	38	b.d	b.d	1	b.d	b.d	b.d	b.d	b.d		
Background Potassic	3618M22_cpy21_3	b.d	b.d	b.d	b.d	b.d	b.d	b.d	b.d	b.d	b.d	b.d	b.d	6,1	40	b.d	b.d	b.d	b.d	b.d	b.d	b.d	11,2		

Background Potassic	3618M22_cpy21_4	b.d	b.d	b.d	b.d	b.d	1,37	b.d	2,78	b.d	b.d	b.d	b.d	b.d	b.d	b.d	b.d	b.d	b.d						
Background Potassic	3618M22_cpy21_5	b.d	b.d	b.d	b.d	b.d	24,7	1,2	8,67	36,9	b.d	b.d	b.d	b.d	b.d	b.d	b.d	41,1	3,46						
Background Potassic	3618M22_cpy21_8	b.d	b.d	b.d	b.d	b.d	11,6	46	b.d	b.d	b.d	b.d	b.d	b.d	b.d	b.d	b.d	b.d	b.d						
Background Potassic	3618M22_cpy21_9	b.d	b.d	b.d	b.d	b.d	236	b.d	b.d	b.d	b.d	b.d	8,5	14,5	b.d	2,58	b.d	b.d	b.d	b.d	b.d	b.d	b.d	4,7	5,7
Background Potassic	3618M22_cpy24_2	b.d	b.d	b.d	b.d	b.d	1,39	b.d	2,92	1,79	b.d	b.d	b.d	b.d	b.d	b.d	b.d	0,79	b.d						
Background Potassic	3618M22_cpy24_3	b.d	b.d	b.d	b.d	b.d	1,42	b.d	2,78	b.d	b.d	b.d	b.d	b.d	b.d	b.d	b.d	10,9	0,87						
Background Potassic	3618M22_cpy24_4	b.d	b.d	b.d	b.d	b.d	3,02	b.d	2,63	2,42	b.d	b.d	b.d	b.d	b.d	b.d	b.d	1,1	b.d						
Background Potassic	3618M22_cpy25_1	b.d	b.d	b.d	b.d	b.d	1,62	b.d	2,43	b.d	b.d	b.d	b.d	b.d	b.d	b.d	b.d	b.d	0,68						
Background Potassic	3618M22_cpy25_2	b.d	b.d	b.d	b.d	b.d	1,58	b.d	2,38	b.d	b.d	b.d	0,08	b.d	b.d	b.d	b.d	b.d	0,48						
Background Potassic	3618M22_cpy25_3	b.d	b.d	b.d	b.d	b.d	1,23	b.d	2,49	b.d	b.d	b.d	b.d	b.d	b.d	b.d	b.d	b.d	0,61						
Background Potassic	3618M22_cpy25_4	b.d	b.d	b.d	b.d	b.d	12,7	b.d	6,54	35,6	b.d	b.d	b.d	b.d	b.d	b.d	b.d	24,4	2,23						
Background Potassic	3618M22_cpy25_5	b.d	b.d	b.d	b.d	b.d	7,6	53,3	b.d	b.d	b.d	b.d	b.d	b.d	b.d	b.d	b.d	b.d	b.d						
Background Potassic	3618M22_cpy25_6	b.d	b.d	54	b.d	b.d	b.d	19	b.d	b.d	b.d	b.d	7,5	b.d	6,7	42,7	b.d	b.d	b.d	b.d	b.d	b.d	b.d	b.d	b.d
Background Potassic	3618M22_cpy26_1	b.d	b.d	b.d	b.d	b.d	1,36	b.d	2,38	b.d	b.d	b.d	b.d	b.d	b.d	b.d	b.d	b.d	b.d						
Background Potassic	3618M22_cpy26_2	b.d	b.d	b.d	b.d	b.d	2,52	b.d	2,53	1,2	b.d	b.d	b.d	b.d	b.d	b.d	b.d	1,06	2,12						
Background Potassic	3618M22_cpy26_3	b.d	b.d	b.d	b.d	b.d	0,82	b.d	2,54	1,74	b.d	b.d	b.d	b.d	b.d	b.d	b.d	b.d	0,24						
Background Potassic	4587M7_cpy13_2	b.d	b.d	b.d	b.d	b.d	b.d	22	60	b.d	1,10E+04	b.d	b.d	18,8	12,7	b.d	b.d	b.d	b.d	b.d	b.d	b.d	b.d	b.d	b.d
Background Potassic	4587M7_cpy13_3	b.d	b.d	b.d	b.d	b.d	22,8	b.d	b.d	b.d	b.d	b.d	b.d	b.d	b.d	b.d	b.d	b.d	b.d						
Background Potassic	4587M7_cpy13_4	b.d	b.d	b.d	b.d	b.d	18,1	b.d	b.d	b.d	0,8	b.d	b.d	b.d	b.d	b.d	b.d	b.d	b.d						
Background Potassic	4587M7_cpy14_1	b.d	b.d	b.d	b.d	b.d	7,8	b.d	b.d	3,8	b.d	b.d	b.d	b.d	b.d	b.d	b.d	b.d	b.d						
Background Potassic	4587M7_cpy15_1	b.d	b.d	b.d	b.d	b.d	13,8	b.d	20,1	22,4	b.d	b.d	b.d	b.d	b.d	b.d	b.d	b.d	b.d						
Background Potassic	4587M7_cpy15_2	b.d	b.d	b.d	b.d	b.d	b.d	15	b.d	b.d	b.d	b.d	b.d	21,9	22,8	b.d	b.d	b.d	b.d	b.d	b.d	b.d	b.d	b.d	b.d
Background Potassic	4587M7_cpy15_3	b.d	b.d	b.d	b.d	b.d	1,50E+04	b.d	4,9	b.d	19,7	21,1	b.d	b.d	b.d	b.d	b.d	b.d	b.d						
Background Potassic	4587M7_cpy15_4	b.d	b.d	b.d	b.d	b.d	2,20E+04	b.d	7,2	b.d	18,5	17,9	b.d	b.d	b.d	b.d	b.d	b.d	b.d						
Background Potassic	4587M7_cpy16_2	b.d	b.d	b.d	b.d	b.d	b.d	18,6	b.d	b.d	b.d	b.d	1,6	b.d	18,7	5,4	7	b.d	0,22	b.d	b.d	b.d	2,2	b.d	
Background Potassic	4587M7_cpy16_3	b.d	b.d	b.d	b.d	b.d	b.d	17,4	b.d	b.d	b.d	b.d	3,4	b.d	18,4	4,5	b.d	0,2	0,46	b.d	b.d	b.d	4,4	b.d	
Background Potassic	4587M7_cpy18_1	b.d	b.d	b.d	b.d	b.d	b.d	13,3	b.d	b.d	b.d	b.d	1,18	b.d	13,1	4,21	b.d	b.d	b.d	b.d	b.d	b.d	b.d	1,55	b.d
Background Potassic	4587M7_cpy18_2	b.d	b.d	b.d	b.d	b.d	b.d	17	b.d	b.d	b.d	b.d	b.d	12,1	4,95	b.d	b.d	b.d	b.d	b.d	b.d	b.d	b.d	1,38	b.d
Background Potassic	4587M7_cpy18_3	b.d	b.d	b.d	b.d	b.d	b.d	14,9	b.d	b.d	b.d	b.d	0,88	13,6	5,6	b.d	b.d	b.d	0,009	b.d	b.d	b.d	b.d	b.d	
Background Potassic	4587M7_cpy19_1	b.d	b.d	b.d	b.d	b.d	b.d	22,7	b.d	b.d	b.d	b.d	6,5	b.d	16,4	7,7	b.d	b.d	0,32	b.d	b.d	b.d	3,9	b.d	
Background Potassic	4587M7_cpy19_3	b.d	b.d	b.d	b.d	b.d	b.d	43	b.d	b.d	b.d	b.d	8,9	b.d	15,6	b.d	b.d	b.d	b.d	b.d	b.d	b.d	b.d	b.d	

Background Potassic	4587M7_cpy19_4	b.d	b.d	b.d	b.d	b.d	b.d	25,1	b.d	b.d	b.d	b.d	15,4	b.d	14,5	5,2	b.d	3,2	b.d	b.d	b.d	b.d	7,3	5,5	
Background Potassic	7795M9_cpy29_1	b.d	b.d	b.d	b.d	b.d	8,8	b.d	7,5	42,9	b.d	1,3	b.d	0,21	b.d	b.d	6,1	1,63							
Background Potassic	7795M9_cpy29_10	b.d	b.d	b.d	b.d	b.d	10,7	b.d	b.d	b.d	b.d	b.d	b.d	b.d	b.d	b.d	b.d	b.d							
Background Potassic	7795M9_cpy29_2	b.d	b.d	b.d	b.d	b.d	6,2	b.d	6,72	39,6	b.d	b.d	b.d	b.d	b.d	b.d	b.d	b.d							
Background Potassic	7795M9_cpy29_3	b.d	b.d	b.d	b.d	b.d	6,1	b.d	6,44	47	b.d	b.d	b.d	b.d	b.d	b.d	b.d	b.d							
Background Potassic	7795M9_cpy29_4	b.d	b.d	b.d	b.d	b.d	10,6	b.d	7,07	41,9	b.d	b.d	b.d	b.d	b.d	b.d	4,4	2,3							
Background Potassic	7795M9_cpy29_5	b.d	b.d	b.d	b.d	b.d	6,2	b.d	7,4	50,9	b.d	b.d	b.d	b.d	b.d	b.d	10,5	2,97							
Background Potassic	7795M9_cpy29_6	b.d	b.d	b.d	b.d	b.d	7	b.d	6,9	52,9	b.d	b.d	b.d	b.d	b.d	b.d	14,2	2,86							
Background Potassic	7795M9_cpy29_7	b.d	b.d	b.d	b.d	b.d	5,4	b.d	8,4	52,3	b.d	b.d	1	b.d	b.d	b.d	6	1,76							
Background Potassic	7795M9_cpy29_8	b.d	b.d	b.d	b.d	b.d	2,8	b.d	8,1	39,9	b.d	b.d	b.d	b.d	b.d	b.d	4,4	1,91							
Background Potassic	7795M9_cpy29_9	b.d	b.d	b.d	b.d	b.d	4,2	b.d	8,1	48,4	b.d	b.d	b.d	b.d	b.d	b.d	b.d	b.d							
Background Potassic	7795M9_cpy31_1	b.d	b.d	b.d	b.d	b.d	10,5	b.d	33	b.d	b.d	b.d	b.d	b.d	b.d	b.d	26,4	5,5							
Background Potassic	7795M9_cpy31_2	b.d	b.d	b.d	b.d	b.d	9,3	b.d	47	b.d	b.d	b.d	b.d	b.d	b.d	b.d	11	b.d							
Background Potassic	7795M9_cpy31_3	b.d	b.d	b.d	b.d	b.d	22	b.d	7,7	34,2	b.d	b.d	b.d	b.d	b.d	b.d	80	9,7							
Background Potassic	7795M9_cpy31_4	b.d	b.d	b.d	b.d	b.d	7,2	b.d	45	b.d	b.d	b.d	b.d	b.d	b.d	b.d	b.d	b.d							
Background Potassic	7795M9_cpy31_5	b.d	b.d	b.d	b.d	b.d	9,4	b.d	9,4	37,9	b.d	b.d	b.d	b.d	0,14	b.d	b.d	14,6	3,6						
Background Potassic	7795M9_cpy31_6	b.d	b.d	b.d	b.d	b.d	12,5	b.d	9,8	54	b.d	b.d	b.d	b.d	b.d	b.d	b.d	b.d							
Background Potassic	7795M9_cpy31_7	b.d	b.d	b.d	b.d	b.d	7,3	b.d	44	b.d	b.d	b.d	b.d	0,6	b.d	b.d	b.d	b.d							
Background Potassic	7795M9_cpy31_8	b.d	b.d	b.d	b.d	b.d	8,9	b.d	8,3	27	b.d	b.d	b.d	b.d	b.d	b.d	b.d	13	b.d						
Background Potassic	7795M9_cpy37_10	b.d	b.d	b.d	b.d	b.d	14,1	b.d	7,8	34,3	b.d	b.d	b.d	b.d	b.d	b.d	b.d	14,8	7,3						
Background Potassic	7795M9_cpy37_2	b.d	b.d	b.d	b.d	b.d	9,2	b.d	4,86	27,9	b.d	b.d	b.d	b.d	b.d	b.d	b.d	11,8	b.d						
Background Potassic	7795M9_cpy37_3	b.d	b.d	b.d	b.d	b.d	9,4	b.d	6,6	41,9	b.d	b.d	b.d	b.d	b.d	b.d	b.d	7,1	1,42						
Background Potassic	7795M9_cpy37_4	b.d	b.d	b.d	b.d	b.d	6,7	b.d	6,07	39,6	b.d	4,3	b.d	b.d	b.d	b.d	b.d	6,5	1,24						
Background Potassic	7795M9_cpy37_5	b.d	b.d	b.d	b.d	b.d	9,5	b.d	6,53	46,9	b.d	b.d	b.d	b.d	b.d	b.d	b.d	b.d	b.d						
Background Potassic	7795M9_cpy37_6	b.d	b.d	b.d	b.d	b.d	2,9	b.d	5,5	45,3	b.d	b.d	b.d	0,3	b.d	b.d	b.d	b.d	b.d						
Background Potassic	7795M9_cpy37_7	b.d	b.d	b.d	b.d	b.d	5,8	b.d	6,22	45,6	b.d	b.d	b.d	b.d	b.d	b.d	b.d	4	b.d						
Background Potassic	7795M9_cpy37_8	b.d	b.d	b.d	b.d	b.d	b.d	11,2	b.d	b.d	b.d	b.d	7,3	b.d	6,67	40,8	b.d	0,1	b.d	b.d	b.d	b.d	b.d	7,6	1,2
Background Potassic	7795M9_cpy37_9	b.d	b.d	b.d	b.d	b.d	15,6	b.d	5,5	38,8	b.d	b.d	b.d	b.d	b.d	b.d	b.d	30,7	3,3						
Background Potassic	7795M9_cpy38_1	b.d	b.d	b.d	b.d	37	b.d	b.d	b.d	b.d	b.d	b.d	9,4	b.d	7,9	36,3	b.d	b.d	b.d	b.d	b.d	b.d	b.d	21,3	b.d
Background Potassic	7795M9_cpy38_10	b.d	b.d	b.d	b.d	b.d	b.d	32	b.d	b.d	b.d	b.d	13,1	b.d	10	56,6	b.d	b.d	b.d	b.d	b.d	b.d	b.d	20,5	2,9
Background Potassic	7795M9_cpy38_11	b.d	b.d	b.d	b.d	b.d	15	b.d	7,6	53,1	b.d	b.d	b.d	b.d	b.d	b.d	0,25	14,3	1,7						

Background Potassic	7795M9_cpy38_12	b.d	b.d	b.d	b.d	b.d	b.d	22,5	b.d	b.d	b.d	b.d	13	b.d	8,4	53	b.d	b.d	b.d	b.d	b.d	0,07	13,6	1,63	
Background Potassic	7795M9_cpy38_13	b.d	b.d	b.d	b.d	b.d	23,1	b.d	9,2	68,2	b.d	b.d	b.d	0,06	b.d	b.d	42,9	7,2							
Background Potassic	7795M9_cpy38_14	b.d	b.d	b.d	b.d	b.d	26,2	b.d	8,2	61,5	b.d	b.d	b.d	b.d	b.d	b.d	53,8	4,83							
Background Potassic	7795M9_cpy38_15	b.d	b.d	b.d	b.d	b.d	19,9	b.d	8	57,4	b.d	b.d	b.d	b.d	b.d	b.d	18,6	2,32							
Background Potassic	7795M9_cpy38_2	b.d	b.d	b.d	b.d	b.d	12,4	b.d	7,73	48,3	b.d	6,6	b.d	b.d	b.d	b.d	29	2,01							
Background Potassic	7795M9_cpy38_3	b.d	b.d	b.d	b.d	b.d	b.d	25,1	b.d	b.d	b.d	b.d	10,1	b.d	7,9	46,1	b.d	b.d	b.d	0,13	b.d	b.d	14,8	1,41	
Background Potassic	7795M9_cpy38_4	b.d	b.d	b.d	b.d	b.d	16,2	b.d	8,3	53	b.d	b.d	b.d	b.d	b.d	b.d	15,9	2,38							
Background Potassic	7795M9_cpy38_5	b.d	b.d	b.d	b.d	b.d	15,1	b.d	8,4	51,6	b.d	b.d	b.d	b.d	b.d	b.d	25,1	2,98							
Background Potassic	7795M9_cpy38_6	b.d	b.d	b.d	b.d	b.d	16,4	b.d	7,8	54,7	b.d	b.d	b.d	b.d	b.d	b.d	14,8	2,39							
Background Potassic	7795M9_cpy38_7	b.d	b.d	b.d	b.d	b.d	18,8	b.d	8,4	51,9	b.d	b.d	b.d	b.d	b.d	b.d	39,2	5,5							
Background Potassic	7795M9_cpy38_8	b.d	b.d	b.d	b.d	b.d	31,4	b.d	8,8	62,6	b.d	b.d	b.d	b.d	b.d	b.d	83	9,6							
Background Potassic	7795M9_cpy38_9	b.d	b.d	b.d	b.d	b.d	b.d	23	b.d	b.d	b.d	b.d	23	b.d	8,3	53,1	b.d	2,5	0,23	b.d	b.d	b.d	11,5	2,7	
Background Potassic	7795M9_cpy40_1	b.d	b.d	b.d	b.d	b.d	5,9	4,6	6,86	50,6	b.d	b.d	b.d	b.d	b.d	b.d	4,9	1,84							
Background Potassic	7795M9_cpy40_2	b.d	b.d	b.d	b.d	b.d	4,6	b.d	6,32	39,2	b.d	b.d	b.d	b.d	b.d	b.d	4,2	1,55							
Background Potassic	7795M9_cpy40_3	b.d	b.d	b.d	b.d	b.d	5,4	b.d	5,95	25,8	b.d	b.d	0,26	b.d	b.d	b.d	9,7	1,03							
Intense Potassic	7808M21_cpy43_1	b.d	b.d	b.d	b.d	b.d	3,6	b.d	1,65	6,18	b.d	b.d	b.d	0,45	b.d	b.d	1,58	2,92							
Intense Potassic	7808M21_cpy43_2	b.d	b.d	b.d	b.d	b.d	4,96	b.d	1,77	3,67	b.d	b.d	b.d	0,58	b.d	b.d	1,92	3,69							
Intense Potassic	7808M21_cpy43_3	b.d	b.d	b.d	b.d	b.d	2	b.d	5,87	b.d	b.d	b.d	0,22	b.d	b.d	1,7	1,32								
Intense Potassic	7808M21_cpy43_4	b.d	b.d	b.d	b.d	b.d	1,08	b.d	5,8	b.d	b.d	0,11	0,3	b.d	b.d	b.d	2,03								
Intense Potassic	7808M21_cpy43_5	b.d	b.d	b.d	b.d	b.d	2,29	b.d	2,59	4,9	b.d	b.d	b.d	0,57	b.d	b.d	1,7	2,51							
Intense Potassic	7795M10_cpy68_3	b.d	b.d	b.d	b.d	b.d	3,06	16,1	b.d	b.d	0,13	b.d	b.d	0,22	b.d	b.d	b.d								
Intense Potassic	7795M10_cpy68_4	b.d	b.d	b.d	b.d	b.d	2,5	b.d	3,11	11,2	b.d	b.d	b.d	b.d	b.d	b.d	b.d								
Intense Potassic	7795M10_cpy68_5	b.d	b.d	b.d	b.d	b.d	3	b.d	4,4	14	b.d	b.d	b.d	b.d	b.d	b.d	b.d								
Intense Potassic	7795M10_cpy68_6	b.d	b.d	b.d	b.d	b.d	6,01	21,6	b.d	b.d	b.d	b.d	b.d	b.d	b.d	b.d									
Intense Potassic	7795M10_cpy69_4	b.d	b.d	b.d	b.d	b.d	5,3	b.d	5,32	23,7	b.d	b.d	b.d	b.d	b.d	b.d	b.d								
Intense Potassic	7795M10_cpy69_5	b.d	b.d	b.d	b.d	b.d	5,4	b.d	6,02	25	b.d	b.d	b.d	b.d	b.d	b.d	b.d								
Intense Potassic	3618M25_cpy44_1	b.d	b.d	b.d	b.d	b.d	22,6	b.d	3,06	25,4	b.d	b.d	b.d	b.d	b.d	b.d	26	2,4							
Intense Potassic	3618M25_cpy44_2	b.d	b.d	b.d	b.d	b.d	15,3	b.d	3,04	24,9	b.d	b.d	b.d	b.d	b.d	b.d	4,6	1,39							
Intense Potassic	3618M25_cpy44_3	b.d	b.d	b.d	b.d	b.d	350	b.d	16,7	b.d	3,17	19,9	b.d	b.d	b.d	b.d	b.d	15	6,99						
Intense Potassic	3618M25_cpy44_4	b.d	b.d	b.d	b.d	b.d	14,1	b.d	3,26	21,7	b.d	b.d	b.d	b.d	b.d	b.d	b.d	1,86							
Intense Potassic	3618M25_cpy44_5	b.d	b.d	b.d	b.d	b.d	5,1	b.d	3,5	24,4	b.d	b.d	b.d	b.d	b.d	b.d	b.d	0,97							

Intense Potassic	3618M25_cpy44_6	b.d	23,2	b.d	3,5	16,3	b.d	b.d	b.d	b.d	b.d	b.d	b.d	2,2	3,89													
Intense Potassic	3618M25_cpy44_7	b.d	20,3	b.d	3,93	21,5	b.d	b.d	b.d	b.d	b.d	b.d	b.d	0,15	2,3	1,94												
Intense Potassic	3618M25_cpy44_8	b.d	32,4	b.d	4,95	21,2	b.d	b.d	b.d	b.d	b.d	b.d	b.d	1,8														
Intense Potassic	3618M25_cpy46_1	b.d	15	b.d	4,93	29,6	b.d	b.d	b.d	b.d	b.d	b.d	b.d	b.d	1,22													
Intense Potassic	3618M25_cpy46_2	b.d	23,4	b.d	5,39	22,9	b.d	b.d	b.d	b.d	b.d	b.d	b.d	b.d	2,49	4,5												
Intense Potassic	3618M25_cpy46_3	b.d	23,2	b.d	5,87	21,9	b.d	b.d	0,61	b.d	b.d	b.d	b.d	11,5	11,3													
Intense Potassic	3618M25_cpy46_4	b.d	9,3	b.d	5,61	21,7	b.d	b.d	b.d	b.d	b.d	b.d	b.d	1,42	3,07													
Intense Potassic	3618M25_cpy46_5	b.d	4,8	b.d	5,13	26,2	b.d	b.d	b.d	b.d	b.d	b.d	b.d	b.d														
Intense Potassic	3618M25_cpy46_6	b.d	11,1	b.d	6,14	27,4	b.d	b.d	b.d	b.d	b.d	b.d	b.d	b.d	2,05	2,02												
Intense Potassic	3618M25_cpy46_7	b.d	b.d	b.d	3,7	b.d	8,9	b.d	5,23	23	b.d	b.d	b.d	b.d	b.d	b.d	b.d	b.d										
Intense Potassic	3618M25_cpy48_4	b.d	3,71	b.d	4	8	b.d	b.d	b.d	b.d	b.d	b.d	b.d	b.d	0,97	1,32												
Intense Potassic	3618M25_cpy48_5	b.d	2,6	b.d	4,69	16,3	b.d	b.d	b.d	b.d	b.d	b.d	b.d	b.d		1,22												
Intense Potassic	3618M25_cpy48_6	b.d	3,5	b.d	4,51	10,1	b.d	b.d	0,18	b.d	b.d	b.d	b.d	b.d	0,95													
Intense Potassic	3618M25_cpy48_7	b.d	10,2	b.d	4,45	4,7	b.d	b.d	b.d	b.d	b.d	b.d	b.d	b.d		1,92												
Quartz-sericite	3618M24_cpy77_1	b.d	10,2	b.d	2,08	14,6	b.d	b.d	b.d	b.d	b.d	2,3	b.d	4,83		2,15												
Quartz-sericite	3618M24_cpy77_2	b.d	4,7	b.d	3,92	31,3	b.d	b.d	b.d	b.d	b.d	b.d	b.d	b.d														
Quartz-sericite	3618M24_cpy77_3	b.d	8,8	b.d	3,22	18,7	b.d	b.d	b.d	b.d	b.d	b.d	b.d	b.d		1,59												
Quartz-sericite	3618M24_cpy78_1	b.d	1,85	b.d	3,02	27	b.d	b.d	b.d	b.d	b.d	b.d	b.d	b.d														
Quartz-sericite	3618M24_cpy78_2	b.d	11,7	b.d	3,25	25,7	b.d	b.d	b.d	b.d	b.d	b.d	b.d	b.d	0,91	1,72												
Quartz-sericite	3618M24_cpy78_3	b.d	15	b.d	2,96	26,1	b.d	b.d	b.d	b.d	b.d	b.d	b.d	b.d		0,96												
Quartz-sericite	3618M24_cpy78_4	b.d	25,2	b.d	3,16	29,6	b.d	b.d	b.d	b.d	b.d	b.d	b.d	b.d	2	1,04												
Quartz-sericite	3618M24_cpy80_1	b.d	b.d	5,5	b.d	16	b.d	11,5	b.d	2,14	13,5	b.d	b.d	b.d	b.d	b.d	b.d	b.d	4,17	0,57								
Quartz-sericite	3618M24_cpy80_10	b.d	6,32	b.d	2,24	25,7	b.d	b.d	b.d	b.d	b.d	b.d	b.d	b.d	2,98	0,64												
Quartz-sericite	3618M24_cpy80_11	b.d	15	b.d	6,19	b.d	3,66	25,8	b.d	b.d	b.d	b.d	b.d	b.d	b.d	1,14	0,66											
Quartz-sericite	3618M24_cpy80_12	b.d	10	b.d	6,1	b.d	2,14	24,7	b.d	b.d	b.d	b.d	b.d	b.d	b.d	2,26	1,01											
Quartz-sericite	3618M24_cpy80_13	b.d	11,1	b.d	5,1	27,9	b.d	b.d	b.d	b.d	b.d	b.d	b.d	b.d	3,56	1,04												
Quartz-sericite	3618M24_cpy80_14	b.d	5,05	b.d	3,81	25,7	b.d	b.d	b.d	b.d	b.d	b.d	b.d	b.d	0,95	1,38	1,2											
Quartz-sericite	3618M24_cpy80_15	b.d	8,64	b.d	1,96	18,6	b.d	b.d	b.d	b.d	b.d	b.d	b.d	b.d	3,82	1,26												
Quartz-sericite	3618M24_cpy80_16	b.d	13,8	b.d	2,36	26	b.d	b.d	b.d	b.d	b.d	b.d	b.d	b.d	4,68	1,42												
Quartz-sericite	3618M24_cpy80_17	b.d	9,98	b.d	2,56	18,6	b.d	b.d	b.d	b.d	b.d	b.d	b.d	b.d	4,29	1,53												
Quartz-sericite	3618M24_cpy80_18	b.d	390	b.d	12,9	b.d	2,3	19	b.d	b.d	b.d	b.d	b.d	b.d	b.d	4,29	2,61											

Quartz-sericite	3618M24_cpy80_2	b.d	120	b.d	3,98	b.d	2,28	23,3	b.d	b.d	b.d	b.d	b.d	b.d	1,76	0,6											
Quartz-sericite	3618M24_cpy80_3	b.d	30	b.d	5,59	b.d	4,25	26,3	b.d	b.d	b.d	b.d	b.d	b.d	1,37	0,61											
Quartz-sericite	3618M24_cpy80_4	b.d	9,5	b.d	2,24	18	b.d	b.d	b.d	b.d	b.d	b.d	2,75	0,62													
Quartz-sericite	3618M24_cpy80_7	b.d	10,1	b.d	2,32	19,3	b.d	b.d	b.d	b.d	b.d	b.d	4,83	1,9													
Quartz-sericite	3618M24_cpy82_1	b.d	360	b.d	12	b.d	4,83	26,1	b.d	b.d	b.d	0,291	b.d	b.d	2,58	0,88											
Quartz-sericite	3618M24_cpy82_10	b.d	13,5	b.d	3,64	19,7	b.d	b.d	b.d	b.d	b.d	b.d	1,7	0,91													
Quartz-sericite	3618M24_cpy82_2	b.d	35	b.d	19,1	b.d	5,16	27,8	b.d	b.d	b.d	0,295	b.d	b.d	2,23	0,93											
Quartz-sericite	3618M24_cpy82_3	b.d	42	b.d	27,5	b.d	4,9	19,1	b.d	b.d	b.d	b.d	b.d	b.d	10,9	2,32											
Quartz-sericite	3618M24_cpy82_4	b.d	27	b.d	17,4	b.d	4,83	22,4	b.d	b.d	0,08	1,26	b.d	b.d	4,21	1,14											
Quartz-sericite	3618M24_cpy82_5	b.d	12	b.d	14,5	b.d	5,01	24,4	b.d	b.d	b.d	0,5	b.d	b.d	1,4												
Quartz-sericite	3618M24_cpy82_6	b.d	9,5	b.d	4,8	26,7	b.d	b.d	b.d	b.d	b.d	b.d	0,74	0,52													
Quartz-sericite	3618M24_cpy82_7	b.d	8,8	b.d	4,31	24,9	b.d	b.d	b.d	b.d	b.d	b.d	0,15	1,3													
Quartz-sericite	3618M24_cpy82_8	b.d	25,6	b.d	6,6	35,6	b.d	b.d	b.d	b.d	b.d	b.d	7,2	2,2													
Quartz-sericite	3618M24_cpy82_9	b.d	8,6	b.d	3,94	23,9	b.d	b.d	0,05	b.d	b.d	b.d	1,49	0,37													
Quartz-sericite	3618M24_cpy83_1	b.d	11,94	b.d	2,33	21,6	b.d	b.d	b.d	b.d	b.d	b.d	2,82	b.d													
Quartz-sericite	3618M24_cpy83_1	b.d	28,1	b.d	3,3	17,9	b.d	b.d	b.d	b.d	b.d	b.d	5,47	1,95													
Quartz-sericite	3618M24_cpy83_2	b.d	22	b.d	3,88	17,7	b.d	b.d	b.d	b.d	b.d	b.d	4,94	1,17													
Quartz-sericite	3618M24_cpy83_3	b.d	b.d	b.d	b.d	5,3	b.d	25,2	b.d	3,55	16,8	b.d	b.d	b.d	b.d	b.d	b.d	8	2,06								
Quartz-sericite	3618M24_cpy83_4	b.d	10	b.d	5,33	b.d	2,31	26,5	b.d	b.d	b.d	b.d	b.d	b.d	1,07	0,49											
Quartz-sericite	3618M24_cpy83_4	b.d	17,9	b.d	3,18	20,9	b.d	b.d	b.d	b.d	b.d	b.d	5,66	1,21													
Quartz-sericite	3618M24_cpy83_5	b.d	21,4	b.d	3,44	20,7	b.d	b.d	b.d	b.d	b.d	b.d	4,55	0,65													
Quartz-sericite	3618M24_cpy84_5	b.d	b.d	6,3	b.d	150	b.d	19,2	3	4,92	26,3	b.d	b.d	b.d	b.d	b.d	b.d	5,9	3,14								
Quartz-sericite	3618M24_cpy84_6	b.d	38,3	b.d	1,68	27,6	b.d	b.d	b.d	b.d	b.d	b.d	25,9														
Quartz-sericite	3618M24_cpy84_6	b.d	350	b.d	45,1	b.d	3,58	25,6	b.d	b.d	b.d	b.d	b.d	b.d	12	7,4											
Quartz-sericite	3618M24_cpy84_7	b.d	16,1	b.d	1,92	25,3	b.d	b.d	b.d	0,17	b.d	b.d	b.d	3,37													
Quartz-sericite	3618M24_cpy84_9	b.d	17,9	b.d	1,93	25,2	b.d	b.d	b.d	0,124	b.d	b.d	b.d	7,06													

Statistic	V	Cr	Mn	Co	Ni	Zn	Ga	Ge	As	Se	Mo	Ag	Cd	In	Sn	Sb	Te	W	Au	Hg	Tl	Pb	Bi
Minimum	-	-	5,50	3,70	5,30	17,00	11,20	60,00	20,00	10,00	8,50	0,82	0,88	1,08	1,20	7,00	0,10	0,05	0,01	0,95	0,02	0,74	0,24
Maximum	-	-	54,00	3,70	37,00	236,00	43,00	60,00	20,00	22000,00	8,50	45,10	4,60	22,80	68,20	7,00	6,60	3,80	1,26	2,30	0,25	83,00	25,90
Mean	-	-	25,18	3,70	21,15	126,50	20,79	60,00	20,00	2358,05	8,50	10,60	2,42	6,39	26,92	7,00	2,56	0,60	0,33	1,63	0,14	9,47	2,65
Median	-	-	20,60	3,70	21,15	126,50	19,00	60,00	20,00	135,00	8,50	8,90	2,10	5,90	25,30	7,00	2,40	0,25	0,26	1,63	0,15	4,40	1,86

ANEXO G: Resultados de análisis LA-ICP-MS en bornita del yacimiento Chuquicamata Subterráneo

Este anexo es equivalente a “Annex 2B” indicado en el manuscrito.

Concentraciones se encuentran en partes por millón (ppm)

b.d.: bajo el límite de detección

Alteration	Sample	V	Cr	Mn	Co	Ni	Zn	Ga	Ge	As	Se	Mo	Ag	Cd	In	Sn	Sb	Te	W	Au	Hg	Tl	Pb	Bi	
Background Potassic	3618M22_bn10_1	b.d	752	b.d	b.d	b.d	b.d	b.d	b.d	b.d	b.d	b.d	4,5	2320											
Background Potassic	3618M22_bn10_2	b.d	730	b.d	b.d	b.d	b.d	b.d	b.d	b.d	b.d	b.d	4,2	2260											
Background Potassic	3618M22_bn10_3	b.d	610	b.d	b.d	b.d	b.d	b.d	b.d	0,16	0,23	b.d	b.d	2960											
Background Potassic	4587M7_bn3_1	b.d	98	b.d	b.d	16,4	b.d	b.d	b.d	b.d	b.d	b.d	2,8	203											
Background Potassic	4587M7_bn3_2	b.d	110	b.d	b.d	11	b.d	b.d	b.d	b.d	b.d	b.d	3,26	207											
Background Potassic	4587M7_bn3_3	b.d	141	b.d	b.d	10	b.d	b.d	b.d	b.d	b.d	b.d	2,75	240											
Background Potassic	4587M7_bn3_4	b.d	110	b.d	b.d	12,9	b.d	31	b.d	b.d	b.d	b.d	1,95	212											
Background Potassic	4587M7_bn4_1	b.d	132	b.d	b.d	19,5	b.d	b.d	b.d	b.d	b.d	b.d	1,82	286											
Background Potassic	4587M7_bn4_2	b.d	227	b.d	b.d	b.d	b.d	b.d	0,12	b.d	b.d	b.d	4,6	388											
Background Potassic	4587M7_bn5_1	b.d	218	b.d	b.d	b.d	b.d	b.d	b.d	b.d	b.d	b.d	b.d	2130											
Background Potassic	4587M7_bn6_1	b.d	152	b.d	b.d	4,2	b.d	b.d	b.d	b.d	b.d	b.d	b.d	338											
Background Potassic	4587M7_bn6_2	b.d	184	b.d	b.d	11,6	b.d	b.d	b.d	b.d	b.d	b.d	b.d	390											
Background Potassic	4587M7_bn6_3	b.d	85	b.d	b.d	9,8	b.d	b.d	b.d	b.d	b.d	b.d	b.d	261											
Background Potassic	4587M7_bn9_1	b.d	550	b.d	276	0,41	b.d	b.d	b.d	b.d	0,045	b.d	b.d	b.d	1422										
Background Potassic	4587M7_bn9_2	b.d	480	b.d	277	b.d	b.d	1,29	b.d	b.d	b.d	b.d	b.d	b.d	b.d	1366									
Background Potassic	4587M7_bn9_3	b.d	770	b.d	338	b.d	b.d	b.d	b.d	b.d	b.d	b.d	b.d	b.d	1,24	1830									
Background Potassic	4587M7_bn9_4	b.d	440	b.d	280	b.d	b.d	2,7	b.d	b.d	b.d	b.d	b.d	b.d	0,67	1500									
Background Potassic	4587M7_bn9_5	b.d	246	0,11	b.d	b.d	b.d	b.d	0,06	b.d	b.d	b.d	0,94	1354											
Intense Potassic	4587M13_bn19_1	b.d	198	b.d	b.d	18	b.d	b.d	b.d	b.d	b.d	b.d	5,4	354											
Intense Potassic	4587M13_bn19_2	b.d	154	b.d	b.d	2,8	b.d	b.d	b.d	b.d	b.d	b.d	2,37	303											
Intense Potassic	4587M13_bn19_3	b.d	169	b.d	b.d	12,6	b.d	b.d	b.d	b.d	b.d	b.d	6,27	255											
Intense Potassic	4587M13_bn19_4	b.d	123	b.d	b.d	12,8	b.d	b.d	b.d	b.d	b.d	b.d	5,9	246											
Intense Potassic	4587M13_bn19_5	b.d	108	b.d	b.d	14,4	b.d	b.d	b.d	b.d	b.d	b.d	0,03	2,14	235										

Intense Potassic	4587M13_bn19_6	b.d	b.d	b.d	b.d	b.d	b.d	b.d	b.d	b.d	b.d	b.d	131	b.d	b.d	20,9	b.d	b.d	b.d	b.d	b.d	b.d	2,27	288	
Intense Potassic	4587M13_bn19_7	b.d	b.d	b.d	b.d	b.d	b.d	b.d	b.d	b.d	b.d	b.d	126	b.d	b.d	15,5	b.d	b.d	b.d	b.d	b.d	b.d	b.d	275	
Intense Potassic	4587M13_bn21_1	b.d	b.d	b.d	b.d	b.d	b.d	b.d	b.d	b.d	b.d	b.d	142	b.d	b.d	b.d	b.d	b.d	b.d	b.d	b.d	b.d	b.d	291	
Intense Potassic	4587M13_bn21_3	b.d	b.d	b.d	b.d	b.d	b.d	b.d	b.d	b.d	b.d	b.d	200	b.d	b.d	6	b.d	b.d	b.d	b.d	b.d	b.d	8,7	296	
Intense Potassic	4587M13_bn21_4	b.d	b.d	b.d	b.d	b.d	b.d	b.d	b.d	b.d	b.d	b.d	110	b.d	b.d	29	b.d	b.d	0,33	b.d	b.d	b.d	2,4	236	
Intense Potassic	4587M13_bn21_5	b.d	b.d	b.d	b.d	b.d	b.d	b.d	b.d	b.d	b.d	b.d	151	b.d	b.d	13,3	b.d	b.d	b.d	b.d	b.d	b.d	1,88	273	
Intense Potassic	4587M13_bn21_6	b.d	b.d	b.d	b.d	b.d	b.d	b.d	b.d	b.d	b.d	b.d	143	b.d	b.d	15,5	b.d	b.d	0,07	b.d	b.d	b.d	b.d	249	
Intense Potassic	7808M21_bn15_1	b.d	b.d	b.d	b.d	b.d	b.d	b.d	b.d	b.d	b.d	b.d	112,6	b.d	b.d	b.d	b.d	b.d	b.d	b.d	b.d	b.d	b.d	326	
Intense Potassic	7808M21_bn15_2	b.d	b.d	b.d	b.d	b.d	b.d	b.d	b.d	b.d	b.d	b.d	88	b.d	b.d	b.d	b.d	b.d	b.d	b.d	b.d	b.d	b.d	267	
Intense Potassic	7808M21_bn16_1	b.d	b.d	b.d	b.d	b.d	b.d	b.d	b.d	b.d	b.d	b.d	690	b.d	b.d	b.d	b.d	b.d	b.d	b.d	b.d	b.d	b.d	278	
Intense Potassic	7808M21_bn16_2	b.d	b.d	b.d	b.d	b.d	b.d	b.d	b.d	b.d	b.d	b.d	490	b.d	101,1	b.d	b.d	b.d	b.d	b.d	b.d	b.d	b.d	317	
Intense Potassic	7808M21_bn16_3	b.d	b.d	b.d	b.d	b.d	b.d	b.d	b.d	b.d	b.d	b.d	83,5	b.d	b.d	b.d	b.d	b.d	b.d	b.d	b.d	b.d	b.d	246	
Intense Potassic	7808M21_bn16_4	b.d	b.d	b.d	b.d	b.d	b.d	b.d	b.d	b.d	b.d	b.d	101,3	b.d	b.d	b.d	b.d	b.d	b.d	b.d	b.d	b.d	b.d	290	
Intense Potassic	7808M21_bn17_10	b.d	b.d	b.d	b.d	b.d	b.d	b.d	b.d	b.d	b.d	b.d	103	b.d	b.d	b.d	b.d	b.d	b.d	b.d	b.d	b.d	b.d	247	
Intense Potassic	7808M21_bn17_5	b.d	b.d	b.d	b.d	b.d	b.d	b.d	b.d	b.d	b.d	b.d	88,3	b.d	b.d	b.d	b.d	b.d	b.d	b.d	b.d	b.d	b.d	209	
Intense Potassic	7808M21_bn17_6	b.d	b.d	b.d	b.d	b.d	22	b.d	b.d	b.d	b.d	b.d	119	b.d	85,8	b.d	b.d	b.d	b.d	b.d	b.d	b.d	b.d	199	
Intense Potassic	7808M21_bn17_7	b.d	b.d	b.d	b.d	b.d	b.d	b.d	b.d	b.d	b.d	b.d	81	b.d	b.d	b.d	b.d	b.d	b.d	b.d	b.d	b.d	b.d	228	
Intense Potassic	7808M21_bn17_9	b.d	b.d	b.d	b.d	b.d	b.d	b.d	b.d	b.d	b.d	b.d	84,1	b.d	b.d	b.d	b.d	b.d	b.d	b.d	b.d	b.d	b.d	229	
Intense Potassic	7808M9_bn27_1	b.d	b.d	b.d	b.d	b.d	25	b.d	b.d	b.d	b.d	b.d	198	7,1	0,83	68	b.d	b.d	b.d	b.d	b.d	b.d	b.d	6,79	306
Intense Potassic	7808M9_bn27_10	b.d	b.d	b.d	b.d	b.d	b.d	b.d	b.d	b.d	b.d	b.d	262	b.d	0,83	34,5	b.d	4,7	b.d	b.d	b.d	b.d	b.d	9	442
Intense Potassic	7808M9_bn27_2	b.d	b.d	b.d	b.d	b.d	38	b.d	b.d	b.d	b.d	b.d	240	b.d	283	b.d	1,56	232	b.d	b.d	b.d	b.d	b.d	23,6	303
Intense Potassic	7808M9_bn27_3	b.d	b.d	b.d	b.d	b.d	21	b.d	b.d	b.d	b.d	b.d	168	5,7	0,85	81,4	b.d	0,32	b.d	b.d	b.d	b.d	b.d	8,5	261
Intense Potassic	7808M9_bn27_4	b.d	b.d	b.d	b.d	b.d	24	b.d	b.d	b.d	b.d	b.d	190	5,8	0,74	51,6	b.d	0,54	b.d	b.d	b.d	b.d	b.d	7,31	268
Intense Potassic	7808M9_bn27_5	b.d	b.d	b.d	b.d	b.d	31	b.d	b.d	b.d	b.d	b.d	198	9,8	1	94	b.d	2	b.d	b.d	b.d	b.d	b.d	5,82	258
Intense Potassic	7808M9_bn27_6	b.d	b.d	b.d	b.d	b.d	24,3	b.d	b.d	b.d	b.d	b.d	167	9,1	0,95	84	b.d	b.d	b.d	b.d	b.d	b.d	b.d	7,15	257
Intense Potassic	7808M9_bn27_7	b.d	b.d	b.d	b.d	b.d	70	b.d	b.d	b.d	b.d	b.d	174	10,8	0,94	200	b.d	b.d	b.d	b.d	b.d	b.d	0,01	8,5	236
Intense Potassic	7808M9_bn27_8	b.d	b.d	b.d	b.d	b.d	23,4	b.d	b.d	b.d	b.d	b.d	191,3	9,2	0,89	77	b.d	b.d	b.d	b.d	b.d	b.d	0,009	8,9	283
Intense Potassic	7808M9_bn27_9	b.d	b.d	b.d	b.d	b.d	17	b.d	b.d	b.d	b.d	b.d	154	11	0,77	89	b.d	b.d	b.d	b.d	b.d	b.d	b.d	9,4	304
Intense Potassic	7808M9_bn33_1	b.d	b.d	b.d	b.d	b.d	b.d	b.d	b.d	b.d	b.d	b.d	212	8,2	0,44	15,5	b.d	0,4	b.d	b.d	b.d	b.d	b.d	6,26	273
Intense Potassic	7808M9_bn33_2	b.d	b.d	b.d	b.d	b.d	b.d	b.d	b.d	b.d	b.d	b.d	190	10,7	0,68	3,7	b.d	b.d	b.d	b.d	b.d	b.d	7	344	
Intense Potassic	7808M9_bn33_3	b.d	b.d	b.d	b.d	b.d	31	b.d	b.d	b.d	b.d	b.d	201	10,8	0,86	86	b.d	b.d	b.d	b.d	b.d	b.d	b.d	8,2	257

Intense Potassic	7808M9_bn33_4	b.d	b.d	b.d	b.d	b.d	b.d	b.d	b.d	b.d	b.d	2,2	199	12,2	0,75	63	b.d	b.d	b.d	b.d	b.d	b.d	b.d	8,4	338
Intense Potassic	7808M9_bn33_5	b.d	b.d	b.d	b.d	b.d	45	b.d	b.d	b.d	b.d	252	12,9	1,24	116	b.d	b.d	b.d	0,08	b.d	b.d	b.d	10,3	319	
Intense Potassic	7808M9_bn33_6	b.d	b.d	b.d	b.d	b.d	b.d	b.d	b.d	b.d	b.d	246	13,3	0,9	75	b.d	b.d	b.d	b.d	b.d	b.d	b.d	7,3	294	
Intense Potassic	7808M9_bn33_7	b.d	b.d	24	b.d	66	203	b.d	b.d	b.d	b.d	326	14,4	1,28	114	b.d	b.d	b.d	b.d	b.d	b.d	b.d	13,7	483	
Intense Potassic	7808M9_bn33_8	b.d	320	127	b.d	450	810	b.d	b.d	b.d	b.d	441	56	2,7	352	b.d	b.d	b.d	b.d	b.d	b.d	b.d	43	1020	
Intense Potassic	7808M9_bn34_1	b.d	b.d	b.d	b.d	b.d	b.d	b.d	b.d	b.d	b.d	187	b.d	0,45	18,6	b.d	b.d	b.d	b.d	b.d	b.d	b.d	6,1	276	
Intense Potassic	7808M9_bn34_2	b.d	b.d	b.d	b.d	b.d	15,8	b.d	b.d	b.d	b.d	162	7	0,96	81	b.d	b.d	b.d	0,031	b.d	b.d	b.d	6,25	248	
Intense Potassic	7808M9_bn34_3	b.d	b.d	b.d	b.d	b.d	32,7	b.d	b.d	b.d	b.d	186	9,1	0,78	89	b.d	b.d	b.d	b.d	b.d	b.d	b.d	9,2	254	
Intense Potassic	7808M9_bn34_4	b.d	b.d	b.d	b.d	b.d	b.d	b.d	b.d	b.d	b.d	187	8,2	0,75	45	b.d	b.d	b.d	b.d	b.d	b.d	b.d	8,1	281	
Intense Potassic	7808M9_bn34_5	8,5	b.d	b.d	b.d	b.d	45	b.d	b.d	b.d	b.d	185	11,1	1,01	138	b.d	b.d	18,9	0,069	b.d	b.d	b.d	7,2	239	
Intense Potassic	7808M9_bn35_1	b.d	b.d	b.d	b.d	b.d	33,9	b.d	b.d	b.d	b.d	242,5	9,6	0,97	107	b.d	2	b.d	0,112	b.d	b.d	b.d	8,4	263	
Intense Potassic	7808M9_bn35_2	b.d	b.d	b.d	b.d	b.d	33,9	b.d	b.d	b.d	b.d	231	8,3	0,803	105	b.d	0,92	b.d	0,125	b.d	b.d	b.d	6,69	238	
Intense Potassic	7808M9_bn35_3	b.d	b.d	b.d	b.d	b.d	18,9	b.d	b.d	b.d	b.d	252	10,4	1,82	46,6	b.d	0,77	b.d	b.d	b.d	b.d	b.d	3,91	266	
Intense Potassic	7808M9_bn35_4	b.d	b.d	b.d	b.d	b.d	9,2	b.d	b.d	b.d	b.d	231	10,1	0,637	29,9	b.d	1,27	0,021	b.d	b.d	b.d	b.d	4,77	247	
Intense Potassic	7808M9_bn36_1	b.d	b.d	b.d	b.d	b.d	44,6	b.d	b.d	b.d	b.d	249	14,2	1,02	122	b.d	b.d	b.d	b.d	b.d	b.d	b.d	6,89	186	
Intense Potassic	7808M9_bn36_2	b.d	b.d	b.d	b.d	b.d	31,3	b.d	b.d	b.d	b.d	240	13,1	0,81	88,9	b.d	b.d	b.d	b.d	b.d	b.d	b.d	7,33	197	
Intense Potassic	7808M9_bn36_3	b.d	b.d	b.d	b.d	b.d	38	b.d	b.d	b.d	b.d	250	13	1,01	114	b.d	b.d	b.d	b.d	b.d	b.d	b.d	7,39	191	
Intense Potassic	7808M9_bn36_4	b.d	b.d	b.d	b.d	b.d	36	b.d	b.d	b.d	b.d	230	13,3	0,83	94,9	b.d	b.d	b.d	0,016	b.d	b.d	b.d	8,06	208	
Intense Potassic	7808M9_bn36_5	b.d	b.d	b.d	b.d	b.d	26,9	b.d	b.d	b.d	b.d	240	14,8	1,06	109	b.d	0,48	b.d	b.d	b.d	b.d	b.d	10,7	219	
Intense Potassic	7808M9_bn36_6	b.d	b.d	b.d	b.d	b.d	24,8	b.d	b.d	b.d	b.d	272	16,8	0,81	83,7	b.d	0,81	b.d	b.d	b.d	b.d	b.d	7,1	203,8	
Intense Potassic	7808M9_bn36_7	b.d	b.d	b.d	b.d	b.d	14,5	b.d	b.d	b.d	b.d	239	11,8	0,57	24	b.d	b.d	b.d	b.d	b.d	b.d	b.d	8,6	220	
Intense Potassic	7808M9_bn37_1	b.d	b.d	b.d	b.d	b.d	73	b.d	b.d	b.d	b.d	334	18,4	1,12	80	b.d	b.d	0,26	b.d	b.d	b.d	b.d	10,7	191	
Intense Potassic	7808M9_bn37_2	b.d	b.d	b.d	b.d	b.d	79	b.d	b.d	b.d	b.d	249	20,6	1,2	72,5	b.d	b.d	b.d	b.d	b.d	b.d	b.d	12,5	184	
Intense Potassic	7808M9_bn37_3	b.d	b.d	b.d	b.d	b.d	14,1	b.d	b.d	b.d	b.d	228	b.d	0,67	42,6	b.d	b.d	b.d	b.d	b.d	b.d	b.d	11,56	182	
Intense Potassic	7808M9_bn37_4	b.d	b.d	b.d	b.d	b.d	b.d	b.d	b.d	b.d	b.d	245	b.d	0,88	98	6,9	b.d	b.d	b.d	b.d	b.d	b.d	b.d	19	282
Intense Potassic	7808M9_bn37_5	b.d	b.d	b.d	b.d	b.d	75	b.d	b.d	b.d	b.d	277	b.d	1,22	83,5	b.d	b.d	b.d	b.d	b.d	b.d	b.d	13,7	264	

Statistic	V	Cr	Mn	Co	Ni	Zn	Ga	Ge	As	Se	Mo	Ag	Cd	In	Sn	Sb	Te	W	Au	Hg	Tl	Pb	Bi
Minimum	8,50	320,00	24,00	-	66,00	9,20	-	-	-	119,00	2,20	81,00	0,11	0,44	1,29	6,90	0,32	0,02	0,02	-	0,01	0,67	182,00
Maximum	8,50	320,00	127,00	-	450,00	810,00	-	-	-	770,00	2,20	752,00	56,00	2,70	352,00	6,90	31,00	18,90	0,23	-	0,03	43,00	2960,00
Mean	8,50	320,00	75,50	-	258,00	63,48	-	-	-	472,38	2,20	210,36	11,92	0,96	62,83	6,90	3,77	2,49	0,10	-	0,02	7,62	461,12
Median	8,50	320,00	75,50	-	258,00	31,15	-	-	-	485,00	2,20	191,30	10,80	0,88	49,10	6,90	0,87	0,14	0,08	-	0,01	7,10	267,50

ANEXO H: Resultados de análisis LA-ICP-MS en pирita del yacimiento Chuquicamata Subterráneo

Este anexo es equivalente a “Annex 2C” indicado en el manuscrito.

Concentraciones se encuentran en partes por millón (ppm)

b.d.: bajo el límite de detección

Alteration	Sample	V	Cr	Mn	Co	Ni	Cu	Zn	Ga	Ge	As	Se	Mo	Ag	Cd	In	Sn	Sb	Te	W	Au	Hg	Tl	Pb	Bi	
Chloritic	8710M1_py11_1	b.d	b.d	b.d	193	123	b.d	b.d	b.d	6,3	b.d	700	b.d	b.d	b.d	b.d	b.d	b.d	b.d	0,03	b.d	b.d	b.d	b.d	1	
Chloritic	8710M1_py11_2	b.d	b.d	b.d	54	43	b.d	b.d	b.d	b.d	b.d	b.d	b.d	b.d	b.d	b.d	b.d	b.d	b.d	b.d	b.d	b.d	b.d	b.d	b.d	
Chloritic	8710M1_py11_3	b.d	b.d	b.d	107	65	b.d	b.d	b.d	b.d	b.d	b.d	b.d	b.d	b.d	b.d	b.d	b.d	b.d	b.d	b.d	b.d	b.d	b.d	0,25	
Chloritic	8710M1_py12_1	b.d	b.d	b.d	340	122	8,8	b.d	b.d	b.d	b.d	b.d	b.d	0,96	b.d	b.d	b.d	b.d	b.d	b.d	b.d	b.d	b.d	b.d	3,9	9,5
Chloritic	8710M1_py12_2	b.d	b.d	b.d	350	100	b.d	b.d	b.d	8,8	b.d	b.d	b.d	b.d	b.d	b.d	b.d	b.d	b.d	b.d	b.d	b.d	b.d	b.d	1,02	
Chloritic	8710M1_py12_3	b.d	b.d	b.d	850	166	b.d	b.d	b.d	b.d	b.d	b.d	0,24	b.d	b.d	b.d	b.d	b.d	b.d	b.d	b.d	b.d	b.d	b.d	0,33	8,8
Chloritic	8710M1_py13_1	b.d	b.d	b.d	1010	175	b.d	b.d	b.d	b.d	b.d	b.d	b.d	b.d	b.d	b.d	b.d	b.d	b.d	b.d	b.d	b.d	b.d	b.d	b.d	
Chloritic	8710M1_py13_2	b.d	b.d	b.d	443	77	b.d	b.d	b.d	b.d	b.d	b.d	b.d	b.d	b.d	b.d	b.d	b.d	b.d	b.d	b.d	b.d	b.d	b.d	b.d	
Chloritic	8710M1_py13_3	b.d	b.d	b.d	570	195	b.d	b.d	b.d	b.d	b.d	b.d	b.d	b.d	b.d	b.d	b.d	b.d	b.d	b.d	b.d	b.d	b.d	b.d	2	
Chloritic	8710M1_py13_4	b.d	b.d	b.d	79	140	8	b.d	b.d	b.d	b.d	170	b.d	150	b.d	0,14	b.d	b.d	23	2,3	8,6	b.d	b.d	206	190	
Chloritic	8710M1_py14_1	b.d	b.d	b.d	354	54	26,3	b.d	b.d	b.d	b.d	b.d	9	b.d	b.d	b.d	b.d	b.d	b.d	b.d	b.d	b.d	b.d	b.d	12,1	11,7
Chloritic	8710M1_py14_3	b.d	b.d	b.d	610	40	b.d	b.d	b.d	b.d	b.d	120	b.d	b.d	b.d	b.d	b.d	b.d	b.d	b.d	b.d	b.d	b.d	b.d	3,3	
Chloritic	8710M1_py14_4	b.d	b.d	b.d	740	43	b.d	b.d	b.d	b.d	b.d	210	b.d	b.d	b.d	b.d	b.d	b.d	b.d	b.d	b.d	b.d	b.d	b.d	b.d	
Chloritic	8710M1_py14_5	b.d	b.d	b.d	750	64	280	b.d	b.d	3,6	b.d	b.d	b.d	b.d	b.d	b.d	b.d	b.d	b.d	b.d	b.d	b.d	b.d	b.d	3,9	2,8
Chloritic	8710M1_py14_6	b.d	b.d	b.d	264	62	3,4	b.d	b.d	3,4	b.d	b.d	b.d	0,5	b.d	b.d	b.d	b.d	b.d	b.d	b.d	b.d	b.d	b.d	b.d	0,64
Chloritic	8710M1_py14_7	b.d	b.d	b.d	1090	129	990	b.d	b.d	b.d	b.d	b.d	30	b.d	b.d	b.d	b.d	5,2	b.d	b.d	b.d	b.d	b.d	b.d	37	16,7
Chloritic	8710M1_py15_1	b.d	b.d	b.d	274	71	b.d	b.d	b.d	b.d	5,7	b.d	1,3	b.d	b.d	b.d	b.d	b.d	b.d	0,021	b.d	b.d	b.d	b.d	0,72	
Chloritic	8710M1_py15_2	b.d	b.d	b.d	119	59	b.d	b.d	b.d	3,7	b.d	b.d	b.d	b.d	b.d	b.d	b.d	b.d	b.d	b.d	b.d	b.d	b.d	b.d	2,07	
Chloritic	8710M1_py15_3	b.d	b.d	b.d	780	106	3,2	b.d	b.d	b.d	b.d	b.d	0,47	b.d	b.d	b.d	b.d	b.d	2,2	b.d	b.d	b.d	b.d	b.d	0,73	13,5
Chloritic	8710M1_py15_4	b.d	b.d	b.d	171	61	b.d	b.d	b.d	2,4	b.d	b.d	b.d	0,47	b.d	b.d	b.d	b.d	b.d	b.d	b.d	b.d	b.d	b.d	82	2,49
Chloritic	8710M1_py15_5	b.d	b.d	b.d	780	110	b.d	b.d	b.d	10,1	b.d	b.d	b.d	b.d	b.d	b.d	b.d	b.d	0,35	b.d	b.d	b.d	b.d	b.d	0,98	
Chloritic	8710M1_py15_6	b.d	b.d	b.d	252	50	b.d	b.d	b.d	4,7	b.d	b.d	b.d	b.d	b.d	b.d	b.d	b.d	b.d	b.d	b.d	b.d	b.d	b.d	b.d	
Chloritic	8710M1_py15_7	b.d	b.d	b.d	313	16,2	b.d	b.d	b.d	b.d	b.d	b.d	b.d	b.d	b.d	b.d	b.d	b.d	b.d	b.d	b.d	b.d	b.d	b.d	9,7	

Chloritic	8710M1_py16_3	b.d	b.d	5,5	400	174	62	b.d	4,2	7,2	b.d	b.d	2,2	b.d	0,036	b.d	b.d	6,8	b.d	b.d	b.d	b.d	47	82	
Chloritic	8710M1_py19_1	b.d	b.d	b.d	225	60	6,2	b.d	1,3	b.d	b.d	b.d	3	b.d	b.d	b.d	b.d	4,5	b.d	b.d	b.d	b.d	56	27,3	
Chloritic	8710M1_py19_2	b.d	b.d	4,8	480	70	15,4	b.d	b.d	b.d	b.d	b.d	2,4	b.d	b.d	b.d	b.d	1,7	b.d	0,1	b.d	b.d	100	21	
Chloritic	8710M1_py19_3	b.d	b.d	9,4	243	80	22,7	b.d	b.d	b.d	b.d	b.d	2,62	1,3	b.d	b.d	b.d	2,4	b.d	b.d	b.d	b.d	14,3	29	
Chloritic	8710M1_py19_5	b.d	b.d	130	470	22	21	b.d	b.d	b.d	b.d	b.d	8,3	b.d	b.d	b.d	b.d	1,7	b.d	b.d	b.d	b.d	53	48	
Chloritic	8710M1_py19_6	3,5	b.d	24	990	71	36	b.d	b.d	5	5,2	b.d	b.d	17,6	b.d	b.d	b.d	b.d	8,5	b.d	b.d	b.d	b.d	35,6	56
Background Potassic	3618M19_py25_1	b.d	b.d	b.d	84	298	510	37	b.d	b.d	25	b.d	b.d	2,4	b.d	0,1	0,79	b.d	b.d	b.d	0,034	b.d	b.d	580	10,5
Background Potassic	3618M19_py25_2	b.d	b.d	b.d	43,1	393	44	b.d	b.d	2,5	b.d	b.d	1,1	b.d	b.d	0,88	b.d	b.d	0,021	b.d	b.d	4,03	b.d	1,91	
Background Potassic	3618M19_py25_3	b.d	b.d	b.d	19,4	310	40	b.d	b.d	3,4	b.d	b.d	5	b.d	0,41	b.d	b.d	b.d	b.d	b.d	b.d	b.d	b.d	3,5	1,38
Background Potassic	3618M19_py25_4	b.d	b.d	b.d	2,8	73	133	b.d	b.d	b.d	15,7	18	b.d	b.d	b.d	b.d	b.d	b.d	b.d	b.d	b.d	b.d	b.d	7,8	1,48
Background Potassic	3618M19_py26_1	b.d	b.d	b.d	28	104	230	68	b.d	5	18	b.d	b.d	1,6	b.d	0,15	0,64	1,5	b.d	b.d	b.d	b.d	b.d	39	23
Background Potassic	3618M19_py26_2	b.d	b.d	b.d	22,5	53	810	b.d	b.d	b.d	40	b.d	b.d	6,4	b.d	b.d	b.d	b.d	b.d	b.d	b.d	b.d	b.d	750	30
Background Potassic	3618M19_py26_3	b.d	b.d	b.d	9,2	147	28,1	b.d	b.d	b.d	b.d	b.d	6,8	b.d	b.d	b.d	b.d	b.d	b.d	b.d	b.d	b.d	b.d	1,20E+03	15
Background Potassic	3618M19_py28_1	b.d	b.d	b.d	10,3	78	2470	b.d	b.d	6,5	20	b.d	b.d	24,6	b.d	b.d	b.d	b.d	b.d	b.d	b.d	b.d	b.d	4	3,28
Background Potassic	3618M19_py28_2	b.d	b.d	b.d	22,5	130	5,60E+03	1200	b.d	5,6	1760	b.d	b.d	20,9	b.d	0,17	31	930	b.d	b.d	b.d	b.d	b.d	224	102
Background Potassic	3618M19_py28_3	b.d	b.d	b.d	1,9	7,5	66	b.d	b.d	b.d	b.d	b.d	b.d	b.d	b.d	b.d	b.d	b.d	b.d	b.d	b.d	b.d	b.d	0,47	b.d
Background Potassic	3618M19_py28_4	b.d	b.d	b.d	0,71	5,3	87	b.d	b.d	b.d	b.d	b.d	b.d	b.d	b.d	b.d	b.d	b.d	b.d	b.d	b.d	b.d	b.d	0,4	b.d
Background Potassic	3618M19_py28_5	b.d	b.d	b.d	7,5	9,9	1080	212	b.d	2,15	379	b.d	b.d	7,7	b.d	b.d	b.d	2,2	b.d	b.d	0,063	b.d	b.d	17,6	79
Background Potassic	3618M19_py28_6	b.d	b.d	b.d	5,9	30	330	b.d	b.d	3,6	b.d	b.d	b.d	1,71	b.d	b.d	b.d	b.d	b.d	b.d	b.d	b.d	b.d	0,66	b.d
Background Potassic	3618M19_py28_7	b.d	b.d	b.d	9,3	29,6	240	b.d	b.d	2,03	b.d	200	b.d	13,4	b.d	b.d	b.d	b.d	b.d	b.d	b.d	b.d	b.d	4,85	0,76
Background Potassic	3618M19_py28_8	b.d	b.d	b.d	2,33	8,2	31,3	b.d	b.d	3,4	b.d	b.d	b.d	b.d	b.d	b.d	b.d	b.d	b.d	b.d	b.d	b.d	b.d	b.d	b.d
Background Potassic	3618M19_py29_1	b.d	b.d	b.d	46	58	1500	b.d	b.d	b.d	29,1	b.d	b.d	46	b.d	0,096	b.d	b.d	b.d	b.d	b.d	b.d	b.d	2250	43
Background Potassic	3618M19_py29_2	b.d	b.d	b.d	166	296	3040	136	b.d	b.d	370	b.d	b.d	82	b.d	b.d	0,46	8,2	10,7	b.d	b.d	b.d	b.d	700	32,6
Background Potassic	3618M19_py29_4	b.d	b.d	1080	102	380	850	770	b.d	b.d	680	b.d	b.d	41	b.d	b.d	b.d	7,1	b.d	1,6	b.d	b.d	b.d	55	7,9
Background Potassic	3618M19_py29_8	b.d	b.d	b.d	71	960	870	33	b.d	2,12	221	b.d	b.d	27,4	b.d	0,163	0,199	13,8	4,5	b.d	0,191	b.d	0,074	473	39,2
Background Potassic	7795M9_py20_1	b.d	b.d	b.d	9,4	b.d	3400	b.d	b.d	b.d	b.d	b.d	15	4,3	0,4	25,2	b.d	b.d	0,23	b.d	b.d	b.d	b.d	84	2,4
Background Potassic	7795M9_py20_2	b.d	b.d	b.d	34,7	4,9	5520	b.d	b.d	b.d	b.d	b.d	34,1	0,37	0,176	18,8	b.d	b.d	b.d	b.d	b.d	b.d	b.d	336	2,3
Background Potassic	7795M9_py20_4	b.d	b.d	b.d	b.d	b.d	1650	b.d	b.d	b.d	b.d	b.d	5,1	b.d	0,067	16,8	b.d	0,31	b.d	b.d	b.d	b.d	b.d	8,8	0,34
Background Potassic	7795M9_py21_1	b.d	b.d	b.d	b.d	b.d	2600	b.d	b.d	b.d	b.d	b.d	39	b.d	0,18	28,1	b.d	b.d	b.d	b.d	b.d	b.d	b.d	66	3,3
Background Potassic	7795M9_py21_2	b.d	b.d	b.d	b.d	25	6,50E+03	b.d	5,3	b.d	b.d	b.d	65	b.d	0,24	47	b.d	b.d	0,14	b.d	b.d	b.d	b.d	147	11,2
Background Potassic	7795M9_py22_1	b.d	b.d	b.d	19,2	b.d	2800	b.d	b.d	b.d	b.d	b.d	8,7	b.d	b.d	41,1	b.d	b.d	b.d	b.d	b.d	b.d	b.d	71	1,14

Background Potassic	7795M9_py22_3	b.d	b.d	b.d	13	b.d	9,70E+03	b.d	b.d	b.d	b.d	b.d	63	b.d	0,43	42	b.d	b.d	b.d	b.d	b.d	b.d	203	10		
Background Potassic	7795M9_py24_10	b.d	b.d	b.d	14,8	14,2	5170	b.d	b.d	b.d	b.d	b.d	11,5	b.d	b.d	15,1	b.d	b.d	b.d	b.d	b.d	b.d	51	b.d		
Background Potassic	7795M9_py24_2	b.d	b.d	17	49	157	6,30E+03	b.d	b.d	b.d	b.d	b.d	423	b.d	0,9	12,1	b.d	b.d	b.d	b.d	b.d	b.d	0,48	280	5,3	
Background Potassic	7795M9_py24_3	b.d	b.d	b.d	4,6	b.d	3000	14	b.d	b.d	b.d	b.d	23,4	b.d	0,22	16	b.d	b.d	b.d	b.d	b.d	b.d	17	0,31		
Background Potassic	7795M9_py24_4	b.d	b.d	b.d	b.d	35,5	1600	21	b.d	b.d	b.d	b.d	57,1	b.d	0,48	17,1	b.d	b.d	b.d	b.d	0,013	b.d	b.d	133	2,02	
Background Potassic	7795M9_py24_6	b.d	b.d	b.d	b.d	380	5,90E+03	b.d	b.d	b.d	b.d	b.d	450	b.d	0,49	32	b.d	b.d	b.d	b.d	0,39	b.d	b.d	337	7,9	
Background Potassic	7795M9_py24_7	b.d	b.d	b.d	15,4	54	5,00E+03	b.d	b.d	b.d	b.d	b.d	114	b.d	0,17	19,3	b.d	b.d	b.d	0,031	b.d	b.d	94	1,37		
Quartz-sercite	3618M1_py93_1	b.d	b.d	b.d	26,2	b.d	367	b.d	b.d	b.d	b.d	b.d	b.d	b.d	b.d	b.d	b.d	b.d	b.d	b.d	b.d	0,024	b.d	b.d	0,8	b.d
Quartz-sercite	3618M1_py93_2	b.d	b.d	b.d	33,5	5,5	63	b.d	b.d	2,2	b.d	b.d	b.d	b.d	b.d	b.d	b.d	b.d	b.d	b.d	b.d	b.d	b.d	b.d	b.d	
Quartz-sercite	3618M1_py93_3	b.d	b.d	b.d	44	b.d	97	b.d	b.d	2,5	b.d	b.d	b.d	b.d	b.d	b.d	b.d	b.d	b.d	b.d	b.d	b.d	b.d	b.d	b.d	
Quartz-sercite	3618M1_py93_5	b.d	b.d	b.d	7,2	b.d	68	b.d	b.d	b.d	b.d	b.d	b.d	b.d	b.d	b.d	b.d	b.d	b.d	b.d	b.d	b.d	b.d	b.d	b.d	
Quartz-sercite	3618M1_py93_6	b.d	b.d	b.d	19,4	13,4	38,1	b.d	b.d	b.d	b.d	b.d	b.d	b.d	b.d	b.d	b.d	b.d	b.d	b.d	b.d	b.d	b.d	b.d	b.d	
Quartz-sercite	3618M1_py93_7	b.d	4,4	b.d	48	3,3	88	b.d	b.d	3	b.d	b.d	b.d	0,51	0,55	b.d	b.d	b.d	b.d	b.d	b.d	b.d	b.d	b.d	0,151	
Quartz-sercite	3618M1_py94_1	b.d	b.d	b.d	363	b.d	1050	b.d	b.d	b.d	b.d	b.d	3,28	b.d	b.d	0,48	b.d	b.d	b.d	b.d	b.d	b.d	b.d	b.d	0,116	
Quartz-sercite	3618M1_py94_2	b.d	b.d	b.d	141	b.d	90	b.d	b.d	2,13	b.d	b.d	b.d	b.d	b.d	b.d	b.d	b.d	b.d	b.d	b.d	b.d	b.d	b.d	b.d	
Quartz-sercite	3618M1_py94_3	b.d	b.d	b.d	356	2,2	29,6	b.d	b.d	1,7	b.d	b.d	b.d	b.d	b.d	b.d	b.d	b.d	b.d	b.d	b.d	b.d	b.d	b.d	b.d	
Quartz-sercite	3618M1_py94_4	b.d	b.d	b.d	42,6	2,1	20,5	b.d	b.d	2,7	b.d	b.d	b.d	b.d	b.d	b.d	b.d	b.d	b.d	b.d	b.d	b.d	b.d	b.d	b.d	
Quartz-sercite	3618M1_py94_8	b.d	b.d	b.d	35,8	b.d	80,1	b.d	b.d	1,63	b.d	b.d	b.d	b.d	b.d	b.d	b.d	b.d	b.d	b.d	b.d	b.d	b.d	b.d	b.d	
Quartz-sercite	3618M1_py95_4	b.d	b.d	b.d	b.d	b.d	327	b.d	b.d	2,5	b.d	b.d	b.d	b.d	b.d	b.d	b.d	b.d	b.d	b.d	b.d	b.d	b.d	b.d	b.d	
Quartz-sercite	3618M1_py95_5	b.d	b.d	b.d	2,87	b.d	95	b.d	b.d	2,18	b.d	b.d	b.d	b.d	b.d	b.d	b.d	b.d	b.d	b.d	b.d	b.d	b.d	b.d	b.d	
Quartz-sercite	3618M24_py58_2	b.d	4,2	b.d	37,5	392	b.d	b.d	b.d	2,4	b.d	b.d	b.d	b.d	b.d	b.d	b.d	b.d	b.d	b.d	b.d	b.d	b.d	b.d	b.d	
Quartz-sercite	3618M24_py58_3	b.d	b.d	b.d	380	620	b.d	b.d	b.d	2,5	b.d	b.d	b.d	b.d	b.d	b.d	b.d	b.d	b.d	b.d	b.d	b.d	b.d	b.d	b.d	
Quartz-sercite	3618M24_py58_4	b.d	b.d	b.d	294	390	36,6	b.d	b.d	5	b.d	b.d	b.d	b.d	1,4	b.d	b.d	b.d	b.d	b.d	b.d	b.d	b.d	b.d	0,28	
Quartz-sercite	3618M24_py58_5	b.d	b.d	b.d	176	270	b.d	b.d	2,73	b.d	b.d	b.d	b.d	b.d	b.d	b.d	b.d	b.d	b.d	b.d	b.d	b.d	b.d	b.d	0,118	
Quartz-sercite	3618M24_py61_10	b.d	b.d	b.d	25,8	4,5	4	b.d	b.d	2,26	b.d	10	b.d	b.d	b.d	b.d	b.d	b.d	b.d	b.d	b.d	b.d	b.d	b.d	b.d	
Quartz-sercite	3618M24_py61_11	b.d	b.d	b.d	26,7	1,84	b.d	b.d	b.d	1,63	b.d	7	b.d	b.d	b.d	b.d	b.d	b.d	b.d	b.d	b.d	b.d	b.d	b.d	b.d	
Quartz-sercite	3618M24_py61_12	b.d	b.d	b.d	3,54	2,8	b.d	b.d	b.d	2,7	b.d	26	b.d	b.d	b.d	b.d	b.d	b.d	b.d	b.d	b.d	b.d	b.d	b.d	b.d	
Quartz-sercite	3618M24_py62_1	b.d	b.d	b.d	39,7	b.d	b.d	b.d	b.d	1,85	b.d	b.d	b.d	b.d	b.d	b.d	b.d	b.d	b.d	b.d	b.d	b.d	b.d	b.d	b.d	
Quartz-sercite	3618M24_py62_10	b.d	b.d	b.d	54,8	2,5	b.d	b.d	b.d	3,48	b.d	b.d	b.d	b.d	b.d	b.d	b.d	b.d	b.d	b.d	b.d	b.d	b.d	b.d	0,15	
Quartz-sercite	3618M24_py62_2	b.d	b.d	b.d	280	3,8	3,5	b.d	b.d	1,64	b.d	b.d	b.d	b.d	b.d	b.d	b.d	b.d	b.d	b.d	0,019	b.d	b.d	b.d	0,387	
Quartz-sercite	3618M24_py62_3	b.d	b.d	b.d	233	11,4	b.d	b.d	b.d	1,76	b.d	b.d	b.d	b.d	b.d	b.d	b.d	b.d	b.d	b.d	b.d	b.d	b.d	b.d	0,18	

Quartz-sercite	3618M24_py62_4	b.d	b.d	b.d	185	6,7	4,1	b.d	b.d	1,47	b.d	b.d	b.d	b.d	b.d	b.d	b.d	b.d	b.d	b.d	b.d	b.d	b.d	b.d	b.d	b.d	0,183	
Quartz-sercite	3618M24_py62_5	b.d	b.d	b.d	155	3,1	b.d	b.d	b.d	b.d	b.d	b.d	b.d	b.d	b.d	b.d	b.d	b.d	b.d	b.d	b.d	b.d	b.d	b.d	b.d	b.d	0,116	
Quartz-sercite	3618M24_py62_6	b.d	b.d	b.d	111	8,3	b.d	b.d	b.d	1,79	b.d	b.d	b.d	b.d	b.d	b.d	b.d	b.d	b.d	b.d	b.d	b.d	b.d	b.d	b.d	b.d	b.d	
Quartz-sercite	3618M24_py62_7	b.d	b.d	b.d	97	5,4	7,3	b.d	b.d	1,64	b.d	b.d	b.d	b.d	b.d	b.d	b.d	b.d	b.d	b.d	b.d	b.d	b.d	b.d	b.d	b.d	0,203	
Quartz-sercite	3618M24_py62_8	b.d	b.d	b.d	66,3	3,8	5,1	b.d	b.d	1,91	b.d	b.d	b.d	b.d	b.d	b.d	b.d	b.d	b.d	b.d	b.d	b.d	b.d	b.d	b.d	b.d	0,292	
Quartz-sercite	3618M24_py62_9	b.d	b.d	b.d	64	b.d	9,5	b.d	b.d	b.d	b.d	b.d	b.d	b.d	b.d	b.d	b.d	b.d	b.d	b.d	b.d	b.d	b.d	b.d	b.d	b.d	1,16	
Quartz-sercite	3618M24_py64_1	b.d	b.d	b.d	12,3	17,3	b.d	b.d	b.d	2,04	b.d	b.d	b.d	b.d	b.d	b.d	b.d	b.d	b.d	b.d	b.d	b.d	b.d	b.d	b.d	b.d	b.d	
Quartz-sercite	3618M24_py64_2	b.d	b.d	b.d	660	96	b.d	b.d	b.d	b.d	b.d	b.d	b.d	b.d	b.d	b.d	b.d	b.d	b.d	b.d	b.d	b.d	b.d	b.d	b.d	b.d	2	b.d
Quartz-sercite	3618M24_py64_3	b.d	b.d	b.d	517	229	b.d	b.d	b.d	1,97	b.d	b.d	b.d	b.d	b.d	b.d	b.d	b.d	b.d	b.d	b.d	b.d	b.d	b.d	b.d	b.d	0,17	b.d
Quartz-sercite	3618M24_py64_4	b.d	b.d	b.d	1530	128	4,4	b.d	b.d	2,2	b.d	b.d	b.d	b.d	b.d	b.d	b.d	b.d	b.d	b.d	b.d	b.d	b.d	b.d	b.d	b.d	b.d	b.d
Quartz-sercite	3618M24_py64_5	b.d	b.d	b.d	295	162	3,8	b.d	b.d	2,37	b.d	b.d	b.d	b.d	b.d	b.d	b.d	b.d	b.d	b.d	b.d	b.d	b.d	b.d	b.d	b.d	b.d	b.d
Quartz-sercite	3618M24_py64_8	b.d	b.d	b.d	555	219	b.d	b.d	b.d	2,4	b.d	b.d	b.d	b.d	b.d	b.d	b.d	b.d	b.d	b.d	b.d	b.d	b.d	b.d	b.d	b.d	b.d	b.d
Quartz-sercite	3618M24_py65_1	b.d	b.d	b.d	29,9	50	b.d	b.d	b.d	3,1	b.d	b.d	b.d	b.d	b.d	b.d	b.d	b.d	b.d	b.d	b.d	b.d	b.d	b.d	b.d	b.d	b.d	b.d
Quartz-sercite	3618M24_py65_2	b.d	b.d	b.d	162	52,3	b.d	b.d	b.d	2,67	b.d	b.d	b.d	b.d	b.d	b.d	b.d	b.d	b.d	b.d	b.d	b.d	b.d	b.d	b.d	b.d	0,23	
Quartz-sercite	3618M24_py65_3	b.d	b.d	b.d	346	73	b.d	b.d	b.d	2,9	b.d	35	b.d	b.d	b.d	b.d	b.d	b.d	b.d	b.d	b.d	b.d	b.d	b.d	b.d	b.d	b.d	
Quartz-sercite	3618M9_py43_1	b.d	b.d	b.d	b.d	145	b.d	b.d	3,3	b.d	45	b.d	b.d	b.d	b.d	b.d	b.d	b.d	b.d	b.d	b.d	b.d	b.d	b.d	b.d	b.d	b.d	b.d
Quartz-sercite	3618M9_py43_2	b.d	b.d	b.d	b.d	b.d	105	b.d	b.d	2,43	b.d	26	b.d	b.d	0,26	b.d	b.d	b.d	b.d	0,025	b.d	b.d						
Quartz-sercite	3618M9_py43_3	b.d	b.d	b.d	b.d	b.d	279	b.d	b.d	1,39	b.d	b.d	b.d	b.d	0,08	b.d	b.d	b.d	b.d	b.d	b.d	b.d	b.d	b.d	b.d	b.d	b.d	b.d
Quartz-sercite	3618M9_py43_4	b.d	b.d	b.d	67,8	b.d	152	b.d	b.d	b.d	33	b.d	b.d	0,45	b.d	b.d	b.d	b.d	b.d	b.d	b.d	b.d	b.d	b.d	b.d	b.d	0,046	
Quartz-sercite	3618M9_py44_1	b.d	b.d	b.d	118	2,7	34,1	b.d	b.d	b.d	b.d	b.d	b.d	1,3	b.d	b.d	b.d	b.d	b.d	b.d	b.d	b.d	b.d	b.d	b.d	b.d	0,114	
Quartz-sercite	3618M9_py44_2	b.d	b.d	b.d	6,7	b.d	224	b.d	b.d	b.d	b.d	b.d	b.d	b.d	b.d	b.d	b.d	b.d	b.d	b.d	b.d	b.d	b.d	b.d	b.d	b.d	b.d	b.d
Quartz-sercite	3618M9_py44_3	b.d	b.d	b.d	14,9	b.d	40,6	b.d	b.d	b.d	b.d	b.d	b.d	b.d	b.d	b.d	b.d	b.d	b.d	0,19	b.d	0,137						
Quartz-sercite	3618M9_py44_4	b.d	b.d	b.d	32	b.d	116	b.d	b.d	b.d	b.d	b.d	b.d	6,8	0,34	b.d	b.d	b.d	b.d	0,04	b.d	0,447						
Quartz-sercite	3618M9_py44_5	b.d	b.d	b.d	8,8	b.d	12,5	b.d	b.d	2,6	b.d	b.d	b.d	b.d	b.d	b.d	b.d	b.d	b.d	b.d	b.d	b.d	b.d	b.d	b.d	b.d	b.d	
Quartz-sercite	3618M9_py44_6	b.d	b.d	b.d	3,27	b.d	17,2	b.d	b.d	2,65	b.d	b.d	b.d	b.d	b.d	b.d	b.d	b.d	b.d	b.d	b.d	b.d	b.d	b.d	b.d	b.d	b.d	
Quartz-sercite	3618M9_py45_1	b.d	b.d	b.d	59	b.d	76,9	b.d	b.d	3	b.d	b.d	b.d	b.d	b.d	b.d	b.d	b.d	b.d	b.d	b.d	b.d	b.d	b.d	b.d	b.d	b.d	
Quartz-sercite	3618M9_py45_10	b.d	b.d	b.d	27,9	b.d	85,2	b.d	b.d	b.d	b.d	b.d	b.d	124	b.d	b.d	b.d	b.d	0,04	0,22	b.d	0,295						
Quartz-sercite	3618M9_py45_11	b.d	b.d	b.d	46,5	b.d	75	b.d	b.d	b.d	b.d	b.d	b.d	b.d	b.d	b.d	b.d	b.d	b.d	b.d	b.d	b.d	b.d	b.d	b.d	b.d	b.d	
Quartz-sercite	3618M9_py45_12	b.d	b.d	b.d	52	b.d	93	b.d	b.d	b.d	b.d	b.d	b.d	260	b.d	b.d	b.d	b.d	0,85	b.d	b.d	b.d	b.d	b.d	b.d	b.d	0,73	
Quartz-sercite	3618M9_py45_2	b.d	b.d	b.d	111	3,7	69,1	b.d	b.d	b.d	b.d	b.d	b.d	b.d	b.d	b.d	b.d	b.d	b.d	b.d	b.d	b.d	b.d	b.d	b.d	b.d	b.d	
Quartz-sercite	3618M9_py45_3	b.d	b.d	b.d	217	5	7,3	b.d	b.d	3,5	b.d	b.d	b.d	b.d	b.d	b.d	b.d	b.d	b.d	b.d	b.d	b.d	b.d	b.d	b.d	b.d	b.d	

Quartz-sercite	3618M9_py45_4	b.d	b.d	b.d	12,1	5,6	57,3	b.d	b.d	2,52	b.d	b.d	b.d	b.d	b.d	b.d	b.d	b.d	b.d	b.d	b.d	b.d	b.d	b.d	b.d	b.d	b.d	
Quartz-sercite	3618M9_py45_5	b.d	b.d	b.d	52,8	b.d	120	b.d	b.d	1,9	b.d	b.d	0,61	b.d	b.d	b.d	b.d	b.d	b.d	b.d	b.d	b.d	b.d	b.d	b.d	b.d	b.d	0,099
Quartz-sercite	3618M9_py45_6	b.d	b.d	b.d	70	b.d	60,5	b.d	b.d	b.d	b.d	b.d	b.d	b.d	b.d	b.d	b.d	b.d	b.d	b.d	b.d	b.d	b.d	b.d	b.d	b.d	b.d	
Quartz-sercite	3618M9_py45_7	b.d	b.d	b.d	800	b.d	46,4	b.d	b.d	b.d	b.d	b.d	2,6	0,35	b.d	b.d	b.d	b.d	b.d	b.d	b.d	b.d	b.d	b.d	b.d	b.d	b.d	0,51
Quartz-sercite	3618M9_py45_8	b.d	b.d	b.d	70	b.d	60,3	b.d	b.d	b.d	b.d	b.d	0,43	b.d	b.d	b.d	b.d	b.d	b.d	b.d	b.d	b.d	b.d	b.d	b.d	b.d	b.d	
Quartz-sercite	3618M9_py45_9	b.d	b.d	b.d	7,1	b.d	21,9	b.d	b.d	b.d	b.d	200	0,74	b.d	b.d	b.d	b.d	b.d	b.d	b.d	b.d	b.d	b.d	b.d	b.d	b.d	b.d	0,64
Quartz-sercite	3618M9_py47_2	b.d	b.d	b.d	13,2	16	61	b.d	b.d	b.d	b.d	b.d	b.d	b.d	b.d	b.d	b.d	b.d	b.d	b.d	0,08	b.d	b.d	b.d	b.d	b.d	b.d	
Quartz-sercite	3618M9_py47_3	b.d	b.d	b.d	201	b.d	6,1	b.d	b.d	b.d	b.d	b.d	b.d	b.d	b.d	b.d	b.d	b.d	b.d	b.d	b.d	b.d	b.d	b.d	0,115	b.d	0,36	
Quartz-sercite	3618M9_py47_5	b.d	b.d	b.d	74	b.d	57	b.d	b.d	b.d	b.d	b.d	3,6	b.d	b.d	b.d	b.d	b.d	b.d	b.d	b.d	b.d	b.d	b.d	b.d	b.d	b.d	0,23
Quartz-sercite	3618M9_py47_7	b.d	b.d	b.d	158	5,2	7,5	b.d	b.d	2	b.d	b.d	46	b.d	b.d	b.d	b.d	b.d	b.d	b.d	0,104	b.d	b.d	b.d	b.d	b.d	0,47	0,53
Quartz-sercite	3618M9_py47_8	b.d	b.d	b.d	45	b.d	17,8	b.d	b.d	b.d	b.d	b.d	10,5	b.d	b.d	b.d	b.d	b.d	b.d	b.d	b.d	b.d	b.d	b.d	b.d	b.d	b.d	
Quartz-sercite	7795M11_py50_1	b.d	b.d	b.d	b.d	b.d	9,5	b.d	b.d	2,5	b.d	340	b.d	b.d	b.d	b.d	b.d	b.d	b.d	b.d	b.d	b.d	b.d	b.d	b.d	b.d	b.d	
Quartz-sercite	7795M11_py50_2	b.d	b.d	b.d	b.d	b.d	1,47	b.d	b.d	b.d	b.d	b.d	b.d	b.d	b.d	b.d	b.d	b.d	b.d	b.d	0,026	b.d	b.d	b.d	b.d	b.d	b.d	
Quartz-sercite	7795M11_py50_3	b.d	b.d	b.d	b.d	b.d	9,2	b.d	b.d	b.d	b.d	b.d	b.d	b.d	b.d	b.d	b.d	b.d	b.d	b.d	b.d	b.d	b.d	b.d	b.d	b.d	b.d	
Quartz-sercite	7795M11_py50_4	b.d	b.d	b.d	b.d	b.d	17	b.d	b.d	b.d	b.d	b.d	b.d	b.d	b.d	b.d	b.d	b.d	b.d	b.d	b.d	b.d	b.d	b.d	b.d	b.d	0,67	
Quartz-sercite	7795M11_py50_5	b.d	b.d	b.d	b.d	b.d	63	b.d	b.d	b.d	b.d	b.d	0,21	b.d	b.d	b.d	b.d	b.d	b.d	b.d	0,18	b.d	b.d	b.d	b.d	b.d	0,148	0,5
Quartz-sercite	7795M11_py50_6	b.d	b.d	b.d	5	32,1	280	b.d	b.d	b.d	b.d	b.d	0,2	b.d	b.d	b.d	b.d	b.d	b.d	b.d	0,012	b.d	0,39					
Quartz-sercite	7795M11_py50_7	b.d	b.d	b.d	b.d	b.d	8,3	b.d	b.d	2,7	b.d	b.d	b.d	b.d	b.d	b.d	b.d	b.d	b.d	b.d	b.d	b.d	b.d	b.d	b.d	b.d	b.d	
Quartz-sercite	7795M11_py50_8	b.d	b.d	b.d	8,8	6,3	200	b.d	b.d	b.d	b.d	2,70E+03	b.d	b.d	b.d	b.d	b.d	b.d	b.d	b.d	b.d	b.d	b.d	b.d	b.d	b.d	0,24	0,64
Quartz-sercite	7795M11_py50_9	b.d	b.d	b.d	b.d	b.d	21	17	b.d	b.d	b.d	b.d	b.d	b.d	b.d	b.d	b.d	b.d	b.d	1,6	b.d	0,061	b.d	b.d	0,86	0,65		
Quartz-sercite	7795M11_py52_2	b.d	b.d	b.d	b.d	b.d	22,3	b.d	b.d	b.d	b.d	b.d	b.d	b.d	b.d	b.d	b.d	b.d	b.d	b.d	b.d	b.d	b.d	b.d	b.d	b.d	b.d	0,105
Quartz-sercite	7795M11_py52_3	b.d	b.d	b.d	b.d	b.d	58	b.d	b.d	b.d	b.d	93	b.d	b.d	b.d	b.d	b.d	b.d	b.d	b.d	b.d	b.d	b.d	b.d	b.d	b.d	1,26	
Quartz-sercite	7795M11_py52_4	b.d	b.d	b.d	b.d	b.d	280	b.d	b.d	b.d	b.d	b.d	1,58	b.d	b.d	b.d	b.d	b.d	b.d	b.d	b.d	1,7	b.d	1,29	1,26			
Quartz-sercite	7795M11_py52_5	b.d	b.d	b.d	b.d	b.d	15	b.d	b.d	1,9	b.d	b.d	b.d	b.d	b.d	b.d	b.d	b.d	b.d	b.d	b.d	b.d	b.d	b.d	b.d	b.d	b.d	0,135
Quartz-sercite	7795M11_py52_6	b.d	b.d	b.d	b.d	b.d	19,2	b.d	b.d	2,1	b.d	b.d	b.d	b.d	b.d	b.d	b.d	b.d	b.d	0,012	b.d	b.d	b.d	b.d	b.d	b.d	b.d	7,29
Quartz-sercite	7795M11_py54_1	b.d	b.d	b.d	b.d	6,6	540	b.d	b.d	b.d	b.d	b.d	5	b.d	b.d	b.d	b.d	b.d	b.d	b.d	0,83	b.d	b.d	5,8	12,3			
Quartz-sercite	7795M11_py54_2	b.d	b.d	4,9	b.d	8,7	4,40E+03	b.d	b.d	b.d	b.d	b.d	3,84	b.d	b.d	b.d	b.d	b.d	b.d	b.d	0,135	b.d	b.d	7,29	56			
Quartz-sercite	7795M11_py54_3	b.d	b.d	b.d	20	b.d	610	27	b.d	b.d	b.d	b.d	3,1	b.d	b.d	b.d	b.d	b.d	b.d	b.d	0,48	b.d	b.d	b.d	b.d	b.d	460	
Quartz-sercite	7795M11_py54_4	b.d	b.d	b.d	1,8	11,2	370	b.d	b.d	b.d	b.d	b.d	b.d	b.d	b.d	b.d	b.d	b.d	b.d	b.d	0,56	b.d	b.d	b.d	b.d	b.d	b.d	0,52
Quartz-sercite	7795M11_py54_5	b.d	b.d	b.d	2,5	53	b.d	b.d	2,4	b.d	b.d	b.d	b.d	b.d	b.d	b.d	b.d	b.d	b.d	0,03	b.d	b.d	b.d	b.d	b.d	b.d	b.d	0,52
Quartz-sercite	7795M11_py55_1	b.d	b.d	b.d	0,72	1,18	4,7	b.d	b.d	b.d	b.d	b.d	b.d	b.d	b.d	b.d	b.d	b.d	b.d	b.d	b.d	b.d	b.d	b.d	b.d	b.d	b.d	0,099

Quartz-sercite	7795M11_py55_2	b.d	b.d	b.d	b.d	b.d	16	b.d	b.d	3,1	b.d	810	b.d	b.d	b.d	b.d	b.d	b.d	b.d	b.d	b.d	b.d	b.d	b.d	b.d	b.d	
Quartz-sercite	7795M11_py55_3	b.d	b.d	b.d	0,95	2,1	4,5	b.d	b.d	b.d	b.d	146	b.d	b.d	b.d	b.d	b.d	b.d	b.d	b.d	b.d	b.d	b.d	b.d	b.d	b.d	
Quartz-sercite	7795M11_py55_4	b.d	b.d	b.d	b.d	1,7	21,6	b.d	b.d	4,3	b.d	b.d	b.d	b.d	b.d	b.d	b.d	b.d	b.d	b.d	b.d	b.d	b.d	b.d	b.d	b.d	
Quartz-sercite	7795M11_py57_1	b.d	b.d	b.d	b.d	b.d	3,93	b.d	b.d	b.d	b.d	b.d	b.d	b.d	b.d	b.d	b.d	b.d	b.d	b.d	b.d	b.d	b.d	b.d	b.d	b.d	
Quartz-sercite	7795M11_py57_2	b.d	b.d	b.d	b.d	b.d	20	b.d	b.d	b.d	b.d	120	b.d	b.d	b.d	b.d	b.d	b.d	b.d	b.d	b.d	b.d	b.d	b.d	b.d	4,9	
Quartz-sercite	7795M11_py57_3	b.d	b.d	b.d	11,7	3,9	73	b.d	b.d	b.d	b.d	b.d	b.d	b.d	b.d	0,019	b.d	b.d	b.d	b.d	b.d	b.d	b.d	b.d	b.d	b.d	
Quartz-sercite	7795M11_py57_4	b.d	b.d	b.d	b.d	b.d	1,03	b.d	b.d	2,5	b.d	b.d	b.d	b.d	b.d	b.d	b.d	b.d	b.d	0,009	b.d	b.d	b.d	b.d	b.d	b.d	
Quartz-sercite	7795M11_py57_5	b.d	b.d	b.d	20,9	5,2	0,96	b.d	b.d	b.d	b.d	56	b.d	b.d	b.d	b.d	b.d	b.d	b.d	0,18	0,025	b.d	b.d	b.d	b.d	b.d	
Quartz-sercite	7795M8_py100_1	b.d	b.d	b.d	7,1	b.d	3	b.d	b.d	1,73	b.d	b.d	b.d	b.d	b.d	b.d	b.d	b.d	b.d	b.d	b.d	b.d	b.d	b.d	b.d	b.d	
Quartz-sercite	7795M8_py100_2	b.d	b.d	b.d	3,44	b.d	20,6	b.d	b.d	2,16	b.d	b.d	b.d	b.d	b.d	b.d	b.d	b.d	b.d	b.d	b.d	b.d	b.d	b.d	b.d	0,049	
Quartz-sercite	7795M8_py100_3	b.d	b.d	b.d	0,73	9,8	b.d	b.d	b.d	2,45	b.d	b.d	b.d	b.d	b.d	b.d	b.d	b.d	b.d	b.d	b.d	b.d	b.d	b.d	b.d	b.d	
Quartz-sercite	7795M8_py100_4	b.d	b.d	b.d	2,11	b.d	395	b.d	b.d	2,7	b.d	b.d	b.d	b.d	b.d	b.d	b.d	b.d	b.d	0,02	b.d	b.d	b.d	b.d	0,61	0,072	
Quartz-sercite	7795M8_py100_5	b.d	b.d	b.d	1,17	b.d	107	b.d	b.d	b.d	b.d	b.d	b.d	b.d	b.d	b.d	b.d	b.d	b.d	b.d	b.d	b.d	b.d	b.d	b.d	b.d	
Quartz-sercite	7795M8_py100_6	b.d	b.d	b.d	1,51	b.d	79	b.d	b.d	b.d	b.d	b.d	b.d	b.d	b.d	b.d	b.d	b.d	b.d	b.d	b.d	b.d	b.d	b.d	b.d	b.d	
Quartz-sercite	7795M8_py106_1	b.d	b.d	5,2	b.d	b.d	267	b.d	b.d	b.d	b.d	b.d	b.d	b.d	b.d	b.d	b.d	b.d	b.d	b.d	b.d	b.d	b.d	b.d	b.d	0,96	0,4
Quartz-sercite	7795M8_py106_2	b.d	b.d	b.d	43,3	b.d	206	b.d	b.d	2,1	b.d	75	77	b.d	b.d	b.d	b.d	b.d	b.d	0,66	0,47	b.d	b.d	b.d	b.d	0,61	0,62
Quartz-sercite	7795M8_py106_3	b.d	b.d	b.d	3,7	b.d	400	b.d	b.d	b.d	b.d	39	b.d	b.d	b.d	b.d	b.d	b.d	b.d	b.d	b.d	b.d	b.d	b.d	b.d	b.d	0,36
Quartz-sercite	7795M8_py106_4	b.d	b.d	b.d	b.d	b.d	248	b.d	b.d	b.d	b.d	b.d	b.d	b.d	b.d	0,28	b.d	b.d	b.d	b.d	b.d	b.d	b.d	b.d	b.d	b.d	
Quartz-sercite	7795M8_py106_5	b.d	b.d	b.d	23	b.d	218	b.d	b.d	b.d	b.d	100	b.d	1,61	b.d	b.d	b.d	b.d	b.d	0,47	b.d	b.d	b.d	b.d	b.d	0,56	1,89
Quartz-sercite	7795M8_py109_1	b.d	b.d	b.d	249	2,4	20,7	b.d	b.d	b.d	b.d	b.d	b.d	b.d	b.d	b.d	b.d	b.d	b.d	b.d	b.d	b.d	b.d	b.d	b.d	b.d	
Quartz-sercite	7795M8_py109_2	b.d	b.d	b.d	72,3	14,6	51	b.d	b.d	2,4	b.d	248	b.d	b.d	0,02	b.d	b.d	b.d	b.d	b.d	b.d	b.d	b.d	b.d	b.d	0,056	
Quartz-sercite	7795M8_py109_3	b.d	b.d	b.d	96	8,2	60	b.d	b.d	2,1	b.d	71	b.d	b.d	b.d	b.d	b.d	b.d	b.d	b.d	b.d	b.d	b.d	b.d	b.d	0,8	
Quartz-sercite	7795M8_py109_4	b.d	b.d	b.d	2,03	b.d	2,64	b.d	b.d	b.d	b.d	81	b.d	b.d	b.d	b.d	b.d	b.d	b.d	b.d	b.d	b.d	b.d	b.d	b.d	b.d	
Quartz-sercite	7795M8_py109_5	b.d	b.d	b.d	42,6	b.d	59,9	b.d	b.d	2,02	b.d	b.d	b.d	b.d	b.d	b.d	b.d	b.d	b.d	b.d	b.d	b.d	b.d	b.d	b.d	b.d	
Quartz-sercite	7795M8_py110_1	b.d	b.d	b.d	241	b.d	14,4	b.d	b.d	2,5	b.d	55	b.d	b.d	1,93	b.d	b.d	b.d	b.d	b.d	b.d	b.d	b.d	b.d	b.d	2,01	
Quartz-sercite	7795M8_py110_2	b.d	b.d	b.d	5,8	20,2	1,85	b.d	b.d	b.d	b.d	210	b.d	b.d	b.d	b.d	b.d	b.d	b.d	b.d	b.d	b.d	b.d	b.d	b.d	b.d	
Quartz-sercite	7795M8_py110_3	b.d	b.d	b.d	5,7	17,6	12,5	b.d	b.d	2,9	b.d	140	b.d	b.d	b.d	b.d	b.d	b.d	b.d	b.d	b.d	b.d	b.d	b.d	b.d	0,42	
Quartz-sercite	7795M8_py110_4	b.d	b.d	b.d	7	64	36	b.d	b.d	b.d	b.d	b.d	b.d	b.d	b.d	b.d	b.d	b.d	b.d	b.d	b.d	b.d	b.d	b.d	b.d	b.d	
Quartz-sercite	7795M8_py110_5	b.d	b.d	b.d	14,7	56	290	b.d	b.d	b.d	b.d	b.d	b.d	b.d	b.d	b.d	b.d	b.d	b.d	b.d	b.d	b.d	b.d	b.d	b.d	0,35	0,45
Quartz-sercite	7795M8_py112_1	b.d	b.d	b.d	0,94	b.d	45	b.d	b.d	b.d	b.d	27	b.d	b.d	b.d	b.d	b.d	b.d	b.d	b.d	b.d	b.d	b.d	b.d	b.d	0,26	2,61
Quartz-sercite	7795M8_py112_2	b.d	b.d	b.d	0,93	b.d	1,46	b.d	b.d	b.d	b.d	14	b.d	b.d	b.d	b.d	b.d	b.d	b.d	b.d	b.d	b.d	b.d	b.d	b.d	b.d	

Quartz-sercite	7795M8_py112_3	b.d	b.d	b.d	b.d	b.d	2,43	b.d	b.d	4	b.d	b.d	b.d	b.d	b.d	b.d	b.d	0,65	b.d	b.d	b.d	b.d	b.d	b.d	
Quartz-sercite	7795M8_py112_4	b.d	b.d	110	1,06	2,4	7,1	b.d	b.d	4,9	b.d	b.d	b.d	b.d	b.d	b.d	b.d	b.d	b.d	0,011	1,25	b.d	b.d	b.d	0,3
Quartz-sercite	7795M8_py112_5	b.d	b.d	b.d	0,84	b.d	1,27	b.d	b.d	b.d	b.d	b.d	b.d	b.d	b.d	b.d	b.d	b.d	b.d	b.d	b.d	b.d	b.d	b.d	b.d
Quartz-sercite	7795M8_py112_6	b.d	b.d	b.d	2,7	b.d	167	b.d	b.d	2,5	b.d	b.d	0,09	b.d	b.d	b.d	b.d	b.d	b.d	b.d	0,027	b.d	b.d	b.d	b.d
Quartz-sercite	7795M8_py50_2	b.d	b.d	b.d	120	4,1	b.d	b.d	b.d	b.d	260	b.d	b.d	b.d	b.d	b.d	b.d	0,19	b.d	b.d	b.d	b.d	b.d	b.d	b.d
Quartz-sercite	7795M8_py50_3	b.d	b.d	b.d	63,5	b.d	2260	b.d	b.d	b.d	110	66	b.d	b.d	b.d	b.d	b.d	0,11	b.d	b.d	b.d	b.d	b.d	b.d	b.d
Quartz-sercite	7795M8_py50_4	b.d	b.d	b.d	83	2,8	b.d	b.d	b.d	3,1	b.d	b.d	0,14	b.d	b.d	b.d	b.d	b.d	b.d	b.d	0,213	0,065			
Quartz-sercite	7795M8_py99_1	b.d	b.d	b.d	41,1	b.d	5,1	b.d	b.d	1,52	b.d	b.d	b.d	b.d	b.d	b.d	b.d	b.d	b.d	b.d	b.d	b.d	b.d	b.d	0,108
Quartz-sercite	7795M8_py99_2	b.d	b.d	b.d	36	32	b.d	b.d	b.d	1,38	b.d	b.d	b.d	b.d	b.d	b.d	b.d	b.d	b.d	b.d	b.d	b.d	b.d	b.d	b.d
Quartz-sercite	7795M8_py99_3	b.d	b.d	b.d	29,8	5,2	4,7	b.d	b.d	1,95	b.d	b.d	b.d	b.d	b.d	b.d	b.d	b.d	b.d	b.d	b.d	b.d	b.d	b.d	b.d
Quartz-sercite	7795M8_py99_4	b.d	b.d	b.d	25	2,8	b.d	b.d	b.d	1,88	b.d	b.d	b.d	b.d	b.d	b.d	b.d	b.d	b.d	b.d	b.d	b.d	b.d	b.d	b.d
Quartz-sercite	7795M8_py99_5	b.d	b.d	b.d	22,8	3,1	b.d	b.d	b.d	1,32	b.d	b.d	b.d	b.d	b.d	b.d	b.d	b.d	b.d	b.d	b.d	b.d	b.d	b.d	b.d

Statistic	V	Cr	Mn	Co	Ni	Cu	Zn	Ga	Ge	As	Se	Mo	Ag	Cd	In	Sn	Sb	Te	W	Au	Hg	Tl	Pb	Bi
Minimum	3,50	4,20	4,80	0,71	1,18	0,96	14,00	1,30	1,32	4,90	5,00	0,09	0,20	0,02	0,02	0,20	1,50	0,02	0,01	0,01	1,25	0,01	0,15	0,05
Maximum	3,50	4,40	1080,00	1530,00	960,00	9700,00	1200,00	5,30	10,10	1760,00	2700,00	260,00	450,00	4,30	0,90	47,00	930,00	23,00	2,30	8,60	1,70	0,48	2250,00	460,00
Mean	3,50	4,30	139,08	159,24	83,91	630,67	230,45	3,30	2,85	224,45	214,29	39,99	34,72	1,02	0,24	18,25	160,47	3,09	0,41	0,75	1,48	0,14	137,84	14,90
Median	3,50	4,30	13,20	45,50	33,80	60,30	37,00	3,30	2,50	22,50	93,00	3,60	6,40	0,50	0,17	16,95	7,65	0,66	0,09	0,06	1,48	0,07	10,45	1,02